Investigations on magnetically hard and mechanically stiff magnetoactive elastomers : From local interactions towards the development of functional structures

Svenja Hermann

UBFC
UNIVERSITÉ
BOURGOGNE FRANCHE-COMTÉ

UNIVERSITÉ DE FRANCHE-COMTÉ

MMT

Thèse de doctorat de l'établissement
Université Bourgogne Franche-Comté
preparée à l'Université de Franche-Comté

École doctorale n^o 37
Sciences Pour l'Ingénieur et Microtechniques

Doctorat de Mécanique

Par

Svenja HERMANN

Investigations on magnetically hard and mechanically stiff magnetoactive elastomers – From local interactions towards the development of functional structures

(Investigations sur les élastomères magnétoactifs magnétiquement durs et mécaniquement rigides – Des phénomènes d'interactions locales vers le développement de structures fonctionnelles)

Thèse présentée et soutenue à Besançon, le 29 juin 2021

Composition du Jury :

Olivier THOMAS	Professeur des Universités (ENSAM)	Président
Konstantinos DANAS	Chargé de Recherche (CNRS LMS)	Rapporteur
Laurent DANIEL	Professeur des Universités (Centrale Supelec)	Rapporteur
Markus KÄSTNER	Professeur des Universités (TU Dresden)	Examinateur
Afef LEBOUC	Directrice de Recherche (CNRS G2Elab)	Examinatrice
Pauline BUTAUD	Maître de conférences (FEMTO-ST)	Directrice de Thèse
Gaël CHEVALLIER	Professeur des Universités (FEMTO-ST)	Directeur de Thèse
Jean-François MANCEAU	Professeur des Universités (FEMTO-ST)	Directeur de Thèse

Acknowledgements

Je tiens à remercier Olivier THOMAS pour avoir présidé mon jury de thèse. Je remercie Kostas DANAS et Laurent DANIEL d'avoir examiné mes travaux en détail en tant que rapporteur. Merci à Thomas KÄSTNER et Afef LEBOUC pour leur participation à ma soutenance de thèse. Je souhaite remercier tous les membres de mon jury de thèse pour leurs questions et l'échange très intéressant lors de la soutenance.

J'exprime ma gratitude à mes directeurs de thèse, Gaël CHEVALLIER, Jean-François MANCEAU et Pauline BUTAUD, qui m'ont fait découvrir le monde de la recherche. Ils m'ont soutenue avec leur expertise et leur enthousiasme au fil des années. C'est leur engagement qui m'a inspiré à vouloir rester dans le monde de la recherche et je leur en suis très reconnaissante. Je tiens aussi à remercier Laurent HIRSINGER pour les discussions autour de la magnéto-élasticité et la recherche en général. Son implication dans la thèse m'a permis de progresser en termes de connaissances scientifiques et aussi en termes d'approches scientifiques ce que j'apprécie beaucoup.

Je remercie l'entreprise Moving Magnet Technologies (MMT) pour avoir financé cette thèse. Je tiens à remercier en particulier Christophe ESPANET, Valentin PRÉAULT et Maxime SAVARY pour les échanges autour des nombreux sujets différents (comme par exemple la caractérisation expérimentale, la modélisation multi-échelle ou le magnétisme en général) pendant lesquels j'ai beaucoup profité de leurs différents domaines d'expertise. Je souhaite également remercier les collègues de MMT avec qui j'ai eu plaisir à travailler pendant ces années et de faire des activités hors travail comme le Trail des Forts, des randonnées, des sorties en course, roller et au bar.

Pour le soutien dans la réalisation des démonstrateurs, et bancs d'essais je remercie particulièrement les collègues dans les ateliers chez MMT et Vincent TISSOT au Département Mécanique Appliquée (DMA) sans qui une grande partie des idées seraient restées au stade du concept. Les caractérisations expérimentales n'auraient pas été possibles sans le soutien de Xavier GABRION, Thomas JEANNIN et Marina RASCHETTI et je les remercie beaucoup pour cela. Au DMA, je tiens à remercier aussi Christine FROIDEVAUX, Isabelle MAILLOTTE, Delphine TRAVAGLINI et le SCI de FEMTO-ST pour leur réactivité et leur gestion des évènements, urgences et imprévus.

Merci beaucoup aux collègues avec qui j'ai passé le plus de temps au DMA pendant les années de thèse : Emmanuel BACHY avec qui j'ai découvert que la science se boit en pinte, Ludovic BEBON qui a été un super coéquipier dans la "Team Matériau" du bureau, Kévin JABOVISTE qui m'a appris que l'eau à une vie remarquable, Justine LARIVIERE qui a remonté une piste rouge avec moi à pied, Gaël MATTEN avec qui j'ai soulevé l'arc de triomphe du pont Battant, Rafael TELOLI avec qui j'ai étudié la possibilité de maximiser le trajet d'un canoë sur une rivière et Margaux TOPENOT qui en plus d'être une très bonne amie est une très bonne colocataire. Au département Micro et Nano Sciences et Systèmes (MN2S) je souhaite remercier Olivia BEN M'BAREK chez qui on va faire un barbecue bientôt, Daniel GUNEYSU qui est surement en train de boire un café soluble en ce moment, Clode HUMBERT avec qui je suis à égalité maintenant dans le défi phonétique, et Sylvain MIDROUET grâce à qui j'ai découvert la pratique d'épeler par des drapeaux. Merci en plus à tous les autres collègues du DMA et de MN2S avec qui j'ai passé des bons moments par exemple en formation, en course de nuit dans les bois, au "Team Building" sportif des STAPS, au ski, à la gare d'eau ou en pause-café.

Ich möchte außerdem meinen Freunden aus der Heimat und aus der Studienzeit danken, die während der letzten Jahre an mich gedacht haben und über deren telefonische Unterstützung und Besuche ich mich immer sehr gefreut habe. Ein besonderer Dank geht an meine Eltern und meine Omas, die mir das Studium ermöglicht haben und die mich, zusammen mit meinem Bruder, in den letzten Jahren immer wieder dazu motiviert haben, neugierig zu bleiben. Zum Schluss möchte ich Tobias von ganzem Herzen für seine uneingeschränkte Unterstützung sowie die Zeit und die Motivation danken, die er mir in den vergangenen Jahren gegeben hat.

Table of Contents

Introduction

Industrial context

This PhD thesis has been prepared in the context of an industrial convention of training by research (*Convention Industrielle de Formation par la Recherche, CIFRE*) between the laboratory FEMTO-ST and the company Moving Magnet Technologies (MMT). The design of electromagnetic solutions is one of the core competencies of MMT, the company is thus interested in emerging mechatronic technologies and new materials. In this context, flexible magnets have been identified as a possible candidate for the development of innovative concepts for actuators and sensors.

Commercially available flexible magnets are usually rubber bound. They can be purchased in form of sheets, stripes or tapes for example (cf. figure 1). Other names, which are currently used, are “magnetic sheets”, “magnetic rubber”, “rubber magnets”, “magnetic tape”, “magnetic strips” or “flexible magnetic tape”. A well-known example of a flexible magnet is the functional element which keeps the door of a refrigerator closed. The datasheets of industrial flexible magnets contain information about the magnetic characteristics of the material, but rarely provide information about the mechanical characteristics. Rubber-bound magnets are more compliant than their sintered counterparts, but show a high mechanical stiffness. A class of magnetically active composite materials with low mechanical stiffness are MagnetoActive Elastomers (MAEs).

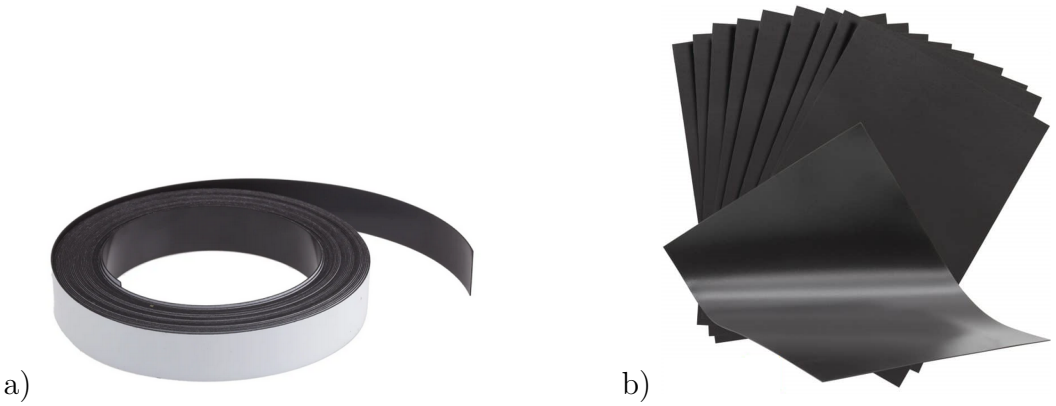

a) b)

Figure 1: Examples of commercially available magnetic strips (a, [RS Components 2020]) and magnetic sheets (b, [TheMagnetShop 2020]).

Magnetoactive elastomers (MAEs)

MAEs are composite materials consisting of magnetic particles and an elastomer matrix. Within the matrix, the particles are randomly dispersed (isotropic structure) or arranged in columns (transversely isotropic structure) as shown in figure 2. The composite material is also called MagnetoRheological Elastomer (MRE) to emphasize that magnetic fields give access to the material's ability to flow (rheological properties). This effect was first discovered in viscous suspensions of magnetically soft particles (MR fluids) where the application of magnetic fields makes the particles align in chains. The modification of the structure, in turn, changes the material behavior [Jolly+ 1999] and causes the so-called "Magneto-Rheological(MR) effect". Similar effects occur in elastomer based composites [Jolly+ 1996a], but compared to liquid based suspensions, the time stability of the material is enhanced: once the matrix is polymerized, the particle sedimentation due to gravity becomes insignificant. Nevertheless, soft matrices (Young's modulus $E \approx 10^4 - 10^5$ Pa) allow particle movements in the matrix and the modification of rheological properties of MRE. In the present work, the more general term "MAE" is used since the focus is not put on the rheological behavior.

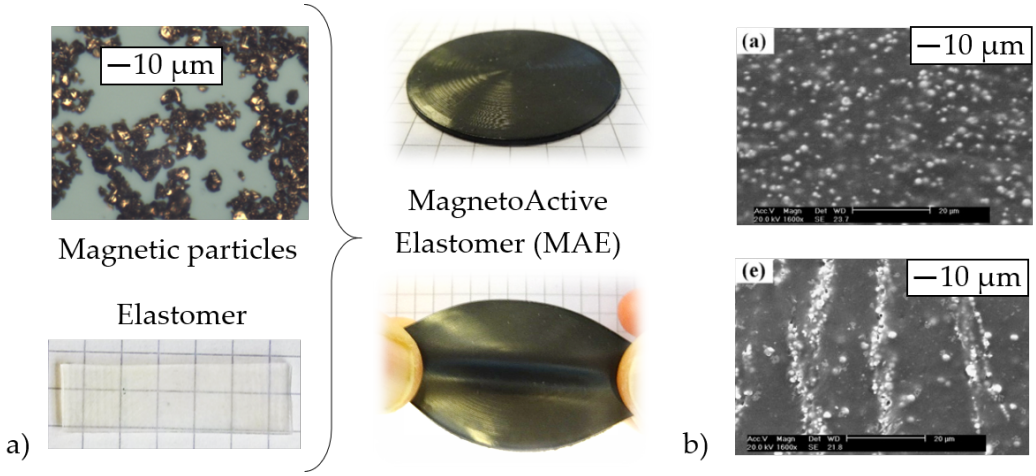

Figure 2: Composition of a MagnetoActive Elastomer (a) and scanning electron microscope (SEM) images obtained by [Chen+ 2007] for a MAE with an isotropic structure (top) and a transversely isotropic structure (bottom) (b).

The fixation of the particles in the matrix offers the possibility to use not only magnetically soft particles, showing nearly no magnetization in absence of a magnetic field, but also magnetically hard particles which remain magnetized within the matrix. The corresponding composite types are called soft(S)-MAE and hard(H)-MAE respectively in the following with the first letter referring to the magnetic properties. H-MAE can be magnetized after the elaboration in strong external magnetic fields ([Stepanov+ 2012]) but specimen have also been realized by 3D printing with magnetized particles in the filament [Kim+ 2018]. Since S-MAE

were discovered first, most of the existing studies are dedicated to the magnetically soft composite. But the increasing number of studies on H-MAE during the last years shows, that the interest in the magnetically hard but mechanically compliant composite material grows steadily.

Objective 1: manufacturing of H-MAE composites

The company MMT is interested in the use of H-MAE; therefore, one of the goals of this PhD thesis was the realization and documentation of the manufacturing process to provide samples for the subsequent analysis.

Material behavior of MAE

A large part of the **experimental studies** on H-MAEs deals with their material properties. The magnetic and mechanical behavior can be analyzed separately to determine the material constants. An important magnetic characteristic of H-MAE is the relation between the magnetic field H and the resulting magnetic flux density B in the specimen. Material constants like the saturation magnetization, the residual flux density and the coercive field strength are commonly used to compare different kinds of composites ([Linke+ 2016]). A mechanical loading can be applied via a displacement or a force to test specimens and aim to describe the relation of the mechanical stress σ and strain ε. Studies of the mechanical behavior of H-MAE show, that the material behavior is viscoelastic (cf. [Kramarenko+ 2015] for example). The test strategy depends on the purpose of the study and can consist of quasi-static tests, aiming to describe the stationary mechanical behavior ([Borin+ 2013]), or include dynamic loadings to determine characteristics like storage and loss moduli ([Kramarenko+ 2015]). In addition to the separate studies in each physical domain, the influence of magnetic fields on the mechanical properties and from mechanical loading in the magnetic behavior can also be analyzed. In this case, the effect of a loading in one physical domain on the state in the complementary physical domain is analyzed (cf. figure 3).
The magneto-mechanical coupling is caused by interaction of the magnetic particles. A recurring research topic for H-MAE is the influence of the permanent magnetization on the mechanical properties in absence of external fields. An increase of the Young's modulus and the time constant as well as residual strain after the formation have been reported [Kramarenko+ 2015; Stepanov+ 2012]. The application of external magnetic fields causes a variation of the quasi-static elastic as well as of the dynamic viscoelastic properties [Borin+ 2013; Kramarenko+ 2015]. In addition, the elongation of S-MAE specimen with isotropic structure in magnetic fields has been observed and explained by particle motions within the soft elastomer matrix [Stepanov+ 2008; Guan+ 2008]. The effect is often called magnetostriction but it is mainly due to the modification of the structure and not to magnetocristalline processes in the particles. Experimental studies on the coupled behavior of MAE require specific measurement equipment, since no standardized test bench is commercially available yet. The experimental setups in magneto-

mechanical tests have to account for the application of mechanical and magnetic loadings and the measurement of mechanical and magnetic quantities, as shown by [Bodelot+ 2018] for example.

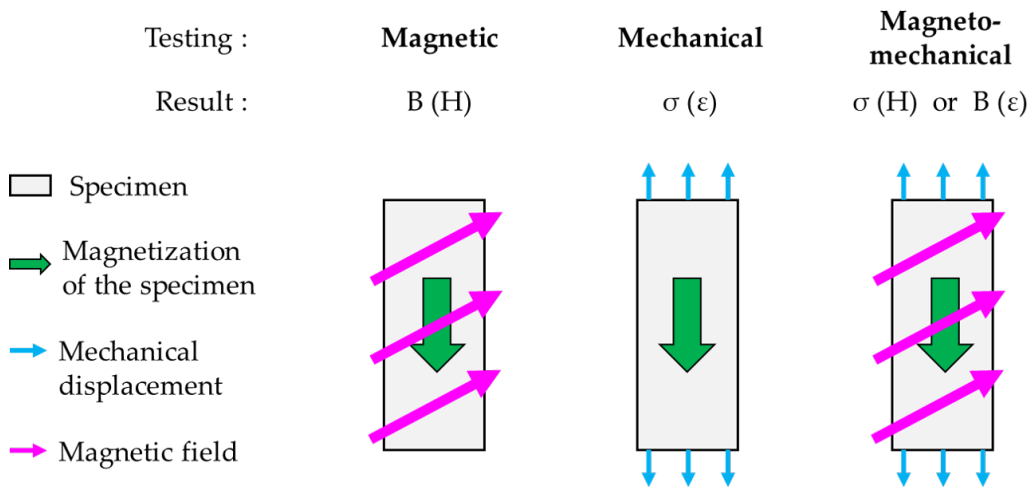

Figure 3: Schematic representation of different experimental testing methods applied on a magnetized H-MAE specimen, B – magnetic flux density, H – magnetic field, σ – mechanical stress, ε – mechanical strain.

Objective 2: experimental characterization of H-MAE composites

The experimental characterization of H-MAE is part of the goals of this PhD thesis. The task comprises the identification and the use of standard characterization tools and procedures for the determination of the uncoupled characteristics of the composite material. In addition, an approach for the characterization of the coupled behavior of H-MAE was sought in the context of this thesis along with a concrete concept for a magneto-mechanical test bench.

The research on the material behavior concerns not only experimental studies but also the development of **material models**. Existing analytic and numerical models contain a different amount of detail, depending on the purpose of the study. They can be roughly separated in microscopic and macroscopic models, referring to the scale on which they are situated. Microscopic models are focused on the interactions between the particles. They contain information about the material properties of the raw materials and represent the microstructure, either explicitly (figure 4 a) or in an abstract manner. Microscopic models of MAE are often used in combination with a homogenization framework which allows the determination of effective macroscopic properties. The relations between the behavior on different length scales are established in so-called multi-scale approaches (cf. figure 4 b). Basic principles of the homogenization theory are well known for the mechanical properties and also for the magnetic properties. In addition, multi-scale models of

MAE include the magneto-mechanical coupling. It is implemented on the microscopic scale and evaluated on the macroscopic scale as an effective characteristic, just like the mechanical and magnetic properties [Ponte Castañeda+ 2011; Kalina+ 2017; Mukherjee+ 2020]. The effective material properties are used to describe the apparent behavior of the MAE in so-called phenomenological models on the macroscopic scale. At this scale, a representation of the microstructure is rarely useful, therefore the MAE is considered as a homogeneous material. Examples of macroscopic properties are the effective magnetization or the Young's modulus of a composite material. As for the heterogeneous models and the scale transition, analytic approaches (continuum models) and numerical approaches exist also on the macroscopic scale [Ogden 2011; Danas+ 2012].

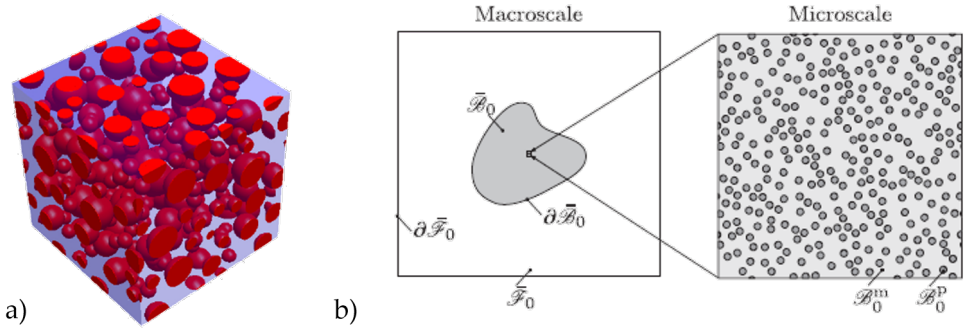

Figure 4: 3D numerical model of a MAE microstructure (a, [Mukherjee+ 2020]) and continuum model of a MAE on the macroscopic scale and the microscopic scale (b, [Kalina+ 2020]).

Objective 3: Modeling of the behavior of H-MAE on different scales

An additional goal of this thesis concerns the modeling of H-MAE under different aspects. One aspect is the design of materials: an industrial use of MAE may require the tailoring of a composite to a specific demand. On this purpose, it is important to know the influence of the choice of primary materials on the effective behavior. A goal of this thesis is the determination of the effective properties of H-MAE composites based on the information about the raw materials and the structure. In addition, the numerical simulation of composite structures is important for in the development process of possible applications. A macroscopic model of MAE is hence also important and targeted in the context of this thesis.

MAE-based applications

The knowledge about the material behavior of MAE and its prediction are essential for the estimation of the success of **concepts for MAE-based devices**. The material behavior of MAE comprises some atypical characteristics which have already paved the way for their use in innovative devices (mostly using S-MAE). The most frequently exploited property in applications based on MAE is the MR effect, more precisely the magnetic field dependent stiffness of the composite material. In the domain of active vibration control, a variety of adaptive damping elements based MAEs has been proposed. In general, the MAE is positioned between a vibrating and an isolated surface and external magnetic fields are used to change the stiffness of the system. In general, the composites already provide interesting damping characteristics since they behave in a viscoelastic manner. Nevertheless, the application of a magnetic field allows an active change of the system's stiffness and thus the possibility of adaptive damping. One example is the sandwich structure developed by [University of Nevada 2004] and represented in figure 5 a. The MAE (purple) is located between two magnetic sheets (activation layers) and the coils (orange), located on various points on the structure allows to change the stiffness locally and hence influence the dynamic behavior of the structure. The MR effect has also led to the development of new kinds of haptic devices. A concept supposed to be easily integrable in cloths or controllers for game consoles has been presented by [Immersion Corp 2018] (cf. figure 5 b). Dynamic magnetic fields are applied by the help of a coil to an overlying MAE element and which changes material stiffness and hence the haptic feedback.

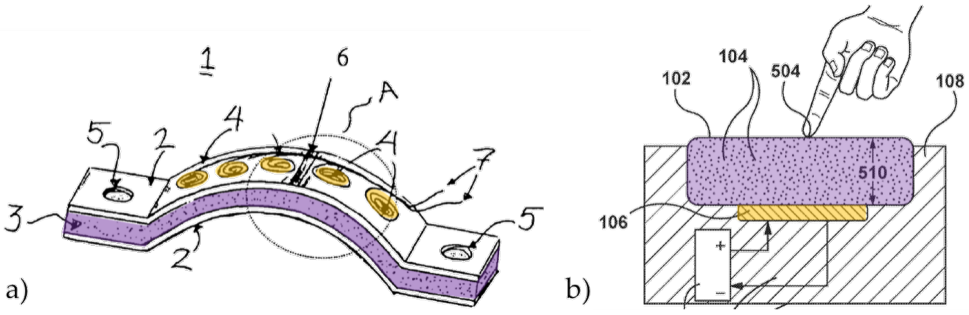

Figure 5: Applications based on the stiffness change of MAE (purple) due to magnetic fields applied via coils (orange) : sandwich structure for vibration damping (a, [University of Nevada 2004]) and haptic device (b,[Immersion Corp 2018].

The combination of a low stiffness and the response to magnetic stimuli make the composite suitable for soft actuators. The research on MAE based membrane actuators for example has advanced largely in the field of valves and pumps. Membranes are already used in fluidic applications but the advantage of a contactless actuation via magnetic fields makes MAE an interesting subject for the research. A concept for a membrane valve has been proposed by [ZF Friedrichshafen AG 2016]

and is shown in figure 6. The valve comprises a perforated S-MAE membrane (purple) positioned in a magnetic circuit. When the coil (orange) generates a magnetic field, the free part of the membrane is attracted to the valve seat preventing the fluid from passing through the valve. When the magnetic field is switched off, the elastic forces are supposed to bring the membrane back into its initial state. Soft actuator devices based on MAE often rely on the elastic restoring forces for which additional elements like springs are used in classic actuator devices. A feature of H-MAE in the context of membrane actuators is the generation of magnetically induced repelling forces with a single external magnetic field generator, allowing a bidirectional actuation by relatively simple means.

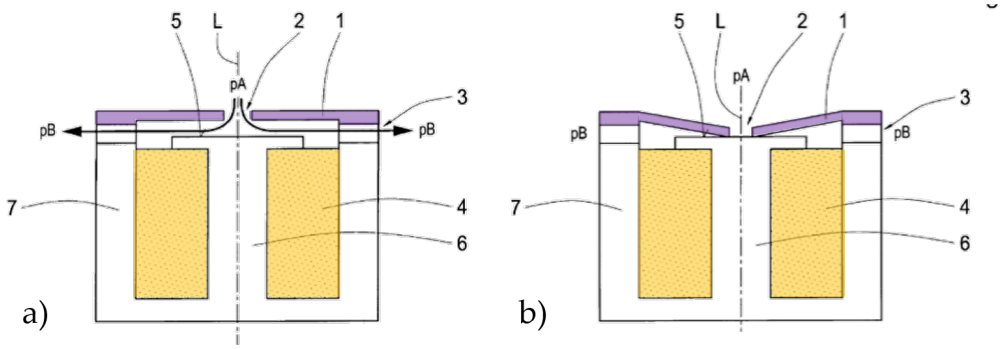

Figure 6: Examples of a MAE membrane actuator (purple) actuated by a coil (orange) in a normally open valve: open state (a) and closed state (b) [ZF Friedrichshafen AG 2016]).

The advantage of H-MAE, compared to S-MAE, is the possibility to provide interaction forces without external supply due to the magnetization. This property is used in the context of fluid control by [Vernay Laboratories 2015]. Figure 7 a shows a valve the closed state, in which the MAE element (purple) is pressed onto the permanent magnet by magnetically induced attraction forces. When the pressure in the lower tube overcomes the magnetic pressure, the valve opens (figure 7 b). The MAE is not only used for its permanent magnetization but also for its sealing capacity provided by the elastomer.

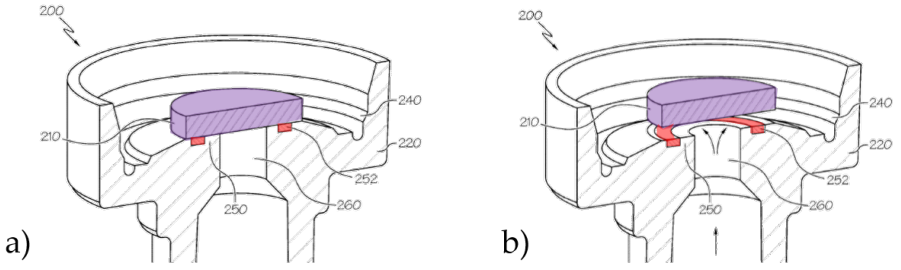

Figure 7: Passive valve, normally closed by the interaction forces between an H-MAE (purple) and a permanent magnet (red) (a), which opens when the pressure overcomes the magnetic forces (b).

The applications presented in this section show that MAE-based applications build upon their unusual material properties. In addition, it is necessary to be able to predict the behavior of MAE materials and MAE structures to identify the feasibility of application concepts.

Objective 4: identification of application cases for H-MAE

A goal of this PhD thesis is the identification of unique properties of H-MAE, which will allow the development of innovative applications relying on these characteristics. In addition, a proof of concept is required for the different concepts to underline the feasibility of the application concepts.

Content and structure of the manuscript

The research work, presented in the following, deals with a MAE composite consisting of magnetically hard NdFeB particles and a comparably stiff matrix (Young's modulus $1-10$ MPa). To facilitate the reading of the subsequent chapters, recurring terms and concepts of continuum mechanics and magnetism are outlined in chapter I. In addition, the **theoretical basics** are supplemented by a description of magneto-mechanical interactions, which is commonly used for continua. The following content can be divided in two main topics: chapter II and chapter III deal with the material behavior of the composite while the chapters IV and V contain proofs of concept for possible H-MAE application cases.

In chapter II, **experimental investigations** on the material behavior are presented. The elaboration procedure of the composite is detailed and structure analysis are presented. Important magnetic properties and mechanical properties are revealed by the help of standard characterization methods. In addition, the influence of the permanent magnetization an external magnetic field on the mechanical behavior are analyzed. A magneto-mechanical test rig, developed in collaboration with the company MMT, is used for the coupled tests involving external magnetic fields in the context of small strain.

Chapter III covers the **multi-scale modeling** of the magnetoactive composite material. Magneto-mechanical interactions between two magnetized objects are studied at the beginning, to enhance the understanding of the interactions between magnetized particles. Afterwards, a homogenization framework for composites with randomly dispersed particles based on numerical simulations is presented. Linear homogenization approaches are applied to determine the effective mechanical and magnetic properties as well as the effects of the coupling. The framework is applied to two dimensional cases with initially magnetized circular particles and the effective properties are determined in vicinity of the initial state. A piezomagnetic model is suggested for the description of the material behavior on the

macroscopic scale. The results of numerical modeling and the experimental investigation are compared at the end of the section.

Chapter IV deals with the **magnetic actuation of H-MAE membranes**. The chapter includes the results of a preliminary study on the forces, generated by magnetized H-MAE composites to demonstrate the influence of the shape and the material properties of the specimens. The study includes experimental tests and numerical simulations. The subsequent part of the chapter focuses on the actuation of H-MAE membranes. Specimens with unidirectional and bidirectional magnetization have been realized for experimental investigations. The leakage magnetic flux density of both types of specimen is compared by the help of experimental results and results of numerical simulations at first. Afterwards, the deflection of the membranes, caused by the interaction with a rigid permanent magnet, is analyzed in experiments. The deflection of the membranes with bidirectional magnetization is also studied in numerical simulations.

In chapter V, the H-MAE is employed in the field of structural dynamics to prove the concept of **magnetically induced friction damping**. The subject comprises the topics experimental modal analysis, nonlinear dynamics and friction damping which are introduced at the beginning of the chapter. A sandwich structure is composed from two ferromagnetic skin and a magnetized H-MAE for the experimental analysis. During the experiment, the cantilevered sample is subjected to a forced periodic excitation with different amplitudes. The responses of the system indicate the presence of three different contact states depending on the excitation amplitude : mainly stick (small amplitudes), partial sliding (moderate amplitudes) and mainly sliding (high amplitudes).

The chapters II to V are structured similar to scientific publications with a state of the art at the beginning followed by an explanation of the research work and a discussion of the results as well as conclusions and perspectives for future work at the end.

Notations

Notation	Signification
$\cdot$	scalar or dot product
$:$	contracted product, i.e. $\mathbb{d} : \varepsilon = \mathbb{d}_{ijk}\varepsilon_{kj}$ or $\mathcal{C} : \varepsilon = \mathcal{C}_{ijkl}\varepsilon_{kl}$
$\times$	cross product
$\otimes$	tensor product
$\lvert\boldsymbol{a}\rvert$	absolute value of the vector $\boldsymbol{a}$
$\hat{\boldsymbol{a}}$	$\dfrac{\boldsymbol{a}}{\lvert\boldsymbol{a}\rvert}$, normalized vector $\boldsymbol{a}$
$\boldsymbol{grad}(s)$	$\dfrac{\partial s}{\partial x_i}\,\boldsymbol{e}_i$, gradient of a scalar field
$\boldsymbol{grad}(\boldsymbol{a})$	$\dfrac{\partial a_i}{\partial x_j}\,\boldsymbol{e}_i \otimes \boldsymbol{e}_j$, gradient of a vector field
$div(\boldsymbol{a})$	$\dfrac{\partial a_i}{\partial x_i}$, divergence of a vector field
$\boldsymbol{div}(\mathbb{T})$	$\dfrac{\partial\, \mathbb{T}_{ij}}{\partial x_j}\,\boldsymbol{e}_i$, divergence of second order tensor field
$\boldsymbol{curl}(\boldsymbol{a})$	$\epsilon_{ijk}\dfrac{\partial a_k}{\partial x_j}\,\boldsymbol{e}_i$, curl of a vector field
$\dot{\boldsymbol{a}}, \ddot{\boldsymbol{a}}$	$\dfrac{\mathrm{D}\boldsymbol{a}}{\mathrm{D}t}$, $\dfrac{\mathrm{D}^2\boldsymbol{a}}{\mathrm{D}t^2}$, material (time) derivative, such that
	$\rightarrow \dfrac{\mathrm{D}\boldsymbol{a}}{\mathrm{D}t} = \dfrac{\partial \boldsymbol{a}}{\partial t}$, material description (Lagrangian variables)
	$\rightarrow \dfrac{\mathrm{D}\boldsymbol{a}}{\mathrm{D}t} = \dfrac{\partial \boldsymbol{a}}{\partial t} + \boldsymbol{grad}(\boldsymbol{a}) \cdot \boldsymbol{v}$, spatial description (Eulerian variables)
ϵ	permutation symbol: $\epsilon_{ijk} = 1$ if $(i,j,k) = (1,2,3)$ or $(3,1,2)$ or $(2,3,1)$, $\epsilon_{ijk} = -1$ if $(i,j,k) = (3,2,1)$ or $(1,3,2)$ or $(2,1,3)$, $\epsilon_{ijk} = 0$ otherwise

Chapter I

Continuum mechanics, magnetism and magnetoelasticity

This section provides an overview over the basics of continuum mechanics, magnetism and the magneto-mechanical coupling which are useful for the work with MagnetoActive Elastomers (MAE). The equations are presented in the MKS system of units and vectors are written as bold letters.

I.1 Introduction to continuum mechanics

This section deals with concepts and expressions which are commonly use in continuum mechanics[1]. Continuum mechanics is a branch of physical science concerned with deformation and motion of continuous media.

I.1.1 Governing equations

There are several fundamental or governing equations, which describe the principles of mechanics. The mass conservation as well as the balance of linear momentum and the resulting fundamental equation of motion are presented in the following.

I.1.1.a Mass conservation

A fundamental postulate of mechanics is the mass conservation. The mass m is supposed to be equally distributed in the volume, such as the mass density ρ^m is similar in each small subvolume ΔV of a material domain $\mathscr{B}$. $\mathscr{B}$ always consists of the same material points. At the instant t_0, the material points are arranged in a configuration $\mathscr{B}_0$, in which the material point M is located at the position $\boldsymbol{X}$. At the instant t, the domain occupies a different region and the material points are regrouped in the configuration $\mathscr{B}_t$ where M is located at the position $\boldsymbol{x}$. The domain still consists of the same material points; hence the mass of the domain is not affected by the time and spatial variation and can be expressed as the volume integral of the mass density in the domain such as

$$m(\mathscr{B}_{t0}) = m(\mathscr{B}_t) = \int_{\mathscr{B}_t} \rho^m \, \mathrm{d}V \ . \tag{I.1}$$

The variation of the position of a material point M in $\mathscr{B}$ is described by the displacement vector u. The displacement links the new position $\boldsymbol{x}$ to a previously occupied position $\boldsymbol{X}$:

$$\boldsymbol{u}(\boldsymbol{X}, t) = \boldsymbol{x} - \boldsymbol{X} \ . \tag{I.2}$$

The definition of the displacement requires the specification of an initial or reference position. The description of mechanical quantities with respect to a reference configuration is also called Lagrangian description. The mass of $\mathscr{B}$ remains unchanged during the motion. The invariance of the mass is stated in the derivative

[1] References can be found in [Kovetz 2000; Coirier 2001] for example

expression in equation (I.3). Since the mass density is dependent on the time and the position, a so–called material derivative is required in the Lagrangian formulation where $\boldsymbol{v}$ corresponds to the velocity of a material point and the divergence operator is defined such as $div(\boldsymbol{v}) = \partial v_i / \partial x_i$. The local form of the mass conservation at each mass point M in the domain $\mathscr{B}$ is stated in equation (I.4).

$$\frac{D}{Dt}\int_{\mathscr{B}_t} \rho^m \,\mathrm{d}V = \int_{\mathscr{B}_t} \frac{D\rho^m}{Dt}\,\mathrm{d}V = \int_{\mathscr{B}_t} \left(\frac{\partial \rho^m}{\partial t} + div(\rho^m \boldsymbol{v}) \right) \mathrm{d}V = 0 \tag{I.3}$$

$$\frac{\partial \rho^m}{\partial t} + div(\rho^m \boldsymbol{v}) = 0 \tag{I.4}$$

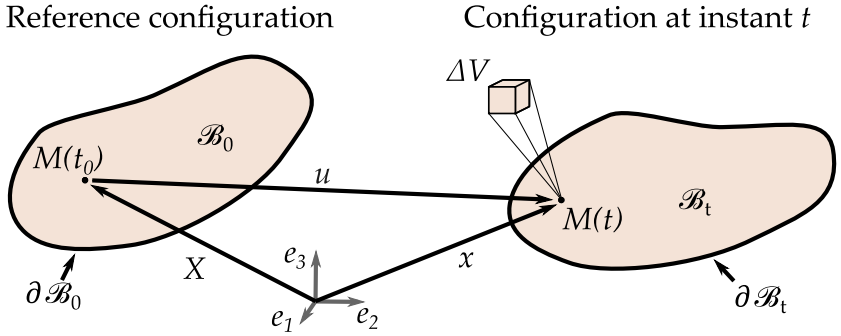

Figure I.1: Different configurations of the material domain $\mathscr{B}$

I.1.1.b Balance of the linear momentum and Cauchy's equation of motion

An additional balance equation in mechanics is the balance of the linear momentum $\boldsymbol{G}$. In continuum mechanics, the linear momentum is described by

$$\boldsymbol{G} = \int \boldsymbol{v} \,\mathrm{d}m \,. \tag{I.5}$$

In an inertial frame with zero acceleration, a variation of the linear momentum can only be caused by an external force $\boldsymbol{F}$. The following relation describes the balance of the linear momentum in continuum mechanics:

$$\frac{D\boldsymbol{G}}{Dt} = \dot{\boldsymbol{G}} = \boldsymbol{F} \,. \tag{I.6}$$

The force $\boldsymbol{F}$ acting on $\mathscr{B}$ is composed of a part acting on the body's surface (surface or contact forces $\boldsymbol{f_S}$) and another part, acting on the volume (volume force $\boldsymbol{f_V}$):

$$\boldsymbol{F} = \oint_{\partial\mathscr{B}} \boldsymbol{f_S}\, dS + \int_{\mathscr{B}} \boldsymbol{f_V}\, dV \,, \tag{I.7}$$

and the balance law can thus be rewritten as

$$\frac{D}{Dt}\int_{D_t} \boldsymbol{v}\, dm = \oint_{\partial D} \boldsymbol{f_S}\, dS + \int_{D_t} \boldsymbol{f_V}\, dV \,. \tag{I.8}$$

The equation above states the global form of the linear momentum balance law. To obtain the local form, the acceleration $\boldsymbol{a}$ is introduced as the time derivative of the velocity and the mass conservation is used to express the linear momentum as volume integral in a first step:

$$\frac{D}{Dt}\int_{\mathscr{B}_t} \boldsymbol{v}\, dm = \int_{\mathscr{B}_t} \frac{D\boldsymbol{v}}{Dt}\, dm = \int_{\mathscr{B}_t} \boldsymbol{a}\, dm = \int_{\mathscr{B}_t} \rho^m \boldsymbol{a}\, dV\ . \tag{I.9}$$

Based on the balance of the linear momentum, it is possible to derive the local form of Newtons first law, the principle of action and reaction, involving the force surface density $\boldsymbol{f_S}$. Supposing that $\boldsymbol{f_S}$ applied at a position with a surface normal $\boldsymbol{n}$, the Cauchy Tetrahedron Argument states, that on each material point M and for every instant t, the dependence of $\boldsymbol{f_S}$ on $\boldsymbol{n}$ is linear. The second order tensor, relating $\boldsymbol{f_S}$ and $\boldsymbol{n}$ is Cauchy's stress tensor σ.

$$\boldsymbol{f_S} = \sigma\, \boldsymbol{n} \tag{I.10}$$

Equation (I.10) can be used to reformulate the surface integral in equation (I.8). In an additional step, the divergence theorem can be used to transform the surface integral into a volume integral. The volume contribution to equation (I.8) is expressed as volume integral instead of a mass integral, which is possible due to the mass conservation:

$$\begin{aligned}\oint_{\partial\mathscr{B}_t} \boldsymbol{f_S}\, dS + \int_{\mathscr{B}} \boldsymbol{f_V}\, dV &= \oint_{\partial\mathscr{B}_t} \sigma\cdot\boldsymbol{n}\, dS + \int_{\mathscr{B}} \boldsymbol{f_V}\, dV \\ &= \int_{\mathscr{B}} \boldsymbol{div}(\sigma) + \boldsymbol{f_V}\, dV\ .\end{aligned} \tag{I.11}$$

The final expressions from equations (I.9) and (I.11) are inserted in equation (I.6) and the fundamental law of dynamics is obtained in its local form :

$$\rho^m \ddot{\boldsymbol{x}} = \boldsymbol{div}(\sigma) + \boldsymbol{f_V}\ . \tag{I.12}$$

I.1.1.c Balance of the angular momentum

The angular momentum $\boldsymbol{L}_P$ is defined with respect to a point P at the position $\boldsymbol{x}_P$ as

$$\boldsymbol{L}_P = \oint (\boldsymbol{x} - \boldsymbol{x}_P) \times \dot{\boldsymbol{x}}\, \mathrm{d}m\ . \tag{I.13}$$

In an inertial frame with zero acceleration, a variation of the angular momentum on P can only be caused by an additional torque $\boldsymbol{T}_P$, defined by

$$\boldsymbol{T}_P = \oint (\boldsymbol{x} - \boldsymbol{x}_P) \times \boldsymbol{f_S}\, \mathrm{d}S + \int (\boldsymbol{x} - \boldsymbol{x}_P) \times \boldsymbol{f_V}\, \mathrm{d}V\ , \tag{I.14}$$

which leads to the balance equation of the angular momentum on the point P:

$$\frac{D\boldsymbol{L}_P}{Dt} = \dot{\boldsymbol{L}}_P = \boldsymbol{M}_P\ . \tag{I.15}$$

Substituting equations (I.13) and (I.14) in equation (I.15), the relation leads to Cauchy's second equation, which states that the second order tensor σ is symmetric:

$$\sigma^{\mathrm{T}} = \sigma \ . \tag{I.16}$$

I.1.2 Displacement and strain

In continuum mechanics, material domains are not only displaced but also deformed. A deformation causes the distances between the material points to change. This change is expressed in expansion tensors and strain tensors. In the first case, the ratio of the new configuration with respect to the old configuration are given and in the second case the amount of the variation. One possibility to express the strain is based on the displacement gradient $\mathbb{H}$. $\mathbb{H}$ can be decomposed in a symmetric and an anti-symmetric part

$$\mathbb{H} = \boldsymbol{grad}(\boldsymbol{u}) = \frac{\partial u_i}{\partial X_j} = \mathbb{H}^{sym} + \mathbb{H}^{asym} \tag{I.17}$$

$$\mathbb{H}^{sym} = \frac{1}{2}(\mathbb{H} + \mathbb{H}^{\mathrm{T}}), \quad \mathbb{H}^{asym} = \frac{1}{2}(\mathbb{H} - \mathbb{H}^{\mathrm{T}}) \ . \tag{I.18}$$

The strain tensor of Green-Lagrange $\mathbb{E}$ for example can be expressed using $\mathbb{H}$ as shown in equation (I.19) below. The comparison with equation (I.18) shows, that the first term corresponds to the symmetric part of $\mathbb{H}$.

$$\mathbb{E} = \frac{1}{2}(\mathbb{H} + \mathbb{H}^{\mathrm{T}}) + \frac{1}{2}\mathbb{H}^{\mathrm{T}}\mathbb{H} \ . \tag{I.19}$$

If the norm of the displacement gradient is considered to be infinitesimally small, the second term in the expression of $\mathbb{E}$ is small compared to the first term. $\mathbb{E}$ can approximately be expressed by the first term by the assumption of so-called small transformations and the remaining expression of $\mathbb{E}$, now corresponding to the symmetric part of $\mathbb{H}$, is also called linearized strain tensor ε:

$$\mathbb{E} \approx \frac{1}{2}(\mathbb{H} + \mathbb{H}^{\mathrm{T}}) = \mathbb{H}^{sym} = \varepsilon \qquad \text{for } ||\mathbb{H}|| \text{ small} \ . \tag{I.20}$$

The second order small strain tensor ε can directly derived from the displacement such as

$$\varepsilon = \frac{1}{2}\Big(\boldsymbol{grad}(\boldsymbol{u}) + \boldsymbol{grad}(\boldsymbol{u})^{\mathrm{T}}\Big) = \frac{1}{2}\left(\frac{\partial u_i}{\partial X_j} + \frac{\partial u_j}{\partial X_i}\right) \ . \tag{I.21}$$

Besides the assumption of small transformations, two additional assumptions are frequently used in continuum mechanics: the assumption of small strains, where the norm of $\mathbb{E}$ is considered infinitesimally small, and small displacements, where $\boldsymbol{u}$ is infinitesimally small before the characteristic length of the structure. The assumptions of small displacement, transformations or strain are not justified mathematically, but has proven to be valid approximations in many experiments.

I.1.3 Behavior of linear elastic materials

The governing equations, presented previously in this section, can be applied to describe any material domain $\mathscr{B}$. However, different materials will not show the same reaction to the same loading and one material will not always behave in the same manner for different types of loading. Relations, which characterize the behavior of certain classes of materials for a certain type of loading are called behavior laws. A mechanical, linear elastic behavior law for example is Hooke's law for continuous media. It relates the linearized strain tensor ε to Cauchy's stress tensor σ by a fourth order tensor $\mathcal{C}$, called stiffness tensor:

$$\sigma = \mathcal{C} : \varepsilon \,. \tag{I.22}$$

The representation of this relation can be simplified in the Voigt notation which reduces the three dimensional fourth order tensor $\mathcal{C}$ to a 6×6 stiffness matrix $\mathbb{C}$ and the second order tensors, σ and ε, to six-dimensional vectors as shown in equation (I.23) and in a simplified, frequently used form in equation (I.24).

$$\begin{pmatrix} \sigma_{11} \\ \sigma_{22} \\ \sigma_{33} \\ \sigma_{23} \\ \sigma_{13} \\ \sigma_{12} \end{pmatrix} = \begin{pmatrix} C_{1111} & C_{1122} & C_{1133} & C_{1123} & C_{1131} & C_{1112} \\ C_{2211} & C_{2222} & C_{2233} & C_{2223} & C_{2231} & C_{2212} \\ C_{3311} & C_{3322} & C_{3333} & C_{3323} & C_{3331} & C_{3312} \\ C_{2311} & C_{2322} & C_{2333} & C_{2323} & C_{2331} & C_{2312} \\ C_{3111} & C_{3122} & C_{3133} & C_{3123} & C_{3131} & C_{3112} \\ C_{1211} & C_{1222} & C_{1233} & C_{1223} & C_{1231} & C_{1212} \end{pmatrix} \cdot \begin{pmatrix} \varepsilon_{11} \\ \varepsilon_{22} \\ \varepsilon_{33} \\ 2\varepsilon_{23} \\ 2\varepsilon_{13} \\ 2\varepsilon_{12} \end{pmatrix} \tag{I.23}$$

$$\begin{pmatrix} \sigma_{1} \\ \sigma_{2} \\ \sigma_{3} \\ \sigma_{4} \\ \sigma_{5} \\ \sigma_{6} \end{pmatrix} = \begin{pmatrix} C_{11} & C_{12} & C_{13} & C_{14} & C_{15} & C_{16} \\ C_{12} & C_{22} & C_{23} & C_{24} & C_{25} & C_{26} \\ C_{13} & C_{23} & C_{33} & C_{34} & C_{35} & C_{36} \\ C_{14} & C_{24} & C_{34} & C_{44} & C_{45} & C_{46} \\ C_{15} & C_{25} & C_{35} & C_{45} & C_{55} & C_{56} \\ C_{16} & C_{26} & C_{36} & C_{46} & C_{56} & C_{66} \end{pmatrix} \cdot \begin{pmatrix} \varepsilon_{1} \\ \varepsilon_{2} \\ \varepsilon_{3} \\ 2\varepsilon_{4} \\ 2\varepsilon_{5} \\ 2\varepsilon_{6} \end{pmatrix} \tag{I.24}$$

The stiffness matrix contains information, which are characteristic for the material like the elastic tensile and shear moduli, E and G, or the Poisson's ratio ν. The properties are arranged in the compliance matrix $\mathbb{C}^{-1}$ as shown in equation (I.25) and equation (I.26). The first matrix, $\mathbb{C}^{-1}_{iso}$, models the behavior of an isotropic material, in which the material properties are not dependent on the spatial direction. The second matrix, $\mathbb{C}^{-1}_{ortho}$, represents the behavior of an orthotropic material with three orthogonal planes of symmetry.

$$\mathbb{C}^{-1}_{iso} = \frac{1}{E} \begin{pmatrix} 1 & -\nu & -\nu & 0 & 0 & 0 \\ -\nu & 1 & -\nu & 0 & 0 & 0 \\ -\nu & -\nu & 1 & 0 & 0 & 0 \\ 0 & 0 & 0 & 2+2\nu & 0 & 0 \\ 0 & 0 & 0 & 0 & 2+2\nu & 0 \\ 0 & 0 & 0 & 0 & 0 & 2+2\nu \end{pmatrix} \tag{I.25}$$

$$\mathbb{C}^{-1}_{ortho} = \begin{pmatrix} 1/E_1 & -\nu_{21}/E_2 & -\nu_{31}/E_3 & 0 & 0 & 0 \\ -\nu_{12}/E_1 & 1/E_2 & -\nu_{32}/E_3 & 0 & 0 & 0 \\ -\nu_{13}/E_1 & -\nu_{23}/E_2 & 1/E_3 & 0 & 0 & 0 \\ 0 & 0 & 0 & 1/G_{23} & 0 & 0 \\ 0 & 0 & 0 & 0 & 1/G_{31} & 0 \\ 0 & 0 & 0 & 0 & 0 & 1/G_{12} \end{pmatrix} \tag{I.26}$$

I.2 Introduction to magnetism

This section gives an overview over the governing equations, used to describe the magnetic quantities in polarizable and non-polarizable materials at the beginning, followed by a description of the behavior of ferromagnetic materials [2].

I.2.1 Governing equations

I.2.1.a Description of non-polarizable domains

Coulomb's law describes the force, that acts on an electric charge q_b, located at P_b, due to the presence of another charge, q_a, located at P_a. In the following example, represented in figure I.2 a, q_a is supposed to be fixed in the frame $\mathbb{R}_2$ which is not necessarily the case for q_b. The distance vector $\boldsymbol{r}$ is pointing from q_a to q_b and its norm r and its direction $\hat{\boldsymbol{r}}$ have an influence on the Coulomb force $\boldsymbol{F}^{Co}_{ab}$, acting on charge q_b due to the presence of q_a (equation (I.27)). The expression of the force comprises the electric constant ε_0.

$$\boldsymbol{F}^{Co}_{ab}(\mathrm{P}_b) = q_b \frac{q_a}{4\pi\varepsilon_0 r^2}\,\hat{\boldsymbol{r}} \qquad \text{in frame } \mathbb{R}_2 \tag{I.27}$$

A similar derivation can be done in for continuous media (figure I.2 b), where the charges are replaced by small, elementary volumes ΔV with a constant charge density ρ^q, which is defined by

$$\rho^q = \Delta q / \Delta V \ . \tag{I.28}$$

The charge density in an electric charge continuum is the equivalent of the previously presented mass density in continuum mechanics. The total charge in an isolated system is conserved which means that if an amount of positive charges appears or disappears in the system, an equal amount of negative charge does likewise. The algebraic sum of the charge remains constant. But in contrast to the mass (always positive), the electric charge may be positive or negative. The

[2] References can be found in [Bozorth 1993; Hirsinger 1994; Lacheisserie+ 1999; Fiorillo 2010] for example.

force on the point P_b is described by equation (I.29) and the electric field $\boldsymbol{E}$ is introduced as the resulting field from of local contributions $\mathrm{d}\boldsymbol{E}$ comprised in the integration volume V which can enclose the entire space.

$$\mathrm{d}\boldsymbol{F}^{Co}(\mathrm{P}_b) = \rho_b^q \, \Delta V_b \, \boldsymbol{E}(\mathrm{P}_b) \; , \qquad \boldsymbol{E}(\mathrm{P}_b) = \int_V \frac{\rho_a^q}{4\pi\varepsilon_0 r^2} \, \hat{\boldsymbol{r}} \, \mathrm{d}V \qquad \text{in frame } \mathbb{R}_2 \; . \tag{I.29}$$

Figure I.2 c shows a situation in which $\mathbb{R}_2$ moves with the constant velocity v_{a1} with respect to another frame $\mathbb{R}_1$. In addition, the elementary volume with the charge density ρ_b^q is supposed to move with the constant velocity v_{b1}. It has been shown mathematically, that an additional force component appears, when the force between the elementary volumes is expressed in $\mathbb{R}_1$ instead of $\mathbb{R}_2$. The contribution is also known as Laplace force $\boldsymbol{F}^{La}$ and the total force is known as Lorentz force $\boldsymbol{F}^{Lo}$.

$$\mathrm{d}\boldsymbol{F}^{Lo} = \mathrm{d}\boldsymbol{F}^{Co} + \mathrm{d}\boldsymbol{F}^{La} \qquad \text{in frame } \mathbb{R}_1 \; . \tag{I.30}$$

When the norm of v_{a1} and v_{b1} are much smaller than the speed of light (non-relativistic approximation), the force can be expressed by equation (I.31). The magnetic flux density $\boldsymbol{B}$ is defined in this relation comprising the magnetic constant μ_0. $\boldsymbol{B}$ expresses a virtual force field that is required to describe the force in a frame that is not related to the frame of the moving charges.

$$\mathrm{d}\boldsymbol{F}^{La} = \rho_b^q \, \Delta V_b \, \boldsymbol{v}_{b1} \times \boldsymbol{B}(\mathrm{P_b}) \; , \quad \boldsymbol{B}(\mathrm{P_b}) = \frac{\mu_0}{4\pi} \int_V \frac{\rho_a^q \, \boldsymbol{v}_{a1} \times \hat{\boldsymbol{r}}}{r^2} \, \mathrm{d}V \quad \text{in frame } \mathbb{R}_1 \; . \tag{I.31}$$

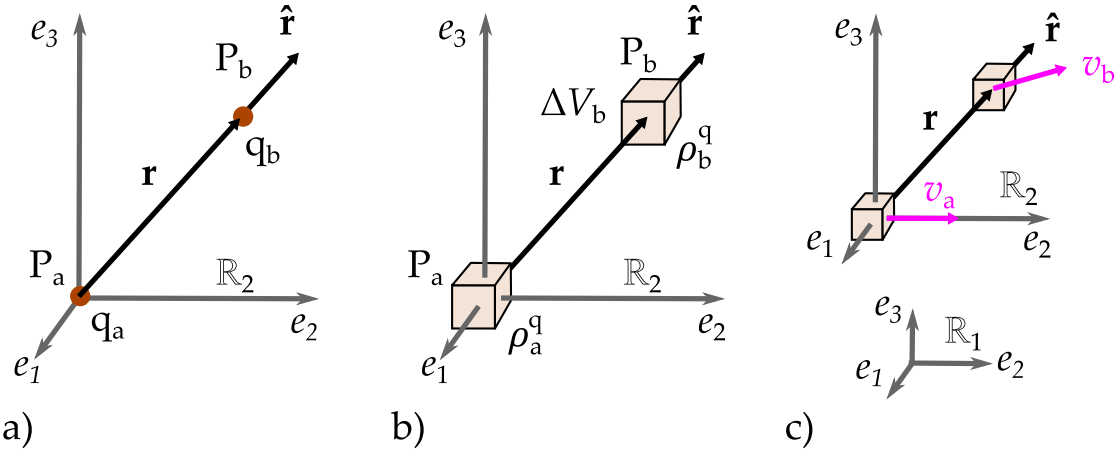

Figure I.2: Schematic representation of two electric charges q (a) and elementary volumes ΔV with the charge density ρ^q (b) and (c), adapted from [Hirsinger 1994].

A moving charge density $\rho^q \boldsymbol{v}$ is defined as current density $\boldsymbol{j}$, the substitution of the corresponding term in equation (I.31) leads to the Biot–Savart law which describes the magnetic flux density at a position $\boldsymbol{x}$:

$$\boldsymbol{B}(\boldsymbol{x}) = \frac{\mu_0}{4\pi} \int_{\mathrm{V}} \frac{\boldsymbol{j} \times \boldsymbol{r}}{r^3} \, \mathrm{d}V \tag{I.32}$$

The mathematical equivalence, shown in equation (I.33), can be used to rewrite the expression of $\boldsymbol{B}$ (equation (I.32)) and to show that it derives from the $\boldsymbol{curl}$ of another field: the magnetostatic vector potential $\boldsymbol{A}$:

$$\boldsymbol{curl}\left(\frac{\boldsymbol{j}}{r}\right) = grad\left(\frac{1}{r}\right) \times \boldsymbol{j} = \frac{\boldsymbol{j} \times \boldsymbol{r}}{r^3} \tag{I.33}$$

$$\boldsymbol{B}(\boldsymbol{x}) = \frac{\mu_0}{4\pi} \int_{\mathrm{V}} \boldsymbol{curl}\left(\frac{\boldsymbol{j}}{r}\right) \mathrm{d}V = \boldsymbol{curl}\left(\frac{\mu_0}{4\pi} \int_{\mathrm{V}} \frac{\boldsymbol{j}}{r} \, \mathrm{d}V\right) = \boldsymbol{curl}(\boldsymbol{A}) \tag{I.34}$$

Equation (I.34) shows, that the divergence of the magnetic flux density is zero, since the expression divergence of the $\boldsymbol{curl}$ of a field equals zero (equation (I.35)). The relation is known as Gauss' law of magnetism and states, that there are not magnetic monopoles.

$$div(\boldsymbol{curl}(\boldsymbol{A})) = div(\boldsymbol{B}) = 0 \tag{I.35}$$

In addition, equation (I.32) can be used to show that the circulation of $\boldsymbol{B}$ on the outer contour of a surface is proportional to the current which passes by the surface, the coefficient of proportionality is μ_0 (Ampère's circuital law). The relation has been expanded by Maxwell by the contribution of the time variation of an electric field and the local form of the relation is stated in equation (I.36). This thesis deals with electrostatic cases ($\partial \boldsymbol{E}/\partial t = \boldsymbol{0}$), in which the absence of currents is supposed ($\boldsymbol{j} = \boldsymbol{0}$). Equation (I.37) shows equation (I.36) under consideration of the two assumptions.

$$\boldsymbol{curl}(\boldsymbol{B}) = \mu_0 \boldsymbol{j} + \mu_0 \varepsilon_0 \frac{\partial \boldsymbol{E}}{\partial t} \tag{I.36}$$

$$\boldsymbol{curl}(\boldsymbol{B}) = \boldsymbol{0} \qquad \text{for } \boldsymbol{j} = 0, \text{ and } \frac{\partial \boldsymbol{E}}{\partial t} = \boldsymbol{0} \tag{I.37}$$

I.2.1.b Description of polarizable domains

Some materials are quantified as magnetically polarizable. In contrast to non-polarizable materials, they have the possibility to contribute to $\boldsymbol{B}$. On the microscopic scale, electrons of the atoms develop magnetic moments $\boldsymbol{m}$ due to their spin and their orbital movement. A macroscopic magnetization vector $\boldsymbol{M}$ can be defined as the volume density of the magnetic moments in an elementary volume ΔV:

$$\boldsymbol{M} = \frac{\boldsymbol{m}}{\Delta V} \, . \tag{I.38}$$

The first order approximation of the magnetic vector potential $\boldsymbol{A}$ generated on the point P by ΔV and outside and far from the latter, states as follows in the magnetostatics case:

$$\boldsymbol{A}(\mathrm{P}) = \frac{\mu_0}{4\pi} \int_V \boldsymbol{M} \times grad\frac{1}{r}\, \mathrm{d}V \tag{I.39}$$

The formulation can be mathematically decomposed into a volume and a surface contribution as shown in equation (I.40) where $\boldsymbol{n}$ represents the surface normal pointing outwards from ΔV. The comparison with equation (I.34) shows, that two numerators in the integrals can be used as fictional volume and surface currents, $\boldsymbol{j}_v$ and $\boldsymbol{j}_s$, to model the effects of the magnetization. They are also called Amperian currents and their expressions are shown in equation (I.41).

$$\boldsymbol{A}(\mathrm{P}) = \frac{\mu_0}{4\pi} \int_{\mathscr{B}} \frac{\boldsymbol{curl}(\boldsymbol{M})}{r}\, \mathrm{d}V + \frac{\mu_0}{4\pi} \oint_{\partial\mathscr{B}} \frac{\boldsymbol{M} \times \boldsymbol{n}}{r}\, \mathrm{d}S \tag{I.40}$$

$$\boldsymbol{j}_V = \boldsymbol{curl}(\boldsymbol{M}) \qquad \boldsymbol{j}_S = \boldsymbol{M} \times \boldsymbol{n} \tag{I.41}$$

The local expression of the magnetic flux density for non-magnetizable materials is shown in equation (I.36). The magnetization can be integrated in this formulation by the addition of the fictional currents $\boldsymbol{j}_V$ in the volume to the physical, free currents:

$$\boldsymbol{curl}(\boldsymbol{B}) = \mu \boldsymbol{j}_{tot} = \mu_0(\boldsymbol{j}_{reel} + \boldsymbol{j}_V) = \mu_0 \boldsymbol{j}_{reel} + \mu_0\, \boldsymbol{curl}(\boldsymbol{M})\ . \tag{I.42}$$

The equation can be rearranged to introduce the magnetic field $\boldsymbol{H}$ as follows

$$\boldsymbol{j}_{reel} = \boldsymbol{curl}\left(\frac{\boldsymbol{B}}{\mu_0} - \boldsymbol{M}\right) = \boldsymbol{curl}(\boldsymbol{H}) \qquad \boldsymbol{H} = \frac{\boldsymbol{B}}{\mu_0} - \boldsymbol{M} \tag{I.43}$$

In electromagnetism, the contribution of the time variation of the electric displacement $\partial \boldsymbol{D}/\partial t$ has to be added to obtain the commonly known Maxwell's fourth equation. This work deals with electrostatic cases and the absence of free currents (quasi stationary magnetic state) is supposed. The equation in polarizable materials hence becomes

$$\boldsymbol{curl}(\boldsymbol{H}) = \boldsymbol{0} \qquad \text{for } \boldsymbol{j} = \boldsymbol{0} \text{ and } \frac{\partial \boldsymbol{D}}{\partial t} = \boldsymbol{0} \tag{I.44}$$

Referring to equation (I.43), the magnetic flux density can be expressed using $\boldsymbol{H}$:

$$\boldsymbol{B} = \mu_0 \boldsymbol{H} \qquad \text{for } \boldsymbol{M} = \boldsymbol{0}\ (\text{non} - \text{polarizable materials}) \tag{I.45}$$

$$\boldsymbol{B} = \mu_0(\boldsymbol{H} + \boldsymbol{M}) \qquad \text{for } \boldsymbol{M} \neq \boldsymbol{0}\ (\text{polarizable materials}) \tag{I.46}$$

Another expression for the quantity $\mu_0 \boldsymbol{M}$ is "magnetic polarization", denoted as $\boldsymbol{J}$, which can also be used to express equation (I.46):

$$\boldsymbol{B} = \mu_0 \boldsymbol{H} + \boldsymbol{J} \qquad (\text{polarizable materials})\ . \tag{I.47}$$

I.2.1.c Demagnetizing fields

It has been shown before, that the behavior of polarizable material can be described by equation (I.46) in the magnetostatic case in absence of currents. When the expression for $\boldsymbol{B}$ is inserted in equation (I.46), the following relations is obtained:

$$div(\boldsymbol{H}) = -div(\boldsymbol{M}) \tag{I.48}$$

The equation states that for $div(\boldsymbol{M}) \neq 0$, there is a field oriented in the opposite direction of the magnetization (field of conservative nature). This situation occurs at places where the magnetization is discontinuous, for example at the interface of a magnetizable and non-magnetizable material (e.g. surface of a sample in the air). The field is called demagnetization field $\boldsymbol{H}_d$, since it is opposed to the magnetization, and it is proportional to the magnetization:

$$\boldsymbol{H}_d = -\mathbb{N}_d \, \boldsymbol{M} \ , \tag{I.49}$$

with $\mathbb{N}_d$ corresponding to the demagnetization tensor. The tensor is reduced to a diagonal form only for ellipsoidal samples and the demagnetization fields of non-ellipsoidal samples can only be calculated approximately. The demagnetization plays an important role for the use of permanent magnets as it reduces their capacity to provide magnetic flux.

I.2.2 Behavior of ferromagnetic materials

The explanations in this section present the magnetic behavior of a material in a specific direction, the magnetic quantities are thus scalar values. In ferromagnetic materials, magnetic moments with the same orientation are regrouped in magnetic domains on the microscopic level. Adjacent domains are separated by a transition region, over which the direction of the magnetization changes: the Bloch walls. When the magnetic moments of the domains compensate each other due to their different orientations, the net magnetization of a specimen on a macroscopic level equals zero. The magnetic moments in ferromagnetic materials tend to align in external magnetic fields. The first magnetization curve of a material is determined by different domain processes: first reversible then irreversible displacement of Bloch walls followed by the alignment of the domains with the external field. At a certain magnitude of the external field the polarization saturates at $J_s = \mu_0 \, M_s$ (figure I.3 a). In this state, all domains are oriented in the same direction and a further increase of the magnetization is not possible. The magnetic flux density B continues to increase (I.3 b), but only due to the increase of H when J_s is reached:

$$B_s = \mu_0 H + J_s \ . \tag{I.50}$$

When the magnitude of the external field is decreased, the magnetization decreases but on a different path as during the magnetization. A residual magnetization M_r persists in absence of the external field and an additional field, $-H_c$ has to

be applied to demagnetize the material completely. The magnitude H_c is called coercive field strength. If the magnetic field is increased and decreased between the saturated states, the magnetization evolves in a hysteresis loop (figure I.3 c).

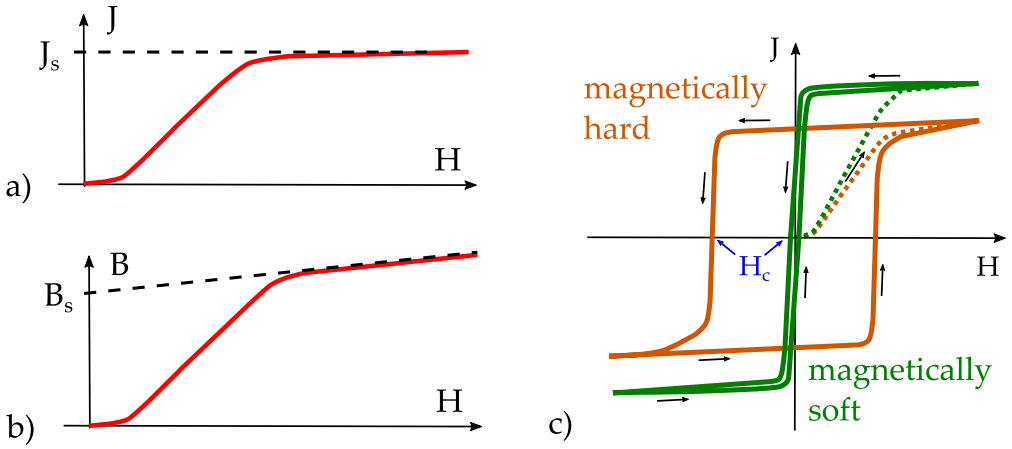

Figure I.3: Schematic representation of the polarization (a) and the magnetic flux density (b) during the first magnetization of a ferromagnetic material and representation of the hysteresis curves of magnetically hard and soft materials (c).

The coercive field strength H_c is used to roughly separate materials with a magnetically soft (low H_c) and hard (high H_c) behavior. There is no precise limit for the distinction, but materials with iron ($H_c \approx 10^1$ A/m) are designated as magnetically soft while hard ferrites ($H_c \approx 10^1$ kA/m) are designated as magnetically hard for example. For small magnetic fields, the magnetic flux density evolves in a nearly linear manner with the magnetic field. It is possible to express J as a function of the magnetic field and the residual magnetic flux density, as equation (I.51) shows. The relation comprises the relative magnetic permeability μ_r, a material parameter that depends on the actual and previous magnetic loading of the material. In the fully magnetized state, μ_r is very small and J is nearly constant.
The evolution of the material behavior can be revealed by the help of the polarization J or the magnetic flux density B figure I.4. For $H = 0$, the residual characteristics J_r and B_r are equivalent. For small magnetic fields in vicinity of the residual polarization, the relative permeability is nearly constant (cf. equation (I.51)) and the magnetic flux density evolves in a nearly linear manner with the magnetic field (figure I.4 b). A frequently used relation for the linear material behavior in this region is given in equation (I.52).

$$J = \mu_0(\mu_r - 1)H + B_r \tag{I.51}$$

$$B = \mu H + Br = \mu_0\mu_r H + Br \tag{I.52}$$

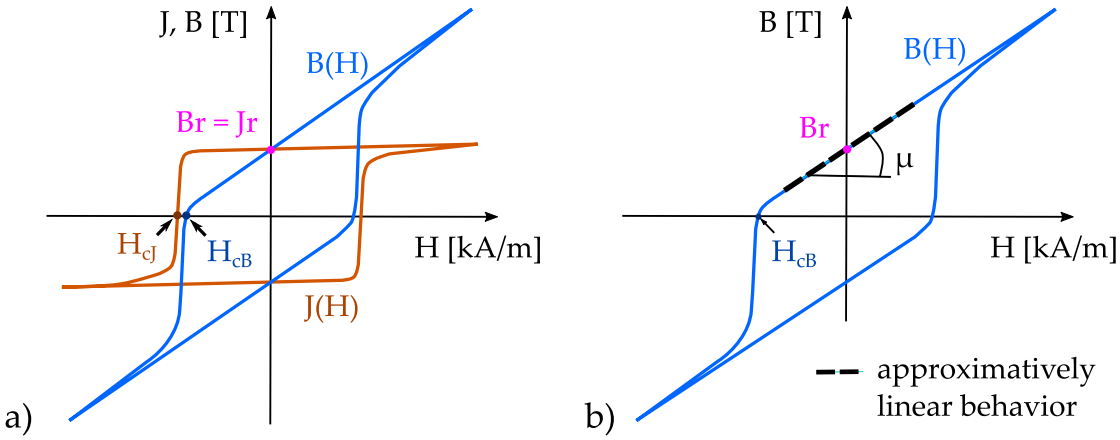

Figure I.4: Schematic representation of the hysteresis loop of J and B (a) and hysteresis curve for B with focus on the magnetic flux density of a magnetize material for small magnetic fields.

I.3 Magneto-mechanical coupling

This section gives an overview over the magneto-mechanical coupling. In the first part, the concept of electromagnetic stress tensors is introduced. The subsequent parts deal with magnetically induced mechanical loadings and magneto-mechanical balance laws. The last part presents a thermodynamic approach for the development of magneto-mechanical balance laws[3].

I.3.1 Electromagnetic stress tensors

The local electromagnetic volume force in a non-polarizable medium is described by the Lorentz force:

$$\boldsymbol{f}_V^{Lo} = \rho^q \boldsymbol{E} + \boldsymbol{j} \times \boldsymbol{B} \,. \tag{I.53}$$

In polarizable materials, the electric and magnetic polarizations contribute not only to the volume force $\boldsymbol{f_V}$, but are also responsible for volume torques $\boldsymbol{c_V}$. The general definition of the two quantities in Newtonian mechanics is given in equations (I.54) and (I.56) respectively (cf. [Eringen+ 1990; Lemaitre+ 2009]), with $\boldsymbol{P}$ corresponding to the electric polarization. The material domain is supposed to move with the velocity $\boldsymbol{v}$ with respect to an inertial frame and equations (I.54) and (I.56) are expressed in the material frame where the quantities $\boldsymbol{\mathcal{E}} = \boldsymbol{E} + \boldsymbol{v} \times \boldsymbol{B}$, $\boldsymbol{\mathcal{J}} = \boldsymbol{j} - \rho^q \boldsymbol{v}$, $\boldsymbol{\mathcal{P}} = \boldsymbol{P}$ and $\boldsymbol{\mathcal{M}} = \boldsymbol{M} + \boldsymbol{v} \times \boldsymbol{P}$ are the corresponding expressions of the electric field, the free currents and the magnetization.

$$\boldsymbol{f}_V^{EM} = \rho^q \boldsymbol{\mathcal{E}} + (\boldsymbol{\mathcal{J}} + \overset{*}{\boldsymbol{P}}) \times \boldsymbol{B} + \boldsymbol{grad}(\boldsymbol{\mathcal{E}}) \cdot \boldsymbol{P} + \Big(\boldsymbol{grad}(\boldsymbol{B})\Big)^{\mathrm{T}} \cdot \boldsymbol{\mathcal{M}} \,, \tag{I.54}$$

[3] References can be found in [Eringen+ 1990; Hirsinger 1994; Kovetz 2000; Bekemans 2006; Lemaitre+ 2009] for example.

$$\overset{*}{\boldsymbol{P}} = \dot{\boldsymbol{P}} - \boldsymbol{grad}(\boldsymbol{v}) \cdot \boldsymbol{P} + \boldsymbol{P}\, \boldsymbol{div}(\boldsymbol{v}) \tag{I.55}$$

$$\boldsymbol{c}_V^{EM} = \boldsymbol{\mathcal{M}} \times \boldsymbol{B} + \boldsymbol{P} \times \boldsymbol{\mathcal{E}} \; . \tag{I.56}$$

For a uniform velocity, the convective time derivative $\overset{*}{\boldsymbol{P}}$ in equation (I.55) reduces to $\dot{\boldsymbol{P}}$. It is mathematically possible to associate a tensor $\mathbb{t}^{EM}$ to the volume force and torque (equation (I.57)), involving the electromagnetic momentum $\boldsymbol{G}^{EM}$ (equation (I.59)). The term $\partial \boldsymbol{G}^{EM}/\partial t$ corresponds to the time variation of the momentum caused by the time variation of an electromagnetic field and ϵ corresponds to the permutation symbol.

$$\boldsymbol{f}_V^{EM} = \boldsymbol{div}(\mathbb{t}^{EM}) - \frac{\partial \boldsymbol{G}^{EM}}{\partial t} \; , \qquad \boldsymbol{c}_V^{EM} = \epsilon : \mathbb{t}^{EM} \tag{I.57}$$

The notation is interesting for quasi-static cases in particular, since $\partial \boldsymbol{G}^{EM}/\partial t$ vanishes and the volume force can be described by the tensor $\mathbb{t}^{EM}$ solely.

$$\begin{aligned} \mathbb{t}^{EM} = {} & \varepsilon_0 \boldsymbol{E} \otimes \boldsymbol{E} + \frac{1}{\mu_0} \boldsymbol{B} \otimes \boldsymbol{B} - \frac{1}{2} \left(\varepsilon_0 \boldsymbol{E} \cdot \boldsymbol{E} + \frac{\boldsymbol{B} \cdot \boldsymbol{B}}{\mu_0} - 2\, \boldsymbol{\mathcal{M}} \cdot \boldsymbol{B} \right) \mathbb{I} \\ & + \boldsymbol{P} \otimes \boldsymbol{\mathcal{E}} - \boldsymbol{B} \otimes \boldsymbol{\mathcal{M}} \; , \end{aligned} \tag{I.58}$$

$$\boldsymbol{G}^{em} = \varepsilon_0 \boldsymbol{E} \times \boldsymbol{B} \; . \tag{I.59}$$

In a frame, where the material velocity $\boldsymbol{v}$ is supposed to be too small to affect the electro-magnetic quantities ($\boldsymbol{v} \approx \boldsymbol{0}$), the tensor $\mathbb{t}^{em}$ is associated to the volume force and torque:

$$\begin{aligned} \mathbb{t}^{em} = {} & \varepsilon_0 \boldsymbol{E} \otimes \boldsymbol{E} + \frac{1}{\mu_0} \boldsymbol{B} \otimes \boldsymbol{B} - \frac{1}{2} \left(\varepsilon_0 \boldsymbol{E} \cdot \boldsymbol{E} + \frac{\boldsymbol{B} \cdot \boldsymbol{B}}{\mu_0} - 2 \boldsymbol{M} \cdot \boldsymbol{B} \right) \mathbb{I} \\ & + \boldsymbol{P} \otimes \boldsymbol{E} - \boldsymbol{B} \otimes \boldsymbol{M} \; , \end{aligned} \tag{I.60}$$

The tensor $\mathbb{t}^{em}$ is not necessarily symmetric due to the contribution of the torque $\boldsymbol{c_V}$. Different proposition for the decomposition in a symmetric and not necessarily symmetric part exist in the literature. [Eringen+ 1990] separate a symmetric part $\mathbb{T}^{MW}$, corresponding to the Maxwell stress tensor, from the remaining part $\mathbb{T}^{E}$:

$$\begin{aligned} \mathbb{t}^{em} &= \mathbb{T}^{MW} + \mathbb{T}^{E} \; , \\ \mathbb{T}^{MW} &= \varepsilon_0 \boldsymbol{E} \otimes \boldsymbol{E} + \frac{1}{\mu_0} \boldsymbol{B} \otimes \boldsymbol{B} - \frac{1}{2} \left(\varepsilon_0 \boldsymbol{E} \cdot \boldsymbol{E} + \frac{\boldsymbol{B} \cdot \boldsymbol{B}}{\mu_0} \right) \mathbb{I} \; , \\ \mathbb{T}^{E} &= \boldsymbol{P} \otimes \boldsymbol{E} - \boldsymbol{B} \otimes \boldsymbol{M} + (\boldsymbol{M} \cdot \boldsymbol{B})\, \mathbb{I} \; . \end{aligned} \tag{I.61}$$

Another frequently used decomposition, shown in [Lemaitre+ 2009] for example, consists of separating the symmetric part $\mathbb{T}^{sym}$ from the part that is not necessarily symmetric, $\mathbb{T}^{nsym}$:

$$\begin{aligned}
\mathbb{t}^{em} &= \mathbb{T}^{sym} + \mathbb{T}^{nsym} \,, \\
\mathbb{T}^{sym} &= \varepsilon_0 \boldsymbol{E} \otimes \boldsymbol{E} + \frac{1}{\mu_0} \boldsymbol{B} \otimes \boldsymbol{B} - \frac{1}{2} \left(\varepsilon_0 \boldsymbol{E} \cdot \boldsymbol{E} + \frac{\boldsymbol{B} \cdot \boldsymbol{B}}{\mu_0} - 2 \boldsymbol{M} \cdot \boldsymbol{B} \right) \mathbb{I} \,, \\
\mathbb{T}^{nsym} &= \boldsymbol{P} \otimes \boldsymbol{E} - \boldsymbol{B} \otimes \boldsymbol{M} \,.
\end{aligned} \tag{I.62}$$

This PhD thesis deals with cases, where the absence of electric fields is assumed ($\boldsymbol{E} = \boldsymbol{0}$) and the velocity of the domain in the observation frame is considered to be too small to affect the magnetic quantities ($\boldsymbol{v} \approx \boldsymbol{0}$). The tensors $\mathbb{T}$ is obtained from $\mathbb{t}^{em}$ with the aforementioned assumptions and shown in equation (I.63). For $\boldsymbol{M} = \boldsymbol{0}$, equation (I.63) also describes the magnetic stress tensor in a non-magnetizable material.

$$\mathbb{T} = \frac{1}{\mu_0} \boldsymbol{B} \otimes \boldsymbol{B} - \left(\frac{\boldsymbol{B}^2}{2\mu_0} - \boldsymbol{M} \cdot \boldsymbol{B} \right) \mathbb{I} - \boldsymbol{B} \otimes \boldsymbol{M} \,. \tag{I.63}$$

I.3.2 Quasi-static magneto-mechanical loading

The general expression of a global, magnetically induced force $\boldsymbol{F}^{em}$ and torque $\boldsymbol{T}^{em}$, acting on a body $\mathscr{B}$, are shown in equation (I.64) and equation (I.65) respectively. The electromagnetic quantities $\boldsymbol{f}_V^{em}$, $\boldsymbol{f}_S^{em}$ and $\boldsymbol{c}_{\boldsymbol{V}}^{em}$ correspond to the surface force density, the volume force density and the volume torque density. The point O is the center of gravity of the body and $\mathrm{P_V}$ and $\mathrm{P_S}$ are the current points in the volume $\mathscr{B}$ and on the boundary $\partial\mathscr{B}$ of the body respectively.

$$\boldsymbol{F}^{em} = \int_{\mathscr{B}} \boldsymbol{f}_{\boldsymbol{V}}^{em} \, \mathrm{d}V + \oint_{\partial\mathscr{B}} \boldsymbol{f}_{\boldsymbol{S}}^{em} \, \mathrm{d}S \,, \tag{I.64}$$

$$\boldsymbol{T}_O^{em} = \int_{\mathscr{B}} \overline{OP}_V \times \boldsymbol{f}_{\boldsymbol{V}}^{em} \, \mathrm{d}V + \oint_{\partial\mathscr{B}} \overline{OP}_S \times \boldsymbol{f}_{\boldsymbol{S}}^{em} \, \mathrm{d}S + \int_{\mathscr{B}} \boldsymbol{c}_{\boldsymbol{V}}^{em} \, \mathrm{d}V \,. \tag{I.65}$$

In the of quasi-static magnetic loadings ($\partial \boldsymbol{G}^{em} / \partial t = \boldsymbol{0}$), the volume force density can be described by the help of $\mathbb{T}$ for isotropic materials:

$$\boldsymbol{f}_{\boldsymbol{V}}^{em} = \boldsymbol{div}(\mathbb{T}) \,. \tag{I.66}$$

The surface force density $\boldsymbol{f}_{\boldsymbol{S}}^{em}$ can also be expressed with $\mathbb{T}$, even though the tensor is discontinuous on the surface. The boundary $\partial\mathscr{B}$ separated the body from other media, hence $\mathbb{T}$ is different on both sides of the boundary and a jump of $\mathbb{T}$ occurs on the interface $\partial\mathscr{B}$. The calculation of the surface force density by the pillbox method is explained with reference to figure I.5 in the following. Two materials, material$^+$ and material $^-$, are separated by the interface S with the surface normal

$\boldsymbol{n}$ pointing in the direction +. A pillbox is generated around a small element $\mathrm{d}S$ of the surface. Its height is set to $2h$ with h in each direction. The force, acting on the pillbox, can be calculated by equation (I.64) with $\mathscr{B}$ corresponding to the volume enclosed by the pillbox and $\partial\mathscr{B}$ to the surface enclosing the pillbox. In the two materials, the tensors $\mathbb{T}^+$ and $\mathbb{T}^-$ are used respectively to calculate the surface forces on the pillbox. When h is decreased to the limit ($h \to 0$), the height of the pillbox approaches zero. At the limit, the resulting force $\mathrm{d}\boldsymbol{f}^{em}$, acting on the pillbox, corresponds to the force density $\boldsymbol{f}_{\boldsymbol{S}}^{em}$ on the element $\mathrm{d}S$. It can be obtained by the help of the tensors $\mathbb{T}^+$ and $\mathbb{T}^-$ as shown by equation (I.67). The jump of the stress tensor $[[\mathbb{T}]]$ on a surface S is defined as the difference of the tensor on both sides of the interface, $\mathbb{T}^+ - \mathbb{T}^-$, where the surface normal of S points in the direction of the domain + (equation (I.68)). The jump of the stress tensor corresponds to the surface force density on a material interface.

$$\mathrm{d}\boldsymbol{f}^{em} = \lim_{h\to 0} \oint_{\partial\mathscr{B}} \mathbb{T}\boldsymbol{n}\,\mathrm{d}S \approx (\mathbb{T}^+\boldsymbol{n}^+ + \mathbb{T}^-\boldsymbol{n}^-)\,\mathrm{d}S = (\mathbb{T}^+ - \mathbb{T}^-)\boldsymbol{n}\,\mathrm{d}S = \boldsymbol{f}_{\boldsymbol{S}}^{em}\,\mathrm{dS} \quad \text{(I.67)}$$

$$\boldsymbol{f}_{\boldsymbol{S}}^{em} = (\mathbb{T}^+ - \mathbb{T}^-)\,\boldsymbol{n} = [[\mathbb{T}]]\,\boldsymbol{n} \quad \text{(I.68)}$$

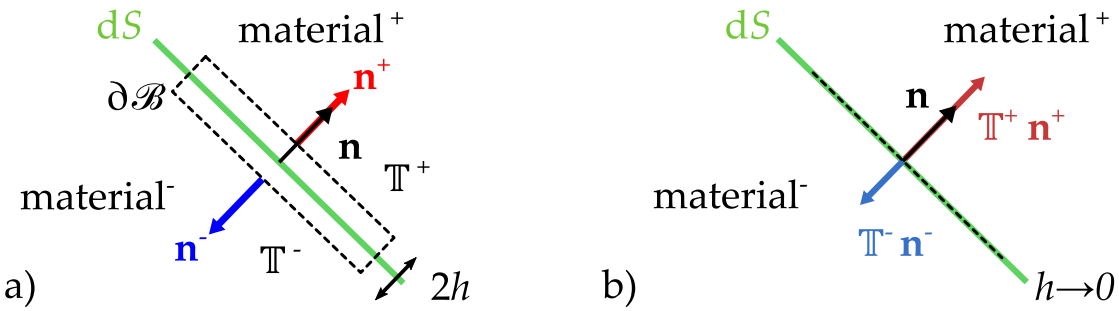

Figure I.5: Schematic representation of the pillbox method applied to obtain the jump of the tensor $\mathbb{T}$ over the surface S, height $2h$ of the pillbox non-negligible (a) and $h \to 0$ (b).

For isotropic materials, the volume torque density vanishes and $\boldsymbol{c}_{\boldsymbol{V}}^{em} = \boldsymbol{0}$ and equations (I.64) and (I.65) can be rewritten by the help of equations (I.66) and (I.68) such as

$$\boldsymbol{F}^{em} = \int_{\mathscr{B}} \boldsymbol{div}(\mathbb{T})\,\mathrm{d}V + \oint_{\partial\mathscr{B}} [[\mathbb{T}]]\,\boldsymbol{n}\,\mathrm{d}S\,, \quad \text{(I.69)}$$

$$\boldsymbol{T}_O^{em} = \int_{\mathscr{B}} \overline{OP}_V \times \boldsymbol{div}(\mathbb{T})\,\mathrm{d}V + \oint_{\partial\mathscr{B}} \overline{OP}_S \times [[\mathbb{T}]]\,\boldsymbol{n}\,\mathrm{d}S\,. \quad \text{(I.70)}$$

Using the divergence theorem, equations (I.69) and (I.70) can be rewritten and lead to the expressions given in equations (I.71) and (I.72) as shown by [Hirsinger+ 2013]. The relations are valid for the aforementioned assumptions: isotropic materials and quasi-static magnetic loadings. For this special case, the resulting force and torque are obtained by the help of the stress tensor $\mathbb{T}^+$ in the material on the side + of the boundary.

$$\boldsymbol{F}^{em} = \oint_{\partial\mathscr{B}} \mathbb{T}^{+}\,\boldsymbol{n}\,\mathrm{d}S \tag{I.71}$$

$$\boldsymbol{T}_O^{em} = \oint_{\partial\mathscr{B}} \overline{OP_S} \times (\mathbb{T}^{+}\,\boldsymbol{n})\,\mathrm{d}S \tag{I.72}$$

In the case that the material + is non-polarizable, the tensor $\mathbb{T}^{+}$ corresponds to the Maxwell stress tensor $\mathbb{T}^{MW}$. The latter can also be expressed in the coordinate system $[\boldsymbol{e}_n\ \boldsymbol{e}_t\ \boldsymbol{e}_{n\times t}]$, associated to the surface normal $\boldsymbol{n}$. With the magnetic flux density $\boldsymbol{B} = B_n\,\boldsymbol{e}_n + B_t\,\boldsymbol{e}_t + 0\,\boldsymbol{e}_{n\times t}$ (figure I.6 b), the expression $\mathbb{T}^{MW}\,\boldsymbol{n}$ corresponds to equation (I.73).

$$\mathbb{T}^{MW}\,\boldsymbol{n} = \frac{B_n^2 - B_t^2}{2\mu_0}\,\boldsymbol{e}_n + \frac{B_n B_t}{\mu_0}\,\boldsymbol{e}_t \tag{I.73}$$

For a magnetic flux density, oriented perfectly perpendicular to the surface, equation (I.73) reduces to the term $B_n^2/(2\mu_0)\,\boldsymbol{e}_n$, also known as magnetic pressure or Maxwell pressure.

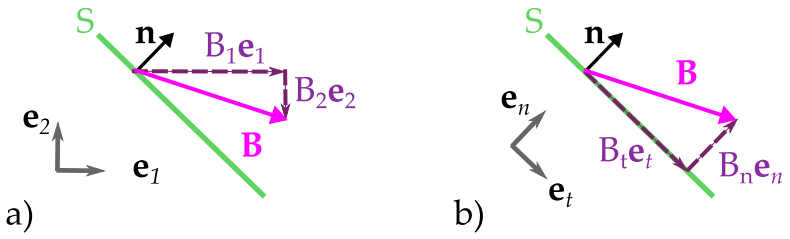

Figure I.6: Components of the magnetic flux density $\boldsymbol{B}$ in the coordinate systems $[\boldsymbol{e}_1\ \boldsymbol{e}_2\ \boldsymbol{e}_3]$ (a) and $[\boldsymbol{e}_n\ \boldsymbol{e}_t\ \boldsymbol{e}_{n\times t}]$ (b).

I.3.3 Quasi-static magneto-mechanical balance laws

To include the magnetic constraints in governing equations of continuum mechanics, magneto-mechanical balance laws have to be established comprising the mass conservation, the balance of the linear momentum and the balance of the angular momentum. Since the magnetic quantities comprise jumps over discontinuity surfaces, the balance laws consist of a part that is verified in the volume of a domain $\mathscr{B}$ and another part, verified on discontinuity surfaces $\partial\mathscr{B}$.
The mass conservation states, that the mass of a material domain $\mathscr{B}$ remains unchanged during the motion of the body (equation (I.4)). When the velocity $\boldsymbol{v}$ is supposed to be uniform, the local form of the mass conservation can be rewritten as shown in equation (I.74). The description of discontinuity surfaces, which are in relative motion with respect to the material domain, requires an additional jump condition on the surface ([Eringen+ 1990]), but the condition is not required in the context of the present thesis.

$$\frac{\partial\rho^m}{\partial t} + \boldsymbol{v}\,\boldsymbol{grad}(\rho^m) = \frac{\mathrm{D}\rho^m}{\mathrm{D}t} = \dot{\rho}^m = 0 \qquad \text{in } \mathscr{B}\ . \tag{I.74}$$

The equation of motion is obtained from the balance of the linear momentum and shown for the purely mechanical case in equation (I.12). It is extended by the electromagnetic volume force $\boldsymbol{f}_{\boldsymbol{V}}^{em}$ in the magneto-mechanical case:

$$\boldsymbol{div}(\sigma) + \boldsymbol{f}_{\boldsymbol{V}}^{em} + \boldsymbol{f}_{\boldsymbol{V}}^{mech} = \boldsymbol{0} \qquad \text{in } \mathscr{B} \,. \tag{I.75}$$

In electrostatic or magnetostatic cases, the volume force is described by the divergence of the stress tensor $\mathbb{t}^{em}$ in a frame with a velocity $\boldsymbol{v} \approx \boldsymbol{0}$. The previous section shows, that the electromagnetic tensor is not necessarily symmetric, hence the mechanical stress tensor is not necessarily symmetric as a consequence of the electromagnetic effects. Several authors (e.g. [Lemaitre+ 2009]) propose the definition of a symmetric stress tensor $\tilde{\sigma}$. The resulting formulation is similar to a classical problem of continuum mechanics :

$$\begin{aligned} &\boldsymbol{div}(\tilde{\sigma}) + \boldsymbol{f}_{\boldsymbol{V}}^{mm} = \boldsymbol{0} \qquad \text{in } \mathscr{B} \,, \\ &\tilde{\sigma} = \sigma + \boldsymbol{P} \otimes \boldsymbol{E} - \boldsymbol{B} \otimes \boldsymbol{M} \,, \quad \boldsymbol{f}_{\boldsymbol{V}}^{mm} = \boldsymbol{div}(\mathbb{T}^{sym}) + \boldsymbol{f}_{\boldsymbol{V}}^{mech} \,. \end{aligned} \tag{I.76}$$

In the context of this thesis, the absence of additional volume forces $\boldsymbol{f}_{\boldsymbol{V}}^{mech}$ and electric fields $\boldsymbol{E}$ is assumed. The equation below states a concise formulation of the problem under these assumptions, which is used in the subsequent chapters:

$$\boldsymbol{div}(\sigma + \mathbb{T}) = \boldsymbol{0} \qquad \text{in } \mathscr{B} \,. \tag{I.77}$$

The general form of the electromagnetic linear momentum balance on discontinuity surfaces $\partial\mathscr{B}$ involves the velocity of the domain $\boldsymbol{v}$. Stationary surfaces move with the same velocity as the domain and have no relative velocity. The magneto-mechanical boundary conditions on $\partial\mathscr{B}$ are stated for free surfaces and material interfaces in equations (I.78) and (I.79). An example for the first case is a body which is surrounded by air (negligible pressure). An example for the second case is a body, which is surrounded by another material domain in which non-negligible mechanical stresses can emerge.

$$\sigma\,\boldsymbol{n} = \boldsymbol{f}_{\boldsymbol{S}}^{mech} - [\![\, \mathbb{t}^{EM} + \boldsymbol{G}^{em} \times \boldsymbol{v} \,]\!]\,\boldsymbol{n} \qquad \text{on } \partial\mathscr{B} \,. \tag{I.78}$$

$$[\![\sigma]\!]\,\boldsymbol{n} = \boldsymbol{f}_{\boldsymbol{S}}^{mech} - [\![\, \mathbb{t}^{EM} + \boldsymbol{G}^{em} \times \boldsymbol{v} \,]\!]\,\boldsymbol{n} \qquad \text{on } \partial\mathscr{B} \,. \tag{I.79}$$

For a domain with a velocity too small to have an effect on the magnetic quantities ($\boldsymbol{v} \approx \boldsymbol{0}$) and in absence of electric fields ($\boldsymbol{E} = \boldsymbol{0}$) and additional mechanical surface forces $\boldsymbol{f}_{\boldsymbol{S}}$, the expression in equation (I.79)can be rewritten as

$$[\![\, \sigma + \mathbb{T} \,]\!]\,\boldsymbol{n} = \boldsymbol{0} \qquad \text{on } \partial\mathscr{B} \,. \tag{I.80}$$

The balance of the angular momentum states the symmetry of the stress tensor. As the symmetry is influenced by the electromagnetic volume torque $\boldsymbol{c}_{\boldsymbol{V}}$, a modification of the law is required for magneto-mechanical cases. The general form of the angular momentum balance in presence of an electromagnetic field is stated below in equation (I.81).

$$\epsilon : \sigma + \boldsymbol{c_V} = \mathbf{0} \; . \tag{I.81}$$

According to [Eringen+ 1990], the jump condition of the angular momentum balance is satisfied identically. Equation (I.57) shows, that the torque can be expressed by the help of the electromagnetic stress tensor and the permutation symbol. Assuming the absence of electric fields ($\boldsymbol{E} = \mathbf{0}$) and using the tensor $\mathbb{T}$, the expression in equation (I.81) can be rewritten:

$$\epsilon : (\sigma - \boldsymbol{B} \otimes \boldsymbol{M}) = \mathbf{0} \; . \tag{I.82}$$

I.3.4 Clausius-Duhem Inequality

The expressions of the first and second principle of thermodynamics constitute the remaining magneto-mechanical balance laws. Their expressions in a continuous domain $\mathscr{B}$ are presented in the following. The first principle of thermodynamics states the conservation of energy: a variation of the sum of the internal and kinetic energies corresponds to the sum of the rate of work (or power) of all forces and torques and the energies that enter or leave the body. According to [Lemaitre+ 2009], the local form of the energy conservation for small strain and displacements (cf. section I.1.2) corresponds to

$$\rho^m \dot{e} = \sigma : \dot{\varepsilon} + \mu_0 \boldsymbol{H} \cdot \dot{\boldsymbol{M}} + \boldsymbol{j} \cdot \boldsymbol{E} + r - div(\boldsymbol{q}) \; , \tag{I.83}$$

where e is the specific internal energy and r and $\boldsymbol{q}$ correspond to a volume heat source and the rate of heat flow respectively. The second principle of thermodynamics states, that the sum of the entropy supply is never bigger than the time rate of change of the total entropy s in a body:

$$\rho^m \dot{s} \geq div\left(\frac{\boldsymbol{q}}{T}\right) - \frac{r}{T} \; , \tag{I.84}$$

where T corresponds to the absolute temperature and is always positive. For this reason, the equation can be multiplied by T. The development of the term describing the heat flux and a rearrangement of equation (I.84) leads to

$$\rho^m T \dot{s} + div(\boldsymbol{q}) - \frac{\boldsymbol{q} \cdot \boldsymbol{grad}(T)}{T} - r \geq 0 \; . \tag{I.85}$$

The Clausius-Duhem inequality (equation (I.85)) is commonly used to derive thermodynamically consistent constitutive relations for materials. Since a constitutive equation is presented in the third chapter of this thesis, the framework for the derivation of local state laws is presented in the following. In a first step, the expression of r, given by equation (I.83) is inserted in equation (I.85) which leads to the expression

$$\rho^m (T\dot{s} - \dot{e}) + \sigma : \dot{\varepsilon} + \mu_0 \boldsymbol{H} \cdot \dot{\boldsymbol{M}} + \boldsymbol{j} \cdot \boldsymbol{E} - \frac{\boldsymbol{q} \cdot \boldsymbol{grad}(T)}{T} \geq 0 \; . \tag{I.86}$$

It is common to use a Legendre transformation to represent the entropy inequality by the help of the generalized Helmholtz free energy Ψ. For the present case, the transformation also includes a variable change for the magnetic term $\mu_0 \boldsymbol{H} \cdot \dot{\boldsymbol{M}}$ since $\boldsymbol{H}$ is supposed to be a state variable. The definition of the free energy comprises the mass magnetization $\mathtt{M} = \boldsymbol{M}/\rho^m$:

$$\Psi = e - Ts - \frac{1}{\rho^m}\mu_0 \boldsymbol{H} \cdot \boldsymbol{M} = e - Ts - \mu_0 \boldsymbol{H} \cdot \mathtt{M} \,. \tag{I.87}$$

The time derivative of equation (I.87) is inserted in equation (I.86) and replaces the terms comprising $\dot{e}$ and $\dot{s}$. The time derivative of the free energy Ψ comprises the relation $\dot{\boldsymbol{M}} = \dot{\rho}^m \mathtt{M} + \rho^m \dot{\mathtt{M}}$. Equation (I.74) states that $\dot{\rho}^m$ is null, $\dot{\boldsymbol{M}}$ thus corresponds to $\rho^m \dot{\mathtt{M}}$ and the Clausius-Duhem inequality is described by

$$\underbrace{-\rho^m(\dot{\Psi} + s\dot{T}) + \sigma : \dot{\varepsilon} - \mu_0 \dot{\boldsymbol{H}} \cdot \boldsymbol{M}}_{(1)} + \underbrace{\boldsymbol{J} \cdot \boldsymbol{E}}_{(2)} - \underbrace{\frac{\boldsymbol{q} \cdot \boldsymbol{grad}(T)}{T}}_{(3)} \geq 0 \,, \tag{I.88}$$

where part (1) corresponds to the intrinsic dissipation processes, (2) to the Joule heating and (3) to thermal dissipation processes. The part (1) of equation (I.88) equals zero for reversible transformations and for a uniform temperature and in absence of an electric field ($\boldsymbol{grad}(T) = 0$ and $\boldsymbol{E} = \boldsymbol{0}$), it reduces to the expression

$$-\rho^m(\dot{\Psi} + s\dot{T}) + \sigma : \dot{\varepsilon} - \mu_0 \dot{\boldsymbol{H}} \cdot \boldsymbol{M} = 0 \,. \tag{I.89}$$

I.3.5 Thermodynamic potential and state laws

The equality, stated in equation (I.89), is used for the development of the local state laws in the following. The free energy in the present example depends on the strain ε, the magnetic field $\boldsymbol{H}$ and the temperature T and its time derivative is described by

$$\dot{\Psi}(\varepsilon, \boldsymbol{H}, T) = \frac{\partial \Psi}{\partial \varepsilon} : \dot{\varepsilon} + \frac{\partial \Psi}{\partial \boldsymbol{H}} \cdot \dot{\boldsymbol{H}} + \frac{\partial \Psi}{\partial T}\dot{T} \,. \tag{I.90}$$

The expression of $\dot{\Psi}$ given in equation (I.90) is inserted in equation (I.89) which leads to the relation shown in equation (I.91). This relation is used to derive the local state laws.

$$\left(\sigma - \rho^m \frac{\partial \Psi}{\partial \varepsilon}\right) : \dot{\varepsilon} - \left(\mu_0 \boldsymbol{M} + \rho^m \frac{\partial \Psi}{\partial \boldsymbol{H}}\right) \cdot \dot{\boldsymbol{H}} - \rho^m \left(\frac{\partial \Psi}{\partial T} + s\right)\dot{T} = 0 \,. \tag{I.91}$$

For constant temperature and magnetic field ($\dot{T} = 0$ and $\dot{\boldsymbol{H}} = 0$ respectively), the equality has to be satisfied for every evolution of $\dot{\varepsilon}$ that is thermodynamically admissible, which includes zero (ε constant). Under these assumptions, the first

of three state laws, shown in equation (I.92), is derived. The remaining two state laws are derived for different thermodynamically admissible evolutions of $\dot{\varepsilon}$, $\dot{\boldsymbol{H}}$ and $\dot{T}$.

$$\sigma = \rho^m \frac{\partial \Psi}{\partial \varepsilon} \,, \qquad \mu_0 \boldsymbol{M} = -\rho^m \frac{\partial \Psi}{\partial \boldsymbol{H}} \,, \qquad s = -\frac{\partial \Psi}{\partial T} \,. \tag{I.92}$$

Table I.1 summarizes the independent variables which define the local state of the material, and their associated variables. The state laws are used to derive the magnetoelastic behavior laws in the third chapter of this work.

Observable state variables	Associated variables
ε	σ
$\boldsymbol{H}$	$-\mu_0 \boldsymbol{M}$
T	$-s$

Table I.1: Independent state variables and associated variables.

Chapter II

Experimental investigations on the behavior of an stH-MAE

II.1 Introduction

This chapter deals with experimental investigations on the material properties of a MagnetoActive Elastomer (MAE). MAEs are composite materials, composed of a viscoelastic elastomer matrix in which magnetic particles are dispersed. The particle content is indicated with respect to the composite material as weight ratio (mass %) or volumetric filling ratio (vol %). MAE are known for characteristic reactions to magnetic fields like the dependence of their material properties on applied magnetic fields, also known as MagnetoRheological (MR) effect ([Rigbi+ 1983; Jolly+ 1996b]) or their deformation in magnetic fields (MagnetoStrictive MS effect [Stepanov+ 2008; Danas+ 2012]). These effects make MAE interesting for actively controlled devices like dampers [University of Nevada 2004; Szmidt+ 2019] or actuators [ZF Friedrichshafen AG 2016; Böse+ 2021]. The characteristics of a MAE depend to a large extend on the choice of the raw materials and the microstructure, which is determined during the elaboration.

II.1.1 Manufacturing processes for MAE

The manufacturing process of a MAE consists of the dispersion of the magnetic particles in the elastomer matrix. The elaboration procedure depends on the matrix viscosity prior to the polymerization: if the material is rather liquid, the magnetic particles are added and the constituents are blended with a mixer to obtain a homogeneous particle distribution. A degassing step under vacuum is performed to remove air bubbles, which can appear during the mixing. The preparation of composites, based on viscous when non-polymerized matrices, requires rolling processes for the dispersion of the particles in the matrix [Danas+ 2012]. In both cases, the mixture is molded and the polymerization takes place during the so–called curing step (cf. [Sutrisno+ 2015] for example). Additional constituents like silicone oil can be added to the mixture to modify the material properties [Stepanov+ 2017].
The blending of the constituents generates structurally isotropic composites since the particles are randomly dispersed (cf. figure II.1 a). When the mixture is polymerized ("cured") in a magnetic field, the particles align in chains along the magnetic field lines [Wen+ 2017; Bodelot+ 2018; Danas+ 2012]. As a result, the composite has a transversely isotropic microstructure (cf. figure II.1 c). The risk of particle sedimentation during the curing is lower for this manufacturing approach since the external field causes magnetic interactions between the particles that are superior to the gravitational forces according to [Stepanov+ 2014]. To inhibit sedimentation in isotropic composite samples, the authors suggest the use of very high frequency (VHF) magnetic fields to accelerate the polymerization process.
To analyze the internal structure of MAE, scanning electron microscopes (SEM) are commonly used [Chen+ 2007; Wen+ 2017] (cf. figure II.1 b). More information on the spatial distribution of the particles and microstructural processes can be obtained by the means of X-ray microtomography as the study of [Schümann+ 2017]

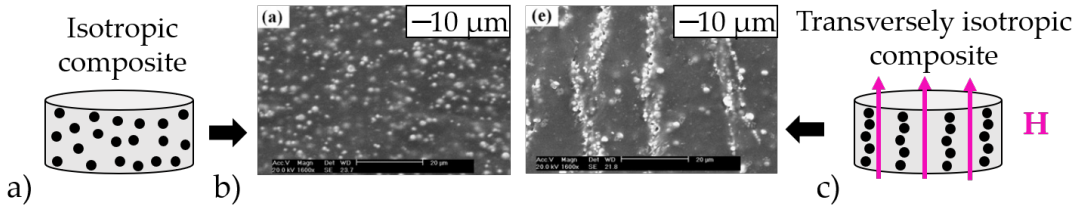

Figure II.1: Schematic representation of MAE with isotropic microstructure (a), transversely isotropic microstructure with the magnetic field H applied during the polymerization (c) and scanning electron microscope images of MAE cured without an external field and in a field of 0.8 T obtained by [Chen+ 2007] (b).

shows. The influence of microstructural aspects like the particle content [Böse+ 2009] or the particle size and their distribution in the matrix [Böse+ 2009; Lokander+ 2003] on the properties of MAE have intensively been studied. Additional studies concern the properties of the raw materials. The matrix material of MAE generally has a very low stiffness (Young's modulus $E \sim 10^4$ Pa to $E \sim 10^5$ Pa) to enhance the MR and MS effects. The magnetic characteristics of the particles also play an important role for the behavior of the composite, as the following section shows.

II.1.2 Distinction between S-MAE and H-MAE

According to the magnetic behavior of the particles, MAE are classified as magnetically soft (S-MAE) or magnetically hard (H-MAE). **S-MAE** contain particles with a high magnetic permeability in small and moderate magnetic fields and a high saturation magnetization [Lokander+ 2003], like carbonyl iron powder. In an external magnetic field, the rigidity of S-MAE increases and their capacity to dissipate energy rises [Jolly+ 1996b; Lokander+ 2003; Norouzi+ 2017]. The MR-effect is stronger in transversely-isotropic composites than in isotropic composites [Wen+ 2017; Bodelot+ 2018]. Furthermore, it has been shown that the MR effect depends on the particle size and distribution [Lokander+ 2003]. Another characteristic effect is the field induced deformation of S-MAE specimen [Guan+ 2008; Stepanov+ 2008; Danas+ 2012]. The deformation is called magnetostriction, even though it is caused primarily by the rearrangement of the particles in the matrix and not by crystalline anisotropy. Therefore, the field-induced deformation is comparatively large with respect to the order of magnitude known for magnetostrictive strain [Voropaieff 2019]. Isotropic S-MAE tend to elongate in external magnetic fields [Guan+ 2008; Han+ 2013; Stepanov+ 2008] while an elongation as well as a retraction have been measured for transversely isotropic MAE according to [Metsch+ 2016]. In absence of an external magnetic field, S-MAE do not show a significant magnetization (figure II.2 a).
Magnetically hard particles like NdFeB are used for the manufacturing of **H-MAE** [Stepanov+ 2012; Borin+ 2013; Linke+ 2016]. In contrast to magnetically soft composites, H-MAE remain magnetized after the exposure to a strong mag-

netic field. The magnetization takes place after the polymerization in general. In addition, a 3D printing device for H-MAE with pre-magnetized particles in the uncured mixture has been presented recently [Kim+ 2018]. This method can be used to generate regions with different orientations of the magnetization in a single structure. However, the magnetization of composites, produced by this method, is lower than the magnetization of the same material magnetized in an external field. To achieve the highest possible remanent magnetization in conventionally magnetized H-MAE, the composite has to be magnetically saturated. The order of magnitude of magnetization fields are about 1.5 T to 2 T [Stepanov+ 2012; Borin+ 2013; Schümann+ 2017]. The intensity of the magnetic field used for the alignment of particles in transversely isotropic structures stays comparatively moderate compared to the magnetization fields [Schümann+ 2017; Wen+ 2017]. Several studies show, that the remanent magnetization increases with the volume fraction [Kramarenko+ 2015; Kim+ 2018]. The magnetic behavior of a composite, containing magnetically soft and hard particles (Fe: 65 % and NdFeB: 35 %), has been studied by [Kramarenko+ 2015] (figure II.2 b). Compared to specimen which contained only NdFeB particles, the saturation magnetization of the hybrid composites increased due to the magnetically soft powder but the remanent magnetization and the coercive field strength decrease at the same time.

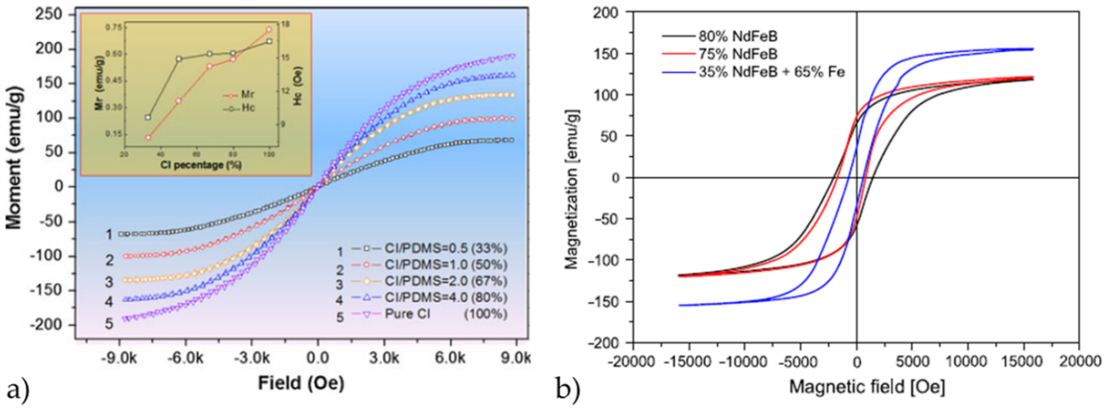

Figure II.2: Magnetization curves for S-MAE with different volume fractions (a), obtained by [Li+ 2011], and for H-MAE and a "hybrid" composite containing magnetically soft and hard particles (b), obtained by [Kramarenko+ 2015].

Three characteristic phenomena of H-MAE are the dependence of the coercivity on the matrix stiffness, a MR effect, caused by the magnetization in absence of external fields, and a MR effect caused by external magnetic fields. The three effects are presented in detail in the following three sections respectively.

II.1.3 Characteristic effects of H-MAE

II.1.3.a Reduced coercivity due to particle motion

Several studies show, that the coercive field strength, Hc, is significantly lower for composites with soft matrices than for composites with stiff matrices [Linke+ 2016; Stepanov+ 2017]. This effect is due to the mobility of the particles: when an externally applied magnetic field and the magnetization of the particles are oriented on different directions, a torque acts on the particles tending to align magnetization with the external field. In soft matrices, the magnetic torque can overcome the resistance of the elastic forces generated by the matrix and instead of being remagnetized in a different direction, the particles rotate [Stepanov+ 2017]. The reversion of the magnetization occurs for lower fields as this process requires less energy than a remagnetization. The rotation of anisotropic magnetic particles in external magnetic fields has been studied by [Schümann+ 2017]. X-ray micro tomography was used in combination with particle tracking in the images. Particles with a high form factor have a higher rotation angle. The dependence of Hc on the matrix material has been studied by [Stepanov+ 2017] on composites based on NdFeB powder and silicone. Different amounts of silicone oil were added to the specimens to reduce their elastic moduli from 90 kPa and their magnetic characteristics were measured by the help of a vibrating sample magnetometer. A decrease of the coercive field with the modulus is stated as well as an asymmetric shape of the hysteresis loops. An asymmetric shape of the hysteresis loop was also observed by [Kramarenko+ 2015] on H-MAE. [Linke+ 2016] compare the major hysteresis loops of a composite with a rigid epoxy matrix and a soft PDMS matrix (figure II.3 a). A great difference of the coercive field is observed: Hc measures about 750 kA/m for the rigid composite and only about 60 kA/m for the soft composite.

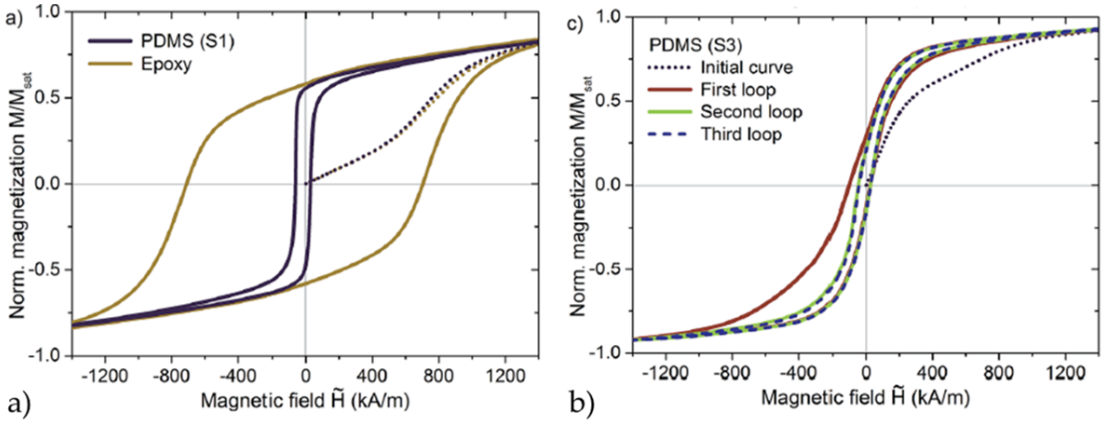

Figure II.3: Magnetization curves for magnetically hard composites with PDMS matrix and epoxy matrix (a) and consecutive hysteresis loops for a composite with PDMS matrix (b) from [Linke+ 2016].

In addition, the major loop was not symmetric: the value of $Hc = 60\,\mathrm{kA/m}$ was measured for the first demagnetization and a value of only $37\,\mathrm{kA/m}$ during the remagnetization. The comparison of subsequent loading cycles shows, that only the first loop is different from the following ones (figure II.3 b). It is stated that the magnetization processes occur during the first cycle and that the magnetic behavior, once the particles are magnetized, is determined by particle rotations. With increasing matrix stiffness, these effects are suppressed as the particle rotation is inhibited.

II.1.3.b MR effects caused by the magnetization

Magnetic fields can cause not only particle rotations, but also a rearrangement of the particles in the soft matrix as shown by [Schümann+ 2017]. During the study, cylindrical specimens were exposed to a magnetic field of 2 T for 5 min. X-ray tomography images, recorded before and after the magnetization, show, that the particles move to align in chains in the soft matrix ($E = 30\,\mathrm{kPa}$). Compression test show an increase of the composites' elastic modulus due to the magnetization. The increase is explained by the formation of particle chains on the microscopic level. The authors also remark, that the movement may induce damage on the microstructural level and, as a consequence, might weaken the fixation of the particles in the matrix. Three types of cylindrical specimens are tested in the study of [Stepanov+ 2012]: non magnetized samples, samples magnetized in a field of 0.3 T and samples magnetized in a field of 1.5 T. The stress-strain relation of the samples was determined in quasi-static shear tests by the help of a rheometer. The displacement was increased at first (loading) and then decreased until the measured reaction force was equal to zero again (unloading). The non-magnetized specimen showed a linear-elastic behavior in the contrast to the magnetized specimen, for which a residual strain was observed (figure II.4 a). The elastic modulus, calculated from the stress-strain relations, increased with increasing magnetization. The authors explain the behavior of the magnetized specimen with the formation of chain like structures of the particles in the matrix due to the remanent magnetization. Additionally, a strain dependence of the modulus was observed for the magnetized specimen. For strain inferior to 0.5 % the modulus was higher than for strain exceeding 0.5 %. The explanation for the two regimes, given by the authors, is the increasing distance between the particles for higher strain which weakens the particle interactions. The strain dependence of the modulus was also observed in tensile test up to 6.6 % of magnetized specimen by [Borin+ 2013]. The specimens in this study were magnetized in fields with different magnitude up to 1.85 T and subjected to a mechanical loading afterwards. Up to a stain of about 0.05 %, the stress increases sharply. The stress increase is much smaller when 0.05 % are exceeded (figure II.4 b). The authors conclude that the elastic modulus is higher for the small strain regime in their tests. In addition, it is shown that the modulus in both regimes increases gradually with the magnetization field for specimens magnetized in fields up to 1.5 T. A further increase of the magnetization field does not influence the stress strain relation in a significant manner.

The effect is explained by the saturation of the NdFeB particles, which occurs for about 1.5 T. An increase of the external field cannot increase the magnetization any further. The dependence of the dynamic shear storage and loss moduli, G' and G'', of transversely isotropic specimens on the magnetization field was analyzed by [Stepanov+ 2014]. During the elaboration, a magnetic field of 0.03 T was used to align the particles in the matrix, whereas the magnetization fields ranged from 0.743 T to 2 T. A rheometer was used for the dynamic mechanical testing. The results of the dynamic tests are in accordance with the findings of the aforementioned quasi-static tests: a modulus increase with the magnetization field was observed up to a certain magnitude of the magnetization field. An additional observation has been made by [Kramarenko+ 2015] and concerns the relaxation behavior of H-MAE. According to the authors, the magnetization of NdFeB-based composites leads to an increase of the relaxation time from several seconds to more than 30 s. It is supposed, that the magnetic interactions between the particles enhance their rearrangement in the matrix, which takes place when the specimen is deformed.

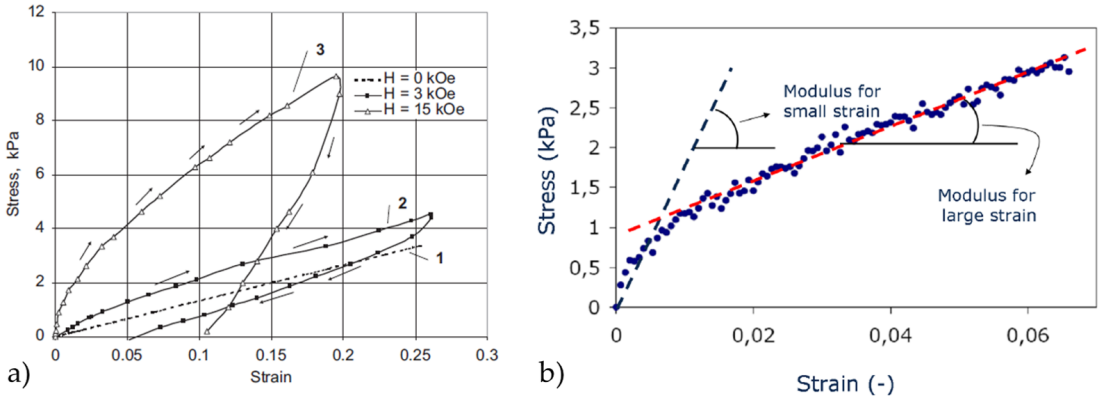

Figure II.4: Stress-strain curves of a non-magnetized specimen and two specimens magnetized in different fields $\boldsymbol{H}$ (a) from [Stepanov+ 2012] and stress strain curve of a magnetized specimen showing two different moduli (b) from [Borin+ 2013]

II.1.3.c MR effects caused by external magnetic fields

The mechanical behavior of H-MAE is not only influenced by the magnetization, but also by external magnetic fields. This is shown, inter alia, by the study of [Stepanov+ 2012]. A field-induced variation of the storage and loss moduli, G' and G'', has been observed during dynamic shear tests. The external magnetic field measured 0.3 T and was either oriented in the direction of the specimens' magnetization ($\boldsymbol{H} \uparrow\uparrow \boldsymbol{M}$) or opposite to it ($\boldsymbol{H} \uparrow\downarrow \boldsymbol{M}$) during the test. For $\boldsymbol{H} \uparrow\uparrow \boldsymbol{M}$, G' and G'' increase. For $\boldsymbol{H} \uparrow\downarrow \boldsymbol{M}$, the moduli first decrease, reach a minimum point and then increase again. This behavior is explained by the disorientation of the magnetic moments of the particles for small to moderate opposed fields, followed by a rearrangement of the particles such as their magnetic moments are reinforced

by further decreasing the magnetic field. The same observation for the modulus has been made by [Wen+ 2017] in dynamic shear test with constant mechanical and cyclic magnetic loading: a magnetic field applied in the opposite direction of the magnetization first weakens and then increases the modulus (figure II.5 a). The authors suppose the magnetic interactions to weaken first and then to increase but base their conclusion on remagnetization processes of the particles. In an additional dynamic study, [Kramarenko+ 2015] have tested magnetized specimen in an external field of 0.3 T with a shear strain amplitude of 0.2 % at a frequency of 1 Hz. It is shown that the variation of the modulus increases with the magnetization of the specimen in the same externally applied magnetic field. When the magnetic field is switched on during the mechanical loading, the behavior of the non-magnetized samples stabilizes in 20 s – 50 s while magnetized specimens are still not stabilized after 150 s. The study also comprises quasi-static shear tests with a maximum strain inferior to 0.06 %. The loading was applied in absence and presence of a magnetic field of 0.15 T. The stress increases stronger with the strain for $\boldsymbol{H} \uparrow\uparrow \boldsymbol{M}$ and less strong for $\boldsymbol{H} \uparrow\downarrow \boldsymbol{M}$ compared to the measurement in absence of a magnetic field (figure II.5 b). The effect is stronger for $\boldsymbol{H} \uparrow\downarrow \boldsymbol{M}$ than for $\boldsymbol{H} \uparrow\uparrow \boldsymbol{M}$.

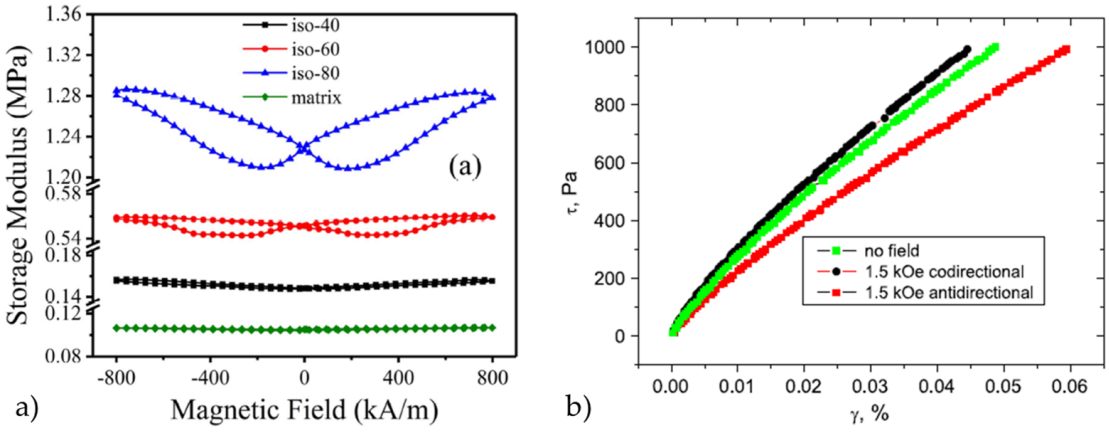

Figure II.5: Storage shear modulus of an H-MAE as a function of the magnetic field for cyclic magnetic loading starting with a field opposite to the magnetization (a) from [Wen+ 2017] and stress-strain relation during the shear loading of an H-MAE for different magnetic fields (b) from [Kramarenko+ 2015].

Quasi-static compression tests of cylindrical H-MAE specimen have been performed by [Schümann+ 2017]. The modulus was calculated based on the data recorded in a strain range from 2.50 % – 8.75 % for non-magnetized and magnetized specimen in absence of a magnetic field and in presence of a field of 240 mT. The modulus of the non-magnetized specimen was not significantly altered by the magnetic field. The modulus of the magnetized specimen on the contrary increased by about 60 %. An overview over the characteristics of some of the H-MAE composites, mentioned in this section, is shown in table II.1.

Table II.1: Characteristics of previously studied H-MAE

Reference	Particles	Particle size	Structure	Particle content	M /Ms / Br	Magnetization field	Hc
[Stepanov+ 2012]	NdFeB	1-100 μm	iso	100 % (powder)	-	15 kOe	1855 Oe
	NdFeB/Fe	1-100 μm/ 3 μm	iso	83 mass % (35/65)	-	15 kOe	-
	NdFeB	1-100 μm	iso	80 mass %	M_s 104 emu/g	15 kOe	1740 Oe
	NdFeB	1-100 μm	iso	75 mass %	M_s 109 emu/g	15 kOe	1271 Oe
[Borin+ 2013]	NdFeB	a μm/50μm	iso	80 mass %	Br 0 T	B 0 T	-
	NdFeB	a μm/50μm	iso	80 mass %	Br 60 T	B 750 T	-
	NdFeB	a μm/50μm	iso	80 mass %	Br 83 T	B 1020 T	-
	NdFeB	a μm/50μm	iso	80 mass %	Br 108 T	B 1500 T	-
	NdFeB	a μm/50μm	iso	80 mass %	Br 110 T	B 1850 T	-
[Kramarenko+ 2015]	NdFeB	50 μm	iso	80 mass %	M 60 emu/g	15 kOe	1.74 kOe
	NdFeB	50 μm	iso	75 mass %	M 60 emu/g	15 kOe	1.27 kOe
	NdFeB/Fe	50 μm / 3-5μm	iso	35/65 mass %	M 35 emu/g	15 kOe	0.65 kOe
	NdFeB	2 μm	iso	75 mass %	M 80 emu/g	15 kOe	1.17 kOe
	NdFeB	2 μm	iso	69 mass %	M 75 emu/g	15 kOe	0.95 kOe
	NdFeB	2 μm	iso	60 mass %	M 59 emu/g	15 kOe	0.70 kOe
[Stepanov+ 2014]	NdFeB	2-70 μm	aniso	30 vol %	-	0	
	NdFeB	2-70 μm	aniso	30 vol %	-	0.743 T	
	NdFeB	2-70 μm	aniso	30 vol %	-	0.868 T	
	NdFeB	2-70 μm	aniso	30 vol %	-	1.020 T	
	NdFeB	2-70 μm	aniso	30 vol %	-	1.250 T	
	NdFeB	2-70 μm	aniso	30 vol %	-	2.000 T	
[Stepanov+ 2017]	NdFeB						2900 Oe
	NdFeB						2700 Oe
	NdFeB						2100 Oe
	NdFeB						700 Oe
	NdFeB						650 Oe
[Linke+ 2016]	NdFeB	46.8 μm	iso	28 vol %			57/(37) kA/m
[Schümann+ 2017]	NdFeB	ca 10-200 μm	iso	40 mass %			

Most of the previously studied composites are based on NdFeB particles while a paper published by [Koo+ 2012] compares H-MAE cantilever structures based on various magnetically hard powders (barium ferrites, strontium, neodymium and samarium cobalt) concerning the magnetically induced deflection of the structure. Under comparable conditions, the composite based on NdFeB particles shows the highest deflection.

II.1.4 Experimental testing of MAE

The material properties in the magnetic and the mechanical domain can be determined by standard test procedures with the corresponding equipment. The previously presented experimental studies concerning the magnetic behavior comprise the recording of hysteresis curves. The latter can be obtained by testing equipment like vibrating sample magnetometers (VSM) which provide high magnetic field intensities for the saturation of the composite material [Linke+ 2016]. Studies on the mechanical behavior focus on elastic or viscoelastic characteristics in quasi-static or dynamic tests respectively. The mechanical properties are obtained by standard testing procedures and equipment like universal testing machines [Borin+ 2013] (quasi static tests), or rheometers (dynamic loading) [Stepanov+ 2012; Kramarenko+ 2015; Wen+ 2017]. The dynamic testing provides information about the viscoelastic properties of the composites. While dynamic tests are generally performed for small or moderate mechanical loading, tensile tests have been used to analyze the large strain behavior as shown on the example of S-MAE specimen [Bodelot+ 2018].
Several experimental setups have been proposed for the analysis of the coupled magneto-mechanical behavior of S-MAE specimen. The experimental conditions in coupled tests have intensively been studied on S-MAE specimen by [Bodelot+ 2018; Voropaieff 2019] in the context of large strain. The authors point out the importance of the magnetic conditions during the tests in particular the influence of the specimen geometry on the internal magnetic field. Since the measurements are based on average quantities, the field homogeneity becomes very important. The latter is influenced by the shape of the specimen, an ellipsoidal specimen geometry is suggested to obtain a homogeneous magnetic field. For the determination of the coupled properties of H-MAE, fewer experimental test benches have been presented so far in comparison to the work on S-MAE. In the study of [Stepanov+ 2012], for example, a solenoid with an inner diameter of 20 mm is placed in a rheometer during shear tests on cylindrical specimens. The same experimental configuration is used in the study of [Kramarenko+ 2015]. In this configuration, the magnetization and the external magnetic field are applied in the direction perpendicular to the mechanical loading. In the work of [Schümann+ 2017], the use of two permanent magnets for the generation of an external magnetic field during quasi-static compression tests is presented. The magnets are positioned at a fixed distance and the loading is applied via a universal testing machine on cylindrical specimen. In this configuration, mechanical loading, magnetization and the direction of the external field are supposed to be oriented in the same direction. Tensile tests in

the small strain regime have been performed on magnetized H-MAE specimen by [Borin+ 2013]. A coil is shown in the description of the experimental setup but not mentioned during the description of the measurements.

II.1.5 Context of the present work

The present work deals with a composite material with a comparably stiff matrix material ($E \sim 1$ to $E \sim 10$ MPa) compared to the stiffness of matrices used in prior studies ($E \sim 10$ to $E \sim 100$ kPa). The composite in this study is thus called stiff (st)H-MAE in the following, to delimit it from previously studied mostly soft (so)H-MAE. The stH-MAE remains easily deformable; however, the increased stiffness of the matrix presumably influences the particle motions in the matrix, which is the cause of characteristic effects observed in H-MAE. According to [Borin+ 2013] for example, a modulus of 200 kPa is the limit for a significant MR effect. On the other hand, the particle motions are responsible for reduced coercive fields [Linke+ 2016; Stepanov+ 2017], the composite can thus be demagnetized more easily. Furthermore, particle motions during the magnetization may reduce the structural integrity of the composite [Schümann+ 2017].
The first chapter of this PhD thesis aims to address these questions and provide information about the magnetic, mechanical and coupled behavior of an isotropic stH-MAE, composed of NdFeB particles and a silicone matrix, by the means of experimental characterizations. The chapter is organized as follows: the first part focuses on the manufacturing process of the composite material and its microstructure. Thereafter, the magnetic characterization of the stH-MAE is presented including cyclic magnetic loading for different filler contents and temperatures as well as the dependence of the residual flux density on the filler content. In the following section, the mechanical characterization is outlined. Quasi-static uniaxial tensile tests on non-magnetized composites are presented at the beginning. Afterwards, the results of Dynamic Mechanical Analysis (DMA) of the matrix material and composites with different filler content are detailed. The last section presents the study of the coupled behavior of stH-MAE. In the first part, the influence of the magnetization on the dynamic mechanical properties is analyzed. In the second and third part of the study, a test bench for the analysis of the coupled behavior in an external magnetic field is presented along with the first test results of magnetomechanical measurements.

II.2 Manufacturing of an isotropic stH-MAE

This section deals with the manufacturing of a mechanically stiff magnetically Hard MagnetoActive Elastomer (stH-MAE). The characteristics of the primary materials are outlined and the manufacturing process is described. In addition, scanning electron microscope images of the microstructure are presented.

II.2.1 Raw materials

The stH-MAE, used for in the present work, is composed of a magnetically hard powder which is dispersed in a silicone matrix. The elastomer MED-4014 [NuSil 2020] is a two-part silicone, that cures with heat via platin catalyzed addition-cure chemistry, provided by NuSil^{TM}. The ratio of mixture of the two parts, A and B, is 1:1. In the uncured state, the consistency of the two parts can be compared to modeling clay. The properties of the silicone, indicated in the material datasheet, are given with reference to several standard testing methods of the American Society for Testing and Materials (ASTM). In the cured state, the silicone has a specific gravity of 1.08 (ASTM D792), a shore hardness of 15 (Durometer type A, ASTM D2240) and develops a tensile stress of maximally 4.8 MPa before the rupture in tensile tests according to ASTM D412. The cured elastomer is transparent as figure II.6 a shows. The magnetic powder MQFP-14-12 consists of NdFeB particles and is provided by Magnequench^{TM} in a non-magnetized state. According to the datasheet, 50 % of the particles have a diameter smaller than or equal to 4.5 µm – 6.5 µm, which is indicated by the PSD50 value. The small diameter is reached by jet milling and the shape of the particles can be described as random (figure II.6 b). According to the datasheet, the particles are magnetically isotropic, the residual flux density Br of the material measures 805 ±20 mT and the internal coercive field strength Hc measures 965 ±55 kA/m. The elaboration of the composite from the two raw materials will be described in the following.

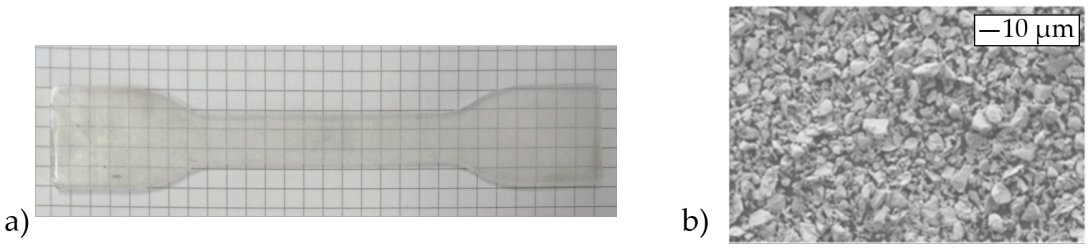

Figure II.6: Transparent, cured silicone specimen in dumbbell form (a) and SEM image of the magnetic powder MQFP-14-12 provided by Magnequench^{TM}.

II.2.2 Manufacturing process of the stH-MAE

A commonly used indicator for the composition of a MAE is the volume fraction Φ. This parameter corresponds to the relation of the magnetic powder volume $V_{particles}$ in a reference composite volume $V_{composite}$:

$$\Phi = \frac{V_{powder}}{V_{composite}} = \frac{V_{powder}}{V_{powder} + V_{matrix}} \tag{II.1}$$

For the manufacturing process however, the mass of the constituents is the more easily accessible than their volume. To elaborate a stH-MAE structure with a specific volume fraction Φ, the required mass of powder and silicone is calculated in a first step by the help of the mass density. The matrix material is viscous in the uncured state, the dispersion of the particles in the matrix requires thus several mixing sequences. The procedure presented in the following is not an industrial process, but allows the manufacturing of specimen with a simple geometric shape (parallelepipedic for example, cf. figure II.7). Before the mixing begins, the silicone parts A and B are passed separately through a two-roll mill several times to soften. Once a part is softened, it is formed into a sheet. Afterwards a small quantity of powder is placed in the middle of the sheet and the silicone is then folded around the powder to enclose it. The mix is passed through the mill, folded again and milled again until the powder is evenly dispersed in the matrix. Small quantities of powder are added until the final volume fraction Φ is reached. The volume fractions of the composite specimen used for this study are comprised between 12.4 % and 36.2 %. They are blended with the particles separately to prevent polymerization during the mixing. When both silicone parts have been prepared, they are milled together. The blended composite is placed into a mold. A pressure of $50 \cdot 10^5\,\mathrm{N/m^2}$ is applied on the mobile part of the mold to press the composite into its final form and evacuate eventual air bubbles. The curing takes place at a temperature of 116 °C during 10 minutes.
For the elaboration of MAE, a very viscous when uncured matrix is less often used [Danas+ 2012] than a matrix that is liquid before polymerization [Linke+ 2016; Sutrisno+ 2015; Wen+ 2017; Bodelot+ 2018; Stepanov+ 2012; Kramarenko+ 2015; Kim+ 2018; Małecki+ 2015], probably because the mixing procedure is more complex. For the present study, composite sheets with different thickness (between 1 mm and 4 mm) and with an area of 200 mm × 250 mm have been realized. The specimens are cut out via a cutting die or a conventional lathe. The magnetization is an additional step, that is exhibited after the cutting process. A specimen is therefore placed in a strong external magnetic field of 4 T generated in a coil by a capacitor discharge and allowing the saturation of the NdFeB particles. When the external field is switched off, the composite retains a permanent magnetization since NdFeB is a magnetically hard material. Since several differently shaped specimens have been used for the experimental characterization, the geometric details are not listed here but in the corresponding section of this chapter.

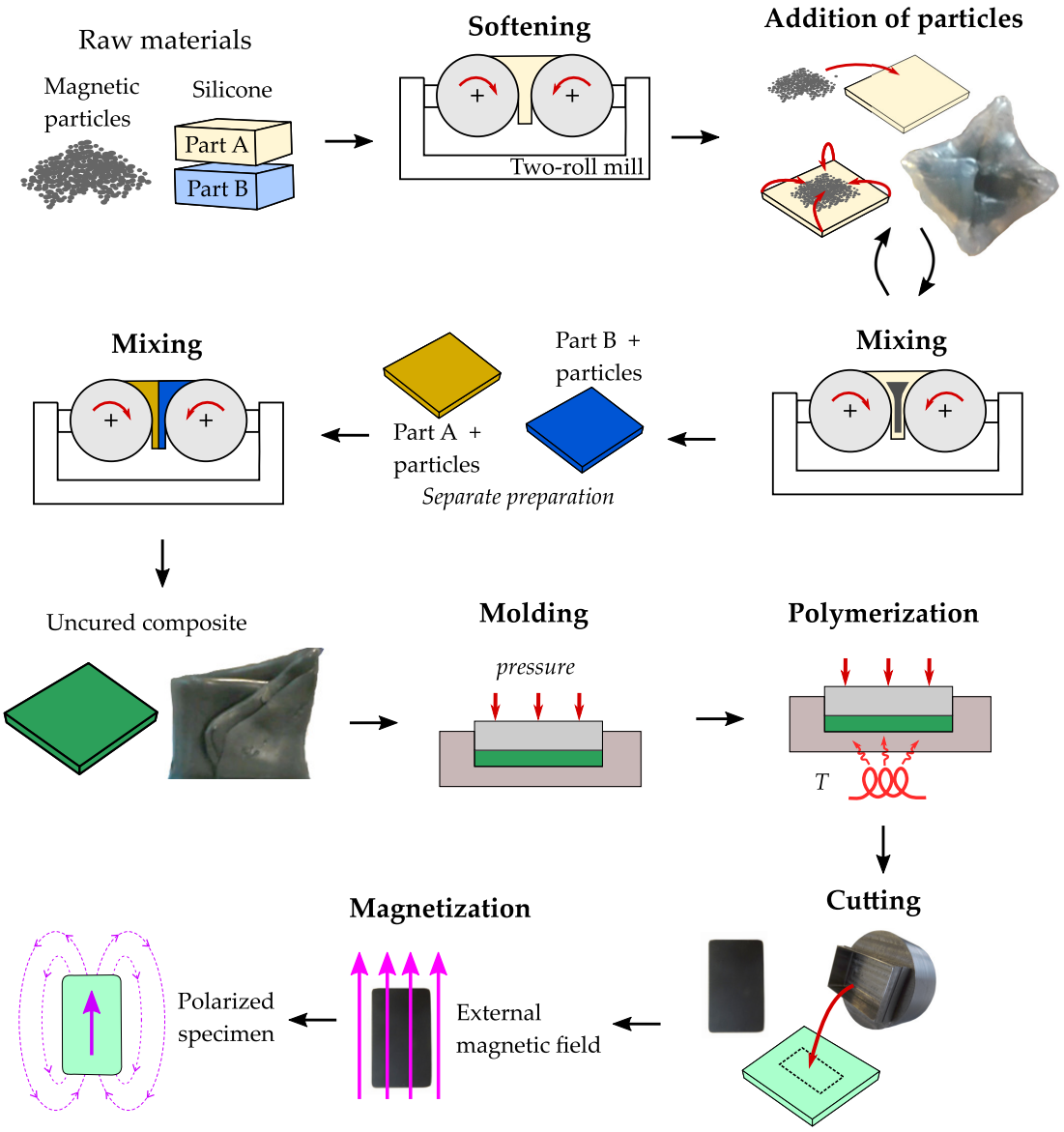

Figure II.7: Elaboration procedure for magnetically hard, magnetized stH-MAE composite specimen.

II.2.3 Microstructure

A Scanning Electron Microscope (SEM) is used to study the microstructure of an stH-MAE with a volume fraction of $\Phi = 19.4\,\%$. The surface of observation lies in the cross section of the material and is obtained by freeze-fracturing. Figure II.8 a shows a SEM image of the fractured surface with 1000x magnification. The particles are denser than the silicone and reflect more electrons, thus they are the lighter spots in the image. They are dispersed randomly in the matrix and do not show a specific spatial orientation. This observation was also made for SEM images of other observation surfaces in the three principal directions of the composite sheet. According to the SEM images, the composite is structurally isotropic.

Figure II.8 b shows a part of the fractured surface with 5000x magnification. A large size distribution as well as irregular forms of the particles are observed. The analysis could only be performed with non-magnetized samples as the magnetic field of magnetized specimens interfered with the electron beam of the SEM and, as a consequence, the images were blurred.

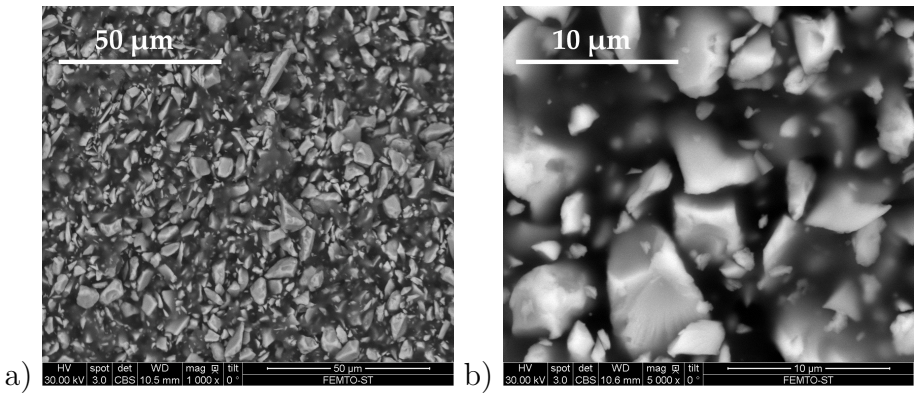

a) b)

Figure II.8: SEM image of a stH-MAE composite with a volume fraction of $\Phi = 19.4\,\%$ for magnifications of 1000x (a) and 5000x (b).

II.3 Magnetic characteristics

In this section, experimental studies concerning the magnetic properties of the stH-MAE are presented. In the first part, the demagnetization behavior of the composite is compared to a compressed powder sample and another composite with different volume fraction. The influence of the volume fraction on the residual flux density is studied in detail in the following part. An additional study, presented afterwards, concerns the temperature dependence of the magnetic properties of the stH-MAE. Details of the specimen are given in each section and are summarized in the appendix (table A.1). As the tests are uni-axial, the magnetic quantities are scalar values corresponding to the magnitude in the tested direction.

II.3.1 Demagnetization and magnetic hysteresis

In a first study, the dependence of the composite's magnetic polarization J on the magnetic field H is analyzed. Therefore, the demagnetization behavior of the magnetic powder is compared to the behavior of a composite material with a volume fraction of $\Phi = 29.8\,\%$. The measurement data of a compressed powder sample have been provided by Magnequench while the composite specimen S_{mag1} has been tested with an extraction magnetometer at the *Institut Néel* in Grenoble. The cylindrical specimen had a diameter of 5.8 mm and a height of 0.85 mm. The demagnetization behavior of the two samples is shown in Figure II.9. At $H = 0$, the remanent polarization J_r (equivalent to the residual flux density Br) can be found.

The polarization decreases under the influence of a magnetic field opposed to the magnetization of the samples. When the coercive field strength Hc is reached, the material is demagnetized ($J = 0$). The comparison of the two materials shows that their coercive field strength Hc differs slightly. It measures 969 kA/m for the powder and 941 kA/m for the composite, both values lie within the range specified for Hc in the powder's datasheet. Their polarization J_r differs much more: it measures 0.809 T for the powder sample and 0.227 T for the composite.

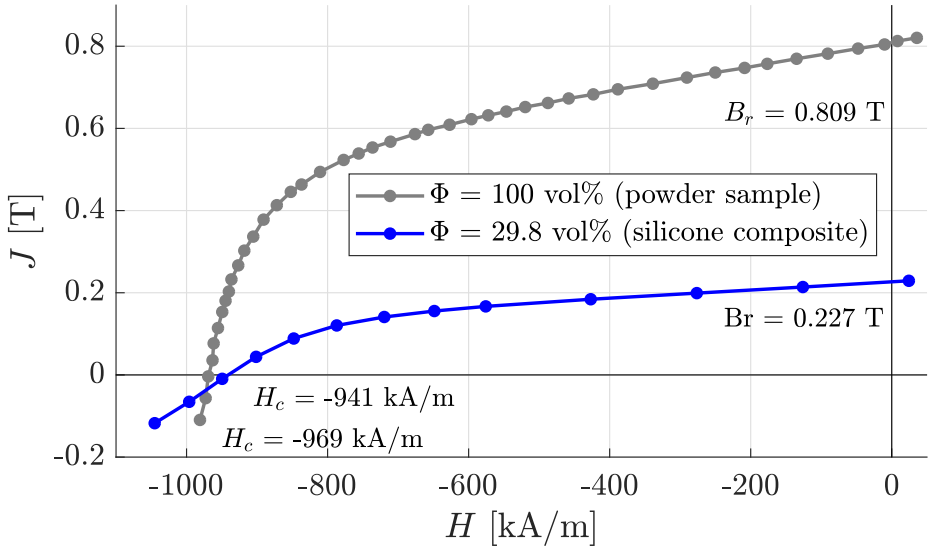

Figure II.9: Demagnetization curves of a compressed powder sample and the specimen S_{mag1}.

The entire first hysteresis loop has been revealed at the *Institut Néel* for specimen S_{mag1} and for an additional specimen with a volume fraction of $\Phi = 21.6\,\%$, a diameter of 5.78 mm and a height of 0.9 mm. In the extraction type magnetometer, the magnetic field was increased to about 6300 kA/m. The measurement was started, the magnetic field was gradually decreased to −6300 kA/m and then increased until the initial value was reached again. Based on the sample geometry, the internal magnetic field was calculated and figure II.10 shows the resulting hysteresis curves. The coercive field Hc is similar for both specimens and, according to the measurements of the first study, equivalent to the coercive field of the magnetic powder. This behavior is normally observed for composites with very stiff matrices, for example epoxy resins [Linke+ 2016] or for soH-MAE beneath the glass transition temperature [Kramarenko+ 2015], but not for soH-MAE in the rubbery state. It is supposed that the stiffness of the matrix apparently inhibits particles motions and that the reversal of the apparent magnetization is due to a remagnetization of the particles. The assumption is supported by the fact that the magnetic hysteresis cycles of the two composite materials are symmetric, which is not the case for the first magnetization loop of soH-MAE [Linke+ 2016; Stepanov+ 2017]. The advantage of a high Hc is a stronger resistance to demagnetization fields. In contrast to the coercive field strength, the residual flux density Br is different for

the two specimens. The material with the lower volume fraction shows a lower residual flux density (Br =0.174 T) compared to the material with the higher volume fraction (Br = 0.227 T). The tendency is similar to the observation made in the first study (cf. figure II.9). The dependence of Br on Φ will be discussed in the following section.

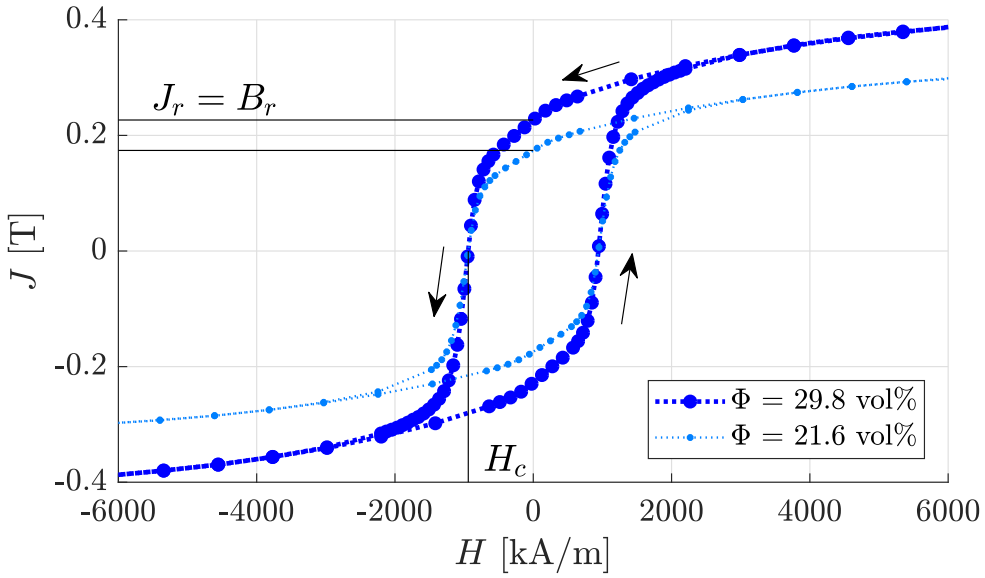

Figure II.10: Magnetic hysteresis loop of the specimens S_{mag1} and S_{mag2} at 20 °C.

II.3.2 Influence of the volume fraction Φ on Br

As stated for the magnetometry tests, the volume fraction has an influence on the residual flux density of the composite. To analyze this dependence more precisely, the residual flux density of four isotropic composite materials with different volume fractions between 12.4 % and 32.2 % has been determined. Three specimens were cut out from each composite (S_{mag4} - S_{mag15}, cf. table A.1). Each specimen had a diameter of 5.5 mm and a height of 0.97 mm. For the tests, the three magnetized specimens of each composite were stacked to form a cylinder with a height of 2.91 mm as for the measurement method described in the following, the geometric form of a long cylinder allows a more precise estimation of Br than flat pastilles. To approximate the residual flux density, the voltage induced by the magnetic cylinders in a pair of Helmholtz coil has been measured. During the measurement the specimen was placed in the coils and the voltage, induced in the coils by this procedure, was summed up by a voltage integrator. Knowing the geometry of the specimen, the number of windings, the resistance and the geometry of the Helmholtz coils as well as the electronic characteristics of the voltage integrator (capacity, resistance, amplification), the residual flux density of the specimen was calculated.
The four cylindrical samples were tested five times each and the mean values are

represented in figure II.11 (pink dots) and in table II.2. The standard deviation of the results due to the measurement method was smaller than 1.06 % and is not shown in the graphic, but a deviation of 5 % due to the specimen form and the resulting approximation on the demagnetizing field is indicated. As the relation between Br and volume fraction seems to be proportional, a linear regression of the measurement values has been performed. The condition applied to the regression was an intersection with the origin of coordinates since a specimen without magnetic particles cannot be magnetized. A proportional factor of 0.0081 [T/%] is obtained from the regression and the corresponding straight is shown as dashed line in Figure II.11. The high correlation coefficient between measurement values and the approximation (0.9998) confirms the assumption of a linear relation.

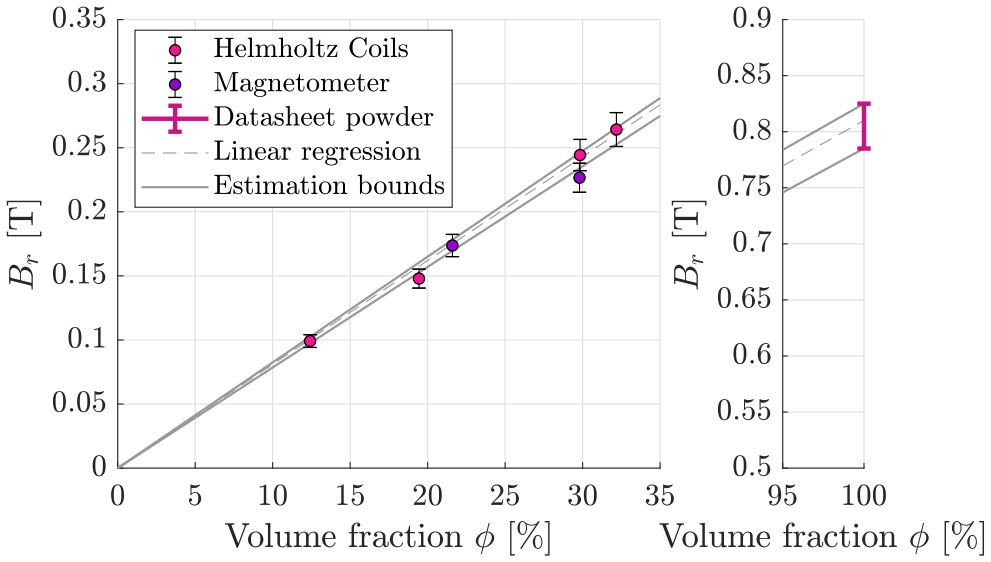

Figure II.11: Dependence of the residual flux density Br of the stH-MAE on its volume fraction Φ.

Φ [%]	Br [T]	obtained by
0.0	0.000	linear regression : $Br = \Phi[\%] \cdot 0.0081$
12.4	0.099	measurement $S_{mag4} - S_{mag6}$
19.4	0.148	measurement $S_{mag7} - S_{mag9}$
29.8	0.244	measurement $S_{mag10} - S_{mag12}$
32.2	0.264	measurement $S_{mag13} - S_{mag15}$
100.0	0.809	measurement of powder sample
100.0	0.810	linear regression: $Br = \Phi[\%] \cdot 0.0081$

Table II.2: residual flux density Br of the stH-MAE for the volume fraction Φ obtained by experiments or an estimation.

A proportional correlation of the residual flux density and the volume fraction can also be observed in the measurement results of previous studies [Kramarenko+ 2015; Kim+ 2018]. The estimation of Br of the composite based on the volume fraction and the range for the Br of the powder, specified in the datasheet, is shown in form of two gray straights in figure II.11. Considering the measurement uncertainties, all experimentally obtained values lie in the range limited by these estimation bounds. Furthermore, the residual flux density obtained from two magnetometry tests (purple dots) also lies within these bounds. To estimate the residual flux density of the stH-MAE of the present study, only the volume fraction and the Br of the powder are necessary.

II.3.3 Influence of the temperature on Br and Hc

In an additional experimental study, the influence of the temperature on the magnetic characteristics has been revealed. Hysteresis curves of specimen S_{mag3} ($\Phi = 29.8\,\%$) were recorded for different temperatures ranging from 50 °C to 150 °C. Figure II.12 shows the measurement results as well as the previous results for a specimen with the same volume fraction (S_{mag1}) recorded at 20 °C. The graphic shows, that the magnetic characteristics of the composite material are diminished with increasing temperature. For the same magnetic field, the magnetic polarization is smaller the higher the temperature. At the same time, the coercive field strength decreases, which means that the material can be demagnetized more easily.

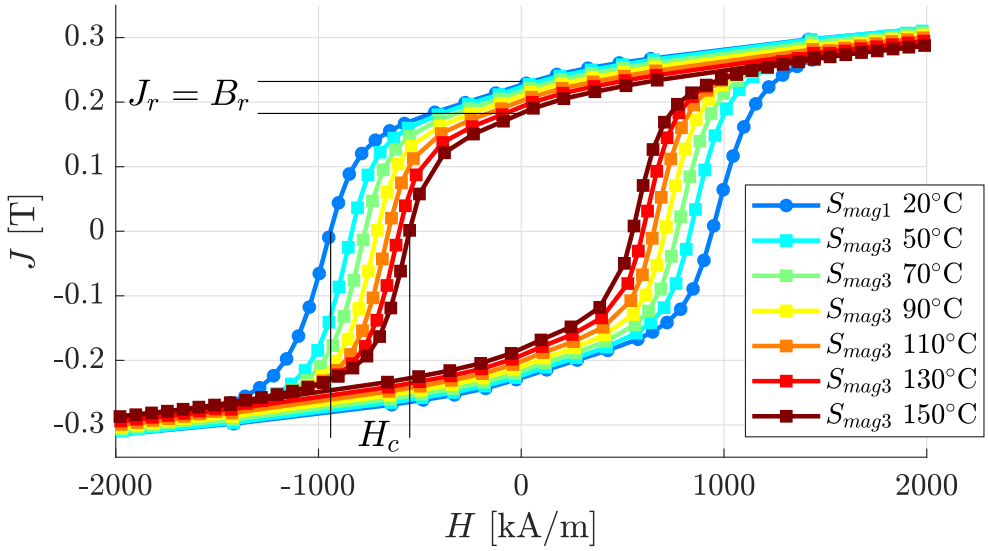

Figure II.12: Magnetic hysteresis loops of the specimens S_{mag1} and S_{mag3} ($\Phi = 29.8\,\%$) at different temperatures.

According to the datasheet, the magnetic properties Br and Hc of the powder are supposed decrease in a linear manner with increasing temperature up to 100 °C. To estimate the decrease, the temperature coefficients α and β are stated in the

document. Starting from an initial temperature T_0, the characteristics of the powder at a temperature T can be estimated by the following relations:

$$Br(T) = Br(T_0) + \alpha \cdot Br(T_0) \cdot (T - T_0), \qquad \alpha = -0.13\,\%/°\mathrm{C}, \tag{II.2}$$

$$Hc(T) = Hc(T_0) + \beta \cdot Hc(T_0) \cdot (T - T_0), \qquad \beta = -0.40\,\%/°\mathrm{C}. \tag{II.3}$$

Equations (II.2) and (II.3) were used to estimate the evolution of Br and Hc for S_{mag3} during the experiment, to check if they are valid not only for the powder but also for the stH-MAE. The initial temperature T_0 was set to 50 °C as this was the lowest temperature during the tests with S_{mag3}. The evolution of Br and Hc is estimated in a temperature range from 20 °C to 100 °C. The lower limit of 20 °C was chosen to include the measurement result of S_{mag1} in the analysis. Figure II.13 a shows the experimental results for the residual flux density of S_{mag1} and S_{mag3} for the corresponding temperatures. The values are also listed in table II.3. A measurement error of 5 % associated with the measurement values of Br is due to the specimen form and the resulting approximations on the demagnetization field. Accordingly, an upper and lower boundary of the estimation are shown in the graphic. They are calculated based on the upper and lower limit of $Br\,(T = 50\,°\mathrm{C})$. The measured values for S_{mag3} are in good accordance with the prediction from equation (II.2). Furthermore, the value measured for S_{mag1} at 20 °C is in good accordance with the estimation as well. The temperature characteristics of the residual flux density Br can be predicted with the help of the temperature coefficient of the powder up to 100 °C.

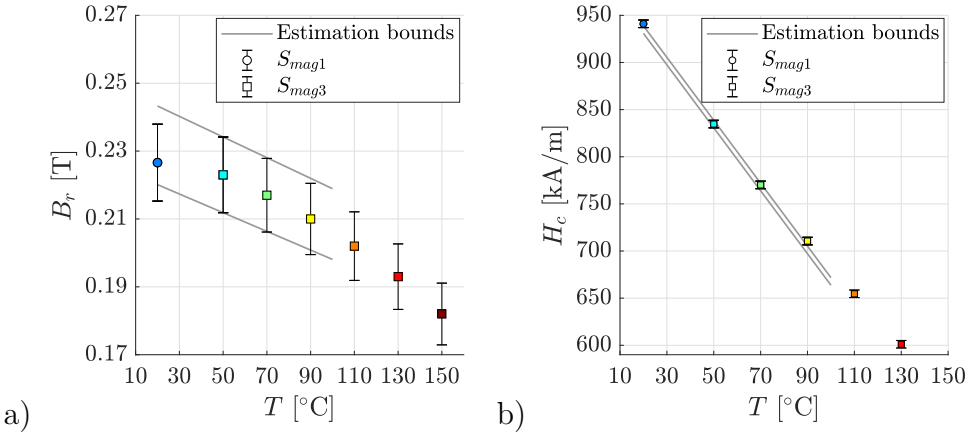

Figure II.13: Dependence of residual flux density Br (a) and coercive field strength Hc (b) on the temperature, measurement values of S_{mag1} and S_{mag3} as well as estimation bounds.

Figure II.13 b shows the evolution of the coercive field strength Hc of S_{mag3} between 50 °C and 130 °C and of S_{mag1} at 20 °C. A measurement uncertainty of 4 kA/m for the magnetic field is specified for the test device and represented for the experimental results. The uncertainty is mainly due to the remanence of the extraction magnetometer. A prediction for the range of Hc was made using equation (II.3) in the same way as for the prediction of Br. While the value for Hc

at 70 °C is in good accordance with the estimation, the value at 90 °C is slightly underestimated by equation (II.3) (cf. table II.3). The coercive field strength of S_{mag1} at 20 °C on the other hand lied in the estimation range under consideration of the uncertainty. As the difference at 90 °C measures only 2 kA/m, it is concluded that the temperature characteristics of the coercive field strength Hc can be reasonably predicted with the help of the temperature coefficient of the powder.

Specimen	T [°C]	Br [T]			Hc [kA/m]		
		LB	measurement	UB	LB	measurement	UB
S_{mag1}	20	0.226	0.227 ± 0.011	0.238	931	941 ± 4	939
S_{mag3}	50	0.217	0.223 ± 0.011	0.229	831	834 ± 4	839
S_{mag3}	70	0.212	0.217 ± 0.011	0.223	763	770 ± 4	712
S_{mag3}	90	0.206	0.210 ± 0.011	0.217	697	711 ± 4	705

Table II.3: Br and Hc of S_{mag1} and S_{mag3} for different temperatures, LB - lower bound from estimation, UB - upper bound from estimation.

II.4 Mechanical properties

In the following section, the determination of mechanical material properties of the stH-MAE is presented. The first study concerns a uniaxial tensile test, in which three specimens were strained until failure. The measurement results for the large strain regime and the small strain regime are discussed and a quasi-static Young's modulus and the Poisson's ratio are determined. The second, presented in this section, concerns the dynamic mechanical properties of the composite in the small strain regime. The storage modulus and the loss factor of the pure matrix material are determined and compared to the properties of stH-MAE with different volume fractions. As the tests are uni-axial, the mechanical quantities are scalar values corresponding to the magnitude in the tested direction.

II.4.1 Uniaxial tensile test

II.4.1.a Specimen and experimental setup

Uni-axial tensile tests have been performed for three composite specimens, S_{mec1} – S_{mec3} with $\Phi = 36.2\,\%$. The specimens were cut out of one composite sheet with a thickness of $h_2 = 4.31\,\text{mm}$ with a cutting die corresponding to Die A of the Standard Dumbbell Dies presented in ASTM D412. Figure II.14 a exemplarily shows one of the specimens, which has a gauge length of $L_0 = 59\,\text{mm}$ and a width of $h_1 = 12\,\text{mm}$. The four specimens were cut out in different directions in the composite sheet: S_{mec2} and S_{mec3} were cut out with an angle of about 90° and 45° with respect to the orientation of S_{mec1} (figure II.14 b).

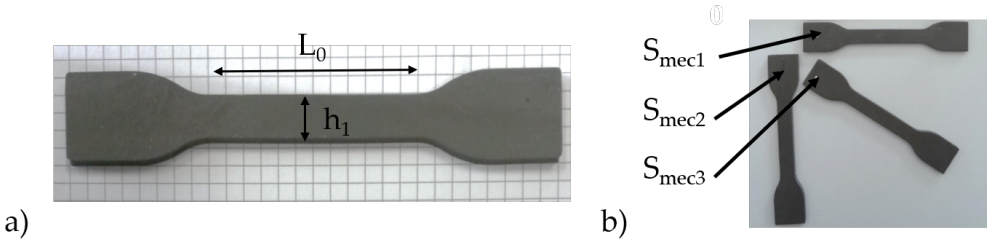

Figure II.14: Dumbbell specimen S_{mec1} (a) and arrangement of the four specimen showing their relative positioning towards each other in the composite sheet (b).

The experimental setup consists of a universal testing machine of MTS (figure II.15) which contains a displacement sensor. A load cell with a maximum force of 1 kN was mounted on the machine along with clamps to fix the dumbbell specimens. During an initial test, the standard clamps shown in figure II.15 a were used, but the lateral contraction of the specimen during the test made the use of adaptive clamps necessary (cf. figure II.15 b). A laser interferometer was used for the measurement of the specimens' displacement. Reflective tape is used to limit the measurement area to a region in the tapered zone (width = h_1), where the stress is supposed to be distributed in a uniform manner. In addition, the surface of the specimen was filmed on the opposite side with a camera to capture the local displacement.

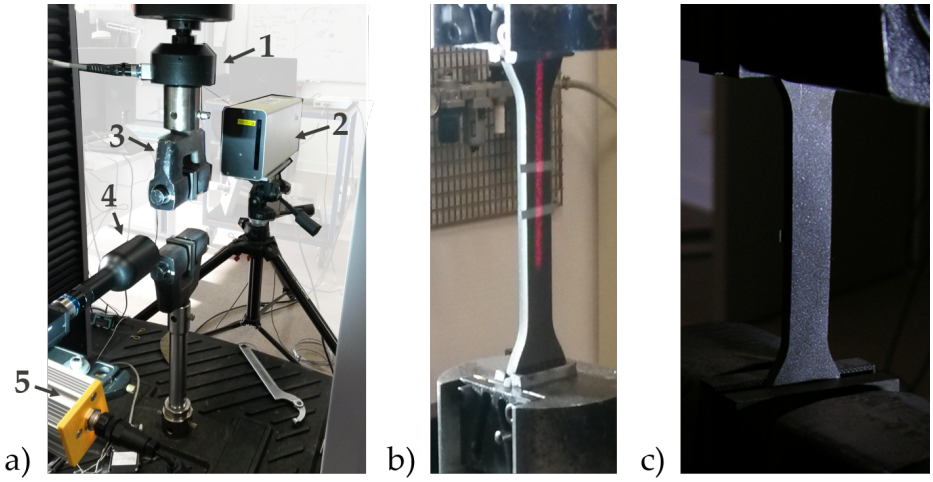

Figure II.15: Measurement setup (a) showing the universal testing machine with components 1 – load cell, 2 – laser interferometer, 3 – clamps, 4 – camera objective and 5 – light source, mounted specimen in a perspective where its surface faces the laser (b) and mounted specimen in a perspective where its surface faces the camera (c).

To perform a digital image correlation (DIC), a high local contrast is required. Therefore, the surface of the specimen was covered with white paint speckles (figure II.15 c). The photograph in figure II.15 c shows the lighting conditions during

the test for which a light source was positioned close to the specimen. The displacement of the upper mobile clamp with a velocity of 0.25 mm/s has been imposed. The resolution of the laser was set to 10 mm/V and the initial distance between the reflective tapes measured between 10.12 mm and 12.38 mm.

II.4.1.b Large strain behavior the composite

The specimens were strained until failure during the tests and their fracture area was analyzed afterwards. Figure II.16 a shows the positions of the fracture area. The fractured regions have irregular forms and extends in the direction of the specimens' length in two of three cases. The region of S_{mec1} is more regular and extends less.

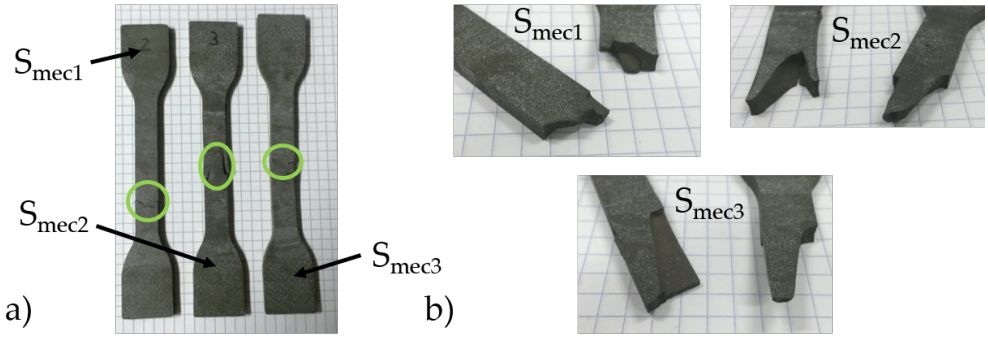

Figure II.16: Fractured specimen with an indication of the fracture position on the specimen (a) and zoom on the fractures (b).

The resulting nonlinear stress-strain relation is shown in figure II.17 a. Since the section of the specimen undergoes a significant change during the test, the true stress σ_t and strain ε_t are calculated under assumption of a constant volume. The quantities are obtained from the measurement of the force F and the displacement ΔL and the geometry of the specimen by

$$\sigma_t = \frac{F}{h_1 h_2}\left(1 + \frac{\Delta L}{L_0}\right), \qquad \varepsilon_t = \ln\left(1 + \frac{\Delta L}{L_0}\right). \tag{II.4}$$

Figure II.17 a shows a good accordance of the measurement results of the three specimens. It is hence concluded that the macroscopic mechanical material behavior is isotropic. The strain ε_t is limited to a maximum of 2 in the graphic to enhance the comparison, even though the failure of specimen S_{mec3} was measured at a nominal strain of 2.13. The stress-strain curves in figure II.17 a can be separated in three different zones, which is characteristic for elastomers and can be associated to different processes at the scale of the polymer chains (cf. [Caborgan 2011] for example). For small strains, up to about 5 % in the present case, the material shows a quasi linear behavior and the loading applies mainly to intermolecular bonds of the polymer chains. With increasing strain, the macromolecular chains are reoriented in the direction of the loading. As long as they can rearrange easily,

the stress-strain curve inclines. This behavior is visible up to a strain of about 30 % in figure II.17 b. An increase of the stress with the strain can be observed in the third part of the curves in figure II.17 a for $\varepsilon_t > 30\,\%$, which increases up to 120 % and remains constant form then on. The molecular chains are oriented in the direction of the loading and the elongation of the chains requires a higher effort than their rearrangement.
As the following investigations on the material behavior concern the small strain regime, the elastic modulus of the three specimen is calculated from the measurement data in a range from 0 % to 1.5 % of the nominal strain, $E(1.5\,\%)$. Figure II.17 c shows a zoom on the corresponding region of the stress-strain curves. The modulus corresponds to the slope of the straight obtained by a linear regression. The deformation of the specimen stays small in this range, therefore the difference of the moduli calculated form the nominal quantities and the true quantities stays negligible. The moduli for the three specimens lie in a range between 3.92 MPa and 4.69 MPa as shown in table II.4.

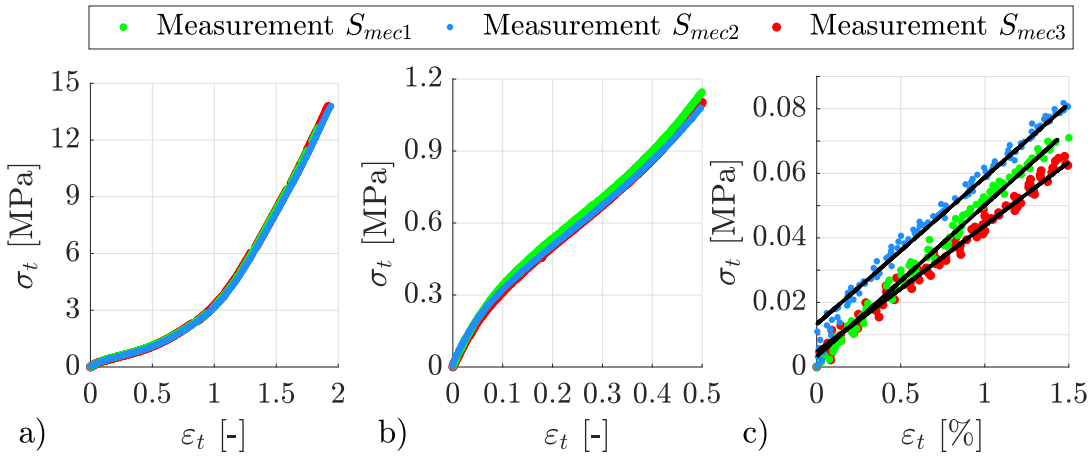

Figure II.17: Nominal stress-strain relations obtained from uniaxial tensile test for S_{mec1} – S_{mec3} represented in a strain range up to $\varepsilon_t = 200\,\%$ (a), $\varepsilon_t = 50\,\%$ (b) and $\varepsilon_t = 1.5\,\%$ (c).

Specimen	ε_t at failure [-]	σ_t at failure [MPa]	Modulus $E(1.5\%)$ [MPa]
S_{mec1}	1.84	12.7	4.69
S_{mec2}	1.95	13.8	4.55
S_{mec3}	2.13	17.1	3.92

Table II.4: True strain and stress at failure and modulus for the deformation range up to 1.5 % obtained from the tensile test for S_{mec1} – S_{mec3}.

II.4.1.c Determination of the Poisson's ratio

A digital image correlation (DIC) was performed for specimen S_{mec1}. Figure II.18 a shows the sample in a non-deformed state. The speckles are visible as well as protruding parts reflective tape from the other side of the specimen. The region of interest (ROI), defined for the DIC, is shown in figure II.18 b. An algorithm, developed at the institute FEMTO-ST (cf. [Amiot+ 2013]), was used to determine the local displacement at the surface of the specimen and to calculate a corresponding average deformation in the directions $\boldsymbol{e}_x$ and $\boldsymbol{e}_y$ of the ROI. During the elongation of the specimen, the ROI is not only deformed, but also displaced in the direction $\boldsymbol{e}_x$. Displacement and deformation are illustrated in figure II.18 c by the help of the protruding reflective tapes. Two images of the specimen are shown, the first in the initial configuration and the second with a calculated average deformation of 8 % of the ROI in the direction $\boldsymbol{e}_x$. Both of the reflecting tapes are displaced but the displacement of the lower tape (green arrow) is smaller than the displacement of the upper tape (yellow arrow). The displacement is determined by the algorithm and subtracted from the results.

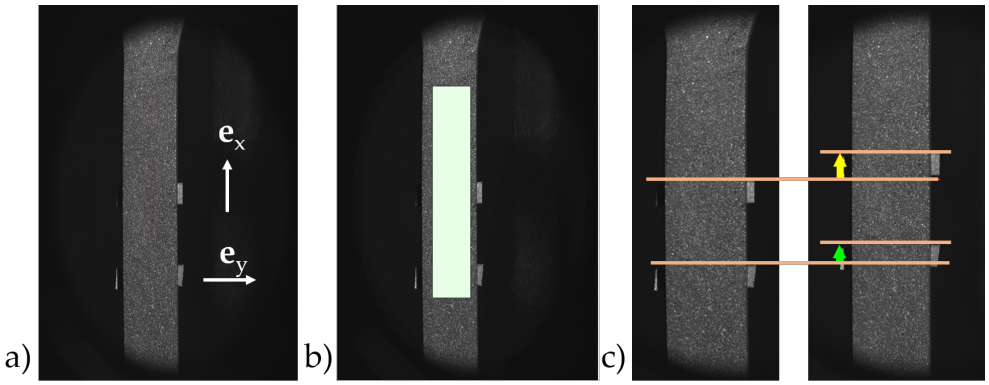

Figure II.18: Camera view on the specimen (a) including the Region Of Interest (ROI) for the Digital Image Correlation (DIC) (b) and visualization of the displacement between the initial configuration and a deformed configuration (c).

In total, 28 images are used for the DIC and the ROI is divided by elements with a length of 150 pixel to generate a mesh. The mean deformation of the ROI in the directions $\boldsymbol{e}_x$ and $\boldsymbol{e}_y$ are calculated. During the correlation, a transformation is applied on the image $n+1$ and the result is compared with the image n. The results for the displacement and the deformation of the ROI are obtained if a sufficient correlation between the images is determined by the method of least squares. In the present study, only the deformation is analyzed and the result of the DIC is shown in figure II.19 as well as the result of a linear regression. The slope of the straight corresponds to the Poisson's ratio which corresponds to 0.49 in the present case. The value is reasonable as the matrix consists of a silicone rubber and rubbery materials are known for a quasi-incompressible behavior with Poisson's ratios near 0.5.

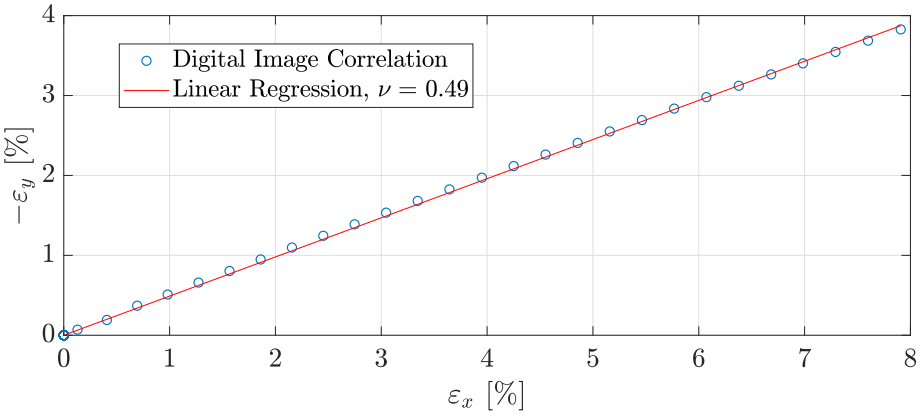

Figure II.19: Relation of the mean deformation of the ROI in the direction $\boldsymbol{e}_x$ and $\boldsymbol{e}_y$ obtained from the DIC and result of a linear regression.

II.4.2 Dynamic Mechanical Analysis (DMA)

Silicone is a viscoelastic material, therefore, its dynamic mechanical properties are dependent on the time/frequency characteristics of the mechanical load. Dynamic mechanical properties are for example the storage modulus E' and the loss factor $\tan(\delta)$. In viscoelastic materials, they do not only depend on the mechanical load but on the temperature as well [Butaud+ 2018]. Methods like the Dynamic Mechanical Analysis (DMA) allow the determination of the parameters necessary to identify the viscoelastic behavior laws [Renaud+ 2011]. In the present composite, the interactions between the particles and the matrix as well as particle-particle interactions can be added to the parameters that determine the mechanical behavior [Fröhlich+ 2015]. In this section, the results of a DMA on the pure matrix material and the non-magnetized composite material are presented. Figure II.20 a shows the experimental setup of a DMA test in traction configuration. The specimen's outer ends are fixed in two clamps. The upper clamp is fixed and connected to a force transducer measuring the reaction force $F(t)$. The lower clamp is mobile and a displacement $u(t)$ is imposed actuated by a shaker. The displacement control is done by a displacement transducer located above the shaker. The harmonic displacement $u(t)$ is applied to the mobile clamp such as

$$u(t) = u_0 + u_d \cos(\Omega\, t), \tag{II.5}$$

including a static displacement u_0 and a dynamic displacement $u_d \geqslant u_0/2$. The reaction force $F(t)$ was measured at the fixed clamp such as

$$F(t) = F_d \cos(\Omega\, t + \delta). \tag{II.6}$$

Figure II.20 b schematically depicts the force and displacement signals. The parameter δ describes the phase shift between displacement and force, the more viscous a material the bigger is the phase shift. The loss factor $\tan(\delta)$ is an indicator

for the energy that is dissipated during the mechanical loading while the storage modulus E' is a measure of the ability of a material to recover from deformation. The two properties are described as follows:

$$E' = \frac{\sigma}{\varepsilon}\cos(\delta)\ , \tag{II.7}$$

$$\tan(\delta) = \frac{\sigma}{\varepsilon}\frac{\sin(\delta)}{E'}\ . \tag{II.8}$$

A DMA is not a local measurement method but gives access to the average values of the local stress σ_d and the local strain ε_d in the specimen's volume V:

$$\sigma = \frac{F_d}{h_1\, h_2} = \frac{1}{V}\int \sigma_d\, dV\ , \tag{II.9}$$

$$\varepsilon = \frac{u_d}{L_0} = \frac{1}{V}\int \varepsilon_d\, dV\ . \tag{II.10}$$

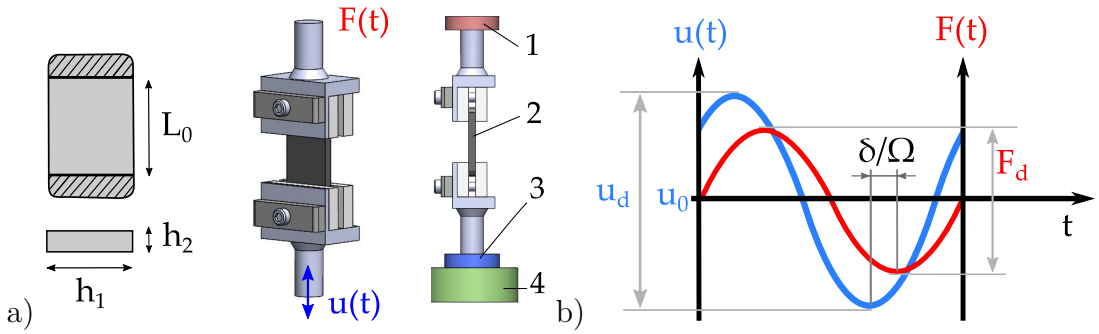

Figure II.20: Geometric parameters of the DMA specimens and experimental setup containing 1−force transducer, 2−specimen, 3−displacement transducer, 4−shaker (a) and schematic representation of force and displacement signals (b).

All dynamic tests presented in the following are conducted with the dynamic mechanical analyzer *DMA +1000* from *Metravib* in the configuration shown in figure II.20 a. The static and dynamic displacements were set to $u_0 = 5/1000\, L_0$ and $u_d = 1/100\, L_0$ respectively. The displacement frequency ranged from 2.15 Hz to 100.00 Hz. The DMA was performed for different temperatures ranging from 20 °C to 150 °C, after each frequency scan the temperature was raised. Two specimens were tested for this study, a pure silicone specimen (S_{mec4}) and two non-magnetized composite specimens with $\Phi = 19.4\,\%$ (S_{mec5}) and $\Phi = 36.2\,\%$ (S_{mec6}) respectively.
Figure II.21 shows the evolution of the storage modulus E' for the three specimen against the frequency. In the given frequency and temperature range, the storage modulus of S_{mec4} lies into the range from 1.29 MPa to 1.78 MPa. The maximum change caused by the temperature is of 11.8 % and the chosen frequency range changes the modulus of 25.4 % maximally. The storage modulus of S_{mec5} lies into a range from 2.28 MPa to 3.41 MPa, the composite is thus stiffer than the pure

silicone. The temperature difference causes a maximum change of 16.4 % and the frequency alters E' by 29.7 %. An increase of the rigid filler content in the composite causes a further increase in the modulus as the results for S_{mec6} show. The modulus of the corresponding specimen lies in a range from 4.7 MPa to 9.04 MPa. The variation of the temperature and the frequency change the modulus of maximally 37.1 % and 31.1 % respectively. The storage modulus is stronger influenced by the frequency and temperature changes, as the pure silicone and the influence increases with the volume fraction. The three materials show a behavior that is typical for elastomers in the rubbery state: the modulus increases with the frequency and a decreases with the temperature. The temperature enhances the chain mobility in the elastomer and the rigidity (respectively the modulus) decreases. Higher frequencies induce more elastic-like behavior of the silicone [Menard 1999]. At low frequencies the viscous behavior predominates, the material flows.

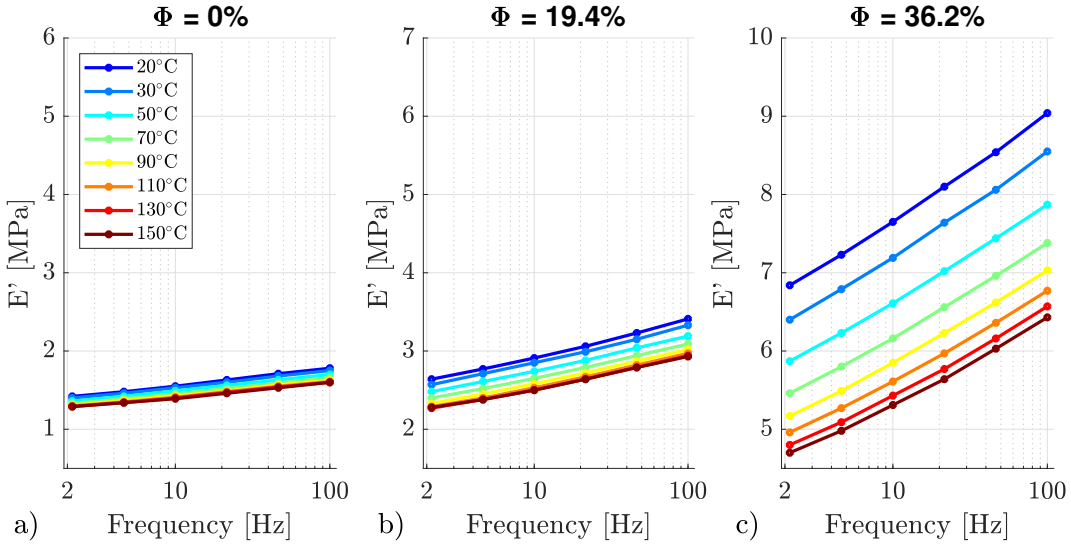

Figure II.21: Storage modulus E' of the pure silicone specimen S_{mec4} (a) and the composite specimens S_{mec5} (b) and S_{mec6} (c) in a frequency range from 2.15 Hz to 100.00 Hz and temperature range from 20 °C to 150 °C at 1 % deformation.

Figure II.22 shows the loss factor of the silicone and the stH-MAEs. For S_{mec4}, it lies in a range from 0.069 to 0.117, while $\tan(\delta)$ of S_{mec5} and S_{mec6} reaches from 0.080 to 0.136 and from 0.106 to 0.179 respectively. An increase in temperature decreases the loss factor. As the polymer chain mobility is increased by the temperature, they displace more easily and the energy dissipated by this process decreases, consequently the loss factor does the same. This behavior can be observed for all specimens, while the magnitude of the loss factor is quite different. A continuous increase in frequency in the contrast does not have a monotonous effect even though an overall decrease of the loss factor from 2 Hz to 100 Hz is observed. In this range, the loss factor seems to decrease in steps for the pure silicone sample and even increase up to a frequency of 10 Hz at higher temperatures. The decrease in steps is less pronounced in the composite material but an increase in

a frequency range up to 10 Hz is also observed at higher temperatures. For both materials, a temperature or frequency change in the given range can alter the loss factor more than 28 %. The loss factor is an indicator for the viscous behavior of the composite. With increasing volume fraction, the dissipation increases as well.

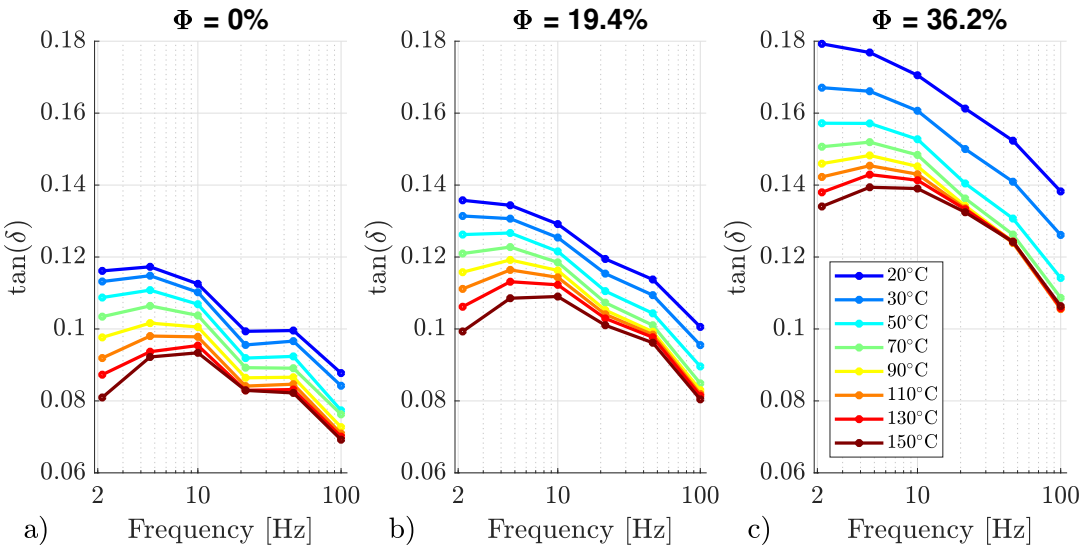

Figure II.22: Loss factor tan(δ) of the pure silicone specimen S_{mec4} (a) and the composite specimens S_{mec5} (b) and S_{mec6} (c) in a frequency range from 2.15 Hz to 100.00 Hz and temperature range from 20 °C to 150 °C at 1 % deformation.

Storage modulus and loss factor of the composites are significantly different from the ones of the silicone. The loading frequency and the temperature however, have the same influence on the mechanical characteristics of the two materials in general. Since the stH-MAE shows a viscoelastic behavior, two additional effects could be part of its mechanical behavior: the Mullins effect and the Payne effect. The Mullins effect is a damage induced and thus irreversible effect that emerges in the form of a decrease in rigidity. It appears for example during cyclic mechanical loading in filled elastomers [Mullins 1969]. The DMA tests were conducted in the so-called stabilized regime after the pre-cycling of the specimen. The Payne effect is the dependence of the dynamic modulus on the strain amplitude which is induced by nonlinear viscoelasticity above a certain strain threshold [Payne 1962]. To avoid this effect as the study lies into linear viscoelasticity, the amplitude was kept small during the dynamic tests. The same precautions were taken for the mechanical loading during the coupled magnetomechanical tests, which will be presented in the following.

II.5 Magneto-mechanical coupling

In the following section, experimental investigations on the magneto-mechanical coupling in the stH-MAE composite are presented. The first part comprises dynamic mechanical analysis, performed with specimens before and after their magnetization. Afterwards a test bench, which allows a mechanical tensile loading in a magnetic field, is presented. Its working principle is explained at the beginning of the section and the results of first magnetomechanical tests are presented subsequently. As the tests are uni-axial, the magnetic and mechanical quantities are scalar values corresponding to the magnitude in the tested direction if not otherwise specified.

II.5.1 Influence of M on the mechanical characteristics

In this section, the influence of a permanent magnetization of the stH-MAE on its mechanical characteristics is studied. The composite specimens in this study have been subjected to a DMA with identical test configurations before and after their magnetization. The eight specimens S_{mm1} - S_{mm8} have been tested in a tensile configuration (Figure II.20 a) three times respectively. Between the three measurements, a specimen has been removed from the machine and mounted again. The strain amplitude was set to 1 %, the temperature to $T = 30\,°C$ and the frequency to $f = 1\,Hz$. Afterwards, the specimens were magnetized. For half of the specimen the direction of magnetization was chosen parallel to their length and hence parallel to the mechanical solicitation (S_{mm1} - S_{mm4}) which is shown schematically in Figure II.23 b. For the other half, the direction was parallel to the specimen's thickness and perpendicular to the mechanical solicitation (S_{mm5} - S_{mm8}), which is depicted in Figure II.23 c. After the magnetization, each specimen was tested again three times. Due to the mounting of the specimen in the machine, the free length L_0 changed for each test. The corresponding values of L_0 for each specimen and test can be found in table A.3.

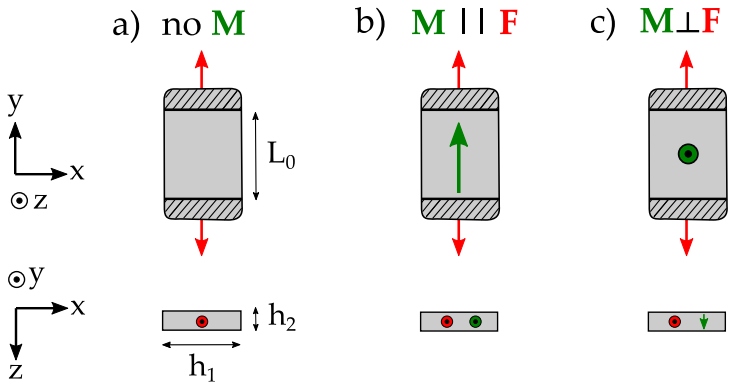

Figure II.23: Scheme of the specimen in tensile DMA configuration (a) magnetized in the direction of its length (b) and its thickness (c).

To analyze the evolution of the dynamic mechanical properties before and after magnetization, relative values are compared. For each specimen the average of the three values of E' and $\tan(\delta)$, obtained before magnetization, are calculated: $\overline{E'}_{bm}$ and $\overline{\tan(\delta)}_{bm}$. The results of each test are divided by this average to obtain the relative quantities E'_{rel} and $\tan(\delta)_{rel}$:

$$E'_{rel} = \frac{E'}{\overline{E'}_{bm}} \qquad \tan(\delta)_{rel} = \frac{\tan(\delta)}{\overline{\tan(\delta)}_{bm}} \tag{II.11}$$

Figure II.24 shows the mean relative storage modulus E'_{rel} before and after magnetization for the eight specimens as well as the standard deviation of the three measurements for each specimen. When the loading and the magnetization are oriented in the same direction ($\boldsymbol{M} \parallel \boldsymbol{F}$), the modulus increases (figure II.24 a). The average increases for the four specimen measures about 3 %. If ($\boldsymbol{M} \perp \boldsymbol{F}$), the modulus decreases by 1.5 % on average (figure II.24 b). While clear tendencies are identified for both configurations, they are not significant for all of the specimen.

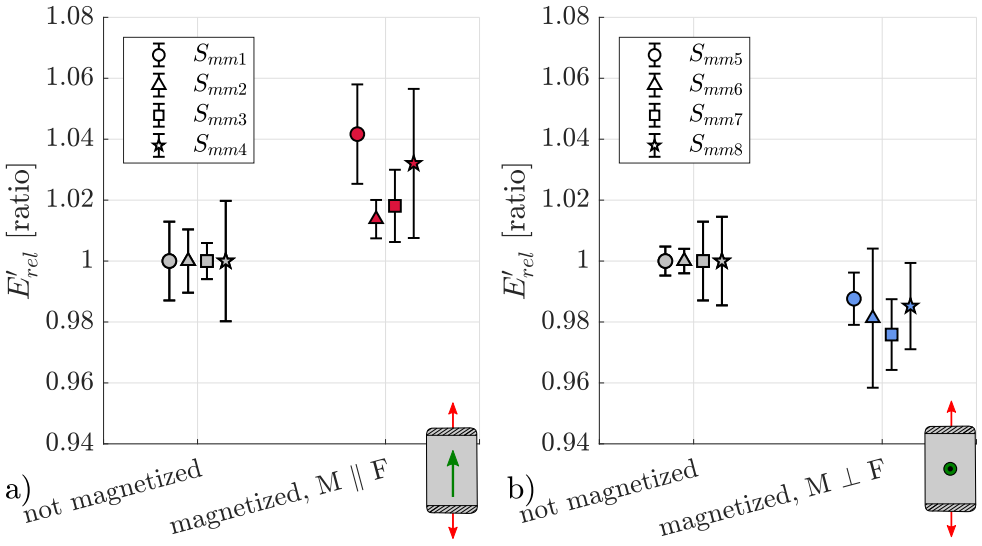

Figure II.24: Relative storage modulus E'_{rel} of the composite material before magnetization (gray) and after magnetization in the direction $\boldsymbol{M} \parallel \boldsymbol{F}$ (a) and $\boldsymbol{M} \perp \boldsymbol{F}$ (b).

Figure II.25 shows the mean relative loss factor $\tan(\delta)_{rel}$ for the eight specimens before and after magnetization as well as the standard deviation of the three measurements for each specimen. The dispersion of the results increases strongly for the specimen magnetized in the direction $\boldsymbol{M} \parallel \boldsymbol{F}$. The increase is present but less pronounced if $\boldsymbol{M} \perp \boldsymbol{F}$. The variation of $\tan(\delta)_{rel}$ due to the magnetization does not show a clear trend like the variation of E'_{rel}. Differences of about ± 2 % are observed for $\boldsymbol{M} \parallel \boldsymbol{F}$ (figure II.25 a) and $\boldsymbol{M} \perp \boldsymbol{F}$ (figure II.25 b). The average increase of 0.3 % and 0.6 % is insignificant.

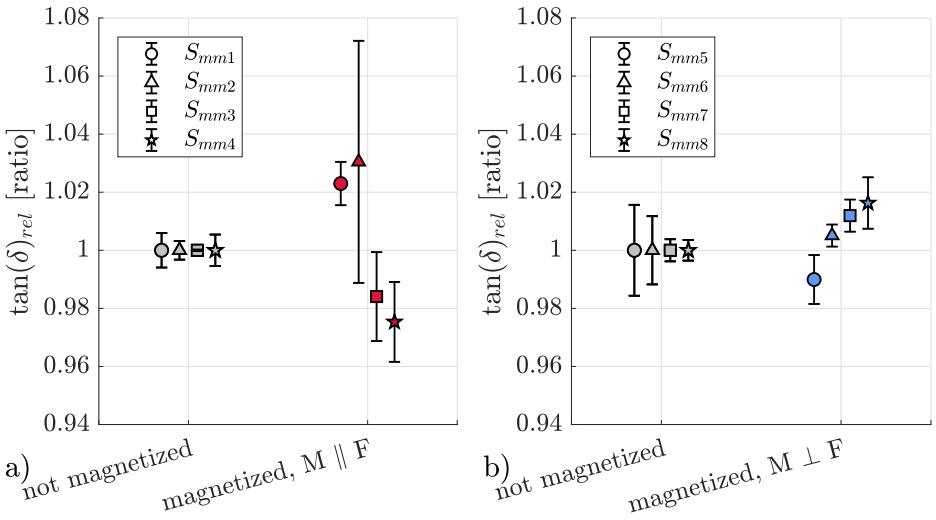

Figure II.25: Relative loss factor $tan(\delta)_{rel}$ of the composite material before magnetization (gray) and after magnetization in the direction $\boldsymbol{M} \parallel \boldsymbol{F}$ (a) and $\boldsymbol{M} \perp \boldsymbol{F}$ (b).

Compared to previous analysis of the dynamic mechanical characteristics of soH-MAE ([Stepanov+ 2014]), the impact of the magnetization in this study is rather small. This is due to the matrix stiffness : the magnetic forces between the particles are small before the elastic forces of the matrix and hence the impact of the magnetization is small. Additionally, the impact of the geometric form of the specimen on the magnetic field distribution has to be considered in the analysis since the self-demagnetization of the specimen due to its form decreases the magnetic flux density inside the material. A numerical simulation of the specimens' self-demagnetization in the air for the two magnetic states, $\boldsymbol{M} \parallel \boldsymbol{F}$ and $\boldsymbol{M} \perp \boldsymbol{F}$, has been performed. In the simulation, Br was calculated from the characteristics of the powder and the volume fraction and hence set to 0.157 T, μ_r was set to 1.1 based on the measurement results of specimen S_{mag1}. The following analysis refers to the middle part of the specimen, on which the measurement of the mechanical characteristics is based.
In the first case, where $\boldsymbol{M} \parallel \boldsymbol{F}$ (figure II.26 a), the flux density is evaluated in the direction of the length of the specimen $\boldsymbol{e}_3$. A volume average of $\boldsymbol{B}$ in $\boldsymbol{e}_3$ of 0.151 T is obtained with a variation up to a maximum of 1.6 %. The specimen is magnetized in a direction with a high aspect ratio, this keeps the demagnetization field small. Consequently, the magnetic flux density in the specimen does not decrease significantly compared to the residual flux density Br. In the second case, where $\boldsymbol{M} \perp \boldsymbol{F}$ (figure II.26 aa), the mean flux density in the evaluation volume is of 0.029 T. The magnetic flux density in the direction $\boldsymbol{e}_1$ is the highest on the outer bounds of the specimen, where closing the magnetic flux lines is easier compared to the middle of the specimen. It decreases rapidly with the distance towards the outer bounds and the variation within the evaluated section of the specimen is superior to 100 %. The magnetic flux density in the mechanically loaded part of the

specimen is not homogeneous and the demagnetization effect causes a very low intensity of B in most of the specimen section. It is concluded that the measurement can be based on a global force and displacement measurement in the configuration $\boldsymbol{M} \parallel \boldsymbol{F}$, since the local flux density is evenly distributed. This is not the case for the configuration $\boldsymbol{M} \perp \boldsymbol{F}$: the flux density shows a strong gradient; hence the global quantities are not representative for the local loading state of the material.

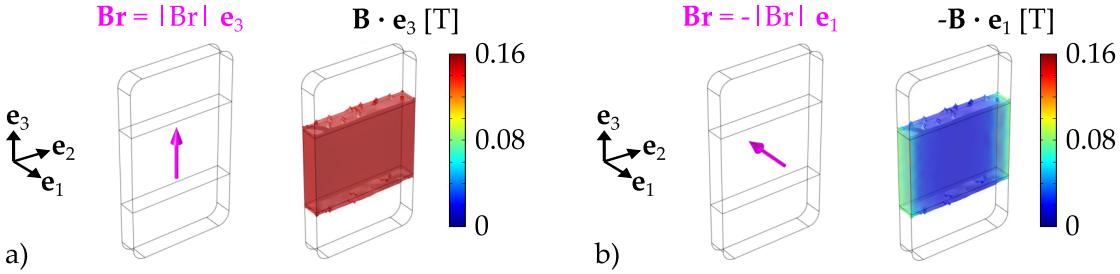

Figure II.26: Numerical results of the residual flux density distribution in the specimen for the configurations $\boldsymbol{M} \parallel \boldsymbol{F}$ (a) and $\boldsymbol{M} \perp \boldsymbol{F}$ (b).

II.5.2 Magneto-mechanical test bench

In this section, investigations on the influence of an external magnetic field on the mechanical behavior of stH-MAE specimens are presented. A testing bench for the coupled testing has been developed in collaboration with the company MMT on this purpose. It allows a tensile mechanical loading in absence and in presence of an external magnetic field. First results for magnetic loadings in stationary mechanical states and mechanical loadings in constant magnetic fields are presented at the end of this section.

II.5.2.a Experimental setup

The experimental setup is shown in figure II.27. Besides the support structure for the specimen, it comprises a micrometric stage, a contactless displacement sensor, a load cell for the measurement of the reaction forces of the specimen and a magnetic reluctant circuit for the generation of an external magnetic field.
The components in this bench are in non-magnetic materials in order to avoid a dispersion of the magnetic flux and a non-uniform magnetic field into the sample tested. Figure II.28 shows the components, responsible for the clamping of the specimen and the mechanical loading, in detail.
The supporting structure (1), manufactured from a POM-C copolymer, comprises a fixed clamp (2) in which the upper part of a specimen (5) is maintained by tightening the screw (figure II.28 c). The lower part of the specimen is fixed in the mobile clamp (3) by the same means. The mobile clamp is connected to a load cell (9) via five brass barres and an intermediate POM-C platform (6). The force obtained from the measurement is called F in the following. The platform (6) is used for the measurement of the displacement of the mobile assembly, u,

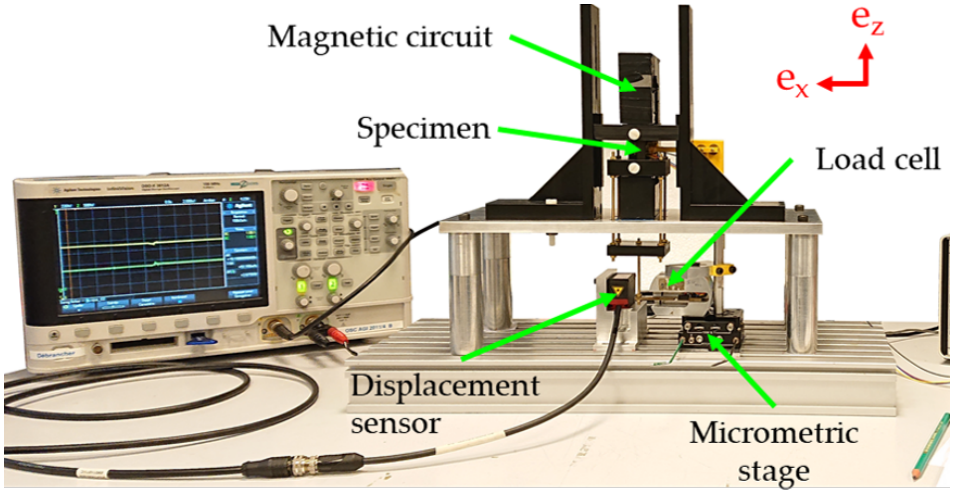

Figure II.27: Experimental setup for the study of the magneto mechanical characteristics of H-MAE in an external magnetic field.

via a displacement sensor (7) from microEpsilon. The load cell is clamped on a micrometric stage by the help of an aluminum holder (8). The micrometric stage is used to impose the displacement of the mobile clamp where sample is maintained. A magnetic circuit (4) is positioned in the setup to generate a quasi-static magnetic field in the sample region. The measurement of displacement and force are recorded by an oscilloscope and exported to csv data. In the following, the working principle of the magnetic and the mechanical part of the setup are detailed.

II.5.2.b Mechanical loading

Before the testing, the specimen is mounted in the test bench according to the following procedure: at first, the specimen is fixed in the mobile clamp. The resulting force generated by the weight of the specimen and set as reference force. Afterwards, the specimen is also fixed in the upper clamp. The compression in the clamping generates a lateral extension of the specimen which, in turn, generates an offset force. The mobile clamp is displaced to remove the initial constraint on the specimen until the global force is equal to the reference force again. For a mechanical loading, the length of the specimen is increased by a displacement of the microscopic linear stage (figure II.29 b). The displacement is measured on the intermediate platform in the measurement setup. The displacement generates stress in the specimen, in the test bench the global reaction force is measured by the force sensor.
The results of the dynamic mechanical tests show that the behavior of the composite material is viscoelastic. In the first tests with the new experimental setup, the focus was put on the elastic part of the behavior. For this reason, the tests are performed in a quasi-static regime. As an example, figure II.30 shows the variation of the displacement and the corresponding variation of the force measured

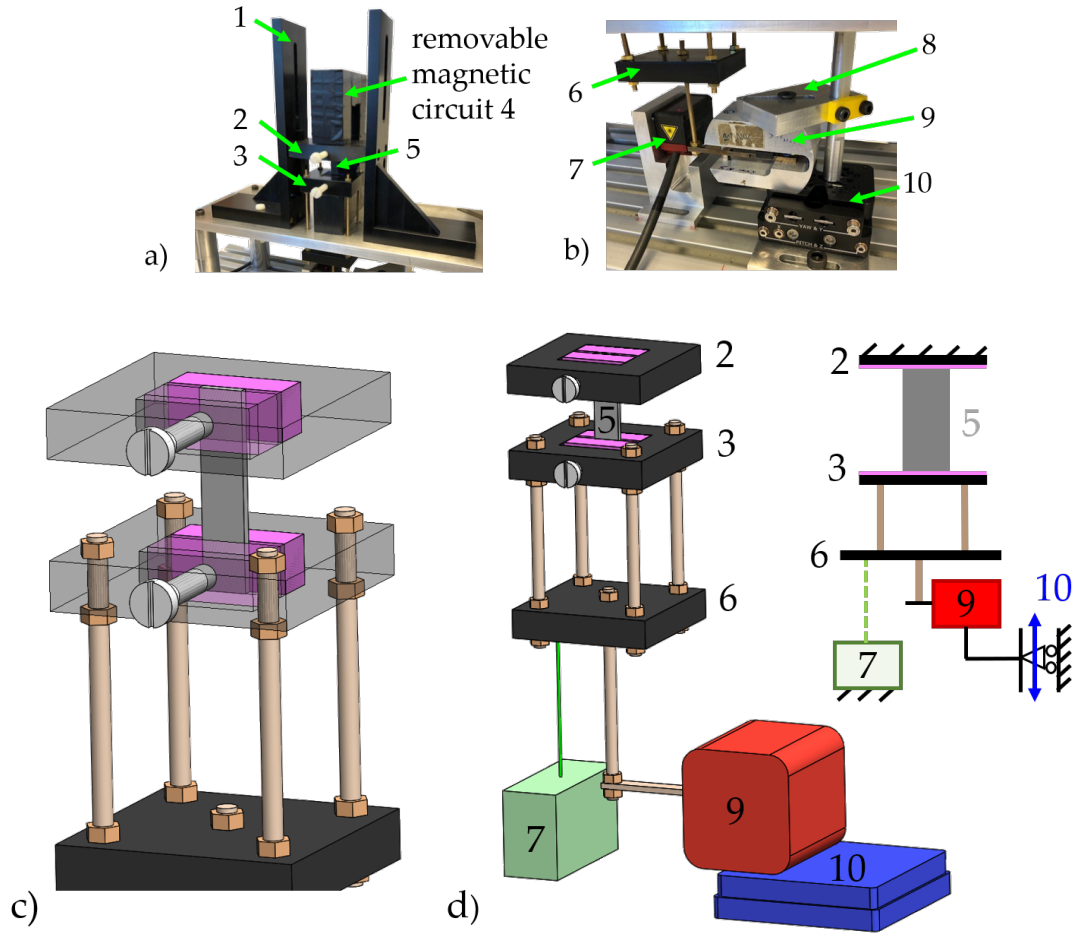

Figure II.28: Mechanical part of the experimental setup : photographs of the upper part (a) showing 1 –basic structure, 2 –upper fixed clamp, 3 –lower mobile clamp, 5 –specimen and of the lower part (b) showing 6 – intermediate platform, 7 – displacement sensor, 8 – aluminum plate, 9 – load cell and 10 – micrometric stage as well as schematic views visualizing the clamping of the specimen (c) and the functional parts for the mechanical loading (d).

for a specimen in the test bench. In addition to the measurement values (light gray), a moving average over 10 values is shown in the graphic (black). During the measurement, the displacement was increased and maintained constant. The force increases with the displacement at first, but decreases when the latter is kept constant (stress relaxation). This behavior is characteristic for viscoelastic materials. The force converges towards a stationary value. In the quasi-static tests, the difference between the stationary values before the loading and after the force relaxation are considered. They are highlighted in green in figure II.30.
Figure II.29 c shows a schematic view of the measurement setup from a mechanical point of view where the components are represented by elastic springs with a stiffness k. The parameters k_{spec}, k_{supa} and k_{supb} correspond to the stiffness of the specimen, the supporting parts between the specimen and the point of the dis-

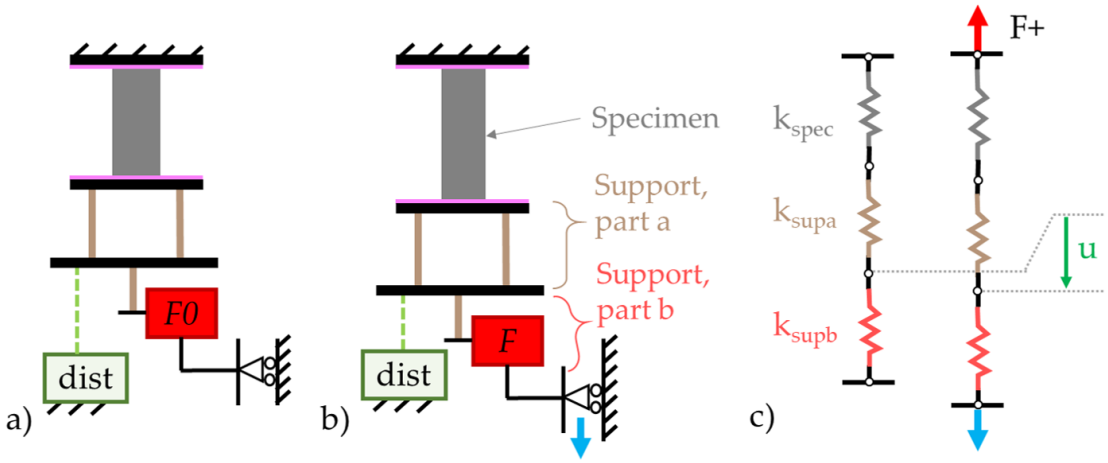

Figure II.29: Illustration of the mechanical loading: initial state of the setup (a) and tensile loading (b) of the specimen and modeling of the tensile tests including the elastic properties of the components (c); dist – distance measurement, $F0$ – reference force, F – force during mechanical loading, blue arrow – stage displacement, u – displacement, k – stiffness.

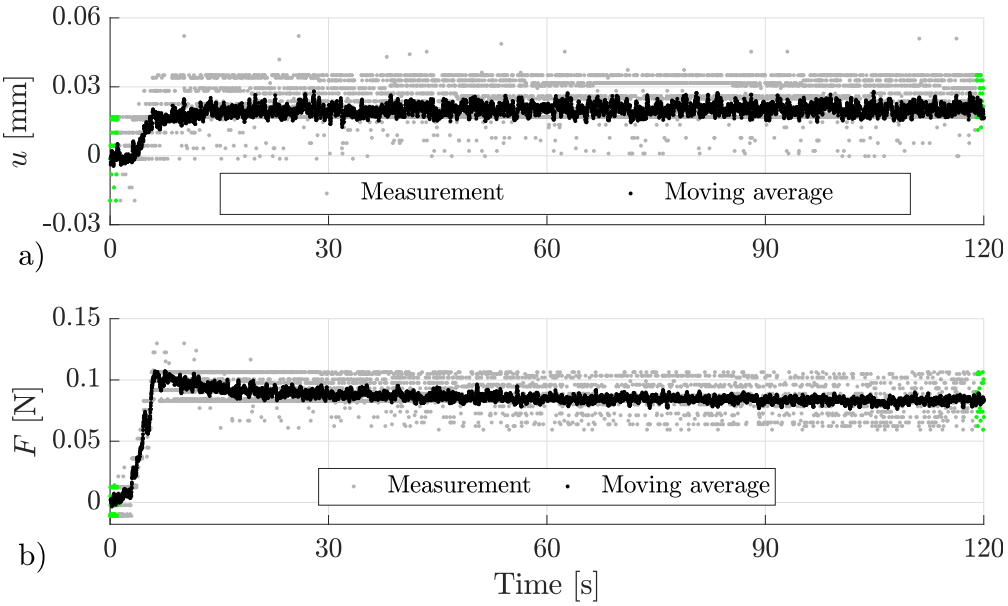

Figure II.30: Evolution of the displacement u (a) and the force F (b) during a loading step, measurement signals and moving average (10 values per point).

placement measurement and the components after the point of the displacement measurement respectively. The scheme is supposed to model the quasi-static tests; therefore, the viscous components are not represented. The elements are connected in series in the experimental setup, therefore the force is the same everywhere. As mentioned previously, the displacement u is not directly measured on the specimen but on a part of the mechanical support. It corresponds to the sum of the

displacement of the specimen, u_{spec}, and the displacement of support part a, u_{supa}. The stiffness of support part a, k_{supa}, is part of the equivalent stiffness k_{eq} as well as the stiffness of the specimen k_{spec}:

$$u = u_{spec} + u_{supa} = \frac{F_{el}}{k_{spec}} + \frac{F_{el}}{k_{supa}} = \frac{F_{el}}{k_{eq}} \,. \tag{II.12}$$

If the stiffness of the system is much larger than the rigidity of the specimen, the total stiffness k_{eq} is approximately equal to the stiffness of the specimen k_{spec} (cf. equation (II.13)), but this hypothesis has not been verified yet. The decomposition of the elastic forces has no influence on the conclusions drawn in the following. However, it is pointed out that elastic constants obtained from the measurement describe the behavior of the specimen and the support part a. To avoid this effect, the displacement has to be measured directly on the specimen in future studies

$$k_{eq} = \frac{1}{\frac{1}{k_{spec}} + \frac{1}{k_{sys}}} \,, \qquad k_{eq} \approx k_{spec} \quad \text{if } k_{sys} \gg k_{spec} \,. \tag{II.13}$$

Purely mechanical tests have been performed to analyze the reproducibility of the measurements in a first step. The magnetized, parallelepipedic specimen S_{mm9} has been used for these tests inter alia. Its cross section $A = h_1 \times h_2$ measured 8.9 mm × 2.0 mm, the total length L measured 40 mm and the free length of the specimen in the setup measured $L_0 = 17$ mm. The volume fraction of the specimen measured $\Phi = 36.2$ % and it was magnetized in the direction of L_0 before the tests. Quasi-static tensile loading steps (figure II.30) are repeated until the macroscopic strain reaches 1 %. Afterwards, the elongation is decreased step by step again until the force is equal to the reference force again. The procedure of subsequent loading and unloading is called loading cycle in the following.
Figure II.31 a shows the force F, acting on the specimen, as a function of the displacement u, measured on the intermediate platform in absence of an external magnetic field. The specimen was subjected to three loading cycles. During the first cycle, a hysteretic behavior with a residual displacement after the unloading phase is observed. The displacement was increased to 1 % of the specimen's free length, 0.17 mm, with respect to the residual deformation. The second and third cycle also present hysteresis phenomena but in the contrary to the first cycle, the residual displacement does not change. A first loading cycle is hence necessary to reach a stabilized behavior. This behavior has also been observed for comparable samples. The residual strain does not disappear when the specimen is kept in the unloaded state for at least one hour. It is therefore concluded that the strain is not due to the viscoelastic behavior of the specimen. It could be caused by friction in the mounting.
A residual displacement after loading has been observed for magnetized soH-MAE specimen in shear tests [Stepanov+ 2012]. Additional tests with magnetized and unmagnetized specimen have to be performed to analyze if the residual displacement is caused by the magnetization or has mechanical origins like friction in

the clamping of in the experimental setup. After the first test, the specimen was demounted from the setup and then mounted again. Two additional loading cycles were performed and the result is shown in figure II.31 b. The two force-displacement curves in figure II.31 are similar for the two first loading cycles. This result was also observed for additional specimen, the experimental setup allows hence to perform a reproducible mechanical loading of H-MAE specimens.

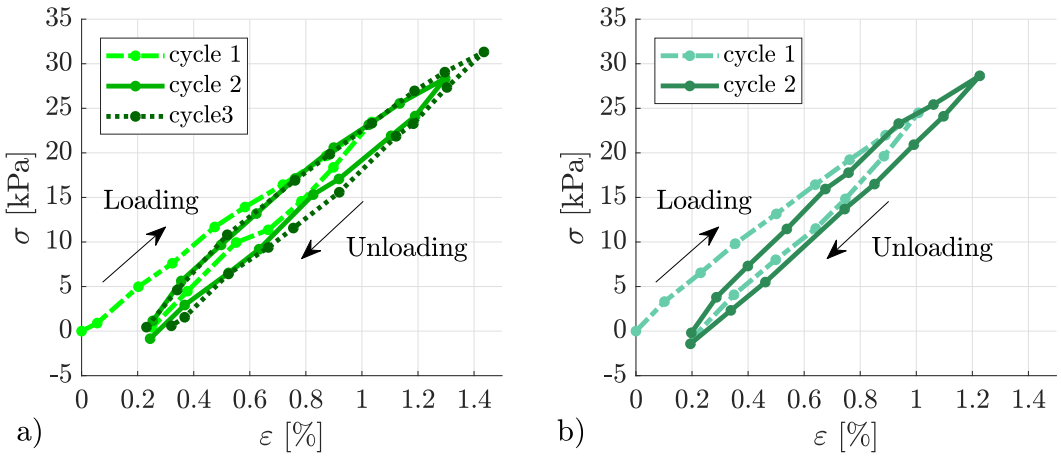

Figure II.31: Force – displacement curves obtained for mechanical loading in absence of an external magnetic field for two consecutive mountings of the specimen, (a) and (b).

II.5.2.c Magnetic loading

Figure II.32 a and b show the magnetic circuit used to generate a magnetic field in the experimental setup. It consists of three parts of pure iron (1, 3 and 4) to guide the magnetic flux. The flux is generated by a cubic permanent NdFeB magnet (2) with a residual flux density of 1.3 T. The cross section of the circuit measures 30 mm × 30 mm, it has a width of 100 mm and a minimum height of 155 mm. Most of the surface of the pure iron parts is covered to prevent the oxidation of the iron which could influence its magnetic characteristics. The magnetic flux passes through the air gap (6) in the magnetic circuit where the specimen is located during the tests. The magnetic field is hence oriented in the direction of the specimen's length. Compared to the use of coils, the use of the magnet generates the stationary magnetic field without heating the assembly. On the other hand, the intensity of the magnetic field cannot directly be controlled by the magnet. The strategy for the variation of the magnetic field intensity, retained in the present study, consists of a variation of the air gap by the motion upwards and downwards of the mobile part along the vertical axis (part 4 in figure II.32 a and b). The variation of the length of the air gap respectively causes a variation of the magnetic field intensity. The protruding length can be used to measure the variation of the air gap during a magnetomechanical test. The measurement of the magnetic flux density in the mid plane of the air gap has been performed for an air gap of 51 mm (cf. 5

in figure II.32). During the test with a measurement device developed by the company MMT, a Hall sensor was displaced in the plane of 32 mm × 32 mm. The sensor was displaced by a linear stepper motor in steps of 1 mm. The magnetic field, calculated from the measurement of the magnetic flux density in the air, is shown in figure II.32.

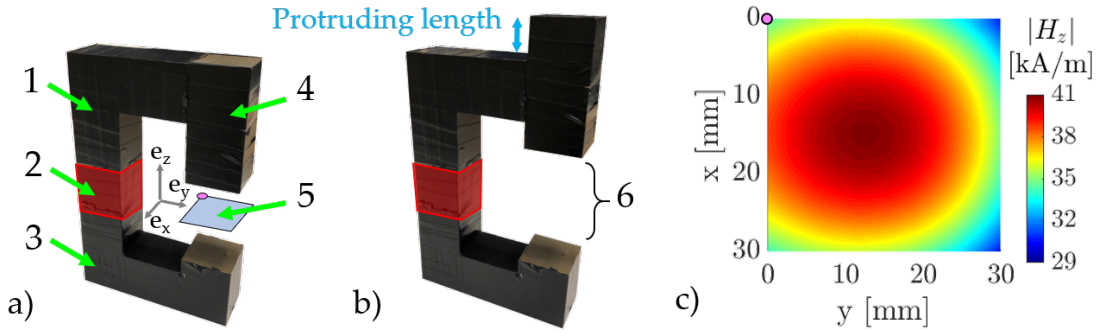

Figure II.32: Magnetic circuit consisting of 1,3 – immobile parts (pure iron), 2 – permanent magnet (NdFeB), 4 – mobile part (pure iron), 6 –air gap (small (a) and a big (b)) and magnetic field in the mid-plane 5 (c) of an air gap of 51 mm.

The graphic figure II.32 shows, that the flux density in the central region of the air gap is relatively homogeneous compared to the outer regions. The maximum field in the air-gap measures 40.89 kA/m. The field in the plane is symmetric in the $\boldsymbol{e}_x$ direction but not symmetric in the $\boldsymbol{e}_y$ direction with respect to the central positions $x = 15$ and $y = 15$ respectively. The asymmetry is caused by the non-symmetric setup: the presence of the circuit on the left side of the plane (figure II.32) influences the magnetic field in the air gap. In addition to the experiments, a numerical simulation of the magnetic part of the setup has been performed. Figure II.33 a shows the model of the magnetic circuit for an air gap of 51 mm. The 3D model allows a spatial representation of the magnetic field which is oriented in a relatively homogeneous manner according to figure II.33 b. The magnetic field component H_z, perpendicular to the mid-plane of the air gap, is shown in figure II.33 c.

The field is strongest in the middle of the plane and slightly asymmetric in the $\boldsymbol{e}_y$ direction. The absolute values for the magnetic field are higher than the values obtained from the measurement but dispersed in the same range of $\Delta H_z = 12\,\mathrm{kA/m}$. It is hence concluded that the quantitative difference results from the material parameters or geometric misalignment in the real setup. As the qualitative results are in good accordance, the presence of a relatively homogeneous field oriented in the $\boldsymbol{e}_z$ direction is assumed for the experimental setup. A specimen is supposed to be located in the center of the air gap, as figure II.33 shows. The location of the fixed specimen in the field is realized by the positioning of the magnetic circuit.

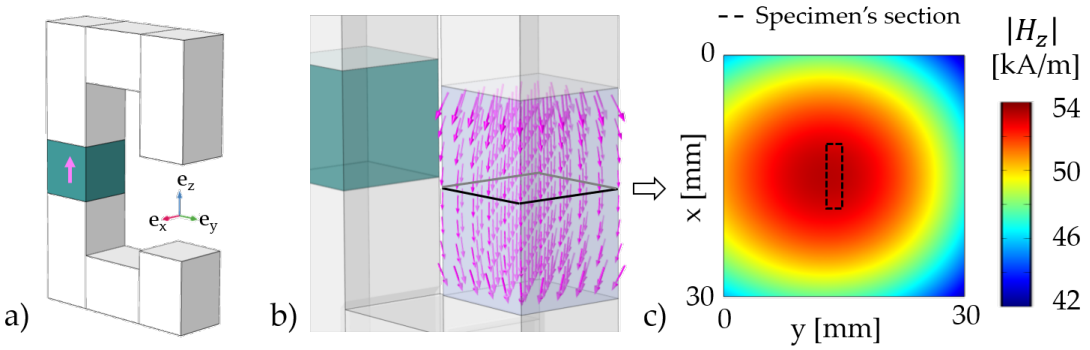

Figure II.33: Numerical model of the magnetic circuit (a), visualization of the magnetic field (pink arrows) in the air gap (b) and magnetic field intensity $|H_z|$ in the $\boldsymbol{e}_x - \boldsymbol{e}_y$ plane in the middle of the air gap (c).

A scheme of the functional parts of the setup including the magnets is shown in figure II.34 a. The circulation of the magnetic flux in the system is depicted in figure II.34 b and the mechanical loading in presence of a magnetic field is shown in figure II.34 c. During the tests, the magnetic circuit is added to and removed from the experimental setup manually. This procedure was preferred to the variation of the air gap for the first tests to observe the material behavior under the strongest possible variation of the magnetic field. Tests with a gradual variation of the magnetic field are planned in future tests. To ensure a reproducible positioning of the circuit in the setup, position markers have been glued on the support of the circuit.

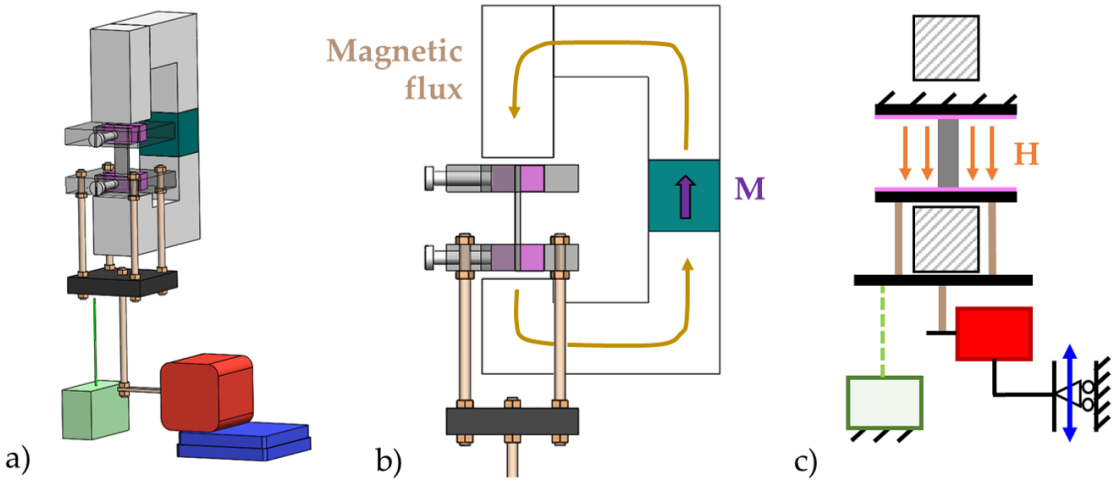

Figure II.34: Schematic view of the experimental setup including the magnetic circuit (a), side view on magnetic circuit and specimen fixation (b) and schematic view of mechanical loading in presence of a magnetic field (c), M – magnetization of the magnet, H – magnetic field in the air gap.

II.5.3 First results for coupled loading

In this section, the first results of coupled magneto-mechanical tests with the previously described experimental setup are presented. In the first test, the mechanical loading was kept constant and the magnetic loading was varied. During the second test, the mechanical loading was varied in a constant magnetic field. The air gap was kept at 51 mm and the magnitude of the magnetic field measured was hence of about 40 kA in the central region.

II.5.3.a Cyclic Magnetic loading for stationary mechanical loading states

During the first type of coupled tests, the magnetic loading of a specimen was varied while the mechanical loading was kept constant. The parallelepipedic specimen S_{mm10}, used for the tests, had a cross section of $A = 7.9\,\text{mm} \times 2.0\,\text{mm}$, a total length L of 40 mm and a free length of $L_0 = 18\,\text{mm}$. The volume fraction of the specimen measured $\Phi = 36.2$ % and it was magnetized in the direction of its length before the tests. The specimen was fixed in the experimental setup according to the protocol described previously. In the first step of the measurement, the magnetic circuit was positioned in the setup. The magnetization of the specimen pointed downwards, in the same direction as the magnetic field in the air gap (cf. figure II.34). The evolution of the force and the displacement during the positioning of the circuit are shown in figure II.35 a. The gray dots show the measurement values while the black dots represent a moving average based on 10 measurement points. Displacement and force signals show a strong variation during the time in which the circuit was positioned (3 s – 15 s) and a difference between the stationary values at the beginning and the end of the process (green and red dots in figure II.35 respectively).

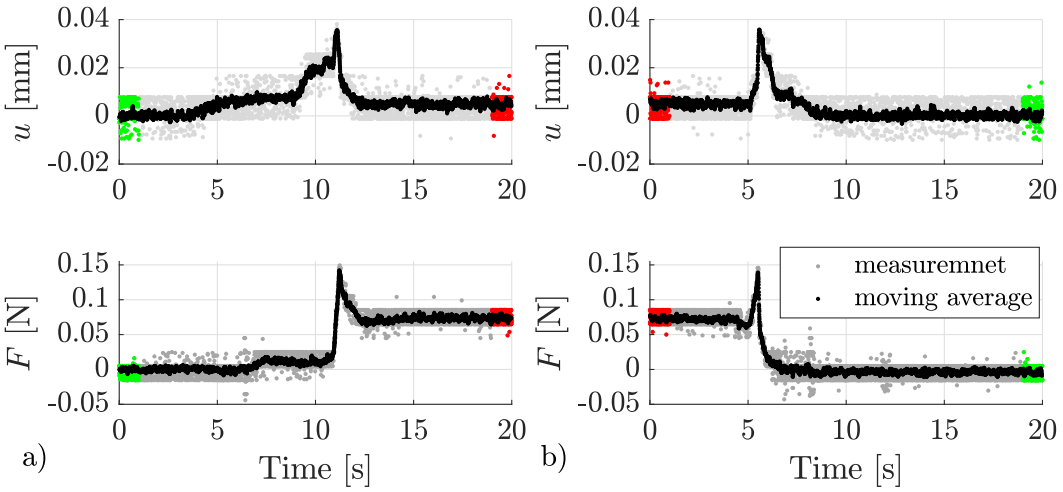

Figure II.35: Evolution of the displacement and the force applied on the specimen during the positioning of the magnetic circuit (a) and its removal (b) from the experimental setup.

The strong variation is due to the in-homogeneous and non-stationary magnetic field the specimen is exposed to during the positioning of the magnetic circuit. The interaction between the magnetic fields of the circuit and the specimen are responsible for the strong variation of the force. The variation of the displacement is presumably due to the fact, that the experimental setup is not completely rigid. This results not only in a strong variation of the displacement during the positioning of the circuit, but also in a difference between the stationary displacements. The difference between the stationary quantities values is discussed later in this paragraph. In the second step of the test, the circuit is removed from the experimental setup. As figure II.35 b shows, there is a transient variation comparable to the variation during the positioning. The stationary force and displacement disappear as soon as the magnetic circuit is completely removed. The positioning and removal of the magnetic circuit are named magnetic loading and unloading respectively in the following.
To analyze, if the stationary differences of force and displacement are reproducible phenomena, the magnetic loading and unloading was repeated five times. The average of the stationary quantities was calculated at the beginning and the end of each test on an interval of one second. As an example, the measurement values, used for the calculation of the average, are highlighted in green (absence of magnetic field) and red (presence of magnetic field) in the time diagrams in figure II.35. After the cyclic magnetic loading, a mechanical tensile loading was applied to the specimen in absence of the magnetic field. The specimen was kept in the loaded state and subjected to a cyclic magnetic loading again. The cyclic magnetic loading was applied for eight different mechanical loading states in total. The maximum displacement during the mechanical loading measured 0.17 mm which corresponds to 1 % of the free length of the specimen. Figure II.36 visualizes the magnetic loading and unloading as well as the mechanical loading.

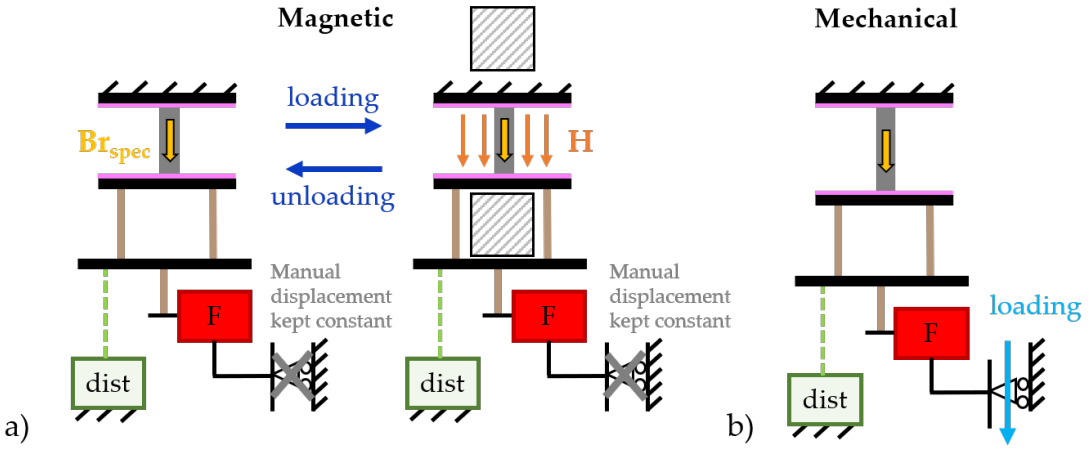

Figure II.36: Schematic view of the experimental setup showing the static magnetically unloaded and loaded state (a) and the mechanical loading (b), B_r – residual flux density of the specimen, H – magnetic field in the air gap.

The result of the eight consecutive tests are shown in figure II.37. Each dot in the graphic corresponds to the average values calculated for a stationary force-displacement state. During a mechanical loading, the displacement is increased and the force increases accordingly. The eight static loading states form a force-displacement curve with slightly decreasing slope. An increase of the stationary force and the displacement is observed for all of the eight loading states which disappears when after the unloading. The force-displacement curve of the stationary loading states in presence of the magnetic field (red dots) evolves in the same manner as the curve formed by the loading states in absence of a magnetic field (green dots). Apparently, magnetic field generates an additional loading, that modifies the stationary state but does not the evolution of the force with the displacement significantly. The effects of the magnetic loading on the mechanical state are analyzed in the following.

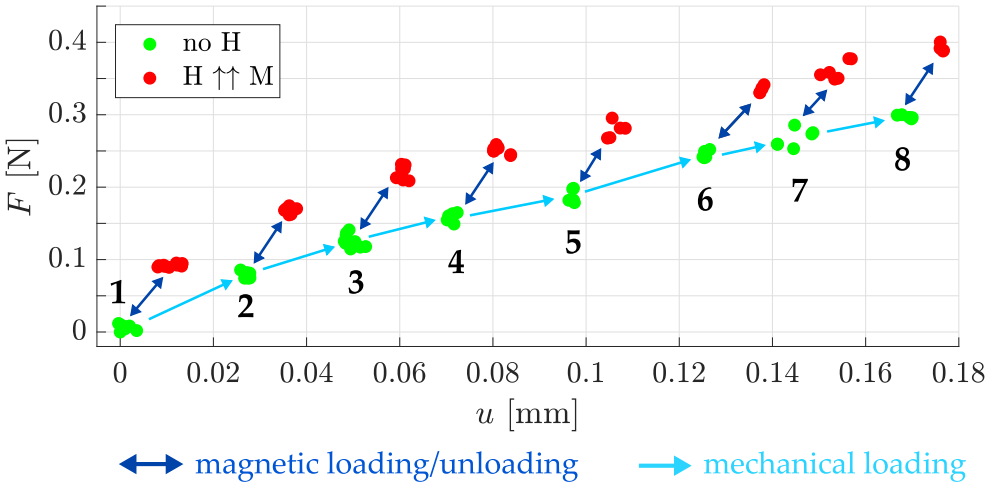

Figure II.37: Force – displacement diagram showing the results of eight quasi-static measurements in absence (green) and presence (red) of the magnetic field for a consecutive magnetic and mechanical loading.

For the comparison of the different load states, the spring models in figure II.38 are used. In accordance with figure II.29, the stiffness constants k_{spec}, k_{supa} and k_{supb} are assigned to the specimen, the mechanical support between specimen and the measurement point of the displacement (part a) and the remaining functional parts of the support respectively (part b). The mechanical loading, which has been explained previously in this section, is represented in figure II.38 b. The representation comprises the displacement u_{el} as well as the elastic force $F_{el\,1}$, acting on the specimen, governed by equation (II.12).
The magnetic loading is represented for two different assumptions concerning the experimental setup in figure II.38 c and d. The measurement results of the magnetic loading show a force increase, which is represented by an additional force in the two graphics. In figure II.38 c, the stiffness of the mechanical support located subsequent to the point of the displacement measurement is assumed to be

infinitely stiff. In this case, a variation of the force would be measured due to the additional contribution from the magnetic field, F_H, but the displacement would stay the same. In figure II.38 d, a displacement u_{mag} is induced by the magnetic interactions, since the stiffness k_{supb} is considered to be low. This displacement adds up to the displacement imposed by the mechanical loading, u_{el}. As a displacement variation is observed in the experimental results, the stiffness of the system subsequent to the point of measurement obviously has a rather low stiffness.
The presence of the displacement raises the question whether the force variation could be caused solely by elasticity. If this was the case, the displacement and the force would be linked by the equivalent stiffness composed of k_{spec} and k_{supa}, just as for the mechanical loading. The slope of the force and displacement variations would be the same for a mechanical loading as for a magnetic loading. According to figure II.37, this is not the case. Nevertheless, a displacement is observed. It is hence concluded, that the magnetic loading is divided in two parts in the setup: one part of the magnetically induced loading generates a displacement u_{mag} which contributes to the mechanical loading. The second part is an additional Force generated by the interaction of the specimen and the magnetic field and called F_H in the following. The variation of the force in the setup is thus described by equation (II.14). The different components of the force are visualized in figure II.39.

$$F = F_{el\,1} + F_{el\,2} + F_H = \left(\frac{1}{k_{spec}} + \frac{1}{k_{supa}}\right)^{-1} \cdot (u_{el} + u_{mag}) + F_H \ . \tag{II.14}$$

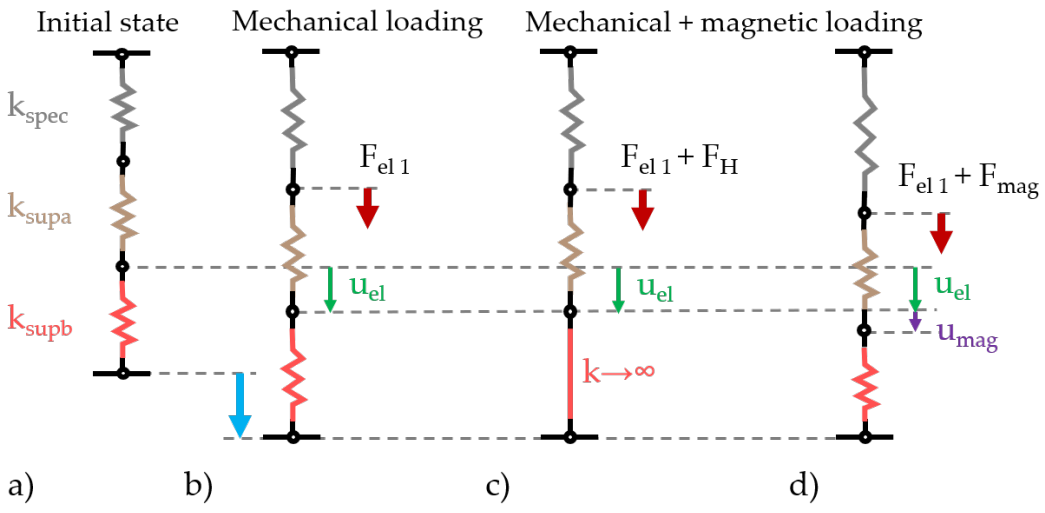

Figure II.38: Mechanical model of the different loading states in the experimental setup.

A numerical model of the test was developed, to verify the hypothesis concerning the displacement and the force variation. On this purpose, the specimen and two additional geometries, representing the two parts of the support, were added to the model of the magnetic circuit (figure II.33). While the geometry of the specimen

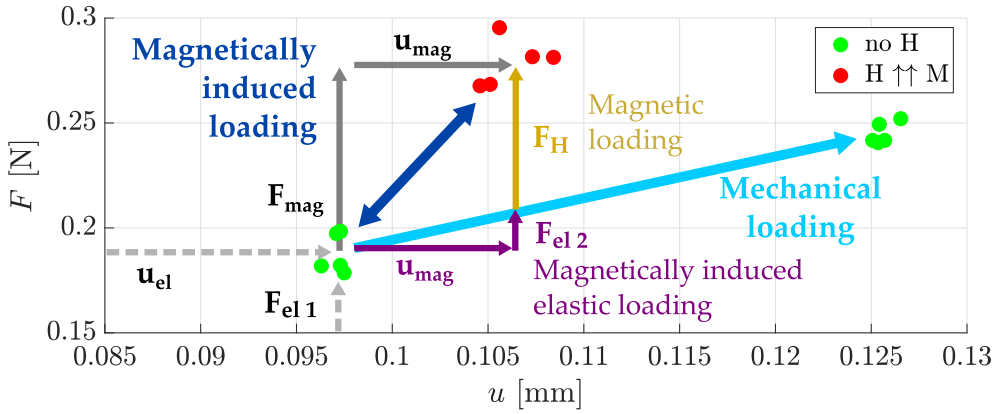

Figure II.39: Zoom on the experimental results containing a decomposition of the magnetically induced loading (F_{mag}, u_{mag}) in an elastic part (u_{mag}, $F_{el\,2}$) and a purely magnetic part (F_H).

and the circuit correspond to the geometry of the experiment, the geometry of the two supporting parts was largely simplified to cuboids (figure II.40 a). The simplification is acceptable for a qualitative analysis while the parts should be modeled in detail for quantitative studies. The three parts of the mechanical test are modeled as linear elastic materials with the modulus E_{spec}, assigned to the specimen, and the modulus E_{sup}, assigned to the two support parts. The material parameters for the specimen were fixed: E_{spec} was set to 3 MPa and Br_{spec} to 0.29 T. A tensile test is performed with the model. Similar to the experimental test, the upper part of the specimen is fixed. A displacement of 1 mm is imposed on the lower surface of support part b (figure II.40 b). The displacement u_{el} is evaluated between the two support parts, similar to the experimental study. Concerning the force, the lower surface of support part b gives access to the reaction force F_{react} of the system which will later be converted to the force F, obtained from the experiment.

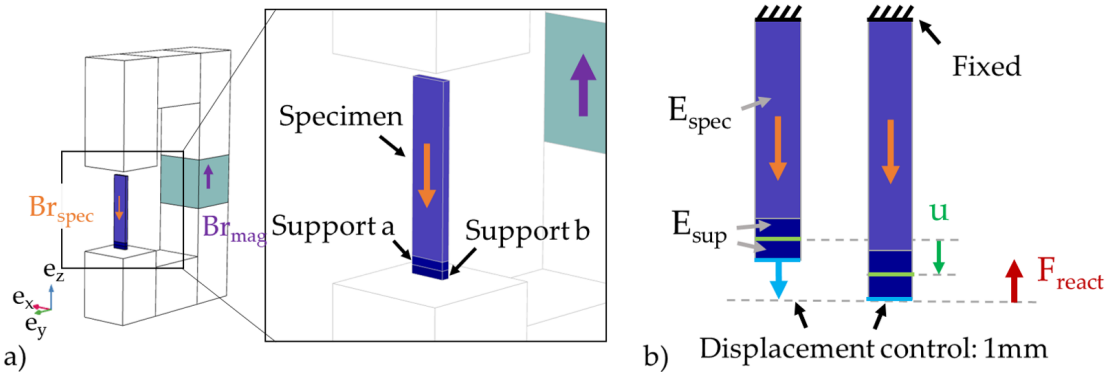

Figure II.40: Geometries used in the coupled numerical simulations (air volume hidden) (a) and schematic view of the mechanical boundary conditions and the evaluation quantities, F_{react} – reaction force.

The tensile test was performed for two sets of elastic moduli: E_{sup} was either equal to E_{spec} or ten times higher to analyze the influence of the stiffness of the supporting parts on the resulting force and displacement. Both tests were conducted either in absence or in presence of the magnetic circuit. For the second study type, the flux density of the magnet Br_{mag} was set either to 0.013 T or to 1.3 T to model weak and strong magnetic fields respectively. In presence of the magnetic field, the jump of the Maxwell stress tensor was calculated on the contour of the specimen by the simulation software and the local forces were applied as a boundary load in the mechanical domain. Six studies were conducted in total, the material parameters and the results of the six simulations are presented in table II.5.

For a qualitative comparison of the tensile tests, u_{el} and F_{react} have been normalized with respect to the first test (no magnetic field, high stiffness of the support). For $E_{sup}/E_{spec} = 10$ (simulations 1 to 3 in table II.5), the displacement does not vary significantly when the magnetic field is applied, even though the force varies. The reaction force decreases when a magnetic field is applied. The reaction forces in the system act against the deformation, a decrease means that the magnetic interactions contribute to the deformation of the specimen. The contribution increases with increasing magnetic field. A comparison of the purely mechanical simulations (1 and 4 in table II.5) shows that the modulus decrease of the supporting parts leads to a decrease of u_{el} and F_{react}. In addition, the ratio F/u (stiffness) decreases with the ratio E_{sup}/E_{spec}. As discussed previously, the stiffness of the support influences the result since the displacement is not measured on the specimen (equation (II.14)). Concerning the influence of the magnetic field, similar tendencies for the force are observed for $E_{sup}/E_{spec} = 1$ (simulations 4 to 6 in table II.5) and $E_{sup}/E_{spec} = 10$. The displacement increases when a magnetic field is added to the tensile test with $E_{sup}/E_{spec} = 1$. The increases is stronger in this configuration than for $E_{sup}/E_{spec} = 10$. As stated before, the magnetic interaction contribute to the deformation of the specimen. If the stiffness of the system is low, the interactions can generate displacement in the system.

Simulation	E_{sup}/E_{spec} ratio	Br_{mag} [T]	u_{el} (norm.) [%]	F_{react} (norm.) [%]
1	10	no circuit (no H)	100.0	100.0
2	10	0.013 (weak H)	100.0	99.5
3	10	1.3 (strong H)	100.1	72.4
4	1	no circuit (no H)	95.9	90.8
5	1	0.013 (weak H)	95.9	90.5
6	1	1.3 (strong H)	97.1	65.8

Table II.5: Parameters and results of the numerical simulations of a tensile test in absence and presence of a magnetic field, the results are normalized with respect to simulation 1.

Figure II.41 visualizes the results listed in table II.5. In addition to the results for the purely mechanical simulations (green dots), the linear force-displacement curve for the two cases is shown as well (light blue line). As stated before, weak and strong magnetic fields generate a weak and strong decrease of the reaction force. The dependence of the displacement on the stiffness of the system is clearly visible in the graphic. To represent the loading state from the experiment, the effect of a high magnetic field on the force-displacement state is converted from the reaction force F_{react}(dark red dots) to the force F, acting on the free end of the specimen (light red dots). Their magnitude is the same but their orientation is opposed. The force difference, induced by the magnetic field, adds up to the force acting on the specimen due to the mechanical loading. The qualitative results of the simulations with $E_{sup}/E_{spec} = 1$ are similar to the experimental observations (figure II.39). In addition, the numerical results confirm the hypothesis that a high stiffness of the support leads to a force increase with negligible displacement variation.

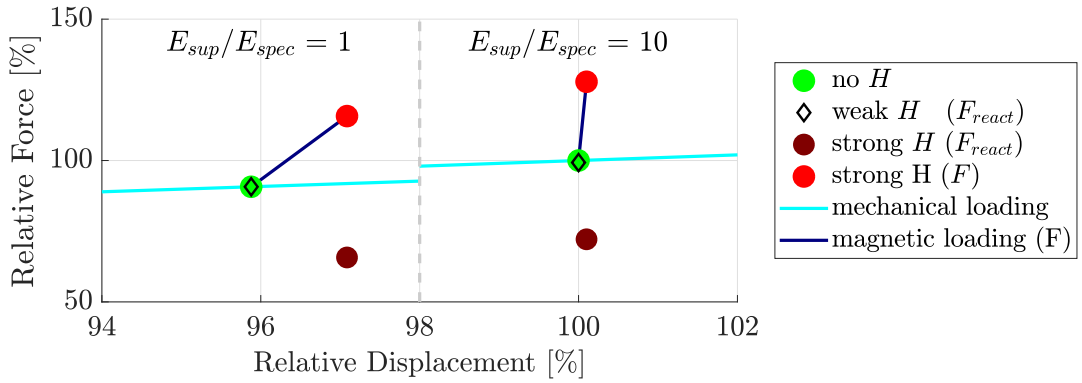

Figure II.41: Visualization of the numerical results: Effects of the magnetic loading on the mechanical loading state represented by using either the reaction force F_{react} or the force acting on the free end of the specimen F.

The experiment indicates the increase of the force acting on the specimen which would elongate the specimen if the displacement was not blocked. The constraints, that act on the specimen are dependent on the magnetic field in the specimen which in turn, depends on the specimen's shape. The shape determines the demagnetization field inside the material and a high demagnetization energy can lead to the deformation of a specimen in a magnetic field. Referring to S-MAE specimens, the presence of interactions caused by the specimens shape in a magnetic field is called "shape effect" by [Voropaieff 2019]. For the present case, the field homogeneity in the specimen can be studied by the help of the numerical model. To visualize the magnetic quantities, the magnetic field in the air gap and the z – component of the magnetic flux density in the specimen are represented in an $x - z$ plane, that cuts the specimen in the middle (figure II.42 a). The first graphic in figure II.42 b shows the specimen in a small external magnetic field. There is a gradient of the flux density inside the specimen, but mainly near the upper and lower boundaries.

The flux density is relatively homogeneous in the major part of the specimen. A comparison of the residual flux density of the specimen (0.293 T) and the average flux density in the specimen in a negligible external field (volume average, 0.282 T) shows a difference smaller than 5 %. The demagnetization of the specimen in the air remains small since the specimen is magnetized in a magnetically favorable direction where the aspect ratio is high. The inhomogeneity of B_z near the upper and lower specimen boundaries is also visible when the specimen is surrounded by an external magnetic field, as the right graphic of figure II.42 b shows. The magnitude of B_z in the specimen increases due to the external field, which is oriented in the same direction as the magnetization of the specimen. The average magnetic flux density in the specimen measures 0.362 T in this configuration. The right graphic in figure II.42 b indicates, that the magnetic field is not significantly deformed by the specimen. This observation is confirmed by a calculation of the average magnetic flux density B_z. Without the specimen, the average magnetic field component H_z in the air measures about 60 kA/m in the region where the specimen is placed. Using the material parameters of the specimen and the relation $B_z = \mu_0\mu_r H_z + Br_z$, a flux density of 0.380 T is obtained. Compared to the average flux density of 0.362 T, obtained by the numerical simulation, the difference is of 5 %. In conclusion, the influence of the field generated by the magnetic circuit on the field generated by the magnetization of the specimen is almost a linear superposition. This behavior is due to the low deformation of the magnetic field by the specimen which has its origins in the low permeability of the magnetized material.

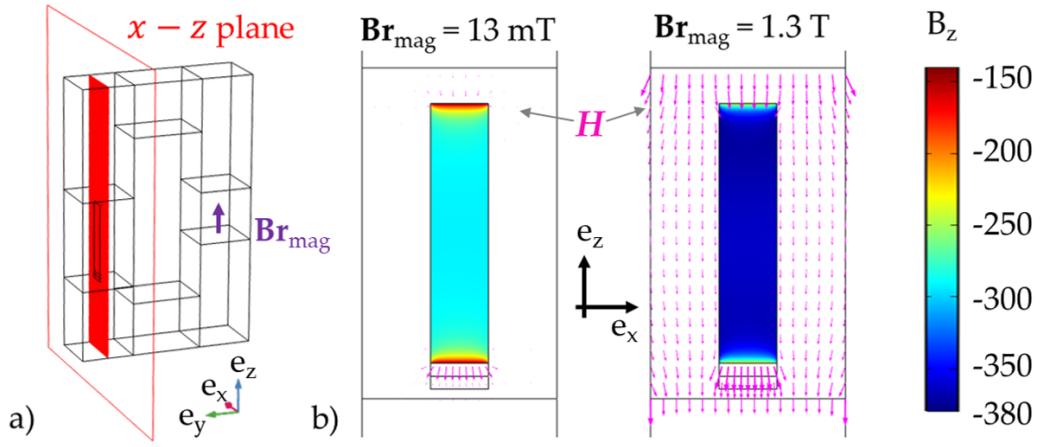

Figure II.42: Numerical simulation of the magnetized specimen positioned in the air gap of the magnetic circuit: geometry with evaluation x–z plane (a) and zoom on the specimen in the x–z plane for different residual flux densities of the magnet (b), $\boldsymbol{H}$ – magnetic field in the air gap, B_z – z component of the magnetic flux density in the specimen.

In the numerical simulation 3 (table II.5), the difference between the average stress in the specimen in the z –direction (volume average) and the ratio of F_{react} and the specimen's section is smaller than 1 %. The material behavior can be assessed

by the help of global measurement parameters. In the experiment, the clamping of the specimen is realized not exactly like in the numerical model. A representation of the actual situation is necessary to evaluate, if the stress is homogeneous enough in the specimen to base the calculation of the local stress on the global quantities. The modeling of the magnetic circuit and the specimen is supposed to be a realistic representation of the experiment in contrast to the mechanical part. The force difference between the tensile test in a negligible and a strong external field (simulations 2 and 3 in table II.5) is 0.38 N. Divided by the specimen's section, a force density of 21.3 kPa is obtained. The expression $B^2/(2\mu_0)$ can be used to calculate the stress component in the z direction: the stress increase between the simulations 2 and 3 is obtained by the help of the average flux densities in the z – direction, $B_z(s2)$ and $B_z(s3)$, from $(B_z(s3)^2 - B_z(s2)^2)/2\mu_0$ and measures 18.5 kPa. The difference of about 15 % is due to the form of the specimen which influences the magnetic flux density in the material. Future experimental tests could be performed on specimen shaped in a manner that favors homogeneous fields as proposed by [Bodelot+ 2018] for example.

The composite specimen is modeled as homogeneous material in the numerical simulations, thus the magnetically induced constraints interactions have their origin in the macroscopic model of the magnetic quantities. But observations of H-MAE on the microscopic scale also show remarkable restructuration processes of the particles in soft matrices: magnetically hard particles tend to align in chains and to align their magnetic moments with the external magnetic field ([Linke+ 2016; Schümann+ 2017; Stepanov+ 2017]). The magnetomechanical interactions due to particle interactions are material effects by [Voropaieff 2019]. The displacements and rotations could contribute to the force increase observed in the experiment, but particle interactions are not part of the homogeneous model and can hence not be evaluated based on the simulations presented above. However, interactions in stH-MAE have been studied by the means of numerical modeling in the context of this thesis and the result will be presented in the next chapter. At this stage, it is not possible to quantify the contributions of the shape and material effects to the force increase in the experimental results. Additional studies have to be performed on this purpose. Tests with specimens with different shapes in combination with numerical simulations could help to quantify the shape effect. On this purpose, the experimental test setup has to be represented in detail in the numerical simulations (actual geometry and material properties). The displacement should furthermore be measured on the specimen. It has been shown that the specimen is subjected to a strong transient loading during the positioning and removal of the magnetic circuit. Even though, the stationary mechanical loading states are reproducible, the magnetic field should be varied by other means like the variation of the air gap in future studies. Another aspect of the first experimental test is the similar evolution of the force-displacement curves in presence and absence of a magnetic field. The mechanical loading in presence of a magnetic field has been studied in a second test and will be presented in the following.

II.5.3.b Mechanical loading in presence of magnetic field

In this study, the specimen S_{mm9} has been subjected to a cyclic magnetic loading in presence of a magnetic field. On this purpose, the magnetic circuit was positioned in the setup after the fixation of the specimen. The magnetic field and the magnetization of the specimen were oriented in the same direction. The magnetic field caused a variation of displacement and force as described in the previous test. A cyclic mechanical loading was applied to the specimen similar to the purely mechanical tests described at the beginning of the section. Two loading cycles were performed with the specimen and the results for each cycle are shown in figure II.43. The graphic also shows the results of the two purely mechanical tests. The magnetic field induces an offset, to enhance the comparison of the measurement results, the variations are compared instead of the absolute values. Figure II.43 shows the variation of the force and the displacement (Δu_{el} and ΔF) with respect to the first measurement point of the cycle. The results for both cycles show that the magnetic field does not significantly influence the loading cycle and hence the elastic properties of the material. This observation is confirmed by a calculation of the slope of the loading and unloading paths, which corresponds to the stiffness k_{eq}. The slope was determined by the following procedure: a "local stiffness" is calculated for each measurement as the slope towards the next measurement point. For the loading and unloading paths, the five values in the middle of the path are used to calculate the average stiffness k_{eq} and the standard deviation. The results are summarized in table II.6. One reason for this surely is the stiffness of the matrix material which inhibits the movement of the particles and generates elastic forces largely superior to the ones generated by particle interactions.

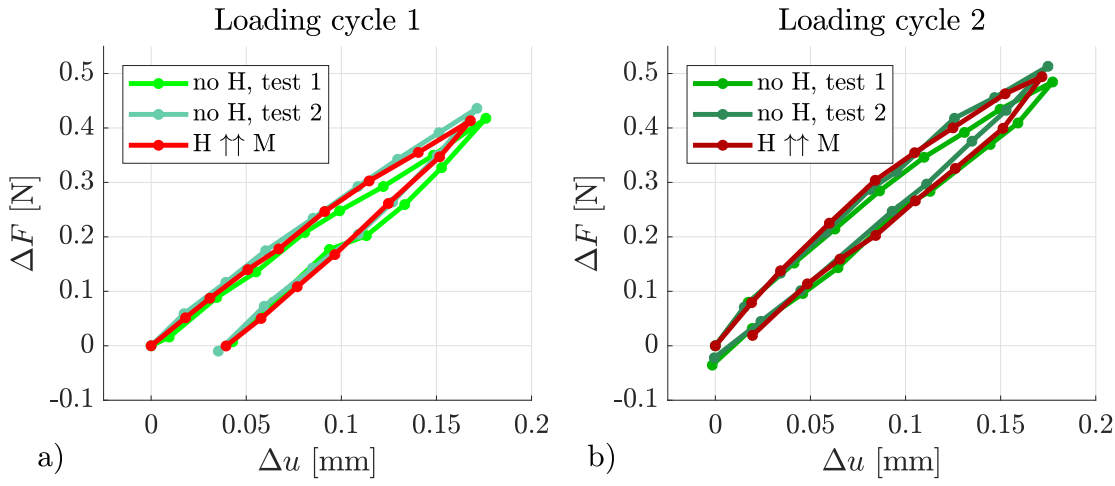

Figure II.43: Comparison of the loading cycles 1 (a) and 2 (b) obtained from the measurements with S_{mm9} for different magnetic loading states.

Configuration	k_{eq} [N/mm], cycle 1 loading	k_{eq} [N/mm], cycle 1 unloading	k_{eq} [N/mm], cycle 2 loading	k_{eq} [N/mm], cycle 2 unloading
no H, mount 1	2.0 ± 0.2	3.0 ± 0.3	2.4 ± 0.3	2.5 ± 0.3
no H, mount 2	2.2 ± 0.1	3.0 ± 0.3	2.6 ± 0.5	2.7 ± 0.3
$H \uparrow\uparrow M$	2.2 ± 0.2	2.9 ± 0.1	2.5 ± 0.5	2.6 ± 0.2

Table II.6: Elastic constant k_{eq} calculated from the mechanical loading of S_{mm9} for different magnetic loading states.

The cyclic loading has been repeated on two consecutive days in absence and presence of a magnetic field. Figure II.44 shows the stabilized cycles of the force and displacement variations with respect to the first measurement point of the cycle. The results are in good accordance which states that reproducible measurement can be performed with the experimental setup.

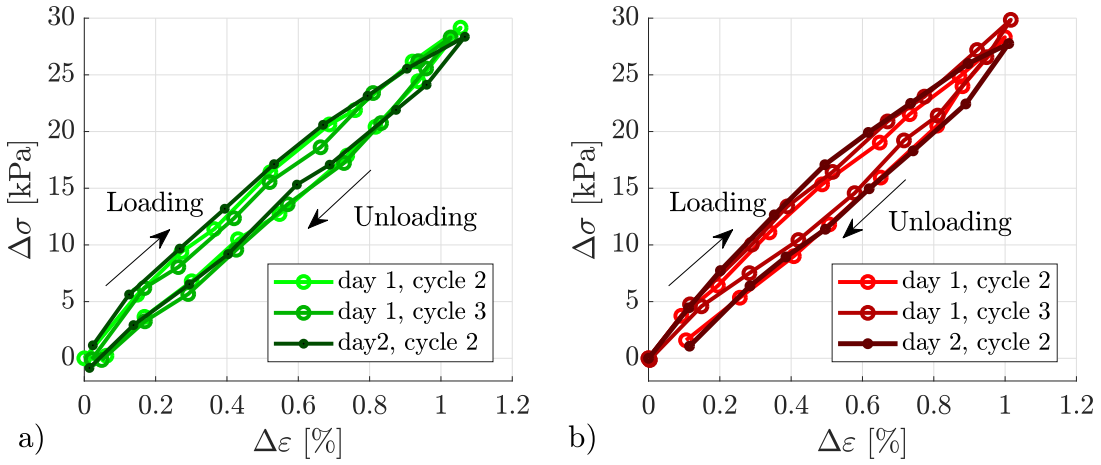

Figure II.44: Stabilized mechanical loading cycles obtained on two consecutive days in absence of a magnetic field (a) and for the configuration $H \uparrow\uparrow M$ (b).

II.6 Conclusions and perspectives

In this chapter, the elaboration and experimental characterization of an isotropic stH-MAE has been presented. Concerning the magnetic characteristics, a characteristic property of this type of MAE is its high coercive field strength. The latter is of the same order of magnitude for the composite as for the magnetic powder, stH-MAE show hence a similar resistance to demagnetization fields. It has also been shown that the residual flux density is related in a linear manner to the residual flux density of the magnetic powder by the volume fraction. The temperature dependence of the residual flux density and the coercive field can be predicted by temperature coefficients from the powder's datasheet. The magnetic behavior of the stH-MAE can hence be predicted by the characteristics of the powder and the particle filling ratio. The uniaxial tensile tests reveal an isotropic mechanical behavior, which has been assumed on the basis of the manufacturing process. Procedures for the determination of the Young's modulus as well as for the Poisson's ratio of the stH-MAE have been outlined. In addition, the dynamic mechanical properties have been revealed for the matrix material and two composite types. The dependence of the material behavior on the loading frequency as well as on the temperature are demonstrated. They are present in the matrix and thus also in the composite material. According to DMA tests, the magnetization of the composite has no influence on the dynamic mechanical properties of the stH-MAE in the tested tensile configuration. In addition, an external magnetic field of 40 kA (i.e. 50 mT in the air) applied during quasi-static tensile tests caused no variation of the elastic properties. Nevertheless, the stationary loading states are influenced by the presence of the external magnetic field in form of an additional constraint. The coupling in the stH-MAE is characterized as relatively weak.

Future studies will be conducted on composites with different elastomeric matrices with various Young's moduli, different filling ratios and for an isotropic or anisotropic MAE. The effect of the microstructure on the residual flux density is an interesting subject for future studies. Additionally, the magnetic properties could be analyzed for dynamic magnetic loadings in future studies. This would provide important information for the use of stH-MAE in "active" applications where the external field is varied constantly. Future studies on the mechanical behavior should focus on the viscous behavior of the material. An increase of the time constant due to the magnetization have been reported for soH-MAE ([Kramarenko+ 2015]). For the composite used in this study, it has been observed that magnetized specimens have a higher tendency to keep their deformed state after large or moderate deformations applied over a long time span than non-magnetized specimen. In addition, the influence of external magnetic fields on the viscous component of the behavior should be studied. The investigations on the coupled behavior will be pursued with the magnetomechanical test bench, presented in this chapter. The displacement measurement should be performed directly on the specimen in future studies. Furthermore, a full field measurement of the displacement directly on the

specimen should be carried out. This would also allow to verify the homogeneity of the displacement field not only for the coupled but also for the purely mechanical tests. The different origins of the magnetic loading should be identified in future tests with the test bench. Modifications of the elastic properties have not been observed during the tests, but an additional loading was generated by the magnetic field. A simple model of this effect is the linear superposition of the two effects such as

$$\Delta\sigma = c \cdot \Delta\varepsilon + \Delta\sigma_H \ , \tag{II.15}$$

where σ and ε correspond to the mechanical stress and the strain respectively, c to an elastic constant and $\Delta\sigma_H$ to an additional stress component, induced by the external magnetic field H. The stress σ_H presumably depends on the intensity of the magnetic field, since stronger magnetic fields are supposed to generate stronger interactions. The numerical model shows, that external magnetic fields superimpose to the field generated by the specimen due to the low permeability of the specimen. Assuming a linear dependence of σ on H for small magnetic loadings, equation (II.15) can be rewritten such as

$$\Delta\sigma = c \cdot \Delta\varepsilon + d \cdot H \ , \tag{II.16}$$

where the coefficient d accounts for the magnetomachanical coupling. Equation (II.16) is also called piezomagnetic behavior law [Electrical+ 1990]. Regarding the measurement results, this model can be used to describe the behavior of the magnetized composite material. The possible application of such a behavior law for the description of the behavior of stH-MAE has been studied by the help of numerical models and will be presented in the next chapter.

Chapter III
Multiscale modeling of an stH-MAE

III.1 State of the art

III.1.1 Introduction to the modeling of MAE

During the last years, the modeling of MagnetoActive Elastomers (MAE) has been pursued with increasing intensity, as the review of [Cantera+ 2017] shows. In their work, a variety of analytic, numerical and empirical models of MAE are summarized. The aim of the modeling is to predict the behavior of MAE in various mechanical and magnetic load cases by appropriate behavior laws. Models of MAE contain material properties of both physical domains, mechanics and magnetism, they are designated as **multi–physical models**. Furthermore, the representation of the magneto–mechanical coupling in MAE is an important characteristic of MAE models. The coupling causes effects like the field–dependent elastic and damping characteristics (MagnetoRheological (MR) effect) or the field–induced deformation (MagnetoStrictive (MS) effect) and is hence an important part of the modeling. These coupling effects are mainly caused by microstructural processes (cf. chapter II), but have measurable effects on the behavior of composite specimen, which are much larger than the particles. The modeling of MAE hence also requires the choice of a **scale**, which is determined by the purpose of the modeling.
Phenomenological models are used on the scale of MAE structures, where the composite is represented as a homogeneous material. One approach for the modeling is the use of the conservation laws of continuum mechanics and magnetism to solve magneto-mechanical problems. Another approach, which has experienced increasing interest during the last years, is the development of behavior laws based on the laws of thermodynamics. This approach consists of the choice of an appropriate formulation of the free energy and the derivation of local state laws (cf. [Lemaitre+ 2009] for example). Both approaches result in the same governing equations ([Danas+ 2012]). The development of thermodynamically consistent formulations has been presented for rigid magnetic bodies by [Brown 1966] and has been extended to finite strain by [Kankanala+ 2004]. MAE are easily deformable; therefore, several modeling approaches aim a description of the magneto-elastic interactions in the context of large strain ([Kovetz 2000; Ogden 2011; Voropaieff 2019]). The material parameters, used in phenomenological models, have to be identified, for example by means of an experimental characterization. In this case the description of the material behavior is limited to the conditions specified by the experiment. Phenomenological models are useful for the description of materials with well-established manufacturing processes, allowing to elaborate materials with reproducible properties. The models are furthermore well suited for the study of large structures (compared to the particles size), complex loading cases and shape dependent effects of MAE structures (e.g. demagnetization fields).
Microscopically motivated models are used for the study of microstructural processes in MAE. An important aspect of the modeling on this scale are the local interactions that occur between the particles (or “inclusions”) in the matrix. The representation of the actual microstructure of a composite is nearly

impossible and microscopic models, which explicitly represent the microstructure, contain assumptions like for example a permanent contact between particles and matrix. Furthermore, several hypothesis are made on the particle's shape, size and distribution. Studies on the microscopic scale concern isotropic and transversely isotropic microstructures (cf. [Metsch+ 2016] for example). Microscopic models are generally developed with the intention to study the influence of processes on the microscopic scale on the macroscopic material properties. The modeling includes a so–called homogenization of the material properties for the scale transition (**multi–scale models**). Definitions and classical homogenization models will be introduced in the subsequent section and more detailed information about microscopically motivated modeling are presented afterwards.

III.1.2 Homogenization: definitions and classical models

Homogenization procedures are applied to composites, which are assembled from at least two materials. The different materials are also called phases. A homogenization procedure is used to calculate the material properties of a homogeneous material, which behaves equivalent to the heterogeneous composite, based on information about material properties of the constituents and the microstructure of the heterogeneous composite. The homogenized material properties are also called effective or apparent properties. Once a model is established, the theoretical analysis is less time and cost intensive than the elaboration and experimental testing of different variants of a composite material. In addition, the microstructure can be optimized for specific purposes, which paves the way for the design of materials. In the following, definitions and classical homogenization models are detailed. The explanations are based on the information in [Bornert+ 2001] if not otherwise specified.
Figure III.1 shows images of a MAE with different magnifications to represent different scales. A characteristic length is associated with every scale from microscopic to macroscopic. The characteristic length depends on the purpose of the homogenization, in this example the transition from the microscopic size of a particle d towards a structure with characteristic length L is presented. On the microscopic as well as on the macroscopic scale, the material properties are homogeneous to the observer. In the first case, they correspond to the property of one phase and in the second case to the effective properties. The effective properties depend not only on the material characteristics of the phases, but also on their arrangement, which is represented on the intermediate mesoscopic scale. The scale transition from the microscopic to the macroscopic scale is performed by the homogenization processes. The characteristic lengths d and L can be set with regard to the primary material and the size of the final structure for example. An important step during the homogenization is the determination of the characteristic length l of the mesoscopic scale, especially for random microstructures. For this type of structure, the details of the phase distribution are unknown. Pictures of

the microstructure, taken by a microscope at different positions, are not identical. But for so-called stationary microstructures, the probability of finding a phase φ on a position $\boldsymbol{x}$ in a volume V does not depend on the position of this point. If the size of the image is big enough, the probability can be determined by a volume average (ergodic hypothesis):

$$\langle \varphi \rangle = \frac{1}{|V|} \int_V \varphi(\boldsymbol{x}) \, \mathrm{d}V \, . \tag{III.1}$$

To fulfill the ergodic hypothesis, l has to be much larger than d. Additionally, if the difference of the characteristic lengths is too small, the effective behavior fluctuates strongly. This fluctuation diminishes when l increases. The characteristic length L has to be much larger than l since the material is considered to be a homogeneous material on the macroscopic scale, where the details of the microstructure are not represented. The condition in equation (III.2) resumes the separation of the scales:

$$d \ll l \ll L \, . \tag{III.2}$$

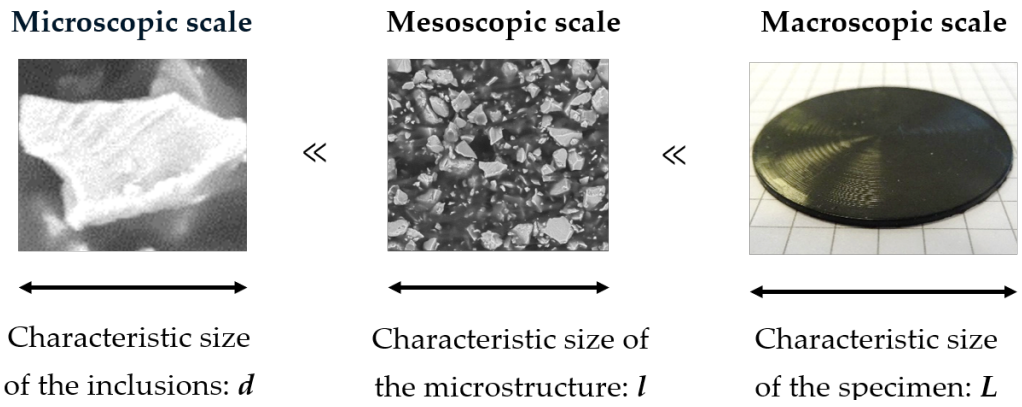

Figure III.1: Representation of important properties and the characteristic size of a MAE composite material on different scales.

A loading, applied on the macroscopic scale, generates a heterogeneous material responses in a composite on the microscopic scale. This is due to the gradient of the material properties. On the macroscopic scale, however, the local fluctuations are not considered. Instead, the average or effective behavior is evaluated. The effective properties of a material can be determined in three consecutive steps: representation, localization and homogenization. The representation corresponds to the description of the microstructure and includes the geometry and the material properties of the constituents as well as their arrangement. The localization concerns the mechanical analysis of the composite, the mechanical loading and the boundary conditions are defined. In the third step (homogenization), the scale transition is realized. Average operators are specified and applied to determine the effective material properties. Different strategies for the determination of the effec-

tive properties are summarized for example by [Pindera+ 2009]. An introduction to some techniques, based on mechanical and magnetic continuum formulations, will be presented in the following.

III.1.2.a Approach based the inclusion problem and effective boundaries

One concept in analytical homogenization is based on the inclusion problem. The method is applied to composites which consist of at least two materials, also called phases. Each phase is modeled as a single, representative inclusion situated in a reference medium considered infinite. The shape of the representative inclusion is determined by the distribution of the phase. An isotropic distribution for example corresponds to a sphere, as both are independent from the spatial direction. The representative inclusions have the same material properties as the underlying phase. The inclusion problem is solved for each phase. If the form of the representative inclusion is elliptical, the problem can be resolved analytically. The material behavior of a homogeneous material, equivalent to the heterogeneous composite in the study, is estimated by a superposition of the individual inclusion problems. Different assumptions for the behavior of the surrounding infinite medium have led to the development of different estimates. The method can be applied to estimate mechanical as well as magnetic effective properties.

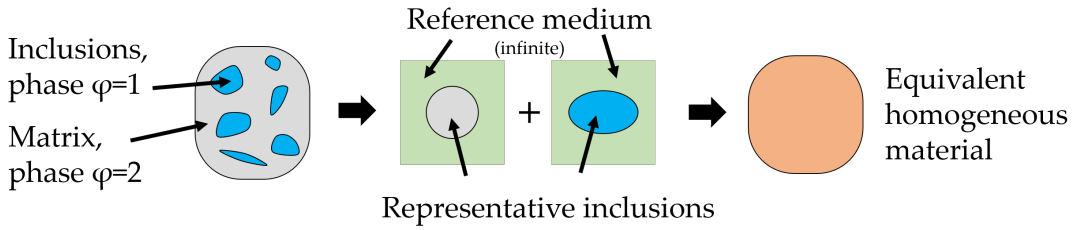

Figure III.2: Schematic representation of an analytical homogenization approach based on inclusion problems for a bi-phase composite material.

In mechanical problems, the result of the homogenization is the effective stiffness tensor $\mathcal{C}$. While the local mechanical quantities ${}^{\varphi}\sigma$ and ${}^{\varphi}\varepsilon$ depend on the stiffness tensor ${}^{\varphi}\mathcal{C}$ of the corresponding phase φ, the effective stiffness tensor links the average strain ε to the average stress σ in the volume V. The relation between the local and effective quantities in V is established by the help of the ergodic hypothesis (equation (III.1)):

$$\sigma = \left\langle {}^{\varphi}\sigma \right\rangle = \mathcal{C} : \left\langle {}^{\varphi}\varepsilon \right\rangle = \mathcal{C} : \varepsilon \,, \tag{III.3}$$

$$\left\langle {}^{\varphi}\sigma \right\rangle = \frac{1}{|V|} \int_V {}^{\varphi}\sigma(\boldsymbol{x}) \, \mathrm{d}V = \sigma \,, \qquad \left\langle {}^{\varphi}\varepsilon \right\rangle = \frac{1}{|V|} \int_V {}^{\varphi}\varepsilon(\boldsymbol{x}) \, \mathrm{d}V = \varepsilon \,. \tag{III.4}$$

If the reference medium is supposed to be infinitely soft, the boundary of Reuss is calculated. With an infinity stiff matrix material, the boundary of Voigt is obtained. The expressions of the Voigt and Reuss estimates for the effective me-

chanical stiffness tensor $\mathcal{C}$ of a bi-phase composite are shown in equation (III.5) and equation (III.6) respectively. In the example, the phase 1 is supposed to be diluted in phase 2 and Φ represents the volume fraction of phase 1 (cf.figure III.2). In mechanics, the approximations of Voigt and Reuss assume uniform strain and uniform stress respectively and they are the physically possible limits, or boundaries, of the effective behavior.

$$\mathcal{C}_R^{-1} = \left\langle {}^{\varphi}\mathcal{C}(x)^{-1} \right\rangle = \Phi\, \mathcal{C}_1^{-1} + (1-\Phi)\, \mathcal{C}_2^{-1} \ . \tag{III.5}$$

$$\mathcal{C}_V = \left\langle {}^{\varphi}\mathcal{C}(x) \right\rangle = \Phi\, \mathcal{C}_1 + (1-\Phi)\, \mathcal{C}_2 \ , \tag{III.6}$$

In the magnetic domain, the boundaries of Voigt and Reuss are known as Wiener bounds [Daniel+ 2007]. Homogenization procedures are applied to determine the effective permeability tensor $\mathbb{\mu}$, which links the average magnetic flux density B to the average magnetic field H:

$$\boldsymbol{B} = \left\langle {}^{\varphi}\boldsymbol{B} \right\rangle = \mathbb{\mu} \cdot \left\langle {}^{\varphi}\boldsymbol{H} \right\rangle = \mathbb{\mu} \cdot \boldsymbol{H} \ . \tag{III.7}$$

Similar to the mechanical homogenization, the effective properties are obtained by the resolution of inclusion problems. In this case, the choice of the permeability of the surrounding medium leads to different estimates. The lower and upper Wiener bounds, μ_{W^-} and μ_{W^+}, are obtained for reference media with zero or infinite permeability. The corresponding expressions for a composite consisting of two phases, with the magnetic permeability μ_1 and μ_2 respectively, are shown in equation (III.8) and equation (III.9) [Daniel+ 2007]. Φ represents the volume fraction of phase 1 which is supposed to be diluted in phase 2.

$$\mu_{W^-} = \left(\frac{\Phi}{\mu_1} + \frac{1-\Phi}{\mu_2} \right)^{-1} \tag{III.8}$$

$$\mu_{W^+} = \Phi\mu_1 + (1-\Phi)\mu_2 \tag{III.9}$$

III.1.2.b Approaches based on an explicit representation of the microstructure

The study of effects on the microscopic scale on the properties on the macroscopic scale can require an explicit representation of the microstructure. In this case, the model represents a subvolume of the heterogeneous composite with the characteristic length l on the microscopic scale. In addition, the boundary conditions have to represent the fact that the subvolume is located in the composite where no physical exterior boundaries exist. According to [Pindera+ 2009], the microscopic modeling of spatially uniform heterogeneous media can be regrouped in two categories: the first category concerns statistically homogeneous composite materials, which are modeled by **representative volume elements (RVEs)**. An RVE corresponds to the smallest subvolume of the microstructure that contains the same phase volume fraction and statistical distributions as the material at a larger scale (cf. figure III.3 a). A concept to model periodic structures are **representative**

unit cells (RUCs) which correspond to the smallest element from which the whole material structure can be constructed by replication [Pindera+ 2009]. An example of a periodic structure is shown in figure III.3 b. The response of an array, constructed from RUC, is identical to the response of a single RUC is both are subjected to the same loading. While the effective properties, obtained for RUC, in which the heterogeneous composite are independent from the number of unit cells used for the assembly of the structure, the results obtained for statistically homogeneous microstructures vary with the size of the volume. The gradient of the material properties in composites generates local fluctuations of the stresses and strains. As a consequence, the effective properties obtained from volumes with only few inclusions are not representative. A convergence of the properties can be achieved by increasing the observation volume. Subvolumes, for which the convergence has been attained, are RVE and their characteristic size corresponds to l.

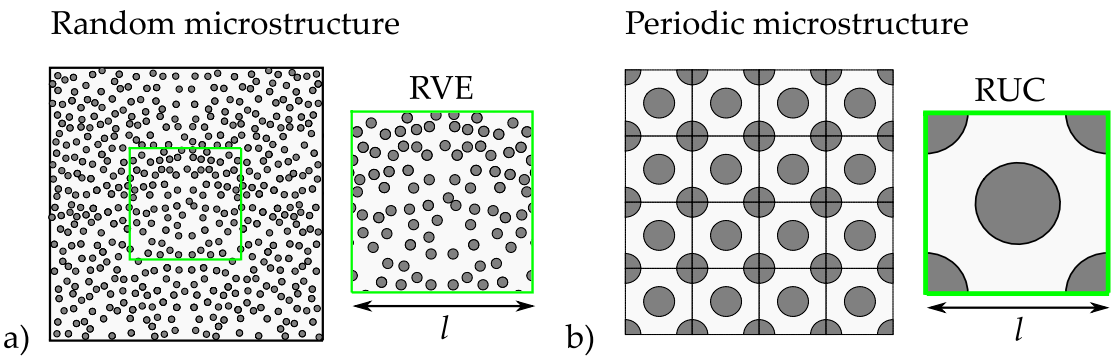

Figure III.3: Schematic representation of a random microstructure with a Representative Volume Element (RVE) (b) and a periodic microstructure with the corresponding Representative Unit Cell (RUC) (a), l – characteristic size.

In continuum mechanics, the heterogeneous microstructure can be represented explicitly by material domains $\mathscr{B}$. Examples of a bi-phase composite, consisting of particles and a matrix, are shown in figure III.4 a and b. The particle domains $\mathscr{B}_p$ and the matrix domain $\mathscr{B}_m$ are separated by a material interfaces $\partial\mathscr{B}_{pm}$. The local field quantities in each domain are governed by separate behavior laws while the field quantities follow a set of constitutive equations. The description of the heterogeneous cell also comprises boundary conditions. In the cell, the behavior on the material interfaces between matrix and particles has to be determined. This chapter deals exclusively with cases with a permanent contact between particles and matrix. Mechanical and magnetic loadings are applied at the scale of the specimen (macroscopic) and hence at an infinite distance from the microscopic cell. The conditions on the outer boundaries of the cell have to represent the fact that the heterogeneous cell belongs to a quasi-infinite volume compared to the size of the RVE or RUC. For an equivalent homogeneous material, the response of the cell to a loading, applied at an infinite distance would be uniform. To achieve this state in a cell, so-called homogeneous loading is applied on its outer boundaries.

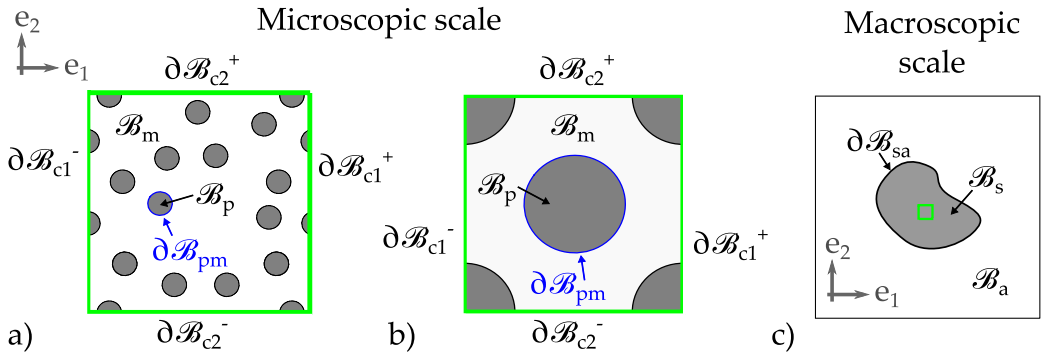

Figure III.4: Continuum models of an RVE (a) and an RUC (b) cell containing particle and matrix domains and continuum model of a specimen surrounded by an air volume, $\mathscr{B}$ – domain, $\partial\mathscr{B}$ – boundary

Homogeneous boundary conditions are explained with an example in the mechanical domain in the following. Applied on the outer boundary $\partial\mathscr{B}$ of a cell, homogeneous strains ε^0 and stresses σ^0 generate displacements $\boldsymbol{u}$ and surface tractions $\boldsymbol{t}$ respectively:

$$\boldsymbol{u}(\partial\mathscr{B}) = \varepsilon^0 \cdot \boldsymbol{x} \qquad \text{or} \qquad \boldsymbol{t}(\partial\mathscr{B}) = \sigma^0 \cdot \boldsymbol{n}\ , \tag{III.10}$$

where $\boldsymbol{x} \in \partial\mathscr{B}$ and $\boldsymbol{n}$ corresponds to the surface normal of $\partial\mathscr{B}$. As stated before, a homogeneous loading would generate a uniform response in the volume of an equivalent homogeneous material. In the heterogeneous RVE, the response is obtained by a volume average, which is supposed to be equivalent to homogeneous loading:

$$\varepsilon_{kl} = \frac{1}{2V}\int_S (u_k n_l + u_l n_k)\,\mathrm{d}S = \varepsilon^0_{kl} \quad \text{and} \quad \sigma_{kl} = \frac{1}{V}\int_S t_k x_l\,\mathrm{d}S = \sigma^0_{kl} \tag{III.11}$$

If the subvolume is an RVE, the displacement and the traction are homogeneous on the boundary and the following equation holds according to [Pindera+ 2009]:

$$\frac{1}{2}\int_V {}^{\varphi}\sigma : {}^{\varphi}\varepsilon\,\mathrm{d}V = \frac{1}{2}\sigma : \varepsilon = \frac{1}{2}\sigma^0 : \varepsilon^0\ . \tag{III.12}$$

The periodic behavior of RUC is modeled by the loading on is boundary for which a periodic displacement $\boldsymbol{u}$ and anti-periodic traction $\boldsymbol{t}$ are specified (equation (III.13)).

$$ {}^{\varphi}\boldsymbol{u}(\boldsymbol{x}+\boldsymbol{l}) = {}^{\varphi}\boldsymbol{u}(\boldsymbol{x}) + \varepsilon^0\,\boldsymbol{l} \qquad , \qquad \boldsymbol{t}(\boldsymbol{x}+\boldsymbol{l}) + \boldsymbol{t}(\boldsymbol{x}) = 0\ , \tag{III.13}$$

where $\boldsymbol{l}$ corresponds to vector of which each component is equal to l.
The displacement of the boundary is not only resulting from the average strain but also from the gradient of the material properties in the heterogeneous cell. Exposed to the same strain, the materials react differently, which causes a fluctuation of the stress. Periodic boundary conditions can consider these fluctuations in addition to the displacement induced by the homogeneous or average loading :

$$ {}^{\varphi}\boldsymbol{u}(\partial\mathscr{B}^{+}) = {}^{\varphi}\boldsymbol{u}(\partial\mathscr{B}^{-}) + \varepsilon^{0} \cdot ({}^{\varphi}\boldsymbol{x}(\partial\mathscr{B}^{+}) - {}^{\varphi}\boldsymbol{x}(\partial\mathscr{B}^{-})) \,, \tag{III.14} $$

Figure III.5 visualizes a RUC subjected to a shear loading. The total displacement is composed of a part induced by the average response (red) and local, periodic fluctuations of the displacement (blue).

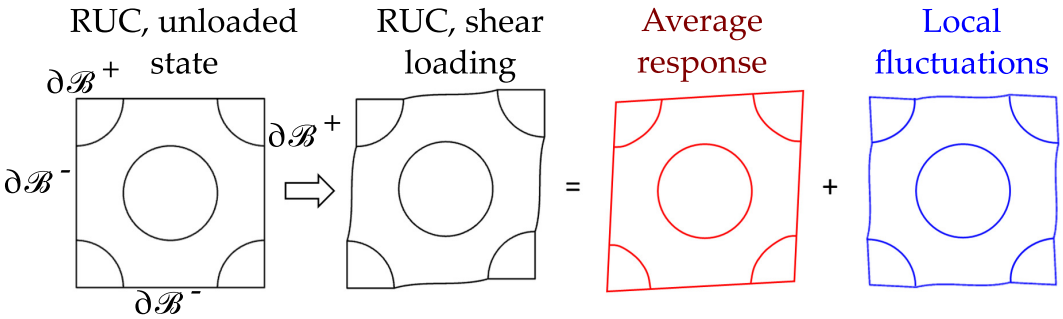

Figure III.5: Schematic representation of an RUC, the displacement is decomposed in an average part (red) and the fluctuations on the boundaries (blue).

For a consistent transition between the microscopic and the macroscopic scale, it has to be assured that the macroscopic work is equivalent to the spatial average of the microscopic work in the RVE. This condition is called Hill-Mandel condition in the mechanical domain (equation (III.15)), in electromagnetism it is known as Tellegen's theorem (equation (III.16)) according to [Corcolle 2009].

$$ \frac{1}{V}\int_{V} {}^{\varphi}\sigma : {}^{\varphi}\varepsilon \, \mathrm{d}V = \left\langle {}^{\varphi}\sigma : {}^{\varphi}\varepsilon \right\rangle = \left\langle {}^{\varphi}\sigma \right\rangle : \left\langle {}^{\varphi}\varepsilon \right\rangle = \sigma : \varepsilon \tag{III.15} $$

$$ \frac{1}{V}\int_{V} {}^{\varphi}\boldsymbol{H} \cdot {}^{\varphi}\boldsymbol{B} \, \mathrm{d}V = \left\langle {}^{\varphi}\boldsymbol{H} \cdot {}^{\varphi}\boldsymbol{B} \right\rangle = \left\langle {}^{\varphi}\boldsymbol{H} \right\rangle \cdot \left\langle {}^{\varphi}\boldsymbol{B} \right\rangle = \boldsymbol{H} \cdot \boldsymbol{B} \tag{III.16} $$

III.1.3 Multi-scale modeling of MAE

This section presents an overview over the existing work on the multi-scale modeling of MAE based on an explicit representation of the microstructure. On a microscopic scale, the models contain information about the mechanical and magnetic material properties of the matrix and the particles and account for the microstructure. The coupling between the physical domains is established on the microscopic scale. On this purpose, the particles are either modeled as magnetic dipoles or as continua. Examples for both approaches will be presented in the following with a focus on the continuum modeling.

III.1.3.a Particles modeled as magnetic dipoles

In several analytic studies concerning MAE, the particles are modeled as magnetic dipoles, more precisely, by the magnetic dipole moment $\boldsymbol{m}$. The dipole moment corresponds to the ratio of the residual flux density and the volume of an object. Its expression for a spherical particle with the radius R is shown in equation (III.17). The magnetic dipole representation is explained in the following on the example of two particles, p_1 and p_2. The analytic expressions for the interaction energy as well as the force and torque acting on particles p_2 from the interaction with p_1, are stated in equation (III.18). The interaction energy e corresponds to the product of the magnetic dipole moment of p_2 and the magnetic flux density generated by p_1 at the position of p_2. It has the same magnitude for both particles. The force $\boldsymbol{F}^{p_2}$ acting on particle p_2 corresponds to the gradient of the magnetic energy. The torque $\boldsymbol{T}^{p_2}$ acting on particle p_2 corresponds to the cross product of the magnetic dipole moment of p_2 and the flux density generated by p_1 at the position of p_2.

$$\boldsymbol{m} = \frac{3}{4\mu_0 \pi R^3} \boldsymbol{B}\boldsymbol{r} \tag{III.17}$$

$$e = -\boldsymbol{m}^{p_2} \cdot \boldsymbol{B}^{p_1} \qquad \boldsymbol{F}^{p_2} = \boldsymbol{grad}\,(\boldsymbol{B}^{p_1} \cdot \boldsymbol{m}^{p_2}) \qquad \boldsymbol{T}^{p_2} = \boldsymbol{m}^{p_2} \times \boldsymbol{B}^{p_1} \tag{III.18}$$

The three quantities e, $\boldsymbol{F}$ and $\boldsymbol{T}$ can be expressed as functions of magnetic dipole moments of the two interacting particles and the distance vector $\boldsymbol{r}$ as shown for example by [Lacheisserie+ 1999], [Yung+ 1998] and [Landecker+ 1999] respectively. The corresponding relations are stated in equations (III.19) to (III.21). The symbol "$\hat{}$" stands for a normalized vector. In models, which are based on the interaction energy between magnetic particles and their equilibrium with elastic forces in the matrix, the determination of the macroscopic properties does not require the explicit resolution of local mechanical and magnetic fields ([Metsch+ 2016]).

$$e = -\frac{\mu_0}{8\pi} \boldsymbol{m}^{p_2} . \left[3\frac{(\boldsymbol{m}^{p_1} . \boldsymbol{r}\,)\boldsymbol{r}}{|\boldsymbol{r}\,|^5} - \frac{\boldsymbol{m}^{p_1}}{|\boldsymbol{r}\,|^3} \right] \tag{III.19}$$

$$\boldsymbol{F}^{p_2} = \frac{3\mu_0}{4\pi |\boldsymbol{r}|^4} \Big((\hat{\boldsymbol{r}} \times \boldsymbol{m}^{p_1}) \times \boldsymbol{m}^{p_2} + (\hat{\boldsymbol{r}} \times \boldsymbol{m}^{p_2}) \times \boldsymbol{m}^{p_1} - 2\hat{\boldsymbol{r}}(\boldsymbol{m}^{p_1} . \boldsymbol{m}^{p_2}) + 5\hat{\boldsymbol{r}}\Big((\hat{\boldsymbol{r}} \times \boldsymbol{m}^{p_1}) . (\hat{\boldsymbol{r}} \times \boldsymbol{m}^{p_2}) \Big) \Big) \tag{III.20}$$

$$\boldsymbol{T}^{p_2} = \frac{\mu_0 |\boldsymbol{m}^{p_1}| |\boldsymbol{m}^{p_2}|}{4\pi |\boldsymbol{r}\,|^3} \left[3(\hat{\boldsymbol{m}}^{p_1} . \hat{\boldsymbol{r}})(\hat{\boldsymbol{m}}^{p_2} \times \hat{\boldsymbol{r}}) + (\hat{\boldsymbol{m}}^{p_1} \times \hat{\boldsymbol{m}}^{p_1}) \right] \tag{III.21}$$

Analysis of dipole interactions can be found for example in the work of [Jolly+ 1996a] or [Lanotte+ 2004], which concern transversely isotropic structures with particles aligned in chains. In the work of [Lanotte+ 2004], the influence of an

external magnetic field on elongated magnetic particles is studied. The model applies to magnetically soft and hard particles showing a shape anisotropy. For this reason, the magnetic field and the magnetization of the particles have different orientations, which results in a magnetic torque. The elastic forces in the matrix are modeled by a torsional elastic coefficient. In the context of a small strain approximation and applied shear stress, it is shown that the stress-strain relation is dependent on the particle polarization and the distances between the particles in the chains inter alia.
An analytical, small strain homogenization model for statistically homogeneous materials has been presented by [Borcea+ 2001]. Spherical, magnetically soft particles are represented as magnetic dipoles in presence of an external magnetic field and distributed in a nonmagnetic matrix material. Since the particles are assumed magnetically and geometrically isotropic, magnetic torques are neglected and the coupling is based on interaction forces. The study contains an analysis of the interactions between two particles in an external magnetic field. It is shown, that the forces strongly depend on the orientation of the distance vector with respect to the magnetic field (figure III.6). Due to the dipole assumption, the authors expect a good accordance of the results for small particles, in which the magnetization is more likely to be uniform. It is also expected, that the model gives good results for large applied magnetic fields, for which the particles magnetically saturate. In addition to these limiting factors, the dipole assumption for magnetic particles is considered to be appropriate only for low volume fractions according to ([Metsch+ 2016]). To study the aspects, that are not accessible with the dipole approach, particles are modeled as continua in other studies.

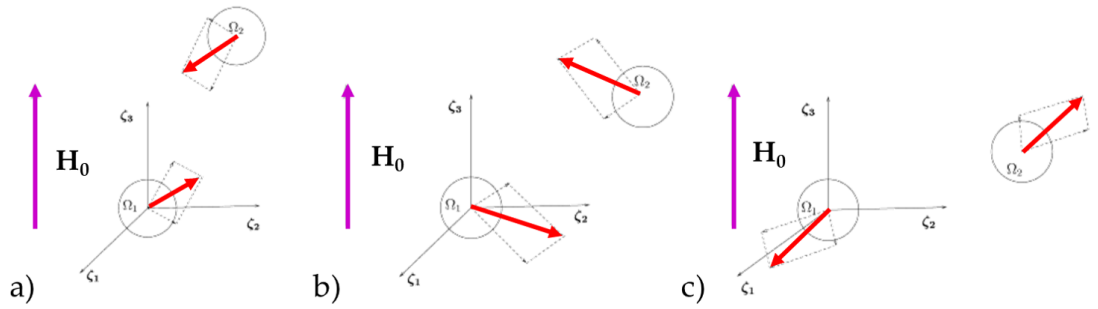

Figure III.6: Interaction forces (red arrows) between two ferromagnetic particles in a magnetic field H_0 for three different relative positions [Borcea+ 2001].

III.1.3.b Particles modeled as continua - Analytic models

The homogenization framework, presented by [Ponte Castañeda+ 2011], has been developed in the context of finite strains. The authors introduce a partial decoupling approximation for the magnetoelastic energy. The latter can be separated into a magnetic and a mechanical part according to the authors, when the magnetic energy of the composite does not depend on the local deformation of the matrix but only on the position and the orientation of the particles. The under-

lying assumptions for the decoupling are a magnetically neutral, relatively stiff matrix and mechanically rigid particles. Based on the study of a composite with ellipsoidal particles, subjected to a shear loading, the authors state that different microstructures show the same macroscopic magnetic behavior but a very different magnetoelastic behavior at the same time. According to the authors, the influence of magnetic torques on the magnetoelastic response should be stronger than the influence of dipole interactions. They refer to [Siboni+ 2012], who introduced a parameter κ, which puts the magnetic forces into a relation with the shear modulus G of the matrix: if $\kappa = |\boldsymbol{B}|^2/(2\mu_0 G) \ll 1$, the decoupling of magnetic and mechanical energy is exact according to [Ponte Castañeda+ 2011].
[Galipeau+ 2012] have used the model of [Ponte Castañeda+ 2011] in the context of small strains under the assumption of a nonlinear magnetic behavior. They study deals, inter alia, with the dependence of the effective magnetization and the magnetoelastic interactions on the particle form, the magnetic susceptibility and volume fraction. The particle form is stated to have no significant influence on the effective magnetization. It is furthermore shown, that an externally applied magnetic field causes a shift of the relation between the average strain and the surface traction on the boundaries of the microscopic subvolume. The shift increases with the applied magnetic field (cf.figure III.7 a) and depends on the shear modulus G of the matrix (soft matrix = strong shift, cf.figure III.7 b). A test with soft matrices shows, that the shift it is also dependent on the volume fraction (Φ high = strong shift) and on particle form (geometric anisotropy generally leads to stronger reaction).

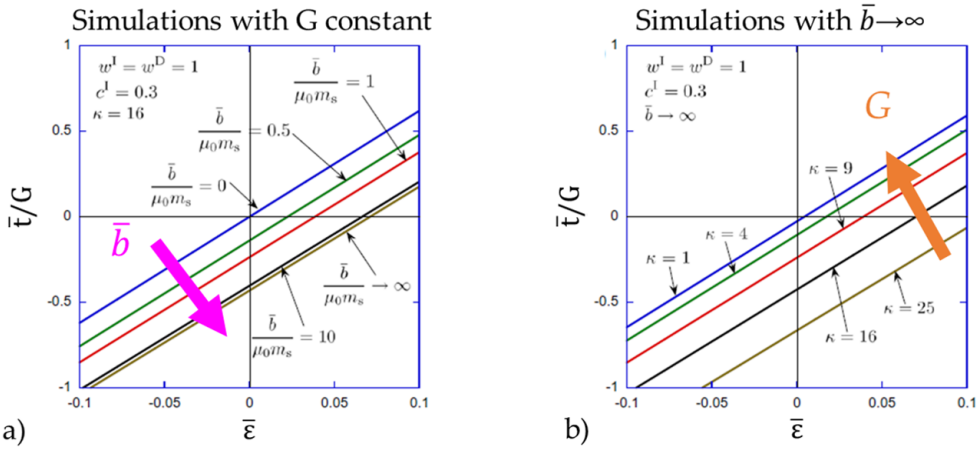

Figure III.7: Results obtained by [Galipeau+ 2012] for a composite with spherical particles, a matrix stiffness G subjected to uniaxial tension in a magnetic flux density $\bar{b}$: surface traction t on the composite boundary as a function of the strain ε for different $\bar{b}$ (a) and G (b).

The study of [Galipeau+ 2012] also shows, that composites with a nonlinear magnetic behavior show to two different regimes for the magneto-mechanical coupling: in small magnetic fields, their magnetic behavior is assumed to be linear. The

coupling is controlled by the magnetic permeability which leads to a strong coupling. When the particles saturate, the predominant parameters for the coupled behavior are the saturation magnetization and the distribution of the particles.
In an additional study, based on the homogenization framework of [Ponte Castañeda+ 2011] and carried out in the context of finite strain, [Galipeau+ 2013a] analyze RUC with an ellipsoidal inclusion subjected to a shear loading. It is shown, that the macroscopic magnetization is independent of the stretch in contrast to the magnetically induced torques. The magnetically induced deformation of the RUC is also analyzed and found to vary by a factor 4, depending on the orientation of the geometrically anisotropic particle with respect to the applied magnetic field. Based on these findings, the authors suggest optimized microstructures for soft actuators ("herringbone structures", cf. [Galipeau+ 2013b]). This example emphasizes, that the understanding of microstructural processes is important for the design of functional materials. According to [Galipeau+ 2013a], the magnetic interactions in 2D plain strain simulations (magnetizable fibers) presumably lead to stronger magnetically induced strains than 3D simulations with magnetizable particles.
[Galipeau+ 2014] have furthermore studied the magneto-mechanical coupling of RUC and RVE in the magnetic pre-saturation regime. The random microstructures is not represented explicitly but statistically (two-point statistical information). The authors introduce a coupling coefficient, which provides information about the magnetic contribution to the stresses in the composite. It is shown, that the coupling coefficient is independent from the stretch for the RVE and that the magnetic contribution to the modulus is weak in RVE in contrast to periodic structures. This result underlines the dependence of magnetoelastic coupling on the microstructure. In addition, it is stated that magneto-elastic effects are principally controlled by the distribution and to a lesser extent by the shape of the particles. As the composite is compressed, the distance between the particles is reduced. If the direction of the compression coincides with the direction of the magnetic field, the particles are moved closer together and the magnetic permeability increases [Galipeau+ 2014].

III.1.3.c Particles modeled as continua - Numerical models

Besides the analytic models, a variety of microscopically motivated numerical models has been presented. Numerical studies are often carried out in a 2D context in the view of the computational costs generated by 3D meshes. It is common to use periodic conditions on the boundaries of RVE: periodic displacements are forced in the mechanical domain and a periodic magnetic potential in the mechanical domain [Zabihyan+ 2018; Kalina+ 2020; Mukherjee+ 2020]. The examples stated in the following are based on 2D simulations with magnetically soft particles if not otherwise specified.
The study of [Metsch+ 2016] concerns the magnetostrictive effect in magnetically soft MAE. The model is based on a microscopically motivated continuum model and the computational homogenization scheme presented by [Spieler+ 2013]. The

model accounts for small strains and magnetically nonlinear behavior. During the study, the magnetically induced strain of different RUC is analyzed (cf. figure III.8). The tested unit cells have a nearly equivalent volume fraction but different microstructures. The results of the magnetically induced strain in the direction of the applied field show a clear dependence on the microstructure. It is furthermore shown, that the magnetic saturation of the particles reduces the magnetostriction.

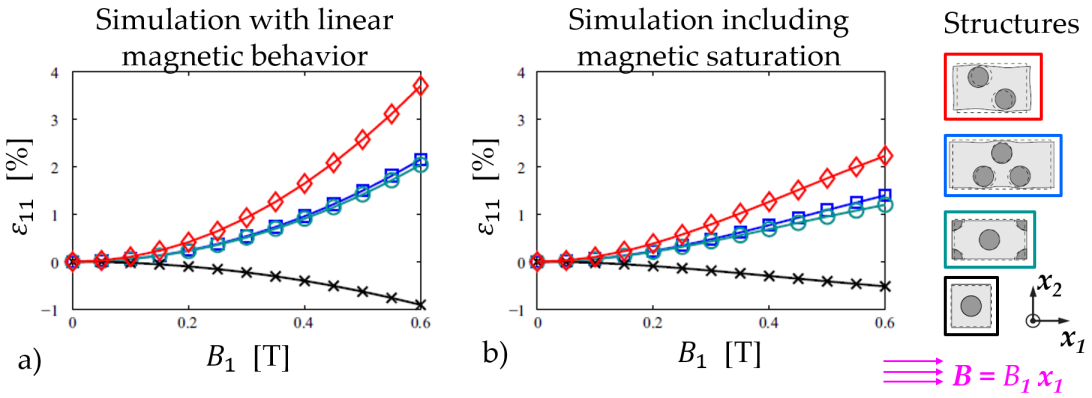

Figure III.8: Magnetostrictive strain as a reaction to an applied magnetic field for RUC with different microstructures and particles with a linear (a) and nonlinear (b) magnetic behavior, results obtained from simulations by [Metsch+ 2016].

Based on the microscopically motivated continuum approach by [Spieler+ 2013], finite element simulations have been carried out by [Kalina+ 2016] to study the effective magnetization and magnetostriction in MAE. The tests were performed for transversely isotropic microstructures, containing particles aligned chains, as well as isotropic microstructures with randomly distributed particles. The highest macroscopic magnetization in the pre-saturation regime is obtained, when the external magnetic field is aligned with the orientation of the particle chains in the transversely isotropic structures. This configuration locally strengthens the magnetic fields within the structure, as the particles are close to each other. The macroscopic magnetization is dependent on the direction of the applied external field in the transversely isotropic samples, which is not the case for the isotropic MAE. The dependence of the strain on the magnetic flux density in transversely isotropic composites is quadratic in the pre-saturation regime and saturates for stronger externally applied fields. It is pointed out by the authors, that the dependence of the stress on the magnetic flux density is also quadratic. For isotropic sample, an elongation in the direction of the magnetic field is observed. The finding is in accordance with experimental results and can be explained by the fact that the particles try to arrange in an energetically favorable configuration, where they are aligned in the direction of the magnetic field.
A microscopically motivated study of the hysteresis loop of a magnetically hard magnetoactive elastomer has been carried out by [Kalina+ 2017]. An RVE with randomly distributed particles is subjected to cyclic magnetic loading. The mag-

netic behavior of the particles is described by a phenomenological vector hysteresis model. The first three hysteresis loops for a mechanically soft ($E = 100\,\mathrm{kPa}$) MAE matrix reveal effects that have been observed experimentally : a strong decrease of the coercive field that stabilizes for repetitive loading (cf. figure III.9). According to the microscopic model, the magnetization of the particles is reversed by a combination of particle rotations and demagnetization.

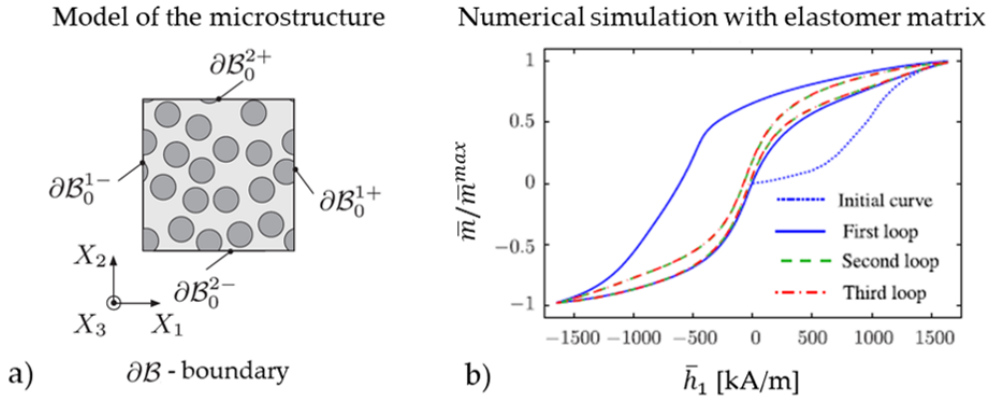

Figure III.9: Models of the microstructure (a) and average magnetization curves (b) obtained from the simulation of an H-MAE composite with hysteretic magnetic behavior by [Kalina+ 2020].

The aforementioned studies analyze the influence of local interactions on the effective material properties. Recent studies go a step further and include the identification of material properties by homogenization into macroscopic material models. The work of [Keip+ 2016] for example comprises a multiscale computational framework for the characterization of MAE. The boundary conditions of the coupled microscopic problem are defined with respect to geometry and loading case on the macroscopic scale. Based on the results of the microscopic problem, the average quantities of the mechanical stress and the magnetic flux density are assigned to the quadrature points of the macroscopic structure. The microscopic and the macroscopic problem are resolved numerically in an iterative manner and the incremental constitutive relations are presented in a form similar to piezoelectric behavior laws (cf. equation 47 in [Keip+ 2016]). A multiscale model, proposed by [Kalina+ 2020], comprises the determination of the effective mechanical and magnetic properties of MAE with a mechanically soft matrix. The coupled material behavior of 2D RVE with different volume fractions is analyzed by the help of different mechanical and magnetic load cases. The microscopic simulations are carried out in the saturation regime of the magnetically soft particles, where the magnetic behavior is assumed to be linear. The macroscopic constitutive equations are obtained by the method of Coleman/Noll where particle interactions are incorporated via a coupling term in the formulation of the free energy. The free energy of the coupling includes three parameters which are identified with the microscopic simulations for each volume fraction. The coupling parameters do not depend in the same manner on the volume fraction, which leads the authors to

the conclusion, that a uniform formulation of the macroscopic model including the volume fraction seems hardly possible.
A comparison of different modeling techniques for magnetically soft MAE has been performed by [Mukherjee+ 2020]. In a first step, phenomenological models are derived by the help of local energies. The models are constructed to recover the purely mechanical response, the nonlinear magnetization and the magnetorheological behavior obtained with an analytic model of [Lefèvre+ 2017]. A calibration of the phenomenological model based on 3D microscopic simulations of RVE is also presented. In this case, the results for parallel and transverse magnetostriction are in good accordance for volume fractions up to 20 %. The magnetization response of the RVE is found to be independent from the mechanical properties of the matrix.

III.1.4 Context and content of this chapter

One focus of this PhD thesis is the determination and the estimation of the material properties of a specific magnetically hard and mechanically stiff magnetoactive elastomer (stH-MAE). Some of its material properties have been revealed by the experimental work, presented in the previous chapter. In addition, a numerical multi-scale model for the material behavior of the magnetized composite with isotropic structure has been developed and will be presented in this chapter. A graphic representation of the different parts of the model is shown in figure III.10 and the content of this chapter is summarized in the following.
The model contains an explicit representation of the microstructure and includes the magneto-mechanical coupling on the **microscopic scale**. To enhance the understanding of the particle interactions, a microscopic study on two magnetic particles in an elastomer matrix is presented prior to the work on multi-particle RVE. In contrast to numerical models for S-MAE, the particles in this work are permanently magnetized. The magnetization generates mechanical constraints in the material even without an external mechanical loading. This is indicated, inter alia, by the results of [Galipeau+ 2012] for S-MAE magnetized in an external field without mechanical loading (cf. figure III.7 a). This initial state, generated by the particle magnetization in H-MAE, is considered as the equivalent of an operating point of the composite in the present study. The model on the macroscopic scale is supposed to describe the behavior on vicinity of the operating point.
The effective material properties are obtained by a **homogenization** procedure based on average field quantities in statistically homogeneous RVE with periodic boundary conditions. The same homogenization approach has been used in prior studies but is integrated in a different framework in this study. The effective properties of the initial state, the mechanical domain, the magnetic domain and the coupling are obtained subsequently by different load cases. The effective properties are compared to the results of the experimental characterization.
On the **macroscopic scale**, the effective properties are used to establish a piezo-like coupled behavior law (cf. [Electrical+ 1990] for example). A small strain approach has been chosen in the mechanical domain due to the stiffness of the

matrix. In addition, the loading is kept small to moderate during the study. From a magnetic point of view, the composite is modeled in its magnetized state in vicinity of its operating point where the magnetic behavior is supposed to be linear for small loadings. The model is tested for different load cases and the results are compared to numerical simulations with heterogeneous RVE.

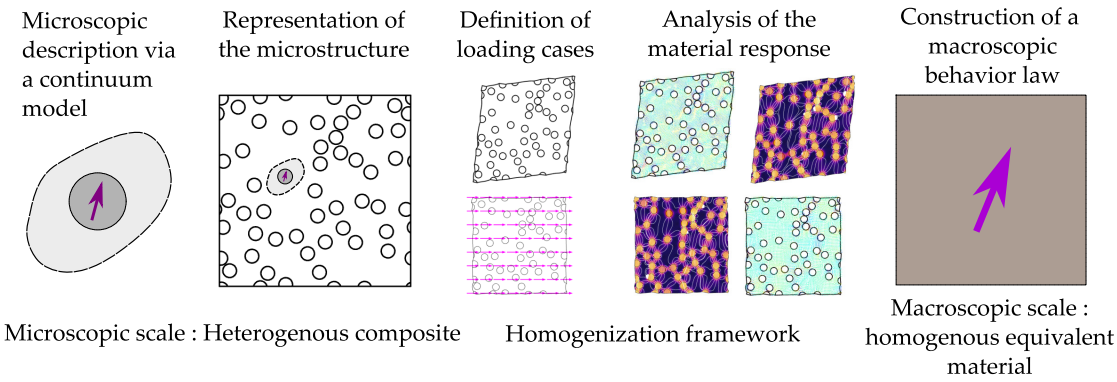

Figure III.10: Summary of the different parts of the multiscale model.

III.2 Modeling on the microscopic scale

This section puts the focus on the microscopic description of the composite. The continuum model, used on this scale, is presented in the first part. Afterwards, studies on the magneto-mechanical interactions between two magnetized particles in absence of an external loading are presented. The aim of the corresponding part of this chapter is to provide a better understanding of the local interactions to facilitate the interpretation of the effective macroscopic behavior. The interaction between two magnetic particles is studied with the numerical model and an analytical dipole approach at first. Afterwards, the effect of the magnetomechanical interactions on the stress in the matrix around the particles is analyzed.

III.2.1 Continuum model

On the microscopic scale, the matrix and the particles are modeled as deformable continua which are perfectly in contact. A stationary regime is supposed for both physical domains, hence creep or relaxation phenomena are not considered in the mechanical domain and a quasi-static magnetic state in absence of electric currents is assumed. The composite, studied in this chapter, consists of two phases: the particles ($\varphi = p$) and the elastomer matrix ($\varphi = e$). Local quantities, associated to a phase, are denoted with the exponent φ on the left of the quantity in the following (e.g. ${}^{\varphi}\boldsymbol{H}$ for the magnetic field in the phase φ). Figure III.11 shows a schematic drawing of a particle magnetized surrounded by a matrix material.

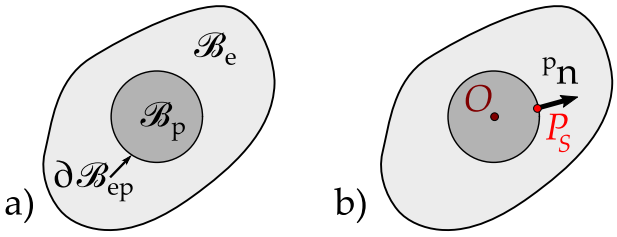

Figure III.11: Schematic representation of a particle surrounded an elastomer matrix, indicating the particle and elastomer domains, $\mathscr{B}_p$ and $\mathscr{B}_p$ respectively, and the interface $\partial\mathscr{B}_{ep}$ (a) as well as the center of gravity O, a point P_S on the boundary and the surface normal $^p\boldsymbol{n}$ of the particle.

The governing equations, valid in the domains of the corresponding phases are stated in the following along with the material models. The magnetic flux is conserved by Gauss's law for magnetism (equation (III.22)). The absence of currents allows the definition of a magnetic scalar potential $^\varphi\psi$ which is related to the magnetic field $^\varphi\boldsymbol{H}$ by equation (III.23). External magnetic fields $^\varphi\boldsymbol{H}^{ext}$ contribute to the overall field $^\varphi\boldsymbol{H}$ in a linear manner. The magnetic behavior of all constituents is assumed to be linear. In this case, the relation between the magnetic field and the magnetic flux density $^\varphi\boldsymbol{B}$ is established by the permeability tensor $^\varphi\mathbb{\mu}$ which is the product of the magnetic constant μ_0 and the relative permeability tensor $^\varphi\mathbb{\mu}_r$. The materials parameters, used in the study, are summarized in table III.1. Additionally, a residual magnetic flux density $^\varphi\boldsymbol{Br}$ is defined for the magnetized particles. Equation (III.24) can be applied to describes the behavior of both phases with $^\varphi\boldsymbol{Br} = \boldsymbol{0}$ for the matrix. The linear behavior of the matrix material can be justified with its magnetically neutral behavior. For the magnetic inclusions, the material model is valid since the particles are already magnetized and the hysteresis loop in vicinity of the residual flux density evolves in a quasi-linear manner. Besides the magnetization of the particles, an isotropic material behavior is assumed for both materials.

$$div(^\varphi\boldsymbol{B}) = {}^\varphi B_{i,i} = 0\ , \tag{III.22}$$

$$^\varphi\boldsymbol{H} = \boldsymbol{grad}(^\varphi\psi) + {}^\varphi\boldsymbol{H}^{ext} = {}^\varphi\psi_{,i} + {}^\varphi\boldsymbol{H}^{ext}\ , \tag{III.23}$$

$$^\varphi\boldsymbol{B} = {}^\varphi\mathbb{\mu} \cdot {}^\varphi\boldsymbol{H} + {}^\varphi\boldsymbol{Br}\ . \tag{III.24}$$

In continuum mechanics, Cauchy's equation reduces to equation (III.25) for the stationary case in absence of volume forces. The mechanical stress $^\varphi\sigma$, for small strains, has thus to be continuous on a boundary between two materials. The strain $^\varphi\varepsilon$ derives from the displacement $^\varphi\boldsymbol{u}$ as shown in equation (III.26). For an isotropic linear elastic behavior, the strain tensor $^\varphi\varepsilon$ is linked to the stress tensor by the stiffness tensor $^\varphi\mathcal{C}$ in each phase (equation (III.27)). The materials are assumed to be mechanically isotropic, hence the stiffness tensor is defined by the Young's modulus E and the Poisson's ratio ν shown in table III.1.

$$\boldsymbol{div}({}^{\varphi}\sigma) = {}^{\varphi}\sigma_{ij,j} = 0 \,, \tag{III.25}$$

$${}^{\varphi}\varepsilon = \frac{1}{2}\Big(\boldsymbol{grad}(\boldsymbol{u}) + \boldsymbol{grad}(\boldsymbol{u})^{\mathrm{T}}\Big) = \frac{1}{2}({}^{\varphi}u_{i,j} + {}^{\varphi}u_{j,i}) \,, \tag{III.26}$$

$${}^{\varphi}\sigma = {}^{\varphi}\mathcal{C} : {}^{\varphi}\varepsilon \,. \tag{III.27}$$

The jump of magnetic stress tensor $[[\mathbb{T}]]$ over the material interface between the particles and the matrix $\partial\mathscr{B}_{ep}$ is established as a magneto-mechanical boundary condition on the surface of the particle (cf. section I.3.3, equation (I.80)) :

$$[[\,\sigma + \mathbb{T}\,]] \cdot \boldsymbol{n} = ({}^{e}\sigma + {}^{e}\mathbb{T} - {}^{p}\sigma - {}^{p}\mathbb{T}) \cdot {}^{p}\boldsymbol{n} = \boldsymbol{0} \quad \text{on } \partial\mathscr{B}_{ep} \,, \tag{III.28}$$

where e and p designate the elastomer and the particle phases respectively. The equivalent force $\boldsymbol{F}^{em}$, acting on the particle's center of gravity O, and the equivalent torque $\boldsymbol{T}_O^{em}$ around O are obtained according to equations (III.29) and (III.30), as shown in section I.3.2:

$$\boldsymbol{F}^{em} = \oint_{\partial\mathscr{B}} {}^{e}\mathbb{T} \cdot {}^{p}\boldsymbol{n} \, \mathrm{d}S \,, \tag{III.29}$$

$$\boldsymbol{T}_O^{em} = \oint_{\partial\mathscr{B}} \overrightarrow{OP_S} \times ({}^{e}\mathbb{T} \cdot {}^{p}\boldsymbol{n}) \, \mathrm{d}S \,. \tag{III.30}$$

Material	E [MPa]	ν	μ_r	$\lvert\boldsymbol{Br}\rvert$ [T]
Matrix	1.4	0.49	1	0
Particles	110 000	0.3	1.1	0.8

Table III.1: Material properties used for the simulation.

III.2.2 Modeling of 2-particle cases

This paragraph deals with the magnetomechanical interactions between two magnetized particles in absence of external magnetic fields. The first study focuses on the interaction between the particles and the second on the stress state in the matrix, generated by the permanent magnetization.

III.2.2.a Magneto-mechanical interactions between the particles

The interactions are studied for two spherical particles, p_1 and p_2 with a radius of $R = 2.5\,\mu\mathrm{m}$. Particles p_1 is placed at the position $\boldsymbol{r}_1 = [0\ 0\ 0]$ m. Particle p_2 is placed at a distance of $d = 11\,\mu\mathrm{m}$ with respect to particle p_1 at the position $\boldsymbol{r}_2 = d \cdot [sin(\theta)\ cos(\theta)\ 0]$. θ corresponds to the angle between the vector $\boldsymbol{r}$, pointing from p_1 to p_2, and the magnetization in the $\boldsymbol{e}_1 - \boldsymbol{e}_2$ plane. The residual flux density

$\boldsymbol{Br}$ of the particles is oriented in the direction $\boldsymbol{e}_2$. When the angle θ is altered, the orientation of p_2 with respect to particle p_1 changes but the distance is kept constant. Figure III.12 a shows two different configurations: $\theta = 0°$ and $\theta = 45°$. The problem is implemented in a numerical code and resolved with two different methods for comparison: the finite element method (FEM) and the boundary element method (BEM). For the boundary element method, only the surface of the particles is meshed, while during the FEM simulations the volume of the particles and an air volume, in which the magnetic flux propagates are meshed. For this reason, there is a significant difference on the number of elements as table III.2 shows. During the simulations, θ was increased by 5° so 37 simulations were performed with each method. The element size in both simulations lay between 20 nm and 1 µm.

Method	domain elements	boundary elements	edge elements
FEM	92 215 513	78 598	1 140
BEM	8 234	1 160	192

Table III.2: Mesh characteristics of FEM and BEM for the simulation of two magnetic particles

In addition to the numerical calculations, the same study was performed by the help of magnetic dipoles $\boldsymbol{m}$. The dipole moment of the two particles is identical and measures 12.22 $\mathrm{mT/\mu m^3}$. The analytic expressions for the interaction energy, as well as the force and torque, acting on particles p_2 due to the interaction with p_1, were calculated according to equations (III.19) to (III.21) by the help of Matlab. The analytic result for the **interaction energy** e is shown as a function of θ in figure III.12 b . The continuous function shows minima for two configurations : $\theta = 0°$ and $\theta = 180°$. The result shows that equilibrium configurations are obtained, when the magnetic moments of the particles are aligned. Two maxima can also be observed for the energy function, they appear for $\theta = 90°$ and $\theta = 270°$. In these configurations, the magnetic moments are aligned in the direction perpendicular towards their orientation. The maxima indicate that these two configurations are also equilibrium configurations but in the contrary to the other arrangements, these two are unstable. Due to the geometric symmetry, The results in the range of $0° \leq \theta < 180°$ correspond to the results in the range of $180° \leq \theta < 360°$.
The in-plane components of the interaction **forces** acting on particle p_2, are shown in figure III.13 as a function of the angle θ. The results of the dipole model as well as from the FEM and BEM simulations are included in the two graphics on the left. The graphic on the right visualizes the position of dipole 1 and 2 for each angle θ and the force acting on p_2 calculated with the analytic expression. The results for the dipole model and the BEM simulation match perfectly while the FEM results show small differences. Assuming that the analytic model gives the correct response, the reason for the difference is probably due to the mesh of the air volume that influenced the calculation of the magnetic flux propagation.

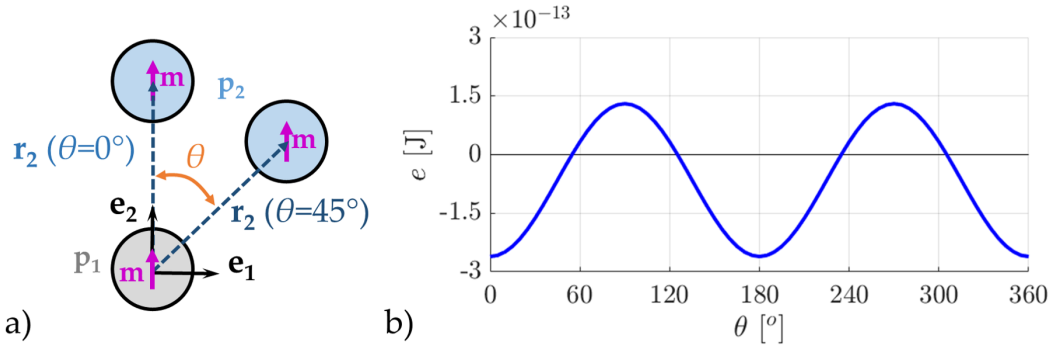

Figure III.12: Schematic representation of the 2 – particle study and results for the interaction energy between the two particles as a function of the angle θ between their alignment and their magnetic moment.

Nevertheless, all results vary in the same manner with the angle θ. The force component in the direction $\boldsymbol{e}_1$ reaches its maximum absolute value at $\theta = 30°$ and $\theta = 150°$. The maxima of the force component in direction $\boldsymbol{e}_2$ are located at $\theta = 0°$ and $\theta = 180°$. The forces acting on p_1 ($\boldsymbol{F}^{p1}$) and on p_2 ($\boldsymbol{F}^{p2}$) are oriented in the opposite direction. In general, attractive forces between the particles appear when the magnetic moments are aligned in the direction of their orientation and repulsive forces appear when the momenta are aligned in the direction perpendicular towards their orientation.

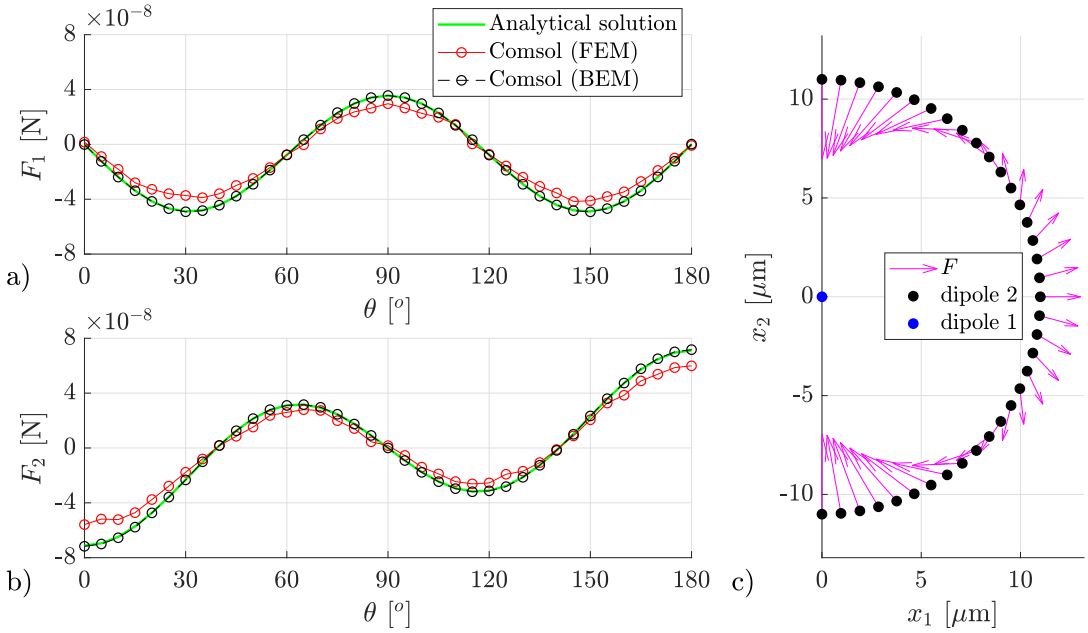

Figure III.13: Components of the force on particle 2 in the $\boldsymbol{e}_1 - \boldsymbol{e}_2$ plane calculated in FEM and BEM simulations and with the dipole model represented as a function of θ (a,b) and in the $\boldsymbol{e}_1 - \boldsymbol{e}_2$ plane (c).

The turning points for which the repulsion switches to attraction have also been calculated analytically for magnetized particles by [Borcea+ 2001]. The findings of this study correspond to the results presented in the analytic study.
The **torque** is generated by the interaction of the magnetic moment with the magnetic flux density (equation (III.21)). The torque, acting on p_2, calculated by the BEM simulation and with the dipole model, are shown in the left graphic of figure III.14, they are almost identical. The torque reaches its maximum values for the angles $\theta = 45°$ and $\theta = 135°$. The torque is equal to zero when the magnetic moments are aligned in the direction of their orientation or perpendicular to it. The evolution of the torque is the same for p_1 and p_2. The results show, that magnetic moments tend to align their orientation.

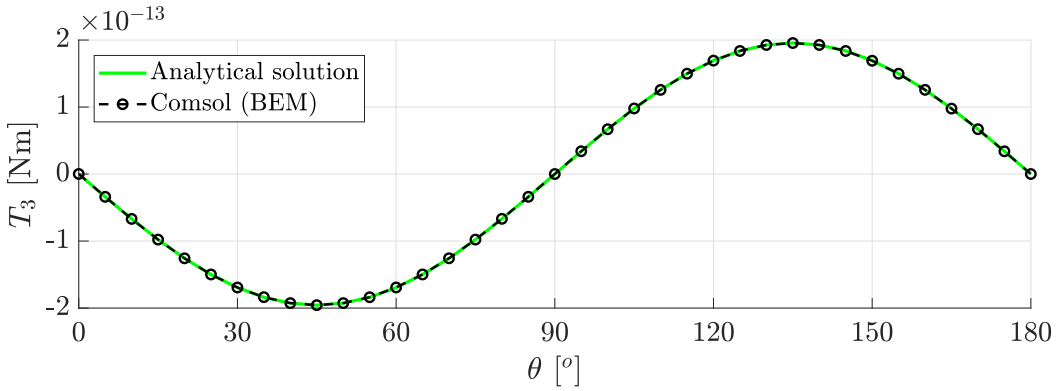

Figure III.14: Components of the torque on particle 2 in the direction $\boldsymbol{e}_3$ calculated by the help of FEM and BEM simulations and with the dipole model represented as a function of θ.

Due to the different meshing methods, the number of elements is drastically reduced for the BEM simulation in comparison to the FEM simulation (cf. table III.2). This also influences the calculation time, the FEM simulation took 12 hours, the BEM simulation only took 14 minutes. The calculation with Matlab was performed in less than 1 second.

III.2.2.b Stress state in a matrix generated by magneto-mechanical interactions of magnetized particles

Since the two particles in the previous study were aligned in one plane, the torque only showed an out of plane component. To demonstrate the influence of the particle interactions on the mechanical stress state in the matrix, a two-dimensional model with a plane stress approximation is used in the following. Figure III.15 shows the model which comprises two particles and the matrix. The matrix is separated in two parts which allows the refinement of the mesh in vicinity of the particles without a big increase in calculation time. The outer boundaries of the elastomer are fixed and magnetically shielded. To avoid an interference of the particle interactions with the boundary conditions, the radius of the elastomer sphere is chosen ten times larger than the particles radius. The particles are

magnetized in the $\boldsymbol{e}_2$-direction. The study comprises three particle configurations, which have also been part of the previous study: θ was set to 0°, 45° and 90°. The angle θ is formed between the e_2-axis and the direction of alignment of the particles.

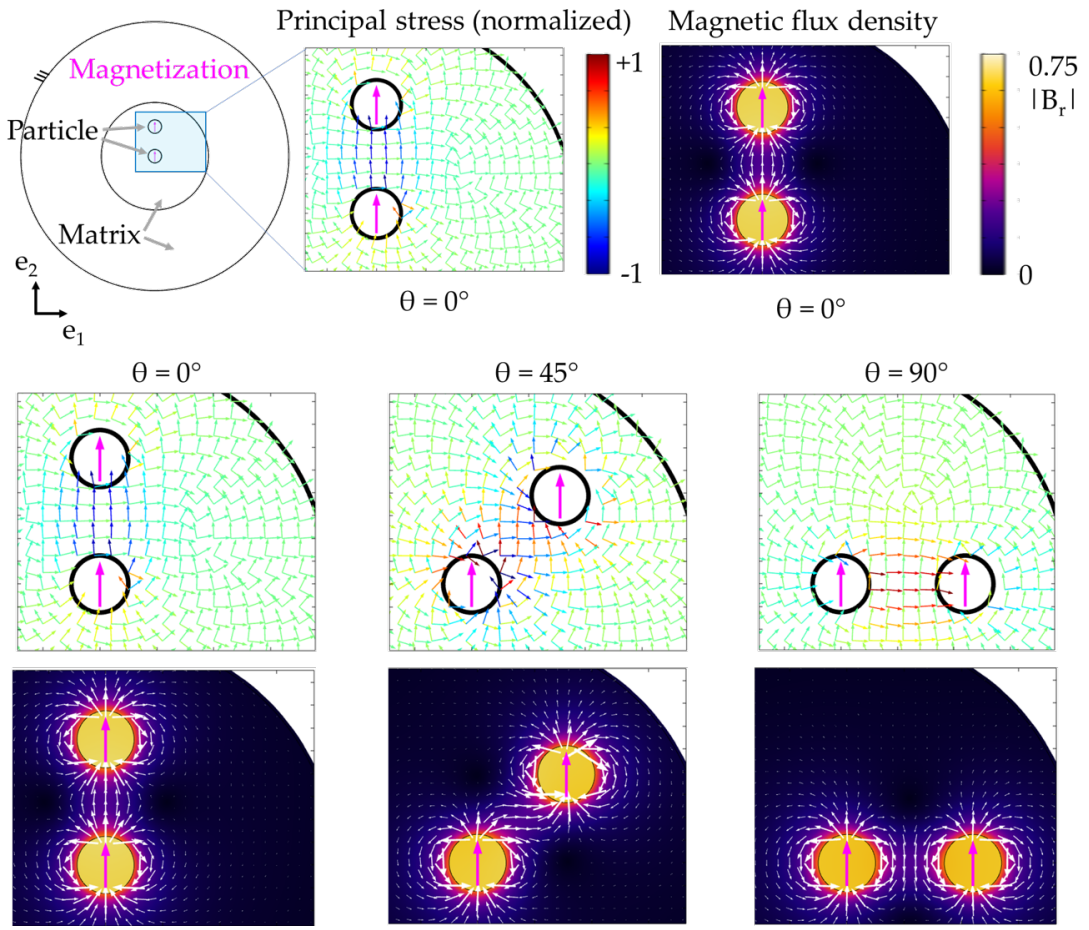

Figure III.15: Numerical results of the local principal stresses and the magnetic flux density resulting from the magnetomechanical interaction of two magnetized particles in a nonmagnetic matrix in three different configurations.

Figure III.15 also shows the principal stresses in the matrix in vicinity of the particles. It has been stated before, that particles, which are aligned in their direction of magnetization, attract each other. As shown in the upper left diagram of figure III.15, the matrix between the particles is compressed as a consequence. In a configuration where θ measures 45°, the magnetic torque reaches its maximum. Both particles turn in the same direction to align their magnetic moments. The rotation of the particles creates a movement in the matrix that induces a shear stress. When θ corresponds to 90°, the particles are aligned in the direction perpendicular to their magnetization. The resulting repulsive forces increase the distance between them and the matrix is stretched. The particle interactions are qualitatively equivalent to the interactions found for the corresponding configura-

tions in the previous section.
The magnetic flux density is also shown in figure III.15. The coloring represents the norm of the magnetic flux density and the white arrows indicate the orientation of the local magnetic flux density. The intensity of the magnetic flux density is proportional to the size of the arrows. A part of the magnetic flux propagates in closed loops around a particle but the interaction of the magnetic fields of both particles is present for all configurations. Between the particles, the magnetic flux, emanating from the lower particles propagates towards the upper particle for $\theta = 0°$ or $45°$. When the particles are aligned perpendicularly to the direction of magnetization, the magnetic flux between them propagates in the direction inverse to the magnetization. The magnetic flux density in the particles is nearly homogeneous in all three cases. Nevertheless, depending on the arrangement of the particles, they mutually strengthen or weaken their magnetization. When the emanated magnetic field and the magnetization have the same orientation, a field strengthening effect occurs (cf. $\theta = 0°$). In the opposite case (cf. $\theta = 90°$), the magnetization is weakened.

III.2.2.c Conclusions

The two examples show that different magnetic and mechanical states are created in a composite material depending on the arrangement of the magnetic inclusions. In the presented case, the two particles have an equal direction of magnetization, after the analysis of particle interactions the stress states in the matrix can be determined intuitively. Besides the fact that the interaction of only two particles has been analyzed here, the study furthermore comprises many assumptions like the in-plane stress state and magnetic field quantities as well as circular inclusions. Transverse contraction of the matrix and the propagation of the magnetic field in three spatial directions create more complicated local states of the composite material. The generation of microstructures with more than two inclusions is presented in the following section.

III.2.3 Automated generation of random microstructures

The two – particle studies are interesting study cases; however, the determination of effective properties requires the representation of microstructures with more than two particles. For the numerical studies, the parametric finite element calculations are controlled by Matlab to generate the microstructure. Material parameters and the characteristic length of the particles and the matrix as well as the volume fraction are the input data for the automatic generation of a study. In the first step, the random positioning of the particles in the matrix is realized. A random number generator in Matlab (rng('shuffle')) generates a set of particle radii. They are distributed on the basis of a normal distribution with a mean value and a standard deviation. The mean value is set to 2.5 µm which corresponds to the mean value of the particles size distribution (PSD50) for the particles used in the experiments (cf. chapter II). The standard deviation can either be used to

distribute the particles size or be set to zero, in which case all particles have the same size. A subset of radii is generated and particles from the first set are added until the volume fraction is reached. Afterwards, the positions of the particles are generated. The first particle is always placed in the center of the matrix. To place the remaining particles, a set of random positions in the matrix volume is generated. The positions are tested one after another on the possibility of overlapping with the already positioned particles. If no intersection with any existing particle is detected, a new particle is placed. If the center of a particle is close to a boundary, a part of the particle lies outside the RVE. For the generation of a periodic cell it is necessary to duplicate the protruding part of the particle on the opposite boundary and to cut the parts that lie outside the matrix. Particles placed in corners are duplicated 7 times (3 times in 2D simulations). Different types of microstructure that can be generated by the algorithm are represented in figure III.16. Figure A.1 in the appendix resumes the algorithm used to generate the particles and their positions in a flow chart. The algorithm has been adapted to the generation of 2D and 3D models.

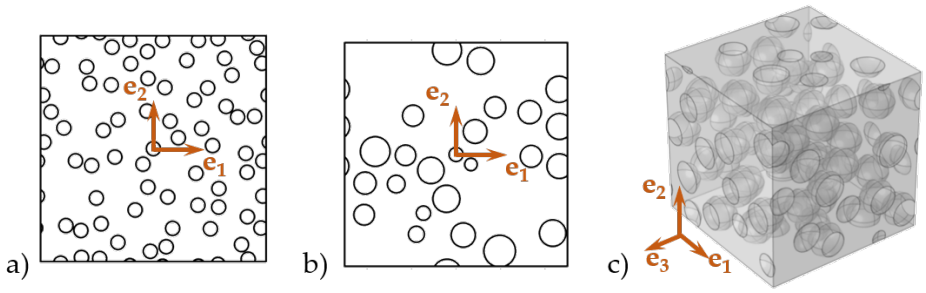

Figure III.16: Different microstructure types: 2D – uniform particles size (a), 2D – distributed particle size (normal law) and 3D – uniform particles size (c).

Once the geometry is generated, the material properties shown in table III.1 are assigned to the corresponding domains by the algorithm. The magnetic behavior is supposed isotropic, the permeability tensor reduces hence to a constant: the relative permeability μ_r. All particles are supposed to be magnetized in the same direction. The magnetic potential is set to zero in the center of the RVE as a reference. On the boundary of each particle, the jump of the Maxwell stress tensor is calculated. In the software, this calculation is realized in the magnetic domain and the resulting stress tensor is applied as boundary load on the particles in the mechanical domain.
The local stress state generated by the magnetization of randomly dispersed particles in a 2D cell with plain stress approximation is exemplarily shown in figure III.17 a. For isolated particle pairs, the local states of the previous study can be observed. Depending on the alignment of the particles, compression, traction or shear stress is induced in the matrix and the local stress state depends strongly on the microstructure. The norm of the magnetic flux density (coloring) as well as the flux lines (white lines) are presented in figure III.17 b. The flux mainly propagates in the $\boldsymbol{e}_2$ direction, which corresponds to the direction of magnetiza-

tion of the particles. It emerges from one particle and propagates towards the next particles present following the $\boldsymbol{e}_2$ direction. The color gradient in the particle domains shows, that the flux density in the particles is not always uniform. The homogenization framework, which is used to model inter alia the continuity of the magnetic flux is presented in the following section.

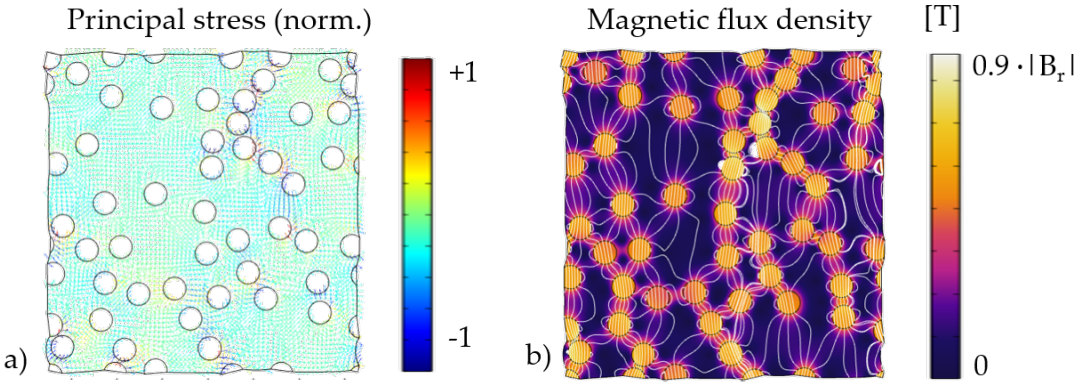

Figure III.17: Local principal stress (a) and magnetic flux density (b) in a two dimensional RVE with randomly dispersed particles.

III.3 Scale transition

In this section, the definition of the scale transition and its application are presented. In the first part, the mechanical and magnetic loading and the boundary conditions for the statistically homogeneous RVE are outlined. The determination of the effective properties and the case studies are presented. The following four parts deal with the determination of the initial state of the RVE, generated by the magnetization, the mechanical properties, the magnetic properties and the coupling in RVE with two different volume fractions. The convergence of the effective properties with the number of the particles is studied for the four characteristics.

III.3.1 Multi-physical homogenization framework

In this section, the definition of boundary conditions and loading is presented as well as the approach for the determination of the effective properties. The study cases, analyzed in the following sections, are introduced at the end of the section.

III.3.1.a Boundary conditions and loading

Periodic boundary conditions are used to model the continuity of the local displacement field ${}^{\varphi}\boldsymbol{u}$ in the mechanical domain. They are applied to the two pairs of opposite, outer boundaries of the heterogeneous cells. In addition, the mechanical loading is defined by an average strain tensor ε. The displacement of a boundary

$\boldsymbol{u}(\partial\mathscr{B}^+)$ is described by equation (III.14). To study the behavior of a cell due to internal constraints generated by the magnetization, the boundaries are left free to deform and the boundary conditions reduce to equation (III.31).

$$^{\varphi}\boldsymbol{u}(\partial\mathscr{B}^+) = {}^{\varphi}\boldsymbol{u}(\partial\mathscr{B}^-) \ . \tag{III.31}$$

In the magnetic domain, the loading consists of a homogeneous external magnetic field $\boldsymbol{H}^{ext}$. The expression for the magnetic field on the outer boundaries (as well as in the domains) is given in equation (III.32). Additionally, a continuous magnetic scalar potential $^{\varphi}\psi$ is defined on opposite boundaries according to equation (III.33).

$$^{\varphi}\boldsymbol{H} = \nabla.\,{}^{\varphi}\psi + \boldsymbol{H}^{ext} = {}^{\varphi}\psi_{,i} + \boldsymbol{H}^{ext} \ , \tag{III.32}$$

$$^{\varphi}\psi(\partial\mathscr{B}^+) = {}^{\varphi}\psi(\partial\mathscr{B}^-) \ . \tag{III.33}$$

The mesh is defined in the next step. In a first step, the boundaries are meshed. The mesh on opposite boundaries is identical to assure the periodic displacement of the mesh nodes. Boundaries and volumes are discretized with a triangular mesh. The studies are carried out in a stationary regime and geometric non-linearities are included. This step is necessary to correct the magnetic constraints: when the matrix is deformed, the distances between the particles change. This, in turn, changes the distribution of the magnetic flux and in consequence the resulting magnetically induced stresses. The mechanical and magnetic calculations are repeated in an iterative manner until the state of both domains is sufficiently close to the equilibrium state.

III.3.1.b Effective properties

The numerical simulations are used to determine the local physical quantities $^{\varphi}\varepsilon$, $^{\varphi}\sigma$, $^{\varphi}\boldsymbol{H}$ and $^{\varphi}\boldsymbol{B}$ in the composite. The average quantities, ε, σ, $\boldsymbol{H}$ and $\boldsymbol{B}$, are obtained by a volume average in the cell. Based on these average quantities, the effective mechanical stiffness tensor $\mathcal{C}$ and the effective magnetic permeability tensor $\mathbb{\mu}$ are obtained and used to establish the behavior law of the equivalent homogeneous material. In the present study, the coupling is modeled as linear contribution to the loading state. Details about the macroscopic model, also called piezomagnetic behavior law, and its derivation are given in the following section while this section puts the focus on the determination of the effective properties. However, an overview over the relation between the physical quantities is provided here to clarify the following steps. In the model, variations of the strain ($\Delta\varepsilon$) or the magnetic field ($\Delta\boldsymbol{H}$) lead to variations of the stress and the magnetic field ($\Delta\sigma$, $\Delta\boldsymbol{B}$) which according to the following relations:

$$\Delta\sigma = \mathcal{C} : \Delta\varepsilon + \mathbb{d} \cdot \Delta\boldsymbol{H} \ , \qquad \Delta\boldsymbol{B} = \mathbb{\mu} \cdot \Delta\boldsymbol{H} - \mathbb{d}^{\mathrm{T}} : \Delta\varepsilon \ , \tag{III.34}$$

where the third order tensor $\mathbb{d}$ accounts for the coupling.

The relations in equation (III.34) describe variations. However, the magnetization of the particles generates initial constraints in the material. This initial state is called Operating Point (OP) in the following and comprises the strain ε^{OP}, the stress σ^{OP}, the magnetic field $\boldsymbol{H}^{OP}$ and the magnetic flux density $\boldsymbol{B}^{OP}$. The behavior law for the absolute stress and magnetic flux density requires the addition of the initial state and is described by the following relations:

$$\Delta\sigma + \sigma^{OP} = \mathcal{C} : (\Delta\varepsilon + \varepsilon^{OP}) + \mathbb{d} \cdot (\Delta\boldsymbol{H} + \boldsymbol{H}^{OP}) \,, \tag{III.35}$$

$$\Delta\boldsymbol{B} + \boldsymbol{B}^{OP} = \mathbb{\mu} \cdot (\Delta\boldsymbol{H} + \boldsymbol{H}^{OP}) - \mathbb{d}^{\mathrm{T}} : (\Delta\varepsilon + \varepsilon^{OP}) \,. \tag{III.36}$$

Consequently, the initial constraints in the material have to be determined prior to the material properties to subtract their effect from the constraints generated by the loading. After the determination of these characteristics, the mechanical and the magnetic properties are determined in a second and third step. For this purpose, the composite is subjected to a loading in one physical domain and the reaction of the material is evaluated in the same physical domain. The operating point is included in the loading and hence also contained in the results:

$$\Delta\varepsilon + \varepsilon^{OP} \rightarrow \Delta\sigma + \sigma^{OP} \qquad \text{and} \qquad \Delta\boldsymbol{H}^{ext} + \boldsymbol{H}^{OP} \rightarrow \Delta\boldsymbol{B} + \boldsymbol{Br} \,. \tag{III.37}$$

To determine the coupling in the next step, the heterogeneous volume is subjected to a loading in one of the physical domains and the material behavior in the complementary physical domain is evaluated:

$$\Delta\varepsilon + \varepsilon^{OP} \rightarrow \Delta\boldsymbol{B} + \boldsymbol{B}^{OP} \qquad \text{and} \qquad \Delta\boldsymbol{H}^{ext} + \boldsymbol{H}^{OP} \rightarrow \Delta\sigma + \sigma^{OP} \,. \tag{III.38}$$

The relations in equation (III.38) show, that the coupling tensor can be analyzed by varying $\boldsymbol{H}$ or ε. The coupling tensors, determined for a constant magnetic field and a constant mechanical strain are called $\mathbb{d}^{H}$ and $\mathbb{d}^{\varepsilon}$ respectively in the following. Table III.3 summarizes the different study steps, which are detailed later in this section.

Study steps		Loading	Reaction	Property
1	Operating point	$\boldsymbol{B}_r$	ε^{OP}, σ^{OP}, $\boldsymbol{H}^{OP}$, $\boldsymbol{B}^{OP}$	–
2	Mechanical properties	$\varepsilon = \Delta\varepsilon + \varepsilon^{OP}$	$\sigma = \Delta\sigma + \sigma^{OP}$	C
3	Magnetic properties	$\boldsymbol{H} = \Delta\boldsymbol{H} + \boldsymbol{H}^{OP}$	$\boldsymbol{B} = \Delta\boldsymbol{B} + \boldsymbol{B}^{OP}$	$\mathbb{\mu}$
4a	Coupled behavior	$\varepsilon = \Delta\varepsilon + \varepsilon^{OP}$	$\boldsymbol{B} = \Delta\boldsymbol{B} + \boldsymbol{B}^{OP}$	$\mathbb{d}^{H}$
4b		$\boldsymbol{H} = \Delta\boldsymbol{H} + \boldsymbol{H}^{OP}$	$\sigma = \Delta\sigma + \sigma^{OP}$	$\mathbb{d}^{\varepsilon}$

Table III.3: Summary of the study steps performed to determine the effective material properties.

III.3.1.c Study cases and load cases

The study cases, analyzed in the following sections, are based on quadratic 2D RVE for which a plain stress and an in-plane magnetic field approximation are used. The circular inclusions have a radius of 2.5 µm. All inclusions have the same size and are dispersed randomly in the composite. Two different volume fractions are studied, Φ measures either 20% or 36%. Convergence studies of the effective properties are carried out for the two volume fractions. Therefore, the size of the cells is increased while the particles size and the volume fraction are kept constant. Figure III.18 exemplary shows four microstructures with a volume fraction of $\Phi = 20\%$. For this volume fractions, the effective properties of 20 different volume elements containing 9, 25, 49 and 65 inclusions respectively are calculated. The size of the composite cell is increased to increase the number of particles while the particle size is kept constant. For $\Phi = 36\%$, the study of the effective properties is based on 20 volume elements with 16, 45 and 89 inclusions respectively. All in all, the study comprises 140 the analysis of microstructures with randomly dispersed particles. The particles are magnetized in the direction $\boldsymbol{e}_2$ which corresponds to one of the principal directions of the cell.

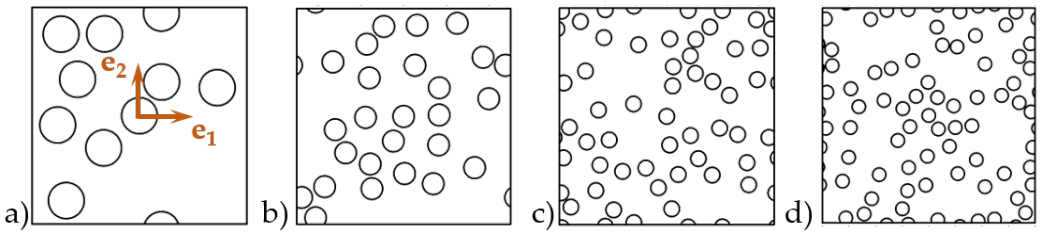

Figure III.18: 2D model with Φ =20 % and different number of uniform particles contained in the RVE (size normalized for visualization purposes, the particle diameter remains constant).

Table III.4 resumes the load cases, which are required to determine the effective properties. No external loading is applied to determine the Operating Point (OP) in the first study step. A tensile mechanical strain of 1 % in the principal directions of the quadratic cells is applied in the cases A and B respectively. A shear strain of 1 % is applied in load case C. The load cases A to C are performed twice for the same microstructure, at first with non-magnetized particles and in the following with magnetized particles. Based on the results, the influence of the magnetization on the mechanical properties is evaluated. For the magnetic loading, a magnetic field of 15 kA is applied in the two principal directions of the cell in the load cases D and E respectively. The values shown in table III.4 correspond to the variation of the magnetic and mechanical quantities around the operating point. In the numerical simulation, the loading is carried out by the application of the sum of the variation and the quantity determined for the operating point (e.g. $\varepsilon_1 = \Delta\varepsilon_1 + \varepsilon_1^{OP}$) as stated in table III.3. All in all, the study comprises 9 coupled numerical simulations for each of the 140 microstructures.

Study steps	Load case	$\Delta\varepsilon_1$ [%]	$\Delta\varepsilon_2$ [%]	$\Delta\varepsilon_6$ [%]	ΔH_1 [kA/m]	ΔH_2 [kA/m]
1	OP	–	–	–	–	–
2,4a	*A*	1	0	0	0	0
2,4a	*B*	0	1	0	0	0
2,4a	*C*	0	0	1	0	0
3,4b	*D*	0	0	0	15	0
3,4b	*E*	0	0	0	0	15

Table III.4: Different load cases applied during the study: no external loading applied (OP), mechanical loading (*A*–*C*) and magnetic loading (*D*–*E*)

III.3.2 Determination of the effective operating point

The operating point OP corresponds to initial constraints in the material caused by the magnetization of the particles without an external loading. An example shows the importance of the determination of the OP for comparative numerical analysis. Two composite materials are supposed to be subjected to a uniaxial strain of 5 % by the simulation. If the magnetization of the material leads to a strain of −2.5 % and a strain of 5 % is prescribed with respect to the non-constraint state, the effective strain in the magnetized composite measures 7.5 %. The loading of the two cases is different and the resulting material properties can hence not be compared. Figure III.19 a depicts behavior laws for materials with the same behavior but different OPs. To obtain the macroscopic operating point of a heterogeneous volume, a simulation without loading is carried out. On the boundaries of the heterogeneous volume, the periodic conditions are applied on the local fluctuations of the displacement and on the magnetic scalar potential. An RVE ($\Phi = 20\%$) with non-magnetized and magnetized particles is shown in its initial states in figure III.19 b and c respectively.

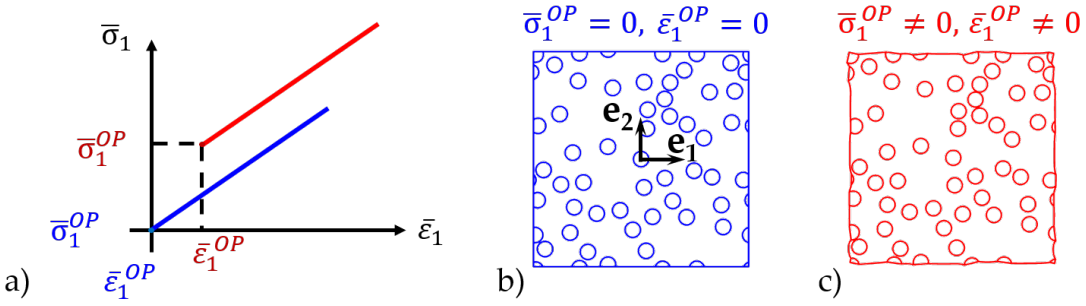

Figure III.19: Schematic representation of a linear mechanical behavior laws with different operating points (a) and initial state of an RVE with non-magnetized (b) and magnetized (c) particles (displacement x10 for visualization purposes).

While the RVE with non-magnetized particles remains in an unconstraint state (figure III.19 b), a periodic fluctuation of the displacement on the boundary and a slight deformation are visible for the composite with the magnetized particles (figure III.19 c). The displacement is increased by a factor 10 in the graphics.
In the parametric study, the operating point of the RVE is reached when stationary magnetic and mechanical states are reached. The results for the effective stress and the effective magnetic flux density of the composites with $\Phi = 20\%$ are shown in figure III.20 as a function of the number of particles N included in the volume. For both quantities, the dispersion of the results decreases with the increase of the number of particles and the results stabilize. But the results also show an increase of the dispersion for σ_1^{OP} for 49 particles and one case for which the flux density component B_1^{OP} is far from the uncertainty range for N=65. Graphics showing all the results for the operating point can be found in the appendix (figures A.2 to A.5). The results are summarized for the two volume fractions in table III.5 for the highest number of particles respectively.

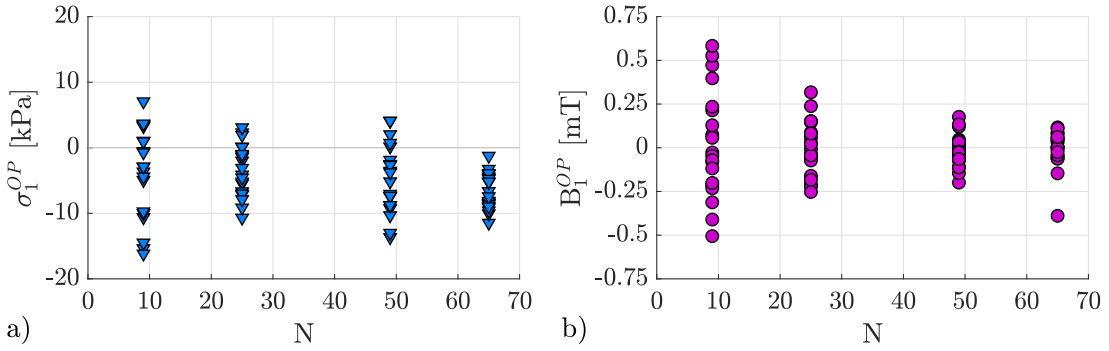

Figure III.20: Results for the mechanical stress σ_1^{OP} (a) and the magnetic flux density B_1^{OP} (b) at the operating point of composites with $\Phi = 20\%$ containing, a different number of particles N (20 samples for each value of N).

The magnetic flux density $\boldsymbol{B}$ is visibly determined by the magnetization of the particles. In the direction $\boldsymbol{e}_1$, perpendicular to the magnetization, it is almost zero for both volume fractions. In the direction of magnetization, it depends on the volume fraction of the composite material, a higher volume fraction leads to a higher flux density in the $\boldsymbol{e}_2$ direction. The magnetic field in the composite is also stronger in the $\boldsymbol{e}_2$ direction than in the $\boldsymbol{e}_1$ direction. The values of the magnetic field are largely inferior to the coercive field strength ($\approx 940\,\mathrm{kA/m}$). In the air the flux density resulting from these fields would not exceed 2 mT. The operating point of the material is situated in the first quadrant of the $\boldsymbol{B}$ – $\boldsymbol{H}$ relation and the resulting $\boldsymbol{B}$ is slightly higher than the residual flux density. But since the magnetic field is relatively weak, the value of $\boldsymbol{B}$ determined on the operating point gives a good approximation of the residual flux density. The strain that is induced by the magnetomechanical interactions is mainly induced in the direction of magnetization and perpendicular to it. The components ε_1 and ε_2 are one order of magnitude greater than ε_6. Interestingly, the average quantities are all

negative which means that the particle magnetization induces a compression of the cell. For the lower volume fraction a weaker compression in $\boldsymbol{e}_2$ direction and a higher compression in $\boldsymbol{e}_1$ direction is visible. This effect can also be observed for the stress: the stress induced in the direction of magnetization is higher for the higher volume fraction while the stress in the direction perpendicular to the magnetization is higher in the volume with less particles. This could be due to the lateral contraction of the matrix, which has a high Poisson's ratio and in addition, a higher number of particles reduced the amount of matrix. More particles can also lead to direct competition of the effects and the attraction forces are higher and result from more stable interactions than repulsive forces. The shear stress of the composite is higher for $\Phi = 20$ % than for $\Phi = 36$ %.

	$\Phi = 20$ % $[N = 65]$		$\Phi = 36$ % $[N = 89]$	
	average	standard dev.	average	standard dev.
B_1^{OP} [T]	<0.001	± <0.001	<0.001	± <0.001
B_2^{OP} [T]	0.156	± <0.001	0.281	± 0.001
H_1^{OP} [A/m]	5.6	± 15.7	16.7	± 33.8
H_2^{OP} [A/m]	398	± 64.4	1305.5	± 110.5
ε_1^{OP} [%]	-0.38	± 0.14	-0.24	± 0.12
ε_2^{OP} [%]	-0.14	± 0.11	-0.62	± 0.12
ε_6^{OP} [%]	-0.02	± 0.06	-0.03	± 0.06
σ_1^{OP} [kPa]	-6.67	± 2.71	-3.54	± 2.51
σ_2^{OP} [kPa]	-2.85	± 1.88	-7.40	± 2.75
σ_6^{OP} [kPa]	-0.16	± 0.68	0.47	± 1.72

Table III.5: Magnetic and mechanical operating point for two composite material with the volume fractions $\Phi = 20\%$ and $\Phi = 36\%$

III.3.3 Effective mechanical properties

The determination of the effective mechanical properties is based on an orthotropic material model (cf. section I.1.3, equation (I.26)). This allows to evaluate the mechanical properties in the two directions $\boldsymbol{e}_1$ and $\boldsymbol{e}_2$ and to check, if the effective behavior is isotropic as intended. The variation of the average stress can be linked to the variation of the average strain by the effective stiffness matrix $\mathbb{C}$, as shown in equation (III.39). The relation contains five unknown variables, the material parameters E_1, E_2, G_6, ν_{12} and ν_{21}. By rearranging the relation and using the three load cases, A, B and C, it is possible to determine the five material parameters (cf. equation (III.40)–equation (III.42)). The letter in the exponent corresponds to the load case and the subscript defined the position in the tensor (e.g. $\varepsilon_1^A =$ strain prescribed in load case A in the direction $\boldsymbol{e}_1$). The deformed configurations corresponding to the load cases A – C are shown in figure III.21. Periodic fluctu-

ations are visible on the boundaries which shows that the operating point is part of the load cases. In 3D simulations, 6 load cases are used to determine the 12 mechanical material parameters.

$$\begin{pmatrix} \Delta\varepsilon_1 \\ \Delta\varepsilon_2 \\ 2\Delta\varepsilon_6 \end{pmatrix} = \mathbb{C}^{-1} \begin{pmatrix} \Delta\sigma_1 \\ \Delta\sigma_2 \\ \Delta\sigma_6 \end{pmatrix} = \begin{pmatrix} 1/E_1 & -\nu_{21}/E_2 & 0 \\ -\nu_{12}/E_1 & 1/E_2 & 0 \\ 0 & 0 & 1/G_6 \end{pmatrix} \begin{pmatrix} \Delta\sigma_1 \\ \Delta\sigma_2 \\ \Delta\sigma_6 \end{pmatrix} \tag{III.39}$$

$$\begin{pmatrix} \Delta\varepsilon_1 \\ \Delta\varepsilon_2 \\ 2\Delta\varepsilon_6 \end{pmatrix} = \begin{pmatrix} \Delta\sigma_1 & \Delta\sigma_2 & 0 & 0 & 0 \\ 0 & 0 & \Delta\sigma_1 & \Delta\sigma_2 & 0 \\ 0 & 0 & 0 & 0 & \Delta\sigma_6 \end{pmatrix} \begin{pmatrix} 1/E_1 \\ -\nu_{21}/E_2 \\ -\nu_{12}/E_1 \\ 1/E_2 \\ 1/G_6 \end{pmatrix} \tag{III.40}$$

$$\begin{pmatrix} \Delta\varepsilon_1^A \\ \Delta\varepsilon_2^A \\ \Delta\varepsilon_1^B \\ \Delta\varepsilon_2^B \\ 2\Delta\varepsilon_6^I \end{pmatrix} = \begin{pmatrix} \Delta\sigma_1^A & \Delta\sigma_2^A & 0 & 0 & 0 \\ 0 & 0 & \Delta\sigma_1^A & \Delta\sigma_2^A & 0 \\ \Delta\sigma_1^B & \Delta\sigma_2^B & 0 & 0 & 0 \\ 0 & 0 & \Delta\sigma_1^B & \Delta\sigma_2^B & 0 \\ 0 & 0 & 0 & 0 & \Delta\sigma_6^I \end{pmatrix} \begin{pmatrix} 1/E_1 \\ -\nu_{21}/E_2 \\ -\nu_{12}/E_1 \\ 1/E_2 \\ 1/G_6 \end{pmatrix} \tag{III.41}$$

$$\begin{pmatrix} \Delta\sigma_1^A & \Delta\sigma_2^A & 0 & 0 & 0 \\ 0 & 0 & \Delta\sigma_1^A & \Delta\sigma_2^A & 0 \\ \Delta\sigma_1^B & \Delta\sigma_2^B & 0 & 0 & 0 \\ 0 & 0 & \Delta\sigma_1^B & \Delta\sigma_2^B & 0 \\ 0 & 0 & 0 & 0 & \Delta\sigma_6^C \end{pmatrix}^{-1} \begin{pmatrix} \Delta\varepsilon_1^A \\ \Delta\varepsilon_2^A \\ \Delta\varepsilon_1^B \\ \Delta\varepsilon_2^B \\ 2\Delta\varepsilon_6^C \end{pmatrix} = \begin{pmatrix} 1/E_1 \\ -\nu_{21}/E_2 \\ -\nu_{12}/E_1 \\ 1/E_2 \\ 1/G_6 \end{pmatrix} \tag{III.42}$$

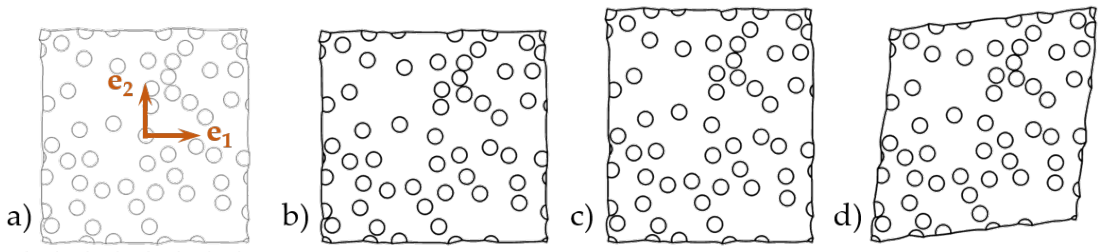

Figure III.21: Representation of the operating point (a) and the load cases A (b), B (c) and C (d) of a composite with $\Phi = 20\%$ (scale factor 10 for the displacements).

Figure III.22 shows the results for E_1 and ν_{12} calculated for the RVE with $\Phi = 20$ %. Both quantities seem to attain stable values with increasing number of particles and the dispersion of the results decreases. The results of the convergence studies for all mechanical properties are part shown graphically in the appendix (figures A.6 and A.7). The effective properties, obtained from simulations with

magnetized and non-magnetized particles, are represented in figure III.22. The results show that the difference in the properties induced by the magnetization of the particles is very small. These observations are made for all effective mechanical properties, as table III.6 shows.

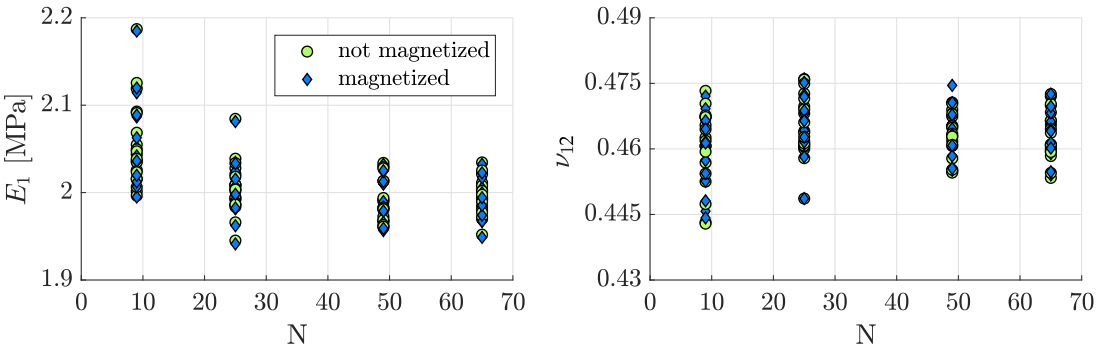

Figure III.22: Convergence study of the elastic modulus E_1 and the Poison's ratio ν_{12} with respect to the number of particles in the composite.

	$\Phi = 20$ % [N =65]		$\Phi = 36$ % [N =89]	
	average	standard dev.	average	standard dev.
	non-magnetized particles			
E_1 [MPa]	1.995	± 0.020	2.753	± 0.031
E_2 [MPa]	1.992	± 0.022	2.754	± 0.036
G_6 [MPa]	0.670	± 0.006	0.949	± 0.011
ν_{12}	0.463	± 0.006	0.440	± 0.006
ν_{21}	0.463	± 0.005	0.440	± 0.006
	magnetized particles			
E_1 [MPa]	1.992	± 0.020	2.745	± 0.031
E_2 [MPa]	1.986	± 0.022	2.731	± 0.034
G_6 [MPa]	0.670	± 0.006	0.945	± 0.011
ν_{12}	0.464	± 0.005	0.440	± 0.006
ν_{21}	0.462	± 0.005	0.438	± 0.006

Table III.6: Mechanical properties for composites with two different volume fractions including non-magnetized particles and magnetized particles.

The tensile moduli of the composite with non-magnetized particles are almost identical in the two tested directions. In general, tensile and shear modulus increase with the volume fraction. Two effects of the magnetization on the tensile modulus can be observed. Firstly, the magnetization tends to decrease the modulus, the difference is shown in the third part of the table. The difference lies has the same magnitude as the stress observed on the operating point. In comparison with the modulus however the difference is small. Secondly, the change in modulus is more

pronounced in the direction of magnetization than in the direction perpendicular to it. The shear modulus is slightly decreased by the magnetization but the effect is smaller than the effect on the tensile modulus. No clear tendency is observed for the change of the Poisson's ratio due to the magnetization.

III.3.4 Effective Magnetic properties

The magnetic behavior of the composite is described by the permeability tensor. To determine the components of the permeability tensor, the RVEs are subjected to a magnetic field according to load cases D and E. The relative permeability of the composite is determined by equation (III.44). Two load cases are necessary in 2D simulations, three in 3D simulations.

$$\begin{pmatrix} \Delta B_1 \\ \Delta B_2 \end{pmatrix} = \begin{pmatrix} \mu_{11} & \mu_{12} \\ \mu 21 & \mu_{22} \end{pmatrix} \begin{pmatrix} \Delta H_1 \\ \Delta H_2 \end{pmatrix} = \begin{pmatrix} \Delta H_1 & \Delta H_2 & 0 & 0 \\ 0 & 0 & \Delta H_1 & \Delta H_2 \end{pmatrix} \begin{pmatrix} \mu_{11} \\ \mu_{12} \\ \mu_{21} \\ \mu_{22} \end{pmatrix} \tag{III.43}$$

$$\begin{pmatrix} \Delta H_1^D & \Delta H_2^D & 0 & 0 \\ 0 & 0 & \Delta H_1^D & \Delta H_2^D \\ \Delta H_1^E & \Delta H_2^E & 0 & 0 \\ 0 & 0 & \Delta H_1^E & \Delta H_2^E \end{pmatrix}^{-1} \begin{pmatrix} \Delta B_1^D \\ \Delta B_2^D \\ \Delta B_1^E \\ \Delta B_2^E \end{pmatrix} = \begin{pmatrix} \mu_{r\,11} \\ \mu_{r\,12} \\ \mu_{r\,21} \\ \mu_{r\,22} \end{pmatrix} \mu_0 \tag{III.44}$$

The magnetic loading is represented in figure III.23. In the load cases D and E, uniform magnetic fields of 15 kA/m are applied in the two principal directions of the cell respectively. The variation of the field considers the operating point of the composite material as figure III.23 a shows.

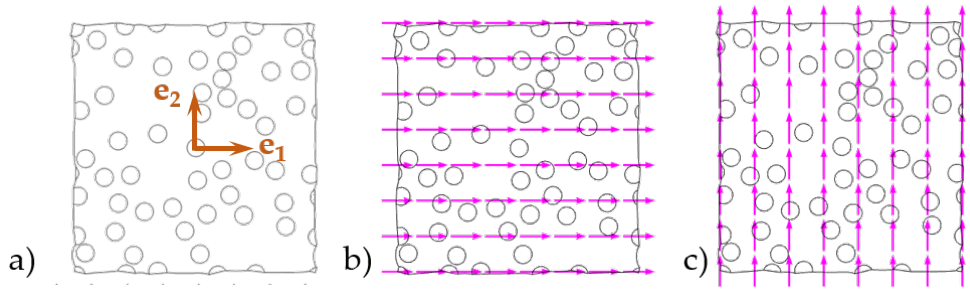

Figure III.23: Schematic representation of a composite at the operating point (a) and the magnetic loading cases in which the magnetic field is applied in the two principal directions of the cell (b-c).

The results of the first the components of the relative permeability tensor are shown in figure III.24. The decrease of the dispersion of the results is observed for $\mu_{r\,11}$ and $\mu_{r\,12}$. The average results seem to stabilize although the values for $\mu_{r\,11}$ increase from 49 particles to 65 particles after having decreased before. This effect

could be due to the particle positioning algorithm. For high particle concentrations, the algorithm tends to position particles preferentially near the boundaries which increases their density and could be responsible for a higher overall permeability. The number of simulations could be another reason for the effect: The dispersion could be higher for a higher number of simulations, in this case the effect observed in figure III.24 is artificial. Nevertheless, as the variation is small, the following conclusions are based on the average of the quasi-converged results. The results of all simulations are shown in the appendix (figures A.8 and A.9) and the average quantities are summarized in table III.7. The relative permeability for the directions $\boldsymbol{e}_1$ and $\boldsymbol{e}_2$ is nearly identical. It is thus concluded that the distribution of the particles is isotropic and since the magnetic behavior of the particles is isotropic. The relative permeability in the principal directions increases with the volume fraction. This is due to the fact that the permeability of the particles is slightly higher than the permeability of the matrix, increasing the content of particles hence increases the effective permeability. It is also observed that the change in the magnetic flux density by a field perpendicular to the direction of observation is close to zero since the components $\mu_{r\,12}$ and $\mu_{r\,21}$ are almost zero.

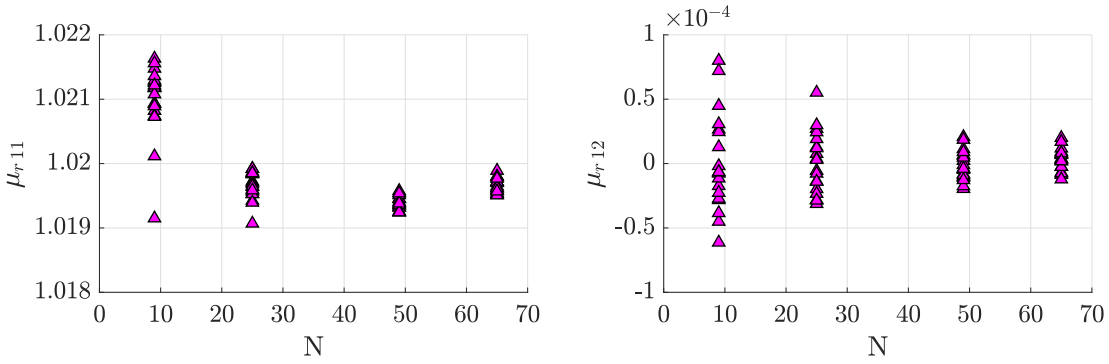

Figure III.24: Convergence study of two components of the relative magnetic permeability, $\mu_{r\,11}$ and $\mu_{r\,12}$, with respect to the number of particles included in the corresponding microstructures.

	$\Phi = 20$ % [N =65]		$\Phi = 36$ % [N =89]	
	average	standard dev.	average	standard dev.
$\mu_{r\,11}$	1.020	± <0.001	1.035	± <0.001
$\mu_{r\,12}$	<0.001	± <0.001	<0.001	± <0.001
$\mu_{r\,21}$	<0.001	± <0.001	<0.001	± <0.001
$\mu_{r\,22}$	1.020	± <0.001	1.035	± <0.001

Table III.7: Effective magnetic permeability of two composite materials with a volume faction of $\Phi = 20\%$ and $\Phi = 36\%$.

III.3.5 Effective Magneto-mechanical coupling

The analysis of the magnetomechanical coupling consists of regarding the influences of a loading in one physical domain on behavior in the complementary physical domain. It means either analyzing the influence of the deformation of the RVE on the magnetic characteristics or analyzing the influence of a magnetic field on the stress. As stated in the introduction of this section, the coupling coefficients are determined for fixed mechanical or magnetic states. The corresponding relations are shown in equation (III.45) and equation (III.47) respectively. Three mechanical load cases are necessary to determine $\mathbb{d}^H$ (equation (III.46)) and two magnetic load cases to determine $\mathbb{d}^\varepsilon$ (equation (III.48)). The load cases from the analysis of the decoupled behavior can be used to analyze the coupled behavior as well.

$$\begin{pmatrix} \Delta B_1 \\ \Delta B_2 \end{pmatrix} = - \begin{pmatrix} d_{11} & d_{12} & d_{16} \\ d_{21} & d_{22} & d_{26} \end{pmatrix}^H \begin{pmatrix} \Delta\varepsilon_1 \\ \Delta\varepsilon_2 \\ \Delta\varepsilon_6 \end{pmatrix}$$

$$= - \begin{pmatrix} \Delta\varepsilon_1 & \Delta\varepsilon_2 & \Delta\varepsilon_6 & 0 & 0 & 0 \\ 0 & 0 & 0 & \Delta\varepsilon_1 & \Delta\varepsilon_2 & \Delta\varepsilon_6 \end{pmatrix} \begin{pmatrix} d_{11} \\ d_{12} \\ d_{16} \\ d_{21} \\ d_{22} \\ d_{26} \end{pmatrix}^H \tag{III.45}$$

$$- \begin{pmatrix} \Delta\varepsilon_1^A & \Delta\varepsilon_2^A & \Delta\varepsilon_6^A & 0 & 0 & 0 \\ 0 & 0 & 0 & \Delta\varepsilon_1^A & \Delta\varepsilon_2^A & \Delta\varepsilon_6^A \\ \Delta\varepsilon_1^B & \Delta\varepsilon_2^B & \Delta\varepsilon_6^B & 0 & 0 & 0 \\ 0 & 0 & 0 & \Delta\varepsilon_1^B & \Delta\varepsilon_2^B & \Delta\varepsilon_6^B \\ \Delta\varepsilon_1^F & \Delta\varepsilon_2^F & \Delta\varepsilon_6^F & 0 & 0 & 0 \\ 0 & 0 & 0 & \Delta\varepsilon_1^C & \Delta\varepsilon_2^C & \Delta\varepsilon_6^C \end{pmatrix}^{-1} \begin{pmatrix} \Delta B_1^A \\ \Delta B_2^A \\ \Delta B_1^B \\ \Delta B_2^B \\ \Delta B_1^C \\ \Delta B_2^C \end{pmatrix} = \begin{pmatrix} d_{11} \\ d_{12} \\ d_{16} \\ d_{21} \\ d_{22} \\ d_{26} \end{pmatrix}^H \tag{III.46}$$

$$\begin{pmatrix} \Delta\sigma_1 \\ \Delta\sigma_2 \\ \Delta\sigma_6 \end{pmatrix} = \begin{pmatrix} d_{11} & d_{21} \\ d_{12} & d_{22} \\ d_{16} & d_{26} \end{pmatrix}^\varepsilon \begin{pmatrix} \Delta H_1 \\ \Delta H_2 \end{pmatrix}$$

$$= \begin{pmatrix} \Delta H_1 & \Delta H_2 & 0 & 0 & 0 & 0 \\ 0 & 0 & \Delta H_1 & \Delta H_2 & 0 & 0 \\ 0 & 0 & 0 & 0 & \Delta H_1 & \Delta H_2 \end{pmatrix} \begin{pmatrix} d_{11} \\ d_{12} \\ d_{16} \\ d_{21} \\ d_{22} \\ d_{26} \end{pmatrix}^\varepsilon \tag{III.47}$$

$$\begin{pmatrix} \Delta H_1^D & \Delta H_2^D & 0 & 0 & 0 & 0 \\ 0 & 0 & \Delta H_1^D & \Delta H_2^D & 0 & 0 \\ 0 & 0 & 0 & 0 & \Delta H_1^D & \Delta H_2^D \\ \Delta H_1^E & \Delta E_2^H & 0 & 0 & 0 & 0 \\ 0 & 0 & \Delta H_1^E & \Delta H_2^E & 0 & 0 \\ 0 & 0 & 0 & 0 & \Delta H_1^E & \Delta H_2^E \end{pmatrix}^{-1} \begin{pmatrix} \Delta\sigma_1^D \\ \Delta\sigma_2^D \\ \Delta\sigma_6^D \\ \Delta\sigma_1^E \\ \Delta\sigma_2^E \\ \Delta\sigma_6^E \end{pmatrix} = \begin{pmatrix} d_{11} \\ d_{21} \\ d_{12} \\ d_{22} \\ d_{16} \\ d_{26} \end{pmatrix}^{\varepsilon} \tag{III.48}$$

To analyze the coupled behavior, the results of the five load cases A to E are used. In contrast to the previous studies, in which the prescribed and observed quantities are studied in the same physical domain, the variation of $\boldsymbol{B}$ due to the mechanical loading and the variation of σ due to the magnetic loading are analyzed in this paragraph. The coupling coefficient d_{22} describes the case where loading and reaction are both aligned in the $\boldsymbol{e}_2$ direction. The results of a convergence study for a composite with $\Phi = 20\%$ are represented in figure III.25. The left diagram shows the coupling coefficient d_{22} obtained for a constant magnetic field. In this load case the external magnetic field is set to zero and $\boldsymbol{H}$ corresponds thus to the operating point $\boldsymbol{H}^{OP}$. A convergence of the average value as well as the decrease of the distribution of the results are observed. The right graphic shows the coupling coefficient d_{22} obtained for a constant mechanical strain. No external loading is applied and the material is at the operating point $\varepsilon = \varepsilon^{OP}$. Convergence of the average quantity as well as the decrease of the dispersion of results are observed as well. The two average quantities converge towards slightly different values. The components of the coupling tensor are summarized in table III.8 for the influence of a mechanical loading on the magnetic flux density or a magnetic field on the stress.

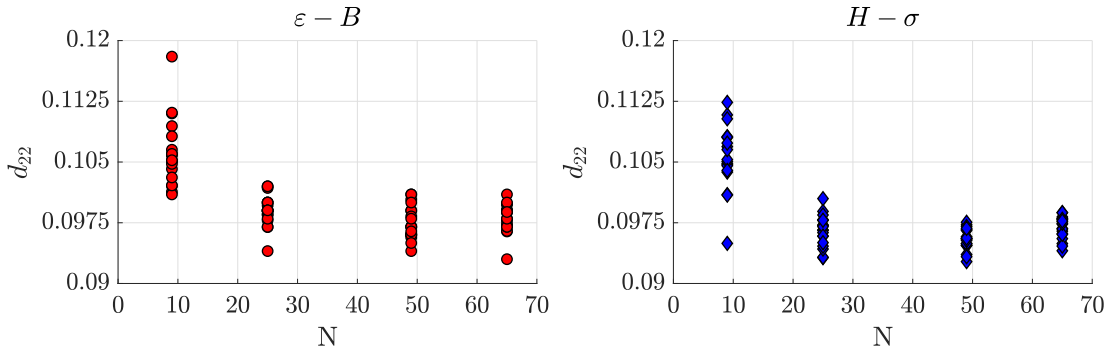

Figure III.25: Convergence study on the coupling coefficient d_{22} obtained for a fixed magnetic field $\boldsymbol{H} = \boldsymbol{H}^{OP}$ (left) or a fixed mechanical strain $\varepsilon = \varepsilon^{OP}$ (right) with respect to the number of particles in the composite.

The coupling, induced by the tensile deformation for $\boldsymbol{H} = \boldsymbol{H}^{OP}$, decreases the magnetic flux density. This is represented by negative coupling factors in the first part of the table. Coupling factors with a positive sign are obtained for the $\boldsymbol{e}_1$ direction. They are close to zero, hence it is concluded that a tensile strain in this

direction has a negligible influence on the magnetic flux density. In addition, a shear strain does not have a significant influence on the magnetic flux density in the $\boldsymbol{e}_2$-direction. The influence of the shear strain on the magnetic flux density is much bigger in the $\boldsymbol{e}_1$-direction. The strongest coupling is observed between the tensile strains and the B_2 component. It is concluded that mechanical loading in the direction of magnetization of the particles has the biggest influence on the magnetic flux density in this direction, followed by the tensile strain perpendicular to this direction. The tendencies are observed both composites independently of the volume fraction. The magnitude of the coupling is stronger for the higher volume fraction since a higher particle density increases number of possible interactions and decreases the distance between the particles which reinforces the interactions. The influence of a magnetic field on the stress ($\varepsilon = \varepsilon^{OP}$) also increases with the volume fraction. In load case D, a magnetic field perpendicular to the magnetization of the particles is applied. The effect on the tensile/compressive stress is small, however the shear stress σ_6 is altered in a significant manner. It is supposed that the magnetic particles rotate to align their magnetic moment with the external magnetic field and thus generate shear stress in the matrix.

		$\Phi = 20$ % $[N = 65]$		$\Phi = 36$ % $[N = 89]$	
factor	coupling	average	standard dev.	average	standard dev.
$d_{11}^{\boldsymbol{H}=\boldsymbol{H}^{OP}}$ [mT]	$\varepsilon_1 \rightarrow B_1$	-||<0.01	± 1.02	-0.17	± 3.05
$d_{12}^{\boldsymbol{H}=\boldsymbol{H}^{OP}}$ [mT]	$\varepsilon_2 \rightarrow B_1$	-0.32	± 0.96	-0.22	± 1.91]
$d_{16}^{\boldsymbol{H}=\boldsymbol{H}^{OP}}$ [mT]	$\varepsilon_6 \rightarrow B_1$	34.28	± 2.59	67.9	± 16.47
$d_{21}^{\boldsymbol{H}=\boldsymbol{H}^{OP}}$ [mT]	$\varepsilon_1 \rightarrow B_2$	60.37	± 1.72	103.13	± 24.38
$d_{22}^{\boldsymbol{H}=\boldsymbol{H}^{OP}}$ [mT]	$\varepsilon_2 \rightarrow B_2$	98.06	± 1.78	173.45	± 40.90
$d_{26}^{\boldsymbol{H}=\boldsymbol{H}^{OP}}$ [mT]	$\varepsilon_6 \rightarrow B_2$	-1.19	± 1.83	-1.68	± 4.54
$d_{11}^{\varepsilon=\varepsilon^{OP}}$ [mT]	$H_1 \rightarrow \sigma_1$	0.90	± 0.77	2.15	± 2.48
$d_{12}^{\varepsilon=\varepsilon^{OP}}$ [mT]	$H_1 \rightarrow \sigma_2$	-1.94	± 0.64	-3.11	± 2.43
$d_{16}^{\varepsilon=\varepsilon^{OP}}$ [mT]	$H_1 \rightarrow \sigma_6$	15.12	± 0.98	47.61	± 11.31
$d_{21}^{\varepsilon=\varepsilon^{OP}}$ [mT]	$H_2 \rightarrow \sigma_1$	61.21	± 1.10	84.60	± 19.94
$d_{22}^{\varepsilon=\varepsilon^{OP}}$ [mT]	$H_2 \rightarrow \sigma_2$	96.90	± 1.38	189.39	± 44.62
$d_{26}^{\varepsilon=\varepsilon^{OP}}$ [mT]	$H_2 \rightarrow \sigma_6$	-0.13	± 0.76	-0.24	± 1.95

Table III.8: Coupling factors for two composites with volume fraction $\Phi = 20\%$ and $\Phi = 36\%$ respectively obtained for a fixed magnetic field (top) or fixed strain (bottom)

The magnetic field aligned with the magnetization of the particles does not have a significant influence on the shear stress for the same reason. On the contrary, this configuration induces tensile/compressive stresses. The highest coupling is obtained in the direction of magnetization. It is supposed that the particles tend to align in the direction of the magnetic field lines and their shift increases the stress in the direction of magnetization. The increase of the stress perpendicular

to the direction of the applied field could be induced by the reinforcement of the magnetic moment of the particles. When they are aligned in a configuration that generates repulsive forces, these forces are increased when the magnetic moment is increased. The strongest couplings are observed in the direction of the magnetization of the particles.

III.4 Modeling on the macroscopic scale

In this section, the focus is put on the modeling on the macroscopic scale. At the beginning, a brief introduction on piezomagnetic behavior laws is given and the model used for the subsequent studies is described. Afterwards, the model is applied in several magnetic and mechanical load cases and the results are compared to numerical simulations. Afterwards, the effective properties obtained in the previous section and by additional, two and three dimensional simulations, are compared to the experimental results presented in chapter II.

III.4.1 PiezoMagnetic (PM) behavior law

The present model is supposed to be valid in vicinity of the operating point of the material in the two physical domains. For small mechanical solicitations and magnetic fields, the behavior is linearized. In the case of a linear magnetoelasticity, state laws similar to the ones obtained for piezoelectricity can be derived from thermodynamic potentials (cf. [Lemaitre+ 2009]). In addition, the term piezomagnetism can be used for the linear coupled magnetomechanical behavior around an operating point according to [Corcolle 2009]. Table III.9 shows the electric and magnetic quantities that are equivalent in piezoelectric and piezomagnetic behavior laws.

Piezoelectric model				Piezomagnetic model
Electric field	$\boldsymbol{E}$	$\leftrightarrow$	$\boldsymbol{H}$	Magnetic field
Polarization	$\boldsymbol{P}$	$\leftrightarrow$	$\mu_0\boldsymbol{M}$	Magnetic constant and magnetization
Initial polarization	$\boldsymbol{\Pi}$	$\leftrightarrow$	$\mu_0\boldsymbol{M}$	Magnetic constant and initial magnetization
Electric displacement	$\boldsymbol{D}$	$\leftrightarrow$	$\boldsymbol{B}$	Magnetic flux density

Table III.9: Equivalent quantities in piezoelectric and piezomagnetic behavior laws.

The derivation of thermodynamically consistent, reversible behavior laws by the help of the free energy Ψ is shown in section I.3.5 (equation (I.92)). A constant temperature is supposed in the following, the state of the material is thus defined by the strain and the magnetic field: $\Psi = \Psi(\varepsilon, \boldsymbol{H})$. The behavior law, developed

in the following, is supposed to be valid for small mechanical and magnetic perturbations of a magnetized composite. According to the experimental results for the small strain regime, the mechanical behavior is approximately linear. A magnetic loading in vicinity of the remanent magnetization also evolves in a quasi-linear manner. The uncoupled mechanical and magnetic behavior can hence be derived from quadratic expressions of Ψ, as shown in [Lemaitre+ 2009] for example. A magnetic contribution to the mechanical loading for constant strain has been observed in the experimental test. Since the loading remains small in the present context the coupling is assumed to be linear in a first time. This assumption is a choice based on the available results that will be evaluated by means of the results of the numerical simulations and has to be verified in future experiments. The resulting expression of Ψ corresponds to a magneto-elastic potential, analogous to potential functions known for piezoelectric materials:

$$\rho^m \Psi(\boldsymbol{H}, \varepsilon) = \frac{1}{2}\varepsilon : \mathcal{C} : \varepsilon - \frac{\mu_0}{2}\boldsymbol{H} \,\chi\, \boldsymbol{H} + \varepsilon : \mathbb{d} \cdot \boldsymbol{H} \;, \tag{III.49}$$

where $\mathbb{d}$ corresponds to the third order piezomagnetic tensor (cf. [Lemaitre+ 2009]). The coupled mechanical behavior law is obtained from the derivative of Ψ with respect to the strain. Equation (III.50) shows that the result comprises the well-known linear elastic behavior law and a contribution of the magnetic field, that is independent from the strain. This description is in accordance with the first results of the experimental observation where the force increase is nearly constant for different strain levels.

$$\sigma = \rho^m \frac{\partial \Psi}{\partial \varepsilon} = \mathcal{C} : \varepsilon + \mathbb{d} \cdot \boldsymbol{H} \tag{III.50}$$

The coupled magnetic behavior law is obtained from the derivative of Ψ with respect to the magnetic field as shown in equation (III.51). By the help of equation (III.52), the relation is expressed as $\boldsymbol{B}(\boldsymbol{H})$ instead of $\boldsymbol{M}(\boldsymbol{H})$ in equation (III.53). The contribution of the strain is independent from the magnetic field.

$$\mu_0 \boldsymbol{M} = -\rho^m \frac{\partial \Psi}{\partial \boldsymbol{H}} = \mu_0 \,\chi\, \boldsymbol{H} - \mathbb{d}^{\mathrm{T}} : \varepsilon \tag{III.51}$$

$$\mu_0 \boldsymbol{M} = B - \mu_0 \boldsymbol{H} \tag{III.52}$$

$$\boldsymbol{B} = (1 + \chi)\mu_0 \boldsymbol{H} - \mathbb{d}^{\mathrm{T}} : \varepsilon = \mu_r \mu_0 \boldsymbol{H} - \mathbb{d}^{\mathrm{T}} : \varepsilon \tag{III.53}$$

Examples of other notations of PM behavior laws can be found in the IEEE standard 319-1990 [Electrical+ 1990] inter alia. The standard defines the anisotropy induced by the permanent magnetization in the third spatial direction. For the two-dimensional model of the present study, the magnetization is oriented in the second spatial direction $\boldsymbol{e}_2$. Effective properties have been determined in the former section to establish a piezomagnetic behavior law. The behavior around an operating point can be represented by the two equations shown in equation (III.34)

but also in a single system as shown in equation (III.54). The following section compares the results obtained for the linear PM behavior law with the results of numerical simulations for different load cases.

$$\begin{pmatrix} \Delta\sigma_1 \\ \Delta\sigma_2 \\ \Delta\sigma_6 \\ \\ \Delta B_1 \\ \Delta B_2 \end{pmatrix} = \begin{pmatrix} C_{11} & C_{12} & 0 & d_{11} & d_{21} \\ C_{21} & C_{22} & 0 & d_{12} & d_{22} \\ 0 & 0 & C_{66} & d_{16} & d_{26} \\ \\ -d_{11} & -d_{12} & -d_{16} & \mu_{11} & \mu_{12} \\ -d_{21} & -d_{22} & -d_{26} & \mu_{21} & \mu_{22} \end{pmatrix} \cdot \begin{pmatrix} \Delta\varepsilon_1 \\ \Delta\varepsilon_2 \\ \Delta\varepsilon_6 \\ \\ \Delta H_1 \\ \Delta H_2 \end{pmatrix} \tag{III.54}$$

III.4.2 PM model compared to heterogeneous composites

In this section, the piezomagnetic (PM) model is compared to the results of numerical simulations of Heterogeneous Composite Cells (HCC). The study is carried out for the two volume fractions, $\Phi = 20$ % and $\Phi = 36\%$. The behavior law of the two microstructures, shown in figure III.26, is established based on the effective properties, determined in the previous section (cf. tables III.6 to III.8), and implemented in Matlab. During the study, different magnetic and mechanical loading cases are applied and the reaction of the HCC and homogenized PM model are compared.

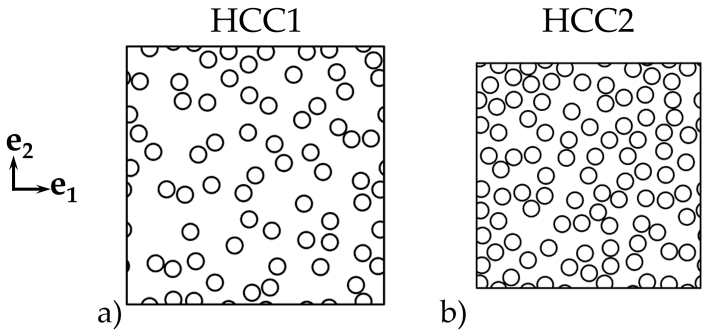

Figure III.26: Heterogeneous Composite Cells (HCC) used for the comparison between the PM model and numerical simulation: $\Phi = 20\%$ (a) and $\Phi = 36\%$ (b).

The first loading case consists of a uniaxial average strain in the direction of the magnetization. For this loading case, the effective coupling coefficients for the magnetic field at the operating point $\mathbb{d}^{H=H^{OP}}$ are determined, since no external magnetic field is applied. During the quasi-static loading, the strain ranges from $-10\,\%$ to $10\,\%$. Figure III.27 shows the results for the effective stress and magnetic flux density obtained from the PM model and numerical simulations with HCC1 ($\Phi = 20\%$). Figure III.27 a and b show the variation of the three stress components around the operating point. In the left graphic, the results are shown for a small variation of the strain ($\pm$ 1 %) and on the right for a larger variation ($\pm$ 10 %). As no magnetic field is applied, the relation between stress and

strain is determined by the mechanical properties. As linear strains are forced in the numerical simulation, the PM model is in good accordance with the results obtained for HCC1. The stresses σ_1 and σ_2 increase for tensile and decrease for compressive loading. The shear stress is not significantly altered by the applied tensile/compressive loading as expected from the mechanical behavior law.
Figure III.27 c and d represent the coupling: the variation of the magnetic flux density in absence of a magnetic field is shown for a small and large strain variation. The magnetic flux density the direction of magnetization shows a significant variation, it increases under compression loads and decreases when tensile loading is applied. For a small variation of the strain, the piezomagnetic model is in good accordance with the results of HCC1, as both behave linearly. With increasing strain magnitude, the magnetic flux density component B_2 behaves in a nonlinear way: a strong variation is observed at the beginning which becomes smaller with increasing strain. This behavior is linked to the inter-particle distance, that is changed by the deformation of the heterogeneous cell, and the magneto-mechanical interactions between the particles, which depend in a non-linear manner on the distance. The magnetic flux density perpendicular to the direction of magnetization is not significantly altered since the coupling is weak (cf. $d_{12}^{\boldsymbol{H}=\mathbf{0}}$ in table III.8). The accordance of the results for HCC1 and the PM model decreases, since the PM model assumes a linear coupling.

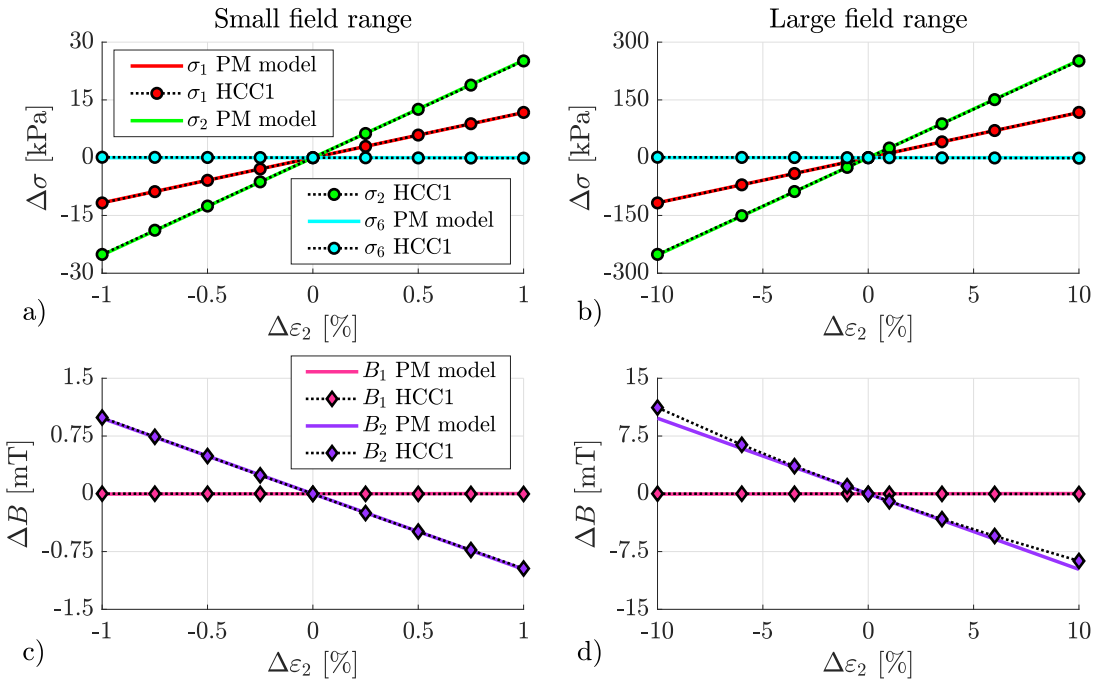

Figure III.27: Influence of mechanical loading in the direction of magnetization on the effective stress (top) and the effective magnetic flux density (bottom) in a small field range (left) and a large field range (right) for a composite with $\Phi = 20\%$, obtained with the PM model and HCC1.

In the second study, a magnetic field in the range of −150 kA/m to 150 kA/m is applied in the direction of magnetization of the particles ($\boldsymbol{e}_2$). The resulting variation of the magnetic flux density and the strain are shown in figure III.28. In figure III.28 a and b, the evolution of the magnetic flux density is shown for small variations (± 15 kA/m) on the left and for large variations of the magnetic field (± 150 kA/m) on the right. The strain is kept constant ($\varepsilon = \varepsilon^{OP}$), hence the variation of the quantities is caused by the magnetic field only. For B_1 no significant change of the flux density is observed in contrary to B_2. The flux decreases for magnetic fields that are oriented in the opposite direction of the magnetization and increases for fields in the direction of magnetization. The PM model and the results of HCC1 are in good accordance for the purely magnetic behavior. As expected, the linear behavior laws, implemented for the primary materials, lead to a linear behavior of the effective properties.

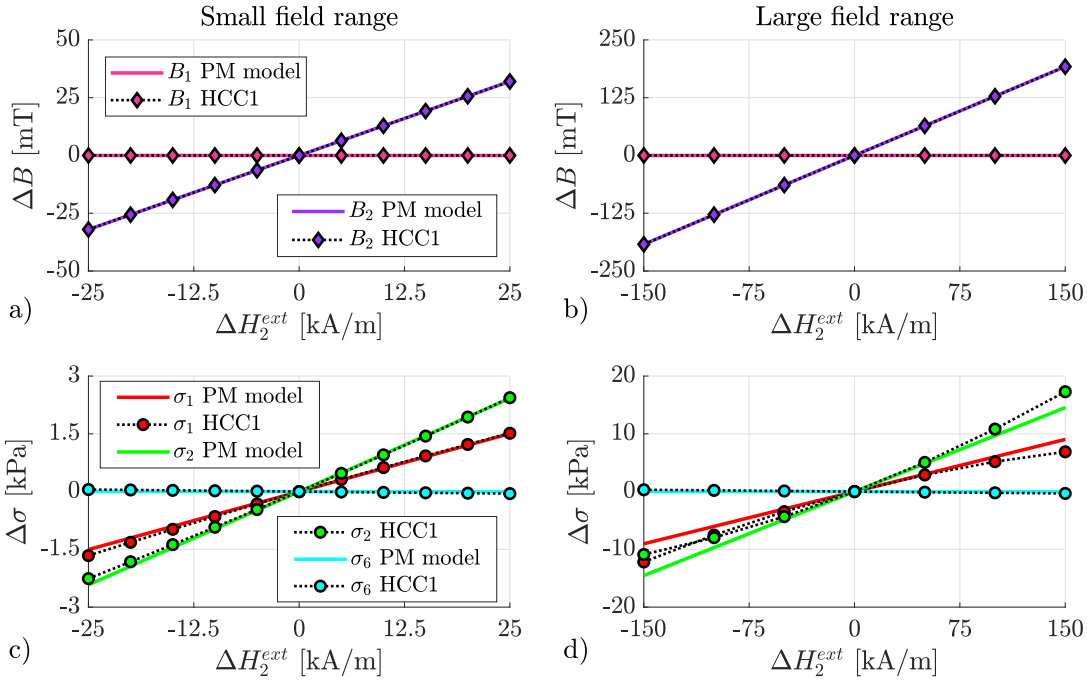

Figure III.28: Influence of magnetic loading in the direction of magnetization on the effective magnetic flux density (top) and the effective stress (bottom) in a small field range (left) and a large field range (right) for a composite with $\Phi = 20\%$, obtained with the PM model and HCC1.

Figure III.28 c and d show the coupling of the effective properties in form of the variation of the stress induced by the magnetic field. As expected from the coupling coefficients the stress in the two principal direction is significantly affected by the application of a magnetic field in the direction of magnetization in contrast to the shear stress. In a small magnetic field range, the results of the piezomagnetic model are in good accordance with the results for HCC1. For larger magnetic fields however, a difference between the results is observed. The stress in the heterogeneous cell evolves in a nonlinear way. The piezomagnetic material model is

a linear approximation, the difference between the results increases thus with the magnitude of the magnetic field.

In the two load cases previously presented, the heterogeneous composite cell HCC2 qualitatively behaves in the same manner as HCC1. Four additional load cases were performed for HCC2 and are shown in figure III.29. The variation of the magnetic flux density as a result of a mechanical loading is represented for the cases $\varepsilon_1 \rightarrow B_2$ and $\varepsilon_6 \rightarrow B_1$. These are the cases showing the second and third strongest coupling (cf. table III.8).

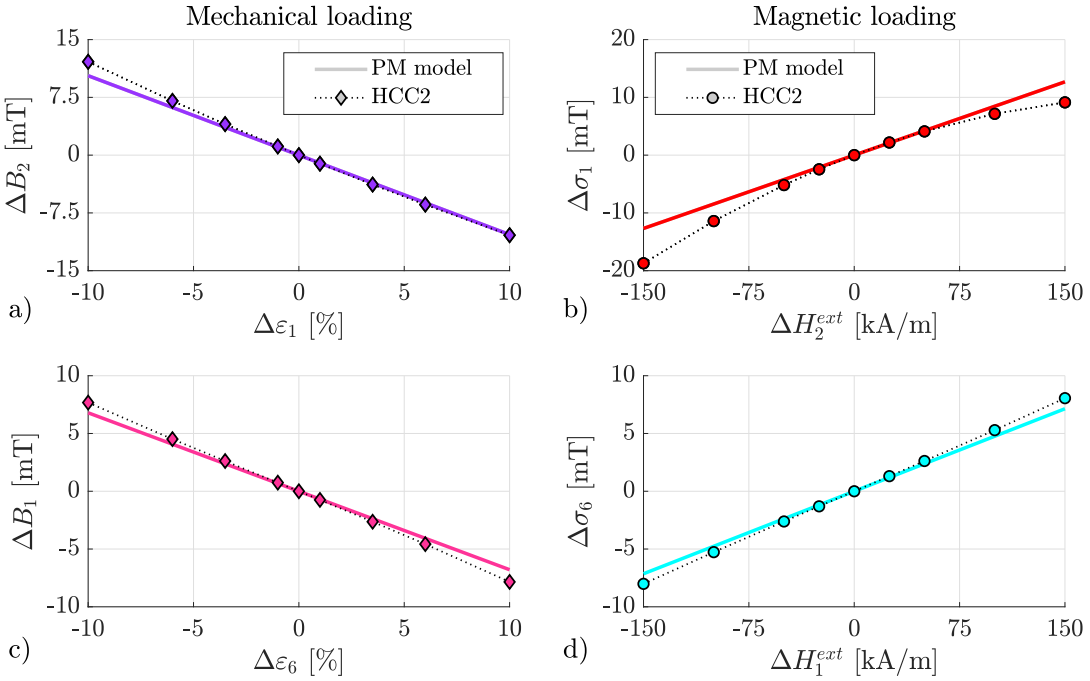

Figure III.29: Influence of different mechanical load cases on the effective magnetic flux density (left) and different magnetic load cases on the effective stress (right)in a large field range for a composite with $\Phi = 36\%$, obtained with the PM model and HCC2.

For a mechanical strain up to $\pm$ 3 %, the results of the piezomagnetic model are in good accordance with those of the heterogeneous model for both mechanical load cases. As the upper left graphic shows, the coupling in the model is valid for higher tensile than compressive loads. The difference between the results of HCC2 (heterogeneous model) and the results obtained by the PM model is symmetric for the variation of the magnetic flux density perpendicular to the magnetization (lower left graphic). This is also the case for magnetic loading: while the difference between numerical results and PM model is different for tensile and compressive stress it remains symmetric for the shear stress. For large magnetic fields, a strong

non-linearity of the relation between the quantities H_2 and σ_1 is observed, which cannot be represented with the linear PM model. The results for small field on the contrary are in good accordance.

III.4.3 PM model compared to experiments

In this section, the macroscopic properties obtained by simulation are compared to experimental results. Details of the experimental investigations are presented in chapter II. The study presented in the previous section has not only been conducted on two dimensional structures with particles of uniform size but also on two dimensional structures in which the particles size was distributed according to a normal law (average = 2.5 µm, standard deviation = 0.5 µm). Furthermore, mechanical properties for three dimensional microstructures have been obtained: structures with randomly distributed particles of uniform size and periodic unit cells containing one particle have been used for these studies. Example of the different microstructures are shown in Figure III.30. Numerical and experimental results are also compared to the analytic estimates obtained by the methods of Voigt and Reuss.

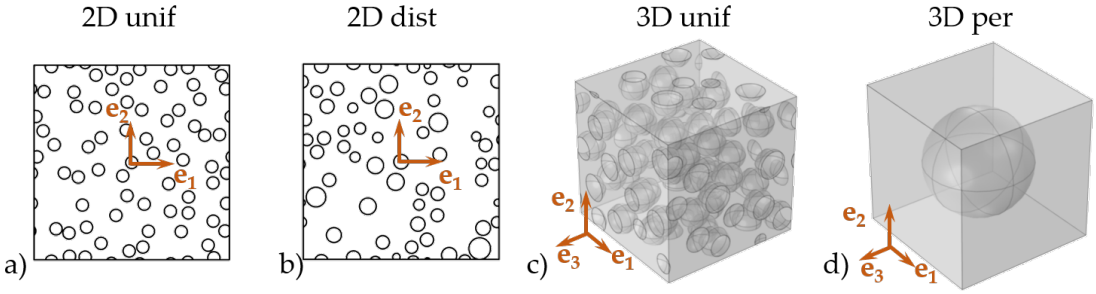

Figure III.30: Microstructures of a composite with $\Phi = 20\%$: 2D random microstructures with uniform inclusion size a) and varying inclusion size (b), 3D statistically homogeneous microstructure with spherical inclusions of uniform size (c) and 3D periodic cell (d).

III.4.3.a Magnetic properties

The results for the relative permeability in the principal direction and the residual flux density in the direction of magnetization are shown in table III.10. The numerical results lie in between the estimates of Voigt and Reuss and are hence physically possible solutions. Both results reveal to be closer to the upper estimate (Voigt). The range of the estimates for the relative permeability seem very small but in contrast to the other material properties the values of the primary materials are of the same magnitude. Interestingly, the estimate of Reuss for the residual flux density is negligible for both volume fractions. The comparison of the results for $\Phi = 20\%$ between the two types of microstructures shows that the variation of the particles size does not influence the magnetic properties.

Φ	Property	Reuss	2D unif	2D dist	Exp	Voigt
20 %	μ_r	1.0185	1.020	1.020	-	1.0200
	Br [T]	0	0.156	0.156	0.148*	0.16
36 %	μ_r	1.0338	1.035	-	-	1.0360
	Br [T]	0	0.281	-	0.305**	0.288

Table III.10: Effective magnetic properties of two composite materials obtained by analytic means (Reuss, Voigt), numerical simulation (2D unif, 2D dist) and experimentally (Exp). $^{*}\Phi_{Exp} = 19.4$ %, $^{**}\Phi_{Exp} = 36.2$ %

The experimental value obtained for $\Phi = 19.4\%$ is enclosed by the estimates of Voigt and Reuss in the contrast to the value obtained for $\Phi = 36.2\%$. The estimate of Voigt is calculated for a lower volume fraction, but even if the calculation is performed for 36.2% it does not exceed the experimentally obtained value. The exceeding residual flux density probably has its origin in the experimental investigation. Due to the fabrication procedure, the volume fraction could be higher than specified and measurement uncertainties can come into play additionally. In general, the accordance between numerical simulation and experimental results is considered as good ($< 8.5\%$) in the view of the simplifying assumptions made during the modeling.

III.4.3.b Mechanical properties

Table III.11 shows the elastic moduli and Poisson's ratios obtained in the two principal directions for two composite materials. The results of the 2D coupled simulations are shown as well as the results obtained from uncoupled 3D simulations with randomly distributed particles of uniform size and from an uncoupled 3D simulation with a periodic unit cell containing one particle. The results for $\Phi = 36\%$ shown for the cases *2D dist* and *3D unif* are obtained from single simulations as well as all results shown for the periodic unit cell. In the first two cases, the simulation was very time consuming, hence only one simulation has been performed and the quantitative evaluation of these results has to be done with caution. In the latter case no more than one simulation is necessary for the RUC. All results are enclosed by the estimates of Voigt and Reuss and hence physically possible solutions.
Concerning the modulus, the range enclosed by the two estimates is very large. This is due to the gradient of the material properties: the elastic modulus of the particles exceeds the matrix modulus by several orders of magnitude. All results are closer to the lower estimate (Reuss) than to the upper estimate. The comparison of the 2D simulation shows that the variation of the size of the magnetic particles does not significantly influence the macroscopic moduli. The 2D approximation on the other hand does: the moduli obtained for the 3D cases are consistently higher than the moduli obtained from 2D simulations and the modulus for the periodic structure is the highest. For this structure, the tensile

Φ	Property	Reuss	2D unif	2D dist	3D unif	3D per	Exp	Voigt
20 %	E_1 [MPa]	1.75	1.992	1.994	2.48	2.83	2.57*	22004
	E_2 [MPa]	1.75	1.986	1.984	2.48	2.83		22004
	ν_{12}	0.49	0.463	0.464	0.489	0.484	-	0.3
	ν_{21}	0.49	0.463	0.463	0.489	0.484	-	0.3
36 %	E_1 [MPa]	2.19	2.745	2.760	3.07	7.01	6.40**	39603
	E_2 [MPa]	2.19	2.731	-	-	7.01		39603
	ν_{12}	0.49	0.440	0.455	0.478	0.484	-	0.3
	ν_{21}	0.49	0.438	-	-	0.484	0.49***	0.3

Table III.11: Effective mechanical properties of two composite materials obtained analytically (Reuss, Voigt), numerical simulation (2D, 3D) and experimentally (Exp). * E' for $\Phi_{Exp} = 19.4$ %, ** E' for $\Phi_{Exp} = 36.2$ %, *** tensile test

loading cases are performed in the direction of shortest distance between the particles. This arrangement is a special configuration for an isotropic composite in which the matrix is maximally constrained on average. Table III.11 also contains the results of the dynamic mechanical analysis, presented in chapter II. The storage modulus obtained from the experimentally investigations lies in between the results obtained from the 3D simulations. The differences between the experimentally and the numerically obtained moduli for the two volume fractions $\Phi = 20\%$ and $\Phi = 36\%$ measure 25% and 80% respectively for the 2D cases, 4% and 30% for 3D simulations with randomly distributed particles and about 10% in both cases for the periodic structure.
For the Poisson's ratio, the estimates of Voigt and Reuss correspond to the material properties of the primary material. The volume fraction does not significantly influence these estimates. The numerical results are closer to the upper estimate (Reuss) than to the lower estimate. The highest value is obtained for the 3D periodic structure followed by the 3D RVE and the 2D simulations. The simulation of a periodic cell shows the best accordance with the experimental results.

III.5 Discussion and conclusions

In the present work, a multiscale model for mechanically stiff and magnetically hard magnetorheological elastomers stH-MAE is presented. On the **microscopic scale**, the inclusions are modeled as continua and the coupling is established by the help of the jump of the magnetic quantities on the particle interfaces. The model has been implemented in a numerical FE code to study the magnetomechanical interactions between two inclusions and the resulting in-plane stress in the matrix. In contrast to comparable studies of microstructural effects in S-MAE, no external load was applied during this study, the stresses were generated by the magnetization of the particles. The numerical results for the resulting forces and

torques are compared to analytic results obtained from the dipole model and a good accordance of the results is found. The analytic expressions therefore provide a good method for a fast calculation of magnetic interactions between particle pairs. The dipole assumption has been used in a number of analytic studies of S-MAE but, as [Borcea+ 2001] point out, it is only valid when the particles are uniformly magnetized, for example for very small particles. According to [Kalina+ 2016] and [Metsch+ 2016], the microstructure is another important factor in view of the dipole assumption. The authors point out that the hypothesis is valid in S-MAE when multiple particles are placed far from each other which is the case for low volume fractions (dilute systems). The numerical analysis of the H-MAE in this study show that the magnetic flux density is nearly homogeneous in the case of two inclusions but not in a network of multiple particles. It is also shown that the torques induced by the magnetization of the particles have a significant influence on the local stress state in the matrix. Torques in magnetically soft particles develop primarily if the geometric axis of anisotropy does not correspond to the direction of the external magnetic field. Spherical particles do not have an anisotropy axis, they are magnetized in the direction of the external magnetic fields. In the present case, the aspect ratio is equal to 1 but the torque intervenes nevertheless because of the magnetic anisotropy induced by the magnetization. A geometric anisotropy of the particles in the direction of magnetization should reinforce the development of magnetic torques. [Ponte Castañeda+ 2011], for example, assume magnetic torques to be the predominant local interactions in MAE with magnetically anisotropic non-spherical particles. Furthermore, it has been shown that the particle form in S-MAE has a significant influence on the net magnetization and the magnetoelastic interactions generated by external magnetic fields [Galipeau+ 2012]. The influence of external magnetic fields on the microstructural effects is a possible subject for future microscopic studies on H-MAE as well.

The multiscale model includes a **homogenization framework** that is applied in a two dimensional case for parametric studies of the **effective properties**. The macroscopic operating point, corresponding to initial stresses generated by the magnetization of the particles, as well as the effective material properties in the magnetic and mechanical domain and for the coupling are determined for a statistically homogeneous composite with inclusions of uniform size. The remanent magnetic flux density of the composite is determined from the operating point. It is shown that the direction of magnetization of the particles determines the direction of magnetization of the composite. Furthermore, the residual flux density increases with increasing volume fraction, which is in accordance with the experimental results shown in the previous chapter. The standard deviation of the magnetic quantities for different microstructures with randomly dispersed inclusions is very low. It is thus concluded that the dependence of the magnetic operating point on the microstructure in isotropic composites is low too. The mechanical operating point on the contrary shows a relatively high fluctuation. The mechanical stresses induced by the magnetization of the particles are hence more dependent on the microstructure than the magnetic properties. The influence of

the particle's magnetization on the effective mechanical properties is relatively weak in this study. One of the reasons is the high stiffness of the matrix since the variation of the modulus is of the same order of magnitude as the stress at the operating point. This variation however is small in comparison with the modulus. In addition, the permeability of the magnetically hard particles is low compared to the permeability of magnetically soft particles, at least in the pre-saturation regime. In this regime, the magnetization of S-MAE is linear and the coupling effects are controlled by the magnetic permeability according to [Galipeau+ 2012]. The coupling is reported much stronger compared to the saturation regime where the saturation magnetization and the distribution of the particles control the coupling effects. An H-MAE may be comparable to an S-MAE in the saturation regime which would explain the weak influence of the magnetization on the modulus and, in addition, the influence of the microstructure (=distribution of the particles) on the operating point. The influence of external magnetic and mechanical loading on the effective properties is also analyzed in this study. The strongest coupling effects are obtained when the magnetic quantity, loading or observation quantity, are aligned with the magnetization of the particles. Nevertheless, a loading perpendicular to the direction of magnetization shows a non-negligible coupling in the transverse direction (magnetically) or induces shear stress. Due to the magnetic anisotropy, the coupling is anisotropic. Concerning the absolute magnitude, the coupling is relatively weak. The most influential coupling coefficient, e_{22}, indicates that a change of 173 mT is achieved by a deformation of 100 %. The underlying model of this study assumes small strain, the variation caused by small strains about 1 % on the magnetic flux density is negligible compared to the residual flux density. To achieve a change in the tensile modulus E_2 of 1 %, which corresponds to 20 kPa, a magnetic field of about 100 kA/m has to be applied.

The effective properties are used to establish a **macroscopic piezomagnetic (PM) behavior law**. The PM model represents the mechanical behavior, the magnetic behavior and the coupling as linear relations. For the numerical simulations, the two first mentioned characteristics are also assigned to the primary material and hence the decoupled effective behavior is in good accordance between the two modeling approaches. The coupling on the other hand is established locally and calculated from magnetomechanical interactions that vary in a nonlinear manner, for example with the distance between particles (cf. equation (III.20) and equation (III.21) for uniformly magnetized particles for example). The local nonlinearity is transmitted to the effective coupled behavior. For S-MAE, a quadratic relation between the magnetic flux density resulting from an externally applied magnetic field and the MS strain has been reported for microstructures with particles aligned in chains [Kalina+ 2016] and for RUC [Metsch+ 2016] for example. In both cases, the quadratic increase diminishes (nearly linear curves [Metsch+ 2016]) when the inclusions reach the magnetic saturation. For the present study, the evolution of the coupling coefficients at $\Delta\varepsilon = 0$ within a magnetic field range of $\pm$ 100 kA/m for either H_1 or H_2 has been studied (cf. figure A.10 in the appendix). The non-negligible coupling coefficients depend on the magnetic field in a linear

manner, hence the dependence of the stress on the magnetic field is quadratic. The coupling coefficients for $H = H^{OP}$ are less dependent on the strain as figure A.10 shows, but the dependence is not linear. The macroscopic coupling phenomena are nonlinear, however, as the present study also shows, the differences between numerical results and the PM model results stay relatively small for a small loading. Hence the model is capable to describe the behavior in vicinity of the operating point.

The multiscale model is applied in several 2D and 3D cases and the **numerical results are compared to the experimental results**, presented in the previous chapter. It is shown that the 2D model is capable to estimate the residual flux density with good accordance. Furthermore, is shown that a variation of the size of the randomly dispersed inclusions has a negligible influence on the effective residual flux density. The numerical results are very close to the analytic estimate for the effective behavior established by Voigt and hence linearly dependent on the volume fraction. This is also observed experimentally, as the previous chapter has shown. Compared to the findings for the magnetic properties, the accordance between the mechanical properties obtained from 2D models and the experimental results is less good. 3D simulations with randomly dispersed particles increase the accordance between model and experimental result but the best accordance is obtained for a 3D periodic cell containing a single inclusion. The experimental results lie between the results obtained with the two 3D models. From a mechanical point of view, the effective properties are closer to the estimate of Reuss than to the estimate of Voigt. A perspective for the modeling is the enhancement of the mechanical description to achieve a better accordance with the experimental results. In order to extend the model, the viscous behavior of the composite should be included in the description of the material behavior. The assumption of a linear coupling has to be validated experimentally by additional tests comparable to the first coupled tests presented at the end of the previous chapter.

Chapter IV

Magneto-elastic interactions and actuation of stH-MAE membranes

IV.1 Introduction

The different studies, presented in this chapter, deal with magnetically induced forces and aim to provide useful information for the design of membrane actuators. The magnetized stH-MAE, which has been studied in the two previous chapters, has been used for the tests, which are presented in the following. The composite has shown a weak magneto-mechanical coupling concerning the material properties, which is therefore considered negligible throughout the study. The material parameters in this chapter are defined according to the results of the experimental studies, presented in chapter II. The beginning of the chapter contains an introduction on the behavior of rigid permanent magnets in electromechanical systems, in which the influence of the shape of a magnet on its magnetization is outlined. The present work is put in the context of the research on membrane actuators in the following. The subsequent sections deal with the capacity of magnetized stH-MAE to generate forces, the influence of magnetization patterns on magnetic characteristics and the magneto-mechanical interactions of stH-MAE membranes.

IV.1.1 Permanent magnets in electromechanical systems

Permanent magnets act as sources of magnetic flux and can provide a certain amount of the stored energy for mechanical interactions. Besides the material properties of the magnet, this amount depends on the demagnetization of the magnet. The demagnetization is influenced by the geometry of the magnet and its environment, as explained in the following[1].
The relation of the magnetic flux density B and the magnetic field H in magnetically hard materials is described by large hysteresis loops (cf. figure IV.1 a). To model the behavior of a permanent magnet in mechatronic applications, the second quadrant of the B–H diagram is of great importance. In this quadrant, the demagnetization behavior of a magnet, also called “principal characteristics", is represented. As the blue curve in figure IV.1 b shows, the principal characteristics are limited by the residual flux density B_r and the coercive field strength H_c. But the evolution of the magnetic flux density with the magnetic field does not necessarily follow the principal characteristics. The following explanation refers to figure IV.1: when magnetic field is decreased from 0 to H_1, which corresponds to the application of a magnetic field opposed to the magnetization, the flux density evolves according to the demagnetization curve (blue curve in figure IV.1 b). But when the magnetic field is increased from H_1 to H_2, the flux density follows another path. To model the behavior of a permanent magnet, this path can be described by a straight line parallel to the tangent on the point $(0|B_r)$ (green line in figure IV.1 b). This representation is a simplified model of the real evolution, which also presents a hysteresis phenomenon (dashed green lines in figure IV.1 b). When the magnetic field is decreased below H_1, B follows the demagnetization curve again during the decrease. An important information for the use of a permanent

[1] The explanations in this sections refer to [Jufer 1998]

magnet is the determination of the lowest point that is attained on the principal characteristics, as it determines the minimum and the maximum of the magnetic flux density the magnet can theoretically provide (B_{min} and B_0 respectively).

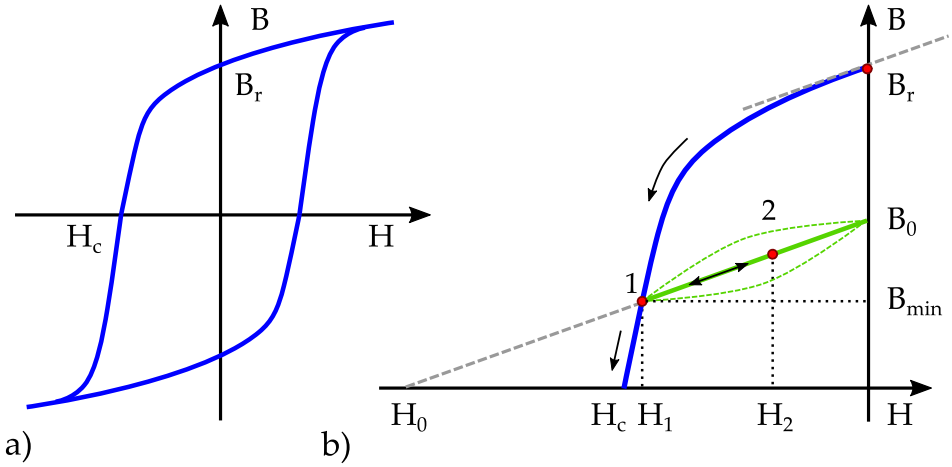

Figure IV.1: Magnetic hysteresis loop (a) and demagnetization curve (b) of a magnetically hard material.

This point is determined by the shape of the magnet and the surrounding environment. To visualize the influences of these parameters, the macroscopic model shown in figure IV.2 a is used. It shows a magnet with the length l_a and cross section A_a. The environment of the magnet, also called external magnetic circuit, is simplified to an equivalent air gap with a length l_e, a cross section A_e and an equivalent permeability μ_e. These characteristics can be used to calculate the magnetic permeance of the equivalent circuit according to the relation $\Lambda_e = \mu_e A_e/l_e$ for a constant permeability μ_e on A_e. To determine the lowest point of the principal characteristics, which are attained by the magnet, the so-called external characteristics of an equivalent magnetic circuit, are calculated. They describe the relation of B and H according to the following relation:

$$B = -\frac{l_a}{A_a} \int_S \frac{\mu_e \, \mathrm{d}A_e}{l_e} \, H = -\Lambda_e \frac{l_a}{A_a} \, H \, . \tag{IV.1}$$

In the B–H–plane, the external characteristics correspond to a straight line with a negative slope, which passes by the origin (cf. orange straight in figure IV.2 b). The intersection of the external characteristic and the characteristic of the magnet corresponds to the demagnetization state of the magnet (red point with $B = B_{min}$ in figure IV.2 b). As equation (IV.1) shows, the shape of the magnet has an influence on the external characteristics and hence on the demagnetization. A high ratio l_a/A_a results in a steep slope of the external characteristics. The intersection point presents a higher magnetic flux density compared to the intersection point of external and principal characteristics for a low ratio l_a/A_a. Exposed to the same magnetic circuit, the demagnetization effect is hence stronger in flat than in elongated structures. In application cases, the geometry of a magnet is generally

fixed. A variation of the external characteristics is due to changes in the surrounding magnetic circuit. This generates a variation of the magnetic permeance limited by a minimum Λ_{min} and a maximum Λ_{max} respectively. The two corresponding external characteristics (orange and yellow straights in figure IV.2 b) are used to determine the minimum and the maximum magnetic flux density of the magnet, B_{min} and B_{max}. The slope of the straight between B_0 and B_{min} corresponds to the equivalent permeability μ_d of the magnet in the circuit. The permeance of the magnet can be calculated and used for the representation of the magnet in an equivalent magnetic circuit (figure IV.2 a) along with a source with a magnetic potential Ψ_{mag}, as shown by [Jufer 1998] for example. Externally applied magnetic fields, which are opposed to the magnetization, are not discussed in detail here but also contribute to the demagnetization in electromagnetic systems.

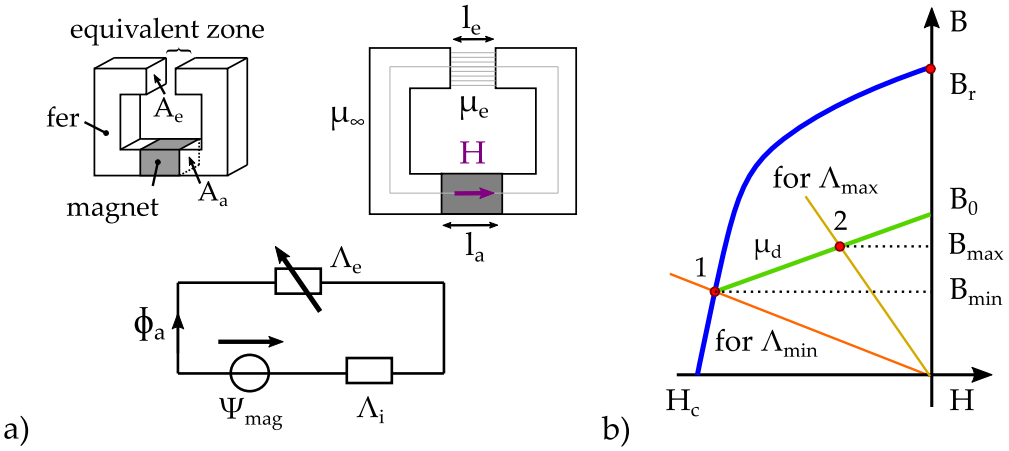

Figure IV.2: Schematic representation of a magnet in its surrounding and corresponding equivalent magnetic circuit (a) as well as demagnetization and external characteristics in the B–H–plane (b)

IV.1.2 Soft actuators based on MAE

The research on the application of MAE in soft actuators is carried out notably in the field of soft robotics and microfluidics. According to [Hilber 2016], iron oxide particles are contained in magnetically soft magnetoactive elastomers (S-MAE) and NdFeB particles in magnetically hard magnetoactive elastomers (H-MAE) in most of the cases. Application examples, presented by the author, are artificial S-MAE cilia and passive valves, which are based on the forces, generated by magnetized H-MAE composites. A review, concerning the application of MAE actuators in soft robotics, has been presented by [Bira+ 2020]. It comprises examples of S-MAE and H-MAE actuators. The presented actuation mechanisms for S-MAE are either based on the high permeability of the magnetically soft particles and an externally introduced field gradient or a structural anisotropy of the material, which causes the deformation of an S-MAE in a homogeneous field. The actuation

mechanisms, presented for H-MAE, are based on the magnetic anisotropy introduced by the permanent magnetization. The authors identify mechanisms for the local control of the magnetic field as one of the key points to further evolution of the application of MAE in soft robotics. They also state the difficulty to miniaturize powerful magnetic field generators.

IV.1.2.a MAE actuators: characteristics and actuation principles

S-MAE composite tubes, based on silicone elastomers and carbonyl iron powder, have been realized by [Diermeier+ 2016]. The actuation mechanism consists of pinching the tube by the help of local field gradients. A prolonged closed state of the tubes could be realized by the help of permanent magnets, according to the authors, since a constant power supply is energy-intensive. The use of this mechanism in medical applications is suggested. Actuation tests of cantilever H-MAE beams have been realized by [Lee+ 2020]. Specimens, measuring 40 mm × 10 mm × 1 mm with elastic moduli between 0.24 MPa and 0.45 MPa, were actuated by the help of a Helmholtz coil. The relatively low field in the air (2.6 mT) was sufficient to generate a deflection of more than a millimeter. A transient response was observed when the magnetic field was turned off until the stabilization of the composite. A study on a fully integrated electromagnetic micro-actuator is presented by [Tao+ 2017]. The study comprises information, that are interesting for the design of MAE actuators, even though the magnetically hard composite, which is employed as actuation element, is based on an epoxy resin and not an elastomer. Firstly, the possibility of a bidirectional actuation with a single planar coil for the generation of the external magnetic field is emphasized. Furthermore, a numerical study on the leakage magnetic flux density of the magnet is presented (figure IV.3 a). According to the authors, the coil is designed such as the distribution of its magnetic field is beneficial for the displacement of the magnet. These considerations exemplary show the design of the external magnetic field in order to optimize the forces. The paper of [Kim+ 2018] presents the 3D printing of H-MAE with different magnetization patterns (figure IV.3 b), based on a viscous suspension which contains pre-magnetized particles.
An electromagnetic coil surrounds the nozzle which allows to modify the orientation of the magnetized magnetic particles during the printing. . The deformation of the composite in external magnetic fields depends on the local direction of magnetization i.e. the magnetic anisotropy. However, the net magnetization of the domains is found to be about 35 % inferior to the magnetization of the same composite material after the polymerization.

IV.1.2.b Membrane actuators

The reviews of [Oh+ 2006] and [Qian+ 2020] concentrate on the application of MAE composites in microvalves. While the first presents mostly membrane actuators, either made from polymer composites or rigid magnetic materials, the second also comprises magnetically actuated cantilever mechanisms. Both reviews men-

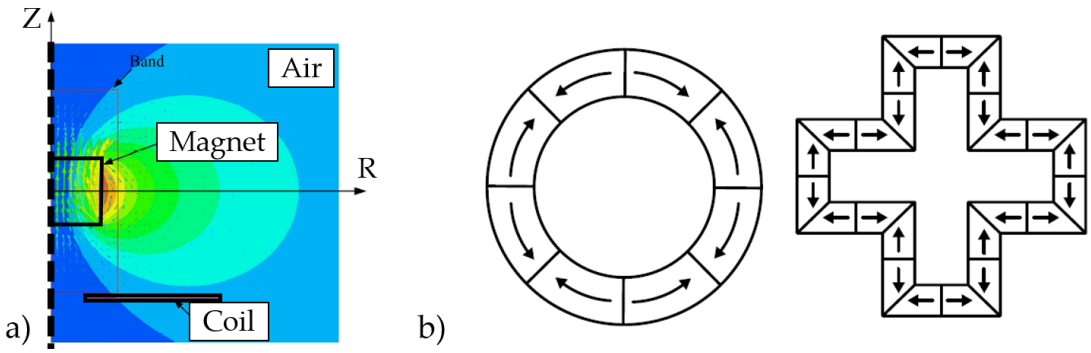

Figure IV.3: Result of a numerical simulation (a) obtained by [Tao+ 2017]: magnetic flux density of a magnetized composite (blue = low, red = high) and schematic view of flat magnetic structures (b) with in-plane magnetization pattern (black arrows), realized by 3D printing by [Kim+ 2018].

tion the use of permanent magnets embedded in soft membranes for microvalves. The example of an electromagnetically actuated valve consisting of a permanent magnet embedded in a PDMS membranes has been presented by [Zhou+ 2011]. The study comprises an analysis of the local stress in the membranes, which is found to be concentrated in the region around the magnet. The transition from the soft elastomer to the rigid magnet gives rise to stress concentration and according to the authors, these regions are potential regions of failure in the assembled structure. Furthermore, an electromagnetically actuated micro-pump, consisting of a H-MAE composite embedded in a PDMS structure, has been presented by [Yamahata+ 2005]. The assembly is actuated by an electromagnetic coil in a magnetic circuit. The influence of the magnetic circuit on the actuation properties is highlighted by the fact, that the stroke of the pump was much higher when the coil contained an iron core.
Besides the magnet-membrane assembly, MAE composites are subject of the research concerning membrane actuators as well. [Singh+ 2014] have presented a membrane valve based on an S-MAE composite containing cobalt nanoparticles dispersed in a PDMS matrix. The mass fraction of the membrane, employed in the valve, measures 50 %, the free diameter of the circular membrane in the valve measures 18 mm and the membrane was actuated by an electromagnet. The maximum stroke obtained for the membrane was 0.68 mm. It is stated that the membrane does not deform in the regions where the magnetic field is uniform. Furthermore, viscous effects are observed for the membrane deflection: the membrane does not recover its original shape in the same manner as it was deformed. [Said+ 2016] embedded NdFeB particles with a diameter between 50 µm and 100 µm in PDMS membranes with an elastic modulus of 0.75 MPa. The actuation properties of two membranes, embedded in actuator structures are studied. The first structure consists of a flat composite membrane and the second one of an embossed membrane, where only the protruding part is made from the composite. The actuation is carried out by an electromagnetic planar coil at distance of 3 mm. Is stated,

that the main challenges for the generation of the deflection are the mechanical fixation and the particle concentration for the flat structure and the loss of flexibility in the embossed structure, which generally showed a lower deflection than the flat structure. The steady state response of the structure was attained after 30 s at the earliest which shows the viscoelastic characteristics of the composite in the presented actuator structures. A concept for the bidirectional actuation of S-MAE membranes was presented by [Paknahad+ 2019]. The micro actuator comprises a PDMS membrane, in which iron nanoparticles are dispersed. The unidirectional actuation is achieved by an electromagnetic planar coil, that generates a magnetic field and hence attracts the magnetically soft composite membrane. The mechanism is duplicated on the opposite side of the membrane which makes a bidirectional actuation possible (figure IV.4). The authors prefer a bidirectional actuation to a unidirectional actuation, since the same stroke causes less mechanical stress in the membrane in the bidirectional configuration.

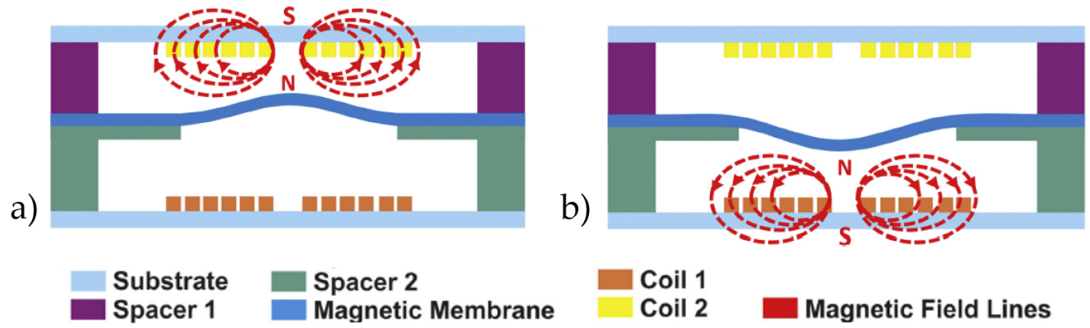

Figure IV.4: Bidirectional actuation mechanism for a S-MAE composite membrane presented by [Paknahad+ 2019] based on the generation of a magnetic field either by coil 1 (a) or coil 2 (b).

A Fe-PDMS membrane actuated by the help of a magnet, is presented by [Nagel+ 2006]. The authors report difficulties due to surface adherence of the membrane to layers, which are placed on top of the actuator. In the case, that other materials were positioned on top of the membrane, the latter did not deform in the actuator. The study of the actuation properties of a Fe-PDMS composite membrane has been performed by [Nanni+ 2012]. The magnet, used for the actuation of the S-MAE membrane, was displaced by micrometer stage during the experiment to vary the air gap. To increase the deflection, one of the edges of the magnet was positioned above the center of the membrane. The reason is the high gradient of the magnetic flux density near the outer regions of the magnet. [Voropaieff 2019] presents the prototype of an actuation mechanism and test results for the actuation of S-MAE composite membranes. The membrane is fixed on its outer boundaries in a magnetic circuit and actuated by an electromagnetic coil. A cooling system for the coil is included, since the continuous supply of energy for the generation of static fields produces heat. The coil comprises a removable tapered iron core, with the thin end pointing towards the center of the membrane. The air gap between the coil and the membrane can be varied in the setup. Isotropic and

different types of structurally anisotropic S-MAE membranes have been tested. It is shown, that the microstructure of the material has an influence on the deflection of the membrane.

IV.1.3 Context of the present work

The present study concerns the forces, magnetized H-MAE composites are able to generate and their use for the actuation of membrane structures. MAE membrane actuators are an intensively studied actuation mechanism and most of the work concerns magnetically soft membranes. H-MAE membranes offer interesting properties, like the possibility of a bidirectional actuation, which has been suggested for S-MAE as well but is more complex to realize. In comparison to embedded–magnet structures, the stress concentration is lower in H-MAE composite membranes and the displacement is more evenly distributed. Two difficulties in the actuation of H-MAE are addressed by the present work:
The first one is the demagnetization. As shown in the paragraph about permanent magnets, the magnetic flux density decreases with the length of a magnet in the direction of magnetization for the same section. Membranes are structures, that demagnetize easily since the ratio of thickness to surface is rather small (l_a/A_a in section IV.1.1). The magnetization is directly linked to the amount of energy, which can be provided for magneto-mechanical interactions, the demagnetization is therefore detrimental for the development of high interaction forces. The influence of the shape of H-MAE specimen on the force, which can be generated provides by the magnetized samples, is studied in the first part of this chapter. In addition to the shape, the influence of the particle content on the force is also demonstrated in experiments. The results are compared to numerical simulations. A solution for the demagnetization of the thin membranes is contained in the subsequent parts of this chapter.
The second difficulty when working with H-MAE membranes is the generation of high displacements. Previous studies show, that uniformly magnetized membrane-like structures show the highest field gradient and flux density in their outer regions. This is the region, where the membrane is generally fixed during the actuation. The present study suggests a solution to generate a field gradient in the middle region of the membrane, where it is the most deformable. Experimental studies of H-MAE membranes with different magnetization patterns have been performed: the magnetic characteristics of differently magnetized membranes are analyzed in a first step. Afterwards, experimental results of the deformation of the membranes due to the interaction with permanent magnets are presented. In addition, the experimental results are compared to numerical simulations.

IV.2 Mechanical forces provided by magnetized H-MAE

In this section, the capacity of magnetized H-MAEs to generate mechanical forces is studied by the help of specimens with different volume fraction and shape. The force, generated by the samples, is analyzed experimentally in a magnetic circuit with varying air gap. Furthermore, a numerical model of the experiment is implemented to study the local magnetic field quantities and to compare the resulting forces with results of the experiment. The section closes with a discussion about the results for the global forces, obtained by experiment and simulation.

IV.2.1 Experimental study

This paragraph presents the experimental study of the forces, generated by four H-MAE specimens. The specimens and the experimental setup are described at the beginning and the measurement protocol is outlined afterwards. The results of the force measurement are presented and discussed at the end of the paragraph.

IV.2.1.a Specimens and experimental setup

For the experimental part of the study, four specimens were cut out of four composite plates with different thicknesses and particle content. The specimens were shaped like flat cylinders. Their geometric characteristics, diameter d and thickness t, as well as the volume fraction Φ and the corresponding residual flux density B_r are summarized in table IV.1. Two different volume fractions, $\Phi_1 = 19.4$ vol% and $\Phi_2 = 36.2$ vol%, have been tested and the specimens were magnetized in the direction of their cylindrical axis in an external field of about 4 T.

Specimens	Φ [vol%]	d [mm]	t [mm]	B_r [T]
mΦ2t2	36.2	47	7.4	0.150 – 0.160
mΦ2t1	36.2	47	1.7	0.150 – 0.160
mΦ1t2	19.4	49	3.2	0.290 – 0.300
mΦ1t1	19.4	49	1.0	0.290 – 0.300

Table IV.1: Geometric and material parameters of the specimens, used for the experimental investigation on the forces induced by the magnetization.

The experimental setup is shown in figure IV.5. It consists of two compression plates, made of 440C steel, that are mounted on a universal testing machine from Instron. The machine contains a displacement sensor in the upper mobile part and a load cell in the static lower part. The measurement range of the load cell covers ±10 kN. As figure IV.5 shows, the setup allows the alignment of the upper and the lower compression plate. The cylindrical specimens were aligned with this axis by the help of concentric marks on the compression plate (cf. figure IV.7 a).

The positioning of a specimen on the lower compression plate is called “pos1” in the following.

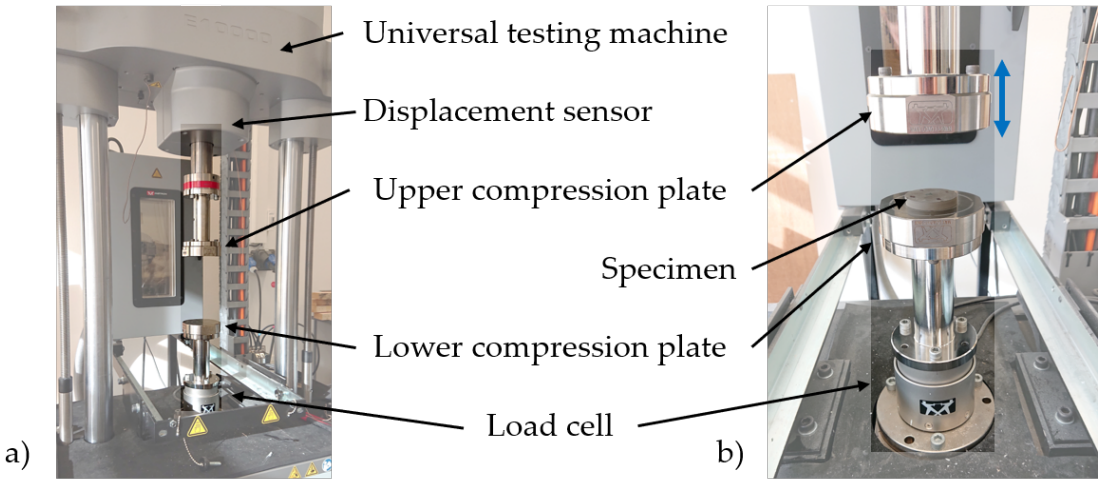

Figure IV.5: Experimental setup, full view (a) and zoom on the setup with a specimen positioned on the lower compression plate (“pos1”) (b).

The magnetized specimens and the ferromagnetic compression plates form a magnetic circuit with an air gap between the specimen and the upper compression plate. At the beginning of a measurement, the latter is kept in a large distance $g = 35\,\mathrm{mm}$ of the specimen surface. It is supposed, that most of the magnetic flux lines are closed in the circuit of the lower compression plate and the specimen in this state (cf. figure IV.6 a). During the measurement, the upper compression plate is moved towards the magnetized specimen and the lower compression plate (cf. figure IV.6 b) in a quasi-static manner (velocity $< 0.03\,\mathrm{mm/s}$). As the air gap reduces, the magnetic flux also propagates in the upper compression plate which becomes part of the magnetic circuit (cf. figure IV.6 c). The distance between a specimen and the upper compression plate is decreased as much as possible without establishing a contact to prevent a compression of the specimen during the measurement. Therefore, the point of first contact is determined manually before a measurement series for each specimen: the upper compression plate is approached in a quasi-static manner and very small steps towards the specimen and the force is observed. As soon as a compression force is observed, the measurement is stopped and the position 0.01 mm above the position of first contact is specified as smallest air gap. A displacement controlled measurement approach was chosen, since the small delay between a detection of contact and the stop signal for the displacement in the machines can already lead to significant compression forces. To prevent an eventual influence of the inertia of the upper compression plate on the position control, the velocity of the plate was decreased for small air gaps. The compression plate was brought back into its initial position at the end of a measurement (cf. figure IV.6 d).

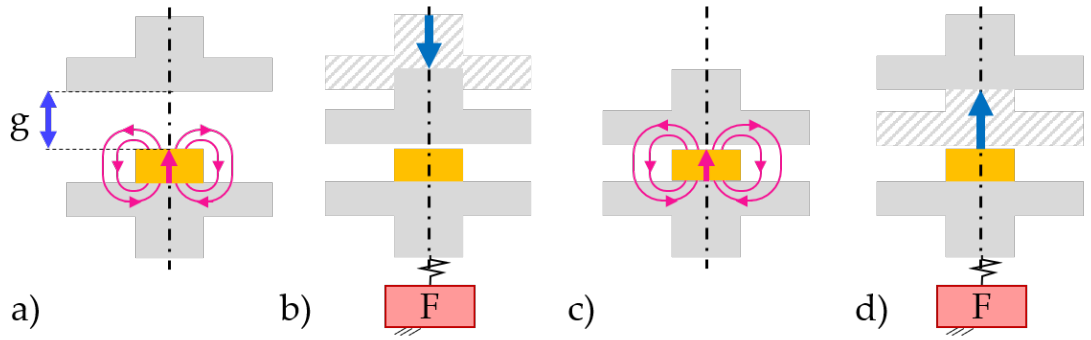

Figure IV.6: Schematic view of the experimental setup: Initial position with the upper plate positioned at a big distance g towards the specimen surface (a), approach phase (b), upper plate positioned near the specimen surface (c) and withdraw phase (d).

During the measurement, the force on the lower compression plate was measured. With decreasing air gap, the magnetic interaction between the specimen and the upper compression plate increases, as more and more of the magnetic flux propagates in the compression plate instead of the air. These interactions induce attraction forces between both components, oriented such as they try to close the air gap. The adhesion of the specimen to the lower compression plate, also induced by magnetic interactions, transmits the forces to the compression plate which allows the measurement of the force by the load cell. The force increases as the air gap is decreased and vice versa. Three measurements are performed in series for each specimen, to test the repeatability of the measurement. In addition, the same measurement protocol was used for a configuration in which the specimen positioned on the upper compression plate ("pos2"). No glue was necessary to position the specimen as the magnetically induced forces kept it in place (cf. figure IV.7 b).

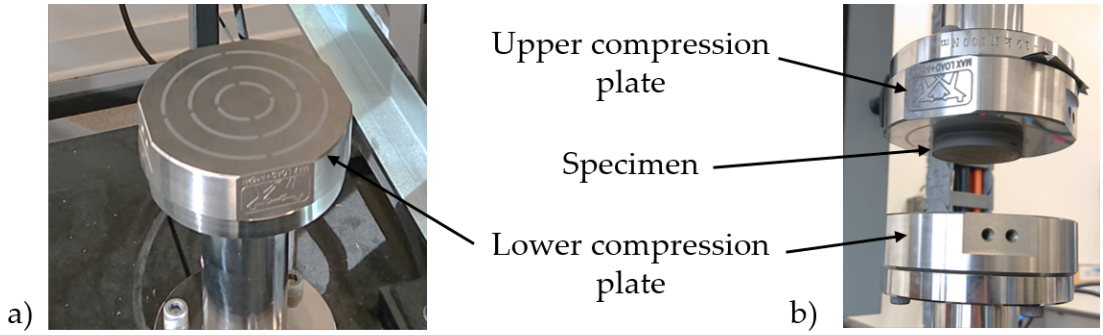

Figure IV.7: Lower compression plate with concentric marks used for the axial alignment of the specimens (a) and configuration with specimen positioned in "pos2" on the upper compression plate (b).

IV.2.1.b Results

Figure IV.8 shows the measurement results of specimen mΦ2t2, positioned on the lower compression plate (pos1). The temporal evolution of the distance of the upper compression plate towards the specimen and the force, measured by the load cell, are represented in figure IV.8 a and b respectively for the entire measurement series. The different slopes in the distance measurement correspond to the different velocities, that are specified for the approach phase ("app"). The velocity in the withdraw phase ("w") is constant. This also shows in the force graphic where the force increase during the approach phase seems to happen in different manners as in the decrease phase, but the difference is only due to the difference in velocity. A small force offset is observed after the first measurement. This offset does not evolve in a significant manner from the second to the third cycle and is also observed for the maximum force. Therefore, it is considered as inherent to the experimental setup. In the results presented in the following, the force offset at the beginning of a cycle is subtracted from the measurement values.

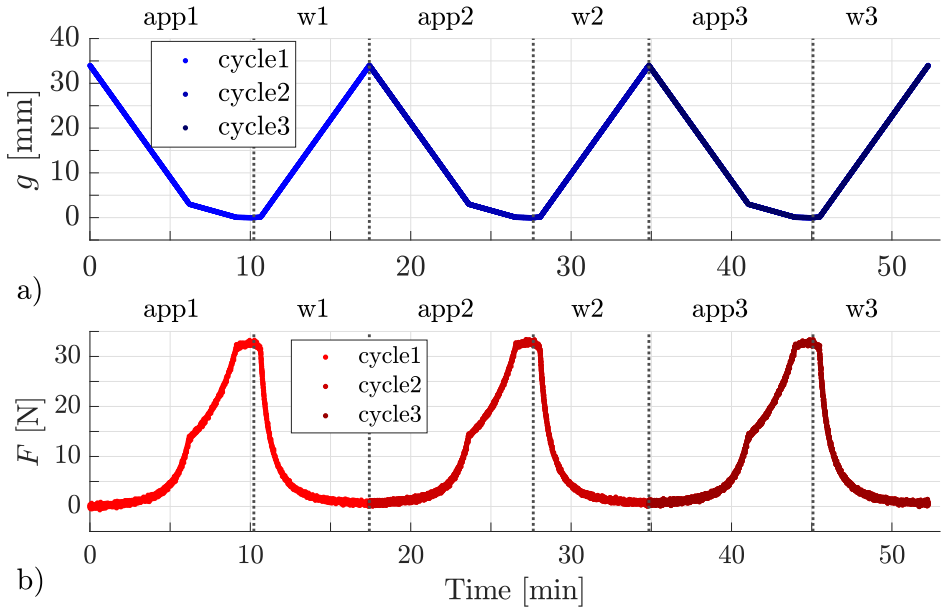

Figure IV.8: Distance g between the specimen and the upper compression plate (a) and the force F on the assembly of specimen mΦ2t2 and the lower compression plate (b) during a measurement series with three cycles.

The measurement values from figure IV.8 a and b are related in the distance-force diagrams shown in figure IV.9. The latter also contains the measurement values of the same specimen positioned on the upper compression plate (pos2). The figure IV.8 a and b of figure IV.9 show the same values, but the distance is represented in a linear scale in figure IV.8 a and in a logarithmic scale in figure IV.8 b. The figure shows, that the force is relatively weak when the distance between the upper plate and the magnet is large. When the distance is inferior to 15 mm, the force increases sharply. A small variation of the distance in this zone

has a high impact on the force. Figure IV.8 b shows, that the increase of the force slows down at a distance of about 2 mm. For distances, smaller than 0.1 mm, the force increases in a quasi linear manner. The measurement results for the three approach phases are in good accordance, the measurement can be carried out in a repeatable manner. Furthermore, the results for the two configurations pos1 (figure IV.5 b) and pos2 (figure IV.7 b) are in good accordance. The position of the specimen in the magnetic circuit is not important as long as the circuit stays the same. The influencing parameter in this measurement setup is the air gap, which indicates a good reproducible of the results with the experimental setup.

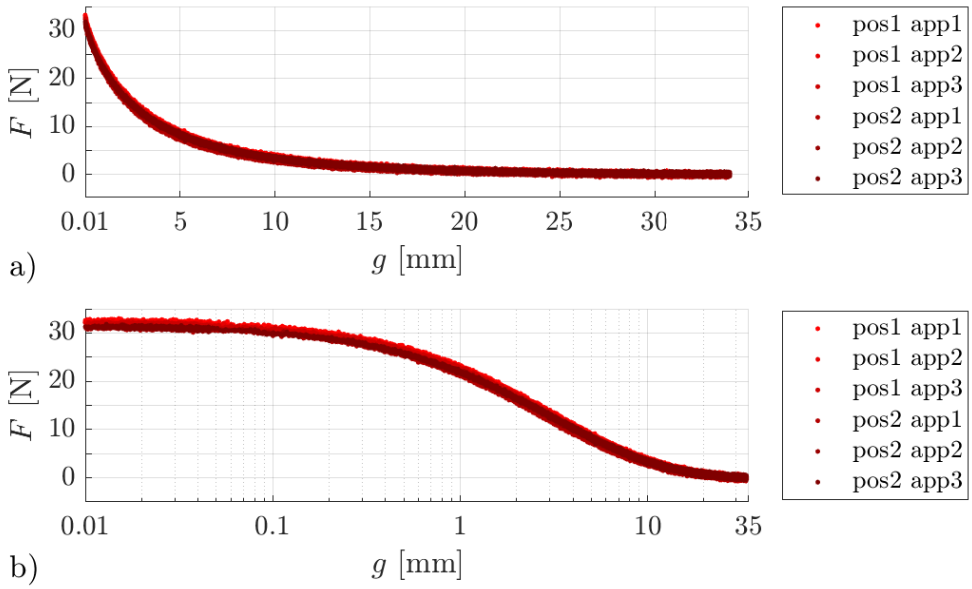

Figure IV.9: Magnetically induced force as a function of the distance between specimen mΦ2t2, placed on the lower or upper compression plate (pos1 or pos2 respectively), on a linear (a) and logarithmic (b) scale during three consecutive approach phases (app).

In figure IV.10, the distance-force relations of the four specimens in the approach phase are represented with a logarithmic scale for the distance. The evolution of the force with the distance is similar for all specimens: The force is zero for a high distance, increases strongly with the decrease of the distance and the increase becomes smaller for small air gaps. The influence of a velocity change is once more visible for a distance between 0.04 mm and 0.05 mm. Due to the decrease of the velocity, the number of measurement points for a position increases and it seems as if the measurement uncertainty increases. While the evolution of the distance-force curves is comparable for the specimen, the absolute values of the force are different. The specimens with the higher volume fraction (mΦ2t2, red dots, and mΦ2t1, yellow dots in figure IV.10) generate higher forces in the experimental setup than the specimens mΦ1t2 and mΦ1t1 (green and blue dots in figure IV.10 respectively). A comparison of the mean values of the force at a distance of 0.01 mm, $\overline{F}_{0.01}$,

demonstrates the differences (cf figure IV.10). The reason for the force difference is the higher particle content, which leads to a stronger remanent magnetization and thus to stronger interaction forces. Another factor, that visibly plays a role for the generation of the force, is the specimens' shape. Comparing the values for an air gap of 0.01 mm, it is stated that a higher thickness t leads to a stronger force for both volume fractions. The origin of this effect is the demagnetization field inside the specimen. The field reduces the effective magnetization of the specimen and, as it is stronger for the flat specimen than for elongated specimen, the force generated by flat specimen is weaker. An additional point, that is visible in the graphic, is a temporary decrease of the force for specimen mΦ1t2 for position pos2 during the first cycle. The specimen was positioned on the upper compression plate, a decrease of the force indicates a contact with the lower part of the setup. However, after a short interval in which the force decreases, it increases abruptly at a distance of 0.045 mm and then again increases slowly. This behavior is only observed once, it may be due to a protruding part on the specimen surface.
As the air gap is reduced to a very small distance where the force no longer varies to a large extend, the force level for low air gaps is considered as representative for a contact force. The presence of a contact force explains, that the specimen is kept in place in position pos2: the forces, that attract the specimen towards the upper compression plate, are superior to the effect of the gravity. The force between the specimen and the compression plate does not show itself in absence of external forces. This behavior is roughly comparable to the action of a mechanical spring element.

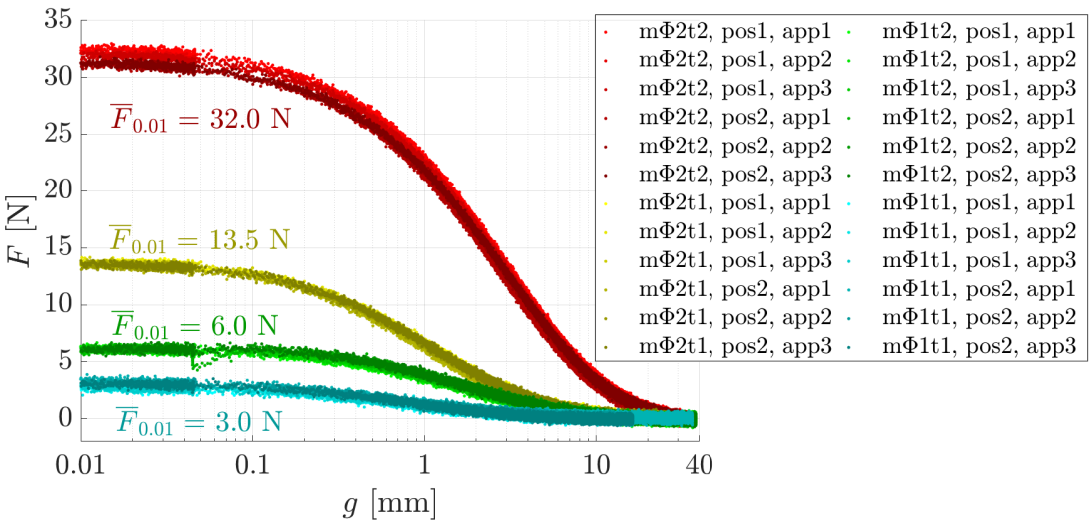

Figure IV.10: Force as a function of the air gap (distance) during three approach phases (app) and two placements of the four specimens mΦ1t1 (blue), mΦ1t2 (green), mΦ2t1 (yellow) and mΦ2t2 (red).

IV.2.2 Numerical modeling of the experiment

This paragraph presents a numerical model of the experimental setup. The implementation of the different parts of the setup is described at the beginning, followed by the description of the study cases. A comparison of the experimental and numerical results is carried out and subsequent parametric studies on the influence of geometry and material parameters on the resulting magnetic force are detailed. The paragraph closes with a discussion of the study. The magnetic behavior of the specimens is also modeled as magnetically linear ($\mu_r = 1.1$) with an additional remanent magnetic flux density B_r dependent on the volume fraction.

IV.2.2.a Implementation of the model

The experimental configuration is implemented by the help of numerical finite element simulations in a 2D axisymmetric model. Figure IV.11 a shows the $\boldsymbol{e}_r$ – $\boldsymbol{e}_z$ plane, in which the geometry is defined. It is supposed, that the main part of the magnetic flux stays in vicinity of the specimen. Therefore, the upper and lower compression plate are modeled only partly and as separate parts. The specimen is placed on the lower compression plate in the model.

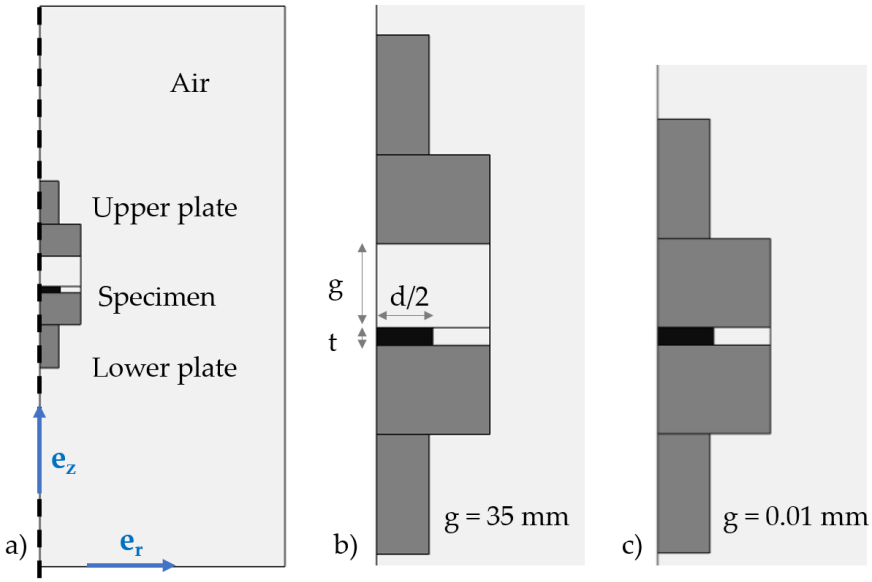

Figure IV.11: 2D axisymmetric simulation of the global force test: full view of the model (a) and zoom on the arrangement of the magnetic parts for the highest (b) and lowest (c) air gap.

The air volume, which is surrounding the magnetic parts, is cut in three parts. This allows a refinement of the mesh near the specimen and as a consequence an increase of the precision of the calculated local quantities. The air is modeled as magnetically neutral material with a relative permeability μ_r of 1. The compression plates are modeled as linear magnetic materials with $\mu_r = 1000$. For Φ_2,

$|\boldsymbol{B}_r|$ measures 0.293 T and for Φ_1 0.157 T. Stationary simulations were performed for each of the four specimens and various air gaps g. The distance between the specimen and the upper compression plate is varied between 35 mm and 0.01 mm. The resulting force on the assembly of lower compression plate and the specimen, which results from the magnetic interaction with the upper compression plate, is calculated by the help of the Maxwell stress tensor (cf. chapter I).
The numerical simulations allow the analysis of the local field quantities. Figure IV.12 shows the local magnetic flux density vector $\boldsymbol{B}$ (pink arrows) for the biggest and the smallest air gap as well as the norm of the magnetic flux density $|\boldsymbol{B}|$ normalized by the remanent magnetic flux density $|\boldsymbol{B}_r|$ for specimen mΦ2t2. The results for $g = 35$ mm are shown in figure IV.12 a. The pink arrows represent the magnitude and the orientation of $\boldsymbol{B}$. The magnetic flux propagates in the lower compression plate and the specimen as well as in the air. The magnitude of $\boldsymbol{B}$ decreases rapidly with increasing distance towards the specimen. The colors in the right graphic of figure IV.12 a indicate that the magnetic flux density is not evenly distributed in the specimen. It is much stronger in the outer region where the magnetic flux forms closed loops easily and the flux density is hence higher. In the configuration shown in figure IV.12 b, the air gap is very small ($g = 0.01$ mm). The pink arrows show that the magnetic flux propagates in the upper compression plate. The magnitude of the magnetic flux density is higher for $g = 0.01$ mm than for $g = 35$ mm, as the comparison of the size of the pink arrows and the colors of figure IV.12 a and figure IV.12 b show. In addition, the flux density is evenly distributed in the configuration with a small air gap.

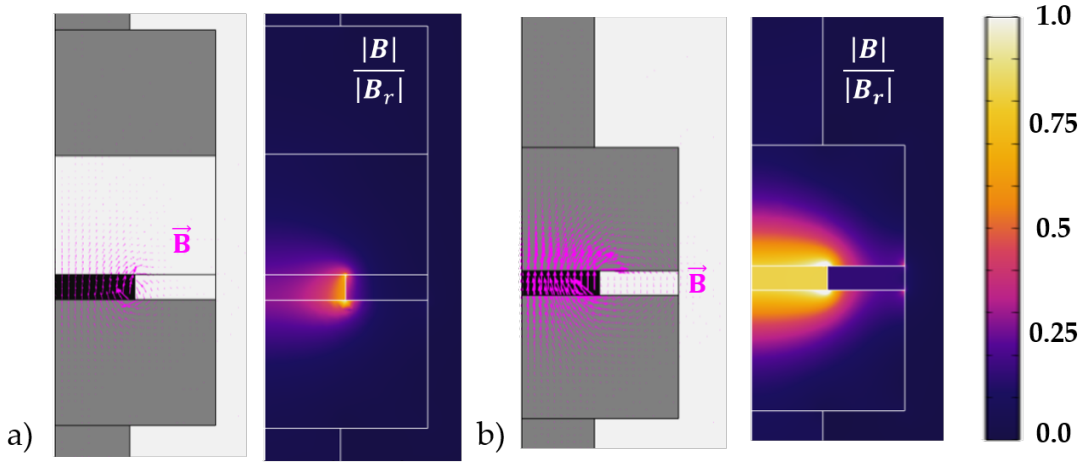

Figure IV.12: Magnetic flux density $\boldsymbol{B}$ and the ratio of $|\boldsymbol{B}|$ and the residual magnetic flux density $|\boldsymbol{B}_r|$ respectively for the biggest (a) and smallest (b) air gap.

The evolution of the force with the air gap g, obtained from the simulation for mΦ2t2, is shown in figure IV.13. The experimental results are also shown for comparison. The forces evolve in the same way in both cases: a strong increase of the force, when the distance is reduced from 15 mm to 2 mm, followed by a slower

increase for smaller distances. The absolute values are not in good accordance: the forces converge to a higher force in the simulation than the experiment. The force at $g = 0.01\,\text{mm}$ obtained from the experiment ($\overline{F}_{0.01}^{exp}$) and the simulations ($F_{0.01}^{simu1}$) for the four specimens are summarized in table IV.2. The difference between the forces from experiment and simulation, $F_{0.01}^{es1}$, shows, that the force is overestimated by the simulation for the four specimens by a large extent. The model does not represent the configuration present in the experimental setup. One possible reason is the modeling of the testing machine via two separate parts, in which the magnetic flux does not circulate. This hypothesis has not been tested yet, but could be verified experimentally in the setup. The smaller force could also be caused by demagnetization of the specimens, which are modeled by the help of a linear magnetic material model. A numerical magnetic simulation of the specimens surrounded by air shows, that the demagnetizing field does not exceed 205 kA/m. Based on the experimental results shown in section II.3.1, the demagnetization of the composite remains moderate in this range and the magnetic behavior is approximately linear in this region. Supposing that the assumption of an axi-symmetric configuration and the magnetic decoupling of the compression plates are valid, several geometric and material parameters of the magnetic circuit have been tested on their influences on the force.

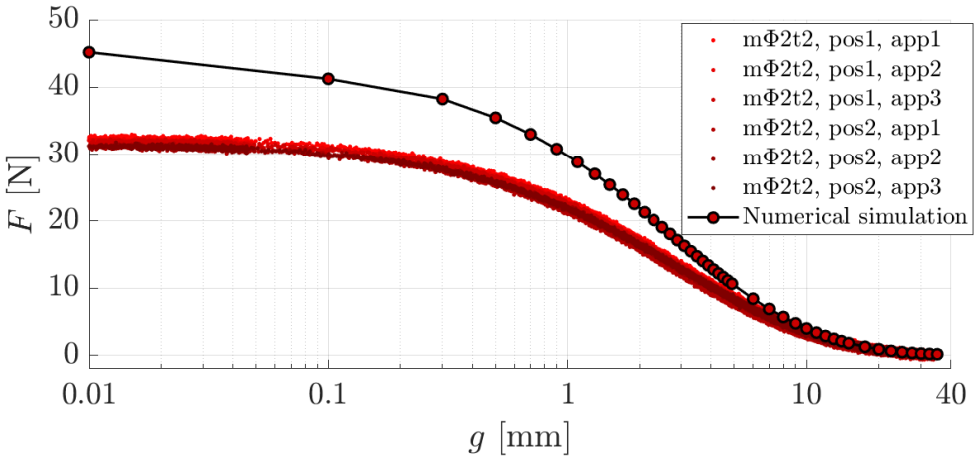

Figure IV.13: Evolution of the force F with the air gap g obtained for mΦ2t2 from the experimental investigations and a numerical simulation.

The parametric study is carried out for the specimen mΦ2t2 for an air gap of $g = 0.1\,\text{mm}$. In a first step, the influence of the thickness of the specimen on the force is analyzed. A decrease of the thickness also decreases the force, but the dependence of the force on t is low: for $t = 5\,\text{mm}$ instead of 7.4 mm, a force of 39.7 N has been obtained, which is still significantly higher than the 32 N measured during the experiment. The measurement uncertainty for the specimen thickness is low and t is not included in further studies. In the next step, the influence of the residual flux density B_r of the specimen mΦ2t2 on the force was analyzed. To obtain the result of the experiment, B_r has to be reduced from 0.293 T to 0.251 T.

Specimen	$\overline{F}_{0.01}^{experiment}$ [N]	$F_{0.01}^{simulation}$ [N]	$\Delta F_{0.01}^{es}$ [N]
$m\Phi$2t2	32	45.2	13.2 (31%)
$m\Phi$2t1	13.5	41.7	28.2 (102%)
$m\Phi$1t2	6.0	13.1	7.1 (74%)
$m\Phi$1t1	3.0	12.2	9.2 (121)%

Table IV.2: Magnetically induced force for an air gap of 0.01 mm obtained for the four specimens from the experiment and numerical simulations and the difference between the results $\Delta F_{0.01}^{es}$.

A linear relation between the particle content and the volume fraction has been observed for the composite material, the difference in the magnetic flux density represents a difference of 5.2 % of the volume fraction. Experimental analysis of the residual flux density of the four specimen confirm the initially used values, hence the uncertainty of the magnetic flux density is too weak to be responsible for the difference between experiment and simulation. A parametric study of the magnetic permeability of the compression plates was conducted in the next step. According to the manufacturer, the plates are made of the magnetic steel 400C and a high permeability of 1000 was chosen as a consequence. To obtain a lower force, the magnetic permeability of the compression plates was reduced in additional studies with the specimen mΦ2t2. The study shows, inter alia, that the magnetic force varies significantly when the permeability falls below 500. The best accordance with the experimental result was obtained for $\mu_r = 18.75$. The value was tested in simulations with the remaining three specimens and the results were also in good accordance with the experimental results. Nevertheless, 18.75 is a very low permeability value for a magnetic steel. It was not possible to experimentally verify the permeability for multiple reasons. Testing the actual material would have meant the destruction of the compression plates. Magnetic testing of a 440C steel tore would probably not be representative, since the compression plates may have undergone mechanical processes during the fabrication and details about the fabrication could not be obtained. It is possible, that hardening processes influenced not only the mechanical but also the magnetic properties of the material in the whole volume or on the surface. The hypothesis of a non-magnetic coating was tested in the next step. A non-magnetic material was inserted on top of the lower compression plate under the specimen mΦ2t2 and between the air gap and the upper compression plate in the simulation. The relative permeability of the coating was set to one. A coating thickness of 1 mm lead to a good accordance between experimental results and the numerical simulation, not only for specimen mΦ2t2, but also for the three remaining ones. The results for the distance-force relations, obtained from the simulations with a non-magnetic coating and a low permeability of the steel material are shown in figure IV.14 along with the experimental results. The two simulation approaches are in good accordance with the experimental results for low air gaps and also according to their evolution.

The parameters have been varied one by one in this study. In the experiment, it is likely that the difference is caused by a combination of the different effects. More information about the correlation of the parameters could be obtained by a multiparameter study. The experiment could furthermore be conducted with a controlled variation of some of the parameters to test the model in future studies.

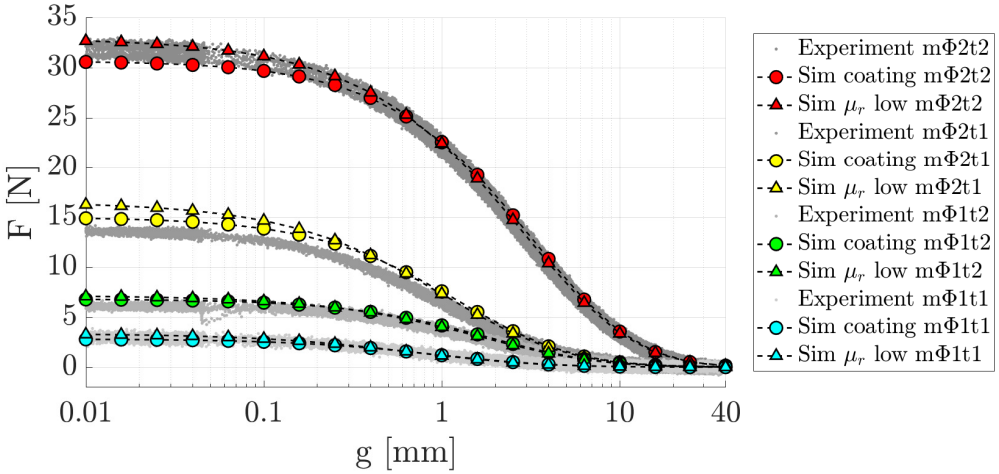

Figure IV.14: Force-distance curves obtained for the four specimens from the experimental investigations and numerical simulation with the assumption of either a non-magnetic coating of 1 mm on the compression plates (Sim coating) or a low permeability of 18.75 of the compression plates (μ_r low).

IV.2.3 Intermediate conclusions

In the first part of this section, an experimental setup and a measurement protocol for the determination of magnetic forces, generated by H-MAE specimens, have been presented. The setup allows a repeatable measurement of the force in the magnetic circuit. The results, obtained for very small air gaps, give an estimation of the contact force. A comparison of the results for the four specimen shows, that the force, generated by an H-MAE, depends on the content of magnetic particles, but also on the shape of the specimen. Furthermore, the magnetic circuit, which surrounds the H-MAE, plays an important role for the generation of magnetic forces. This is not only demonstrated by the experimental results, but also by the numerical mode. For high air gaps, the demagnetization affects the flat cylindrical structures stronger in the central region, where the magnetic flux density is significantly decreased. The modeling of the experiment shows, that the evolution of the force with the air gap can be predicted qualitatively. However, the correct quantitative approximation of the results requires additional knowledge about the magnetic circuit. The material properties of the parts, that compose the magnetic circuit, play an important role for the magnetically induced force. Geometric uncertainties in the setup, like a misalignment of the specimen

and the magnetic compression plates or a variable air gap due to the inclination of the compression plates, have not been included in the study. They should be subject of future studies, since the geometric parameters of the magnetic circuit play an important role and are a crucial part of the preparation of the experiment. A quantitative prediction of the forces at small air gaps would allow the prediction of the magnetically induced global contact force. Investigations on the local force density are presented in the following sections.

IV.3 Bi-directional magnetization of H-MAE membranes

The previous section shows, inter alia, that the central region of flat magnetized structures is stronger affected by demagnetization fields than the outer regions. Strong magneto-mechanical interactions are therefore more likely to develop in the outer regions. Membrane structures, however, are generally fixed on their outer contour, while the central region is actuated. The approach, presented in the following, aims to decrease the influence of demagnetizing fields in the center of H-MAE membranes by means of a bidirectional magnetization. At the beginning, the preparation of the magnetized membrane specimens is described and an analysis of the leakage magnetic flux density is presented afterwards. The results are discussed at the end of the section.
The experimental investigations are carried out for four circular H-MAE membranes with a diameter of $d = 24\,\mathrm{mm}$. They are cut out of composite sheets by a cutting die. Two membranes have a volume fraction of $\Phi_1 = 19.4\ \%$ and a thickness of $1.1\,\mathrm{mm}$, while the other two have a volume fraction of $\Phi_2 = 36.2\%$ and a thickness of $1.5\,\mathrm{mm}$. Two magnets, made from the material BMN-42SH with a diameter of $25\,\mathrm{mm}$ and a thickness of $1\,\mathrm{mm}$, were also tested for comparison. The magnitude of the residual flux density in the out-of-plane direction, B_r^{oop}, has either been measured (membranes) or was specified in the datasheet (rigid magnets). The values are summarized in table IV.3 along with the geometric data of all specimen. Concerning the magnetic polarization, one specimen of each volume fraction is magnetized uniformly in its out-of-plane direction. Therefore, the membranes are exposed to a unidirectional magnetic field of approximately $4\,\mathrm{T}$. The other specimen of each volume fraction respectively is magnetized such as it shows two inverse directions of magnetization figure IV.15. For this purpose, a magnetization tool, developed by the company MMT has been used. A transition zone, or pole transition, with a width of $1\,\mathrm{mm}$ is present in the center of the membrane. An experimental study of the magnetic characteristics of the membranes and the magnets is presented in the following.
Experimental measurements and numerical simulations have been performed to analyze the magnetic characteristics of the membranes and the magnets. For the experimental part, the magnetized specimens were fixed in a test bench, developed by the company MMT, while a triaxial magnetic Hall sensor was displaced in

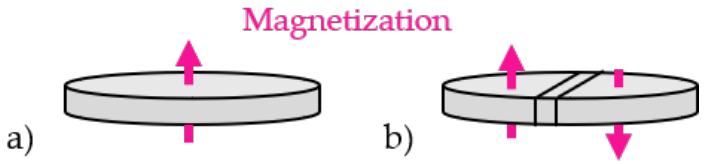

Figure IV.15: Schematic representation of membranes with unidirectional magnetization (a) and bidirectional remanent magnetization (b).

Specimens	Material	d [mm]	t [mm]	B_r^{oop}	magnetization
$m\Phi 1M1$	H-MAE Φ_1	24	1.1	0.150 – 0.160	unidirectional
$m\Phi 1M2$	H-MAE Φ_1	24	1.1	0.150 – 0.160	bidirectional
$m\Phi 2M1$	H-MAE Φ_2	24	1.5	0.290 – 0.300	unidirectional
$m\Phi 2M2$	H-MAE Φ_2	24	1.5	0.290 – 0.300	bidirectional
$mM1$	Magnet	25	1.0	1.290 – 1.330	unidirectional
$mM2$	Magnet	25	1.0	1.290 – 1.330	bidirectional

Table IV.3: Geometric and material parameters of the specimen and the magnets used for the experimental investigation in this study.

a surface parallel to the specimens' surface. A schematic representation of the measurement configuration is shown in figure IV.16. The test bench allows the measurement of the leakage flux density in an amagnetic environment. During a measurement, the sensing element had a distance of 1.2 mm towards the surface as the housing of the sensor did not allow a further approach: the air gap between housing and specimen surface measured 0.2 mm. The sensor was displaced in steps of 1 mm and the magnetic flux density, generated by the membrane in the air, has been measured. In addition, the magnetic flux density in absence of the specimens were measured. It varied between −0.24 mT and −0.08 mT and is considered as negligible for the measurements.

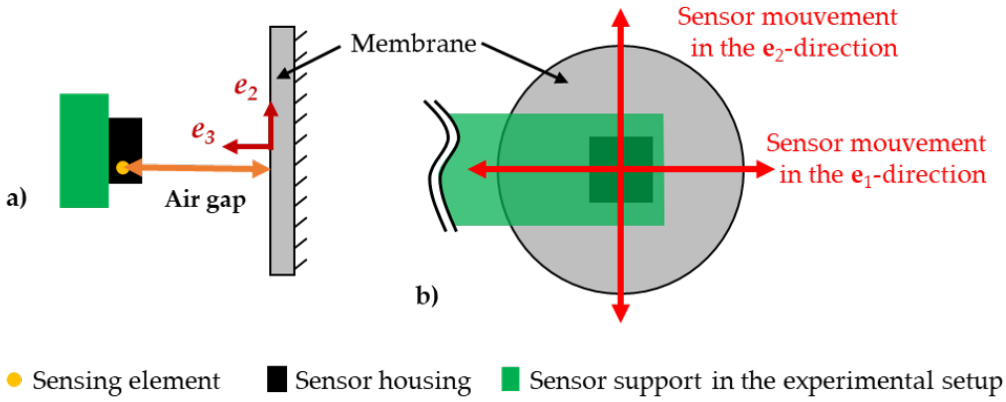

Figure IV.16: Schematic view of the magnetic flux density measurement, side view (a) and top view (b) of principal elements of the experimental setup.

The three graphics in figure IV.17 show the normalized out of plane component of the magnetic flux density for the three specimens with unidirectional magnetization. The results are normalized with respect to the maximum leakage flux density of each test individually. Positive values are obtained for the middle parts of the measurement zone where the magnetic flux propagates in the direction of the sensor element and negative values, where it propagates in the inverse direction. The graphics show the flux density in the air at 1.4 mm distant from the surface, the circle in the graphic does not correspond to the exact diameter of the specimen. Nevertheless, the results show, that the magnetic flux density in the out of plane direction has the highest magnitude in the outer regions. Starting form a position on the radius and going towards the center of a specimen, the magnetic flux density drops about 40 %. The evolution is in accordance with the simulation results of the previous section and show, that the magnetic flux density is high when the flux can propagate in small closed loops in the air. This is the case in vicinity of the boundaries for a unidirectional magnetization. The graphic also shows, that the magnetic flux propagates in an axisymmetric manner in the out of plane direction with respect to the center. The maximum magnetic flux density measures 84 mT for mM1, 26 mT for mΦ2M1 and 11 mT for mΦ1M1. The big difference with respect to the residual flux densities is due to the distance of the sensor to the specimens' surface, as well as to the demagnetization fields in the specimen. A quantitative analysis of the magnetic flux density is performed for each specimen later in this section, the experimental results, used in the corresponding study, are marked with dots in the figure IV.17.

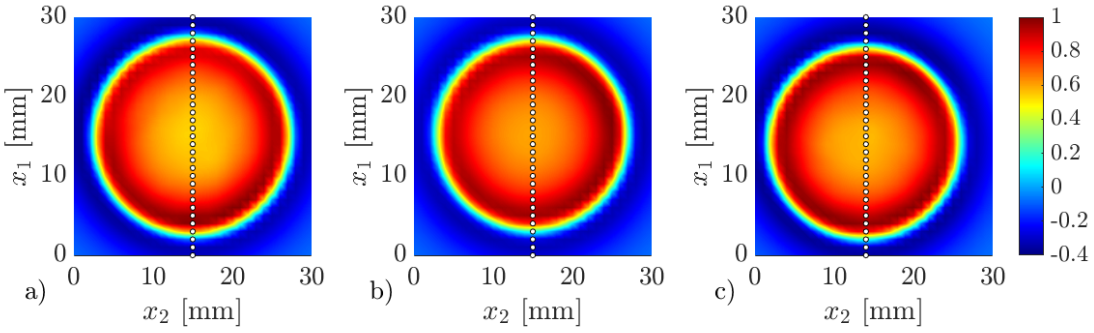

Figure IV.17: Normalized leakage magnetic flux density in the direction $\boldsymbol{e}_3$ at a distance of 1.4 mm of the specimens mM1 (a), mΦ2M1 (b) and mΦ1M1 (c).

The results for the specimens with bidirectional magnetization are shown in figure IV.18. The pole transition was not aligned in the same direction for the three specimens but this is not important for the subsequent analysis. The qualitative results of the three specimens are similar, just like for the specimen with a unidirectional magnetization. The two magnetic poles can be clearly distinct in the graphics by the color, in the region of the pole transition the magnetic flux density has nearly no out of plane component. The flux mitigates from one pole towards the other in the direction, which is perpendicular to the measurement direction. The largest magnetic flux density is obtained in the region near the pole transition,

especially where the pole transition meets the outer boundary of the specimen. On this position, the flux magnetic flux forms the closed lines easily. The weakest intensity for the magnetic flux density is measured in the middle of the magnetic poles, as for the specimens with unidirectional magnetization. In the present case, however, the central region of a pole is not coincident with the central region of the membrane.

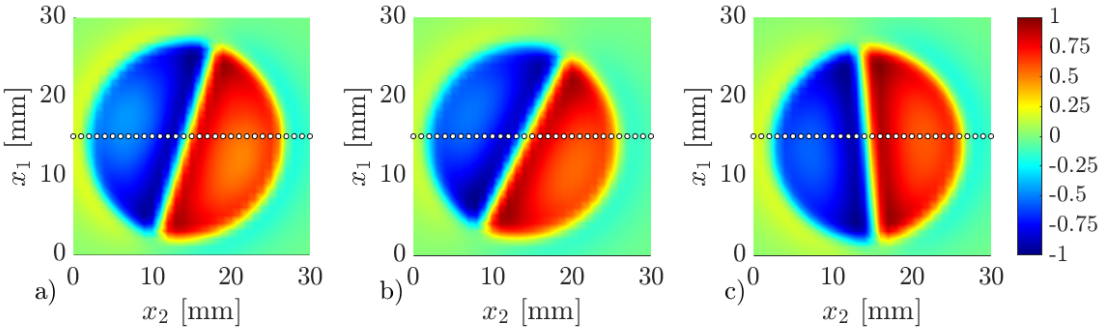

Figure IV.18: Normalized leakage magnetic flux density in the direction $\boldsymbol{e}_3$ at a distance of 1.4 mm from specimens mM2 (a), mΦ2M2 (b) and mΦ1M2 (c).

A quantitative comparison of experimental results and numerical magnetic simulations is presented in figure IV.19. In the numerical 3D model, the specimens were modeled with the geometric parameters of table IV.3. An isotropic material model was chosen and the material parameters for $|\boldsymbol{B}_r|$ and μ_r used in the model are summarized in table IV.4. The boundary element method (BEM) was used to mesh the surface of the geometries and to model a magnetically neutral environment around the magnet. The out–of–plane component B_3 of the magnetic flux density was obtained at positions comparable to the evaluation points of the experiments. The results of simulation and experiment are shown in figure IV.19.

Material	$\lvert\boldsymbol{B}_r\rvert$ [T]	μ_r
Permanent magnet	1.300	1
H-MAE, $\Phi = 36.2\,\%$	0.293	1.1
H-MAE, $\Phi = 19.4\,\%$	0.157	1.1

Table IV.4: Magnetic material parameters used in the numerical simulations.

Figure IV.19 a shows the results for the specimens with unidirectional magnetization. A difference of the magnitude of the magnetic flux density is observed between the materials. Due to the high remanent magnetization, the magnet (red) shows the highest magnitudes followed by the specimen with the higher volume fraction Φ_2 (green) and the less charged composite with Φ_1 (cyan). The quantitative evolution of the flux density in the radial direction confirms the observation made in the qualitative analysis: there is a difference of about 40 % between the flux density measured above the center of the membrane and the boundary area.

The change of direction of the leakage flux density is also visible in the graphic. The results of numerical simulation and the experimental results are in good accordance. Figure IV.19 b shows the results for the specimens with bidirectional magnetization.

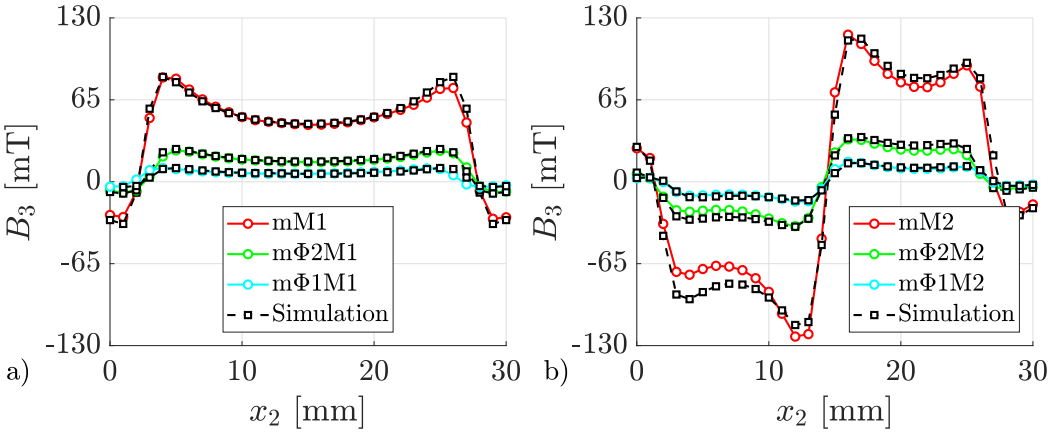

Figure IV.19: Magnetic flux density component B_3 on a diametrical line for the specimens mM1, mΦ2M1, mΦ1M1 (a) and mM2, mΦ2M2, mΦ1M2 (b), results of the measurements and of numerical simulations.

The change of direction of the flux density indicates the pole transition while the slight decrease between two peaks for each pole is due to the fact, that the demagnetization is stronger in the middle of the poles. The reversion of the magnetic flux density at the outer boundaries is also visible. In general, there is a good accordance between experimental results and simulation, except for the results of the rigid magnet in the range of $x_2 = [3\,\text{mm}\ 8\,\text{mm}]$. Since the accordance drops only for one of the two poles, it is supposed that the origin is of experimental nature. It could be due to uncertainties in the alignment of magnet and the sensor during the experiment for example.
The results show two important points, that presumably favor the magnetomechanical interactions of membranes with a bidirectional magnetization. Firstly, the maximum intensity of the out-of-plane magnetic flux density is measured in the center of the membrane. It is hence located at the position where strong interactions are required. Secondly, the residual flux density in vicinity of the pole transition also increases the absolute value of the maximum magnetic flux density. For the magnet for example, the maximum magnitude for B_3 in figure IV.19 measures 83 mT for a unidirectional and 123 mT for a bidirectional magnetization. The pole transition decreases the distances the magnetic flux has to overcome to form closed loops, which increases the density of the magnetic flux lines. For actuation purposes, the magnitude of the magnetic flux density is an important factor, as a higher magnetization generates higher forces. This study concerned the magnetic properties of the specimens, the magneto-mechanical interactions are studied in the next section.

IV.4 Actuation of H-MAE membranes (experiments)

This section presents an experimental study concerning the magnetic actuation of H-MAE membranes. The membranes, studied in the previous section, were actuated with the two rigid magnets, which have also been part of the previous study. The experimental setup, used for the actuation is described at the beginning of this section. In the following, the measurement of the displacement is detailed, including the measurement protocols and the post processing. The experimental results are presented and discussed subsequently.

IV.4.1 Experimental setup

The test bench, which has been developed for the analysis of the membrane displacement, is presented in the following. It consists of two parts: the first part allows to vary the relative position of the rigid magnet with respect to the membrane in a magnetically neutral environment. The second part consists of an optical measurement system, that records the out–of–plane displacement of the membrane, caused by magneto-mechanical interactions with the magnet.

IV.4.1.a Functional principle

The functional principle of the two parts is represented in figure IV.20. While the membrane is fixed on its outer boundaries, the magnet can be displaced in the three orthogonal spatial directions $\boldsymbol{e}_1$, $\boldsymbol{e}_2$ and $\boldsymbol{e}_3$, as figure IV.20 a shows. A variation of the position of the magnet in one of the directions is designated with the corresponding component of the position vector $\boldsymbol{x}$ preceded by the symbol Δ (e.g. Δx_1 for a displacement in $\boldsymbol{e}_1$). Figure IV.20 b visualizes the displacement measurement. Magnet and membrane remain fixed in their positions during the measurement. Their magnetization is oriented such as the same magnetic poles face each other and since identical magnetic poles repel each other, the soft membrane bulges away from the magnet. The optic measurement system measures the distance towards the top surface of the membrane and the data can be used to obtain the displacement of the membrane. The in–plane alignment of magnet and membrane (Δx_1, Δx_2) as well as the influence of the air gap (Δx_3) on the displacement of the membrane can be studied using this functional principle. Repulsive magnetic interactions were chosen for the study to assure a free displacement and the smallest possible air gap at the same time. If the membrane was attracted by the magnet, the latter could limit its displacement. In addition, the lighting conditions were supposed to be better for a convex surface than for a concave surface. Besides, repulsive forces between a membrane and a magnet are an actuation configuration that is not possible with S-MAE membranes, as only attractive forces would be generated.

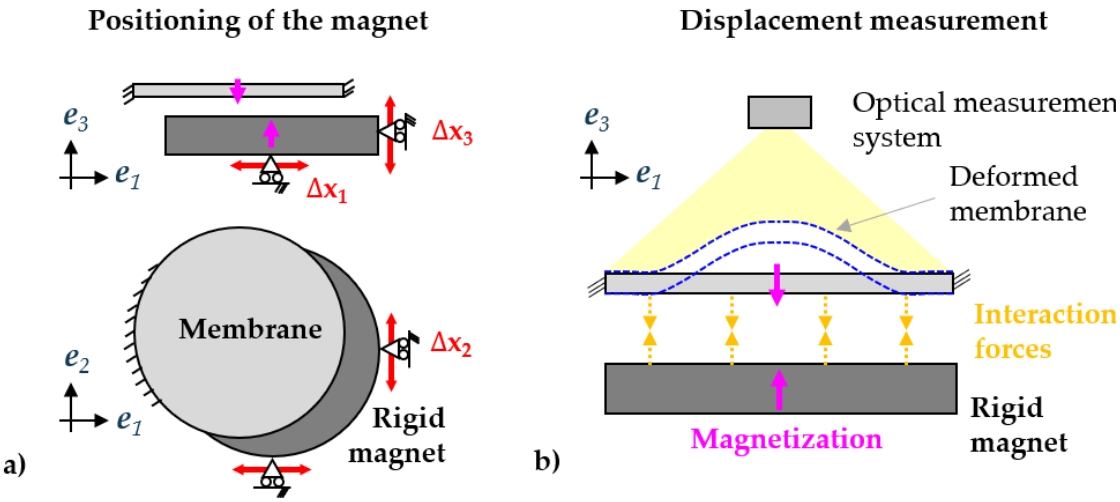

Figure IV.20: Functional principle of the experimental setup, composed of a part responsible for the positioning of the magnet (a) and another part, allowing the measurement of the out–of–plane displacement of the membrane (b).

IV.4.1.b Test rig

The corresponding experimental setup is shown in figure IV.21. The photo on the left contains a general view of the experimental setup while the photo on the right is a zoom on the magnet and the membrane. The different parts of the experimental setup are explained in the following.

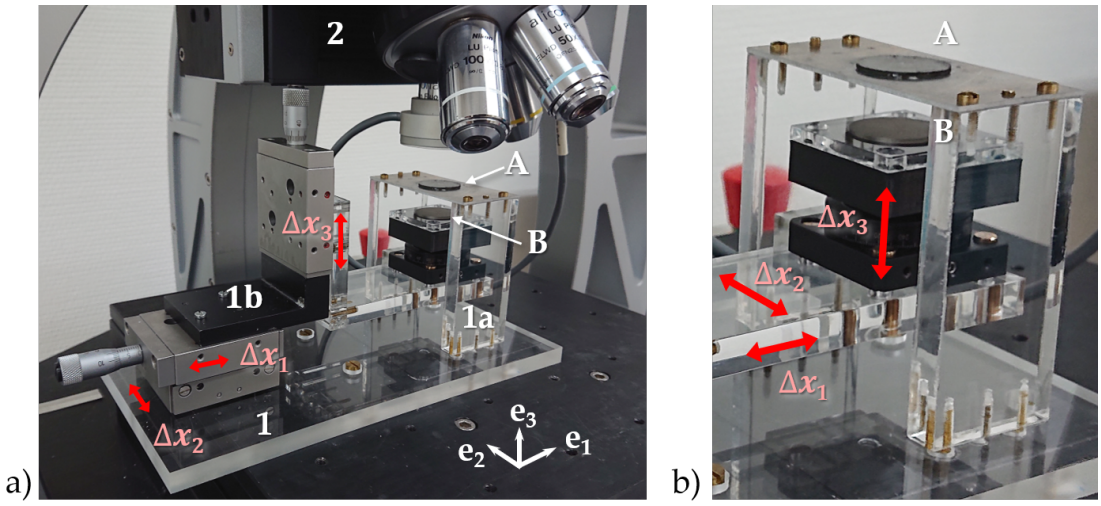

Figure IV.21: Photos of the experimental setup, general view (a) and zoom on membrane and magnet (b), A – Membrane, B – Magnet, 1a – Mechanical support of the membrane, 1b – Mechanical support of the magnet, 2 –Optic measurement system.

The supporting structures for membrane and magnet are mounted on a common base plate, made of acrylic glass. The mechanical support of the membrane is schematically shown in figure IV.22. The membrane is fixed on an aluminum plate, which is supported by two pillars, made of acrylic glass. The aluminum plate has a circular opening with a diameter of 20 mm in the middle. This is the region, where the membrane is left free to deform. It is fixed in the outer region (for $d > 20\,\text{mm}$) to the aluminum plate with the adhesive Super Glue-3 from Loctite. An additional acrylic glass part was used for the positioning of the membranes, it is shown in figure IV.22 b. The membrane was positioned on the positioning part by the help of a circular engraving with the same diameter. For the two membranes with bidirectional magnetization, the pole transition was aligned with two linear engravings that are arranged diametrically opposed around the circular engraving. The positioning part is then aligned with the aluminum part by the help of three pins. The pole transition of specimens with bidirectional magnetization is aligned with the $\boldsymbol{e}_2$ – direction of the experimental setup. All specimens were positioned on separate aluminum plates with a thickness of 1.2 mm.

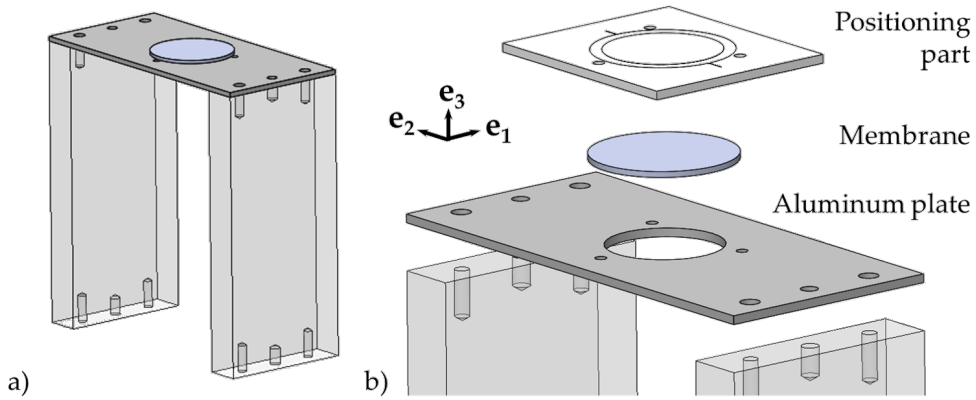

Figure IV.22: Mechanical support of the membrane in the experimental setup: Full view (a) and zoom on the exploded view of several components (b).

The mechanical support of the magnet is schematically shown in figure IV.23. The magnet is fixed on the positioning part by the adhesive Super Glue-3. The part contains a circular engraving to center the magnet and two linear engravings for the alignment of the pole transitions for the magnet with bidirectional magnetization. The positioning part is glued to a PMMA support of which, in turn, the cylindrical part is clamped in an optic lens holder. The lens holder acts as a rotation stage and provides a rotational degree of freedom, which allows the angular adjustment of the magnet with respect to the membrane in the case of a bidirectional magnetization. The three parts, positioning part, support and rotation stage, are aligned by the help of cylindrical axes that were inserted into the holes present in all parts. The axes also assured the alignment of the rotation stage on one of the two acrylic glass parts that form a bracket to connect the assembly to one of the linear micro-translation stages. The lens holder is maintained in its place by two brass screws (not visible in figure IV.23.

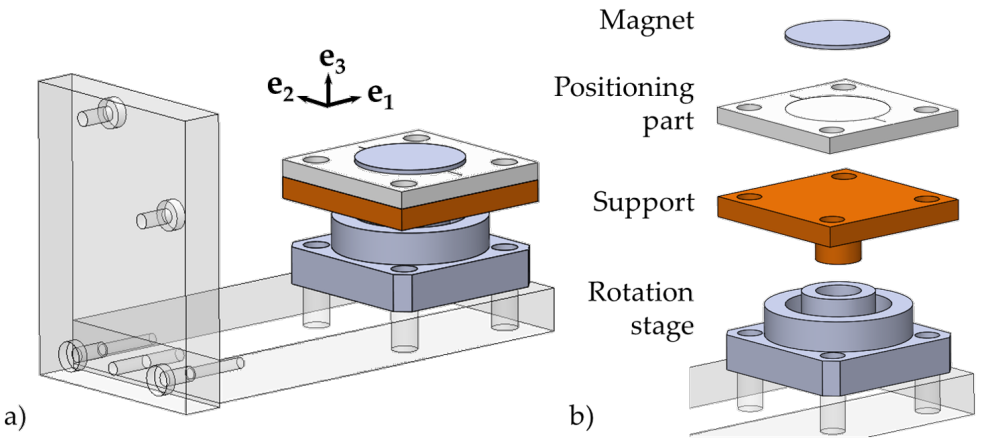

Figure IV.23: Mechanical support of the magnet in the experimental setup: Full view of the assembly connected to the linear stages (a) and zoom on the exploded view of several components (b).

As shown in figure IV.21, the position of the magnet is adjusted by three connected micro-translation stages, type M-105 from Physik Instrumente (PI), each having a linear travel range of 18 mm and a minimum graduation step of 0.01 mm. The position of the magnet is fixed prior to a displacement measurement.
For the observation of the membrane displacement in the out of plane direction, a numerical microscope from Bruker alicona is used. In combination with the corresponding software, the microscope is able to determine the absolute 3D coordinates of points on a surface which is positioned in its the working area. To analyze a surface, a volume, which enclose the surface, has to be defined. The microscope scans the volume with a resolution specified by the user. For each point, a focal range, also specified by the user, is tested and the absolute position of the point in the coordinate system of the microscope is determined by the focal distance. The microscope lens is therefore displaced in the $\boldsymbol{e}_3$ – direction. The scan is performed on several positions in the $\boldsymbol{e}_1$ – $\boldsymbol{e}_2$ plane, which are determined by the resolution and the scanning volume. On this purpose, the studied object is moved in the $\boldsymbol{e}_1$ – $\boldsymbol{e}_2$ –plane by two linear stages. To prevent a movement of the membrane with respect to the linear tables, the base plate of the mechanical part of the experimental setup is fixed to the upper linear tables by four screws (figure IV.21). The enlarger lens with a magnification of 5x of the numerical microscope is used, a measurement resolution of 15 µm is chosen for the directions $\boldsymbol{e}_1$ and $\boldsymbol{e}_2$ and a resolution of 10 µm in the direction $\boldsymbol{e}_3$. The lighting properties specified for the optical measurement are the brightness and the contrast which were set to 127 µs and 0.51 in the software respectively. Furthermore, a polarization filter has been used to improve the lighting of the relatively mat MAE surface.
During this experiment, two types of measurements have been performed. In a first time, a complete surface scan was carried out, but only once for each specimen due to the longs acquisition time (about 2 hours) and the size of the output files. The enclosing volume for the measurement is schematically represented in

figure IV.24 a. In subsequent analysis, only a part of the surface was scanned. A reduced scan was conducted in a volume including the full diameter of the membrane in direction $\boldsymbol{e}_1$, but reduced to a range of $\pm$ 2 mm in the direction $\boldsymbol{e}_2$. Figure IV.24 b shows the enclosing volume for the second measurement type. The range for direction $\boldsymbol{e}_3$ was determined by the thickness of the membrane for both measurement procedures.

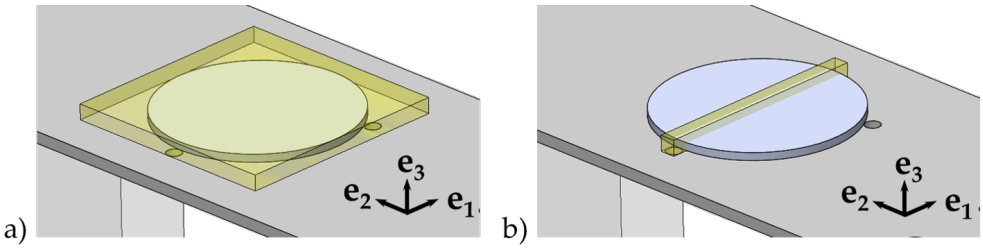

Figure IV.24: Schematic representation of the volume scanned by the numerical microscope to find the focal distance: Full surface scan (a) and reduced surface scan (b).

IV.4.1.c Measurement protocol and post-processing

The membranes are tested one by one. For each membrane, the actuation magnet with the same magnetization type, unidirectional or bidirectional (cf. figure IV.15), was chosen and mounted in a first step. Afterwards, the aluminum plate, which carried the membrane, was mounted. An initial reduced surface scan has been performed with the magnet far away from the membrane. The axes of the magnet and the membrane were aligned thereafter and the magnet was brought as close as possible to the membrane. In this configuration, a complete surface scan (cf. figure IV.24 a) was performed. In the following, the position of the magnet in the $\boldsymbol{e}_1$ – direction was altered. Reduced surface scans were carried out for various misalignments in the positive and the negative direction. The magnet was then brought back into its initial position on $\boldsymbol{e}_1$ and the misalignment measurements were performed in the $\boldsymbol{e}_2$ – direction. Afterwards, with the magnet in its initial position, the distance between the membrane and the magnet was increased in the $\boldsymbol{e}_3$ – direction and reduced surface scans were recorded. While the position of the magnet was altered in three spatial directions, the reduced surface measurement was always recorded for the same scanning volume for these measurements. In case of a different magnetization type, the magnet had to be changed between the measurements of two membranes.
The results of a measurement are the 3D-positions of points on the surface of the deformed membrane in the absolute coordinates of the numerical microscope. The positions were exported as text files and post-processed with Matlab. The four complete surface scans are compared by means of qualitative results, the post processing consists of a normalization with respect to the maximum value and is explained during the presentation of the measurement results. The reduced

surface scans are post-processed such as they show a cross section of the relative displacement in the out of plane direction. Figure IV.25 a shows results of a reduced scan in the form of points, colored in a shade of brown depending on x_3. The data have already been transformed from absolute coordinates in the system of the microscope to the coordinate system of the setup which has its origin at the center of the membrane and on top of the aluminum plate. During a reduced scan, the measurement data are recorded in a range of $x_2 = \pm\ 1\,\text{mm}$. The range is reduced once more for the evaluation to a range of $\pm\ 0.5\,\text{mm}$, the corresponding data points are shown as red points in figure IV.25 a. In discretization intervals of 0.1 mm, the average of the x_1 and x_3 coordinates are calculated. The results are shown in figure IV.25 b. The average values are represented in 2D graphics throughout the rest of this section. An example of average measurement results of the initial and deformed membrane surface is represented in figure IV.26 a. As the measurement results are discretized with the same interval, the displacement of the membrane is calculated as the difference of the deformed surface and initial surface average data. The difference between the two data sets in figure IV.26 a, corresponding to the out of plane displacement u_3, is shown in figure IV.26 b.

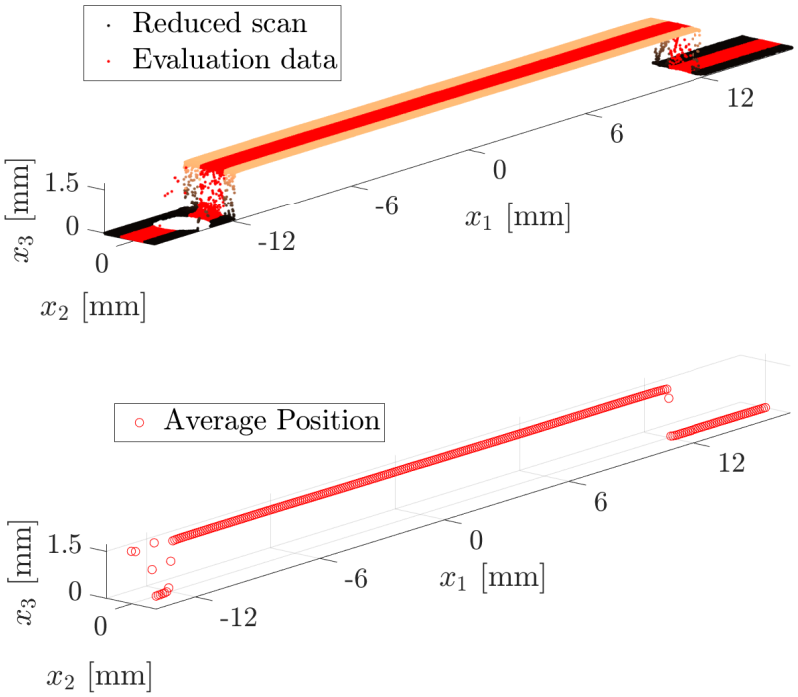

Figure IV.25: Measurement data obtained from a reduced surface scan in a range of $x_2 = \pm\ 1\,\text{mm}$ (reduced scan) and $x_2 = \pm\ 0.5\,\text{mm}$ (evaluation data) (a) and averaged results of the evaluation data (b).

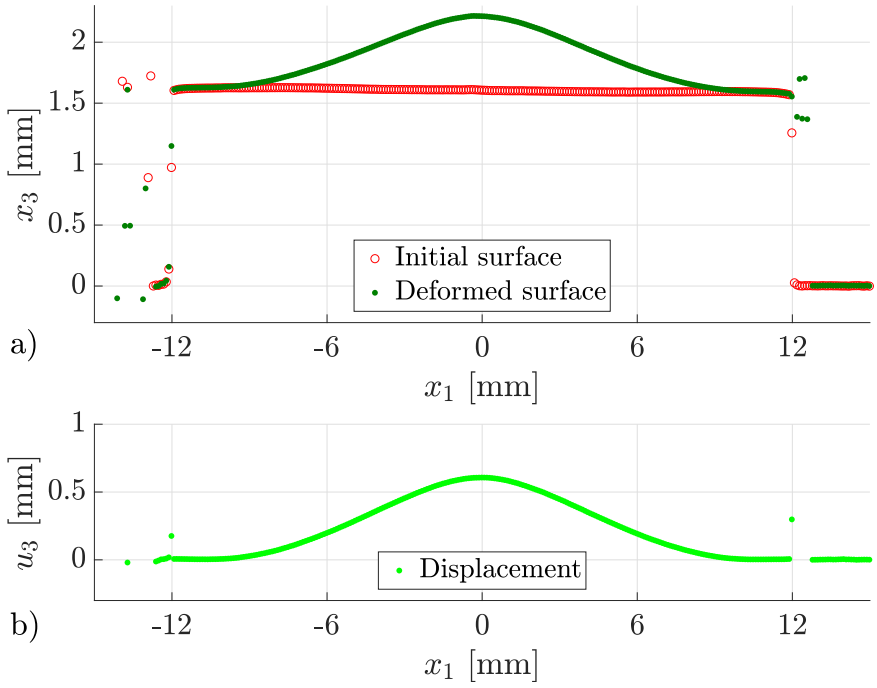

Figure IV.26: Average positions x_3 of a deformed and non-deformed membrane surface (a) and corresponding out–of–plane displacement u_3 (b).

IV.4.2 Results: Displacement of H-MAE membranes

In the following, the experimental results of the out-of-plane displacement measurement are presented. At the beginning, the results of four complete surface scans, one for each of the membrane specimens, are presented. In the following the reduced surface scans for the two specimens with bidirectional magnetization are analyzed. The influence of the relative position of the magnet with respect to the membrane on the displacement of the membrane is studied.

IV.4.2.a Shape of the deformed membranes (complete surface scan)

The first study concerns the out–of–plane displacement of the whole membrane surface. Each of the four specimens has been scanned in a configuration, in which the magnet was brought as close as possible to the membrane and where membrane and magnet were concentrically aligned. Figure IV.27 shows the normalized out of plane displacement $\hat{u}_3$ for the specimens with Φ_2 (a-b) and Φ_1(c-d). The normalized displacement is calculated with respect to the maximum displacement measured for each volume fraction.
The comparison of the specimens with the same volume fraction Φ shows, that the displacement is much larger when the magnetization is bidirectional (M2) for both volume fractions. Furthermore, the membranes with bidirectional magnetization are deformed in the same manner for both volume fractions. The biggest displacement is achieved in the center of the membrane. Going outwards from the

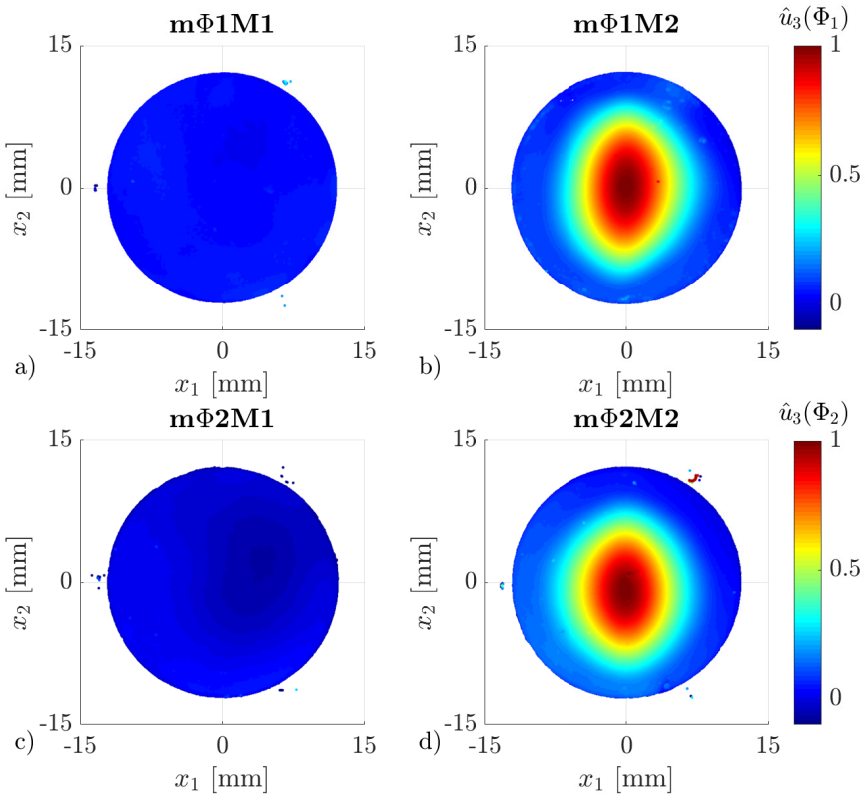

Figure IV.27: Normalized out—of–plane displacement $\hat{u}_3$ of the specimens mΦ2M1 (a), mΦ2M2 (b), mΦ1M1 (c) and mΦ1M2 (d), for each volume fraction the displacement of the two specimens is normalized with respect to the maximum displacement of the membrane with bidirectional magnetization.

center, the evolution of the displacement depends on the spatial direction. The decrease is smaller in the $\boldsymbol{e}_2$-direction, in which the pole transition is oriented, than in the $\boldsymbol{e}_1$-direction. Furthermore, the displacement can be considered as symmetric with respect to the $\boldsymbol{e}_1$–$\boldsymbol{e}_3$–plane as well as to the $\boldsymbol{e}_2$–$\boldsymbol{e}_3$–plane, passing by the center. The findings for the displacement are directly linked to the magnetization of the membranes but also to the mechanical boundary conditions. According to the results for the magnetic characteristics, presented previously in this section, a high density of the magnetic flux is likely to appear in vicinity of the pole transition and on the outer boundaries of the membranes. The interaction should be stronger on these positions as a consequence. As the boundaries of the membranes are mechanically fixed, a high displacement is primarily measured in vicinity of the pole transition. The deformed area of mΦ1M2 is bigger than the deformed area of mΦ2M2 despite the lower volume fraction and presumably weaker interaction forces. The main reason for this is probably the different thickness of the membranes which leads to a higher flexural rigidity of mΦ2M2. The higher stiffness of the composite with the higher volume fraction may also play a role but a conclusion cannot be made from the results of this study. An additional parameter is

the attachment of the membranes to the aluminum plate. An adhesive has been chosen as solution for the first tests, to demonstrate the advantage of bidirectional magnetization for actuation purposes of membranes. This choice should be revised for parametric quantitative studies.

a) 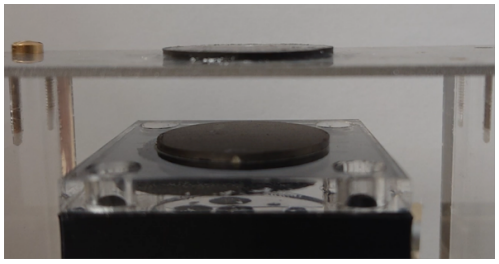 b) 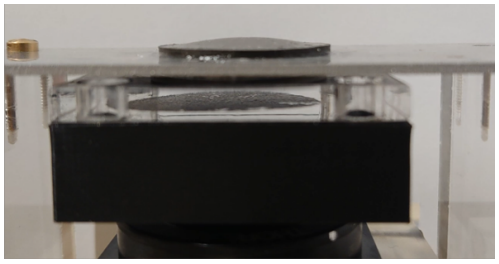

Figure IV.28: Photo of specimen mΦ1M2 in the experimental setup with the magnet positioned far from (a) and near to (b) the specimen.

IV.4.2.b Variation of the magnet position (reduced surface scan)

In the following paragraphs, a study of the misalignment of the magnets and the membranes with bidirectional magnetization in the direction of the pole transition (Δx_2) and perpendicular to it (Δx_1) are presented. Furthermore, the displacement for different air gaps between magnet and membrane (Δx_3) is analyzed for the specimens mΦ1M2 and mΦ2M2. While the analysis of the previous section was based on complete surface scans and normalized values of the displacement, the following study presents the quantitative results of the partial surface scans (cf. figure IV.24 b). The results shown in the following correspond to the average displacement in a region of $\pm$ 0.5 mm around the $\boldsymbol{e}_1$–$\boldsymbol{e}_3$ plane (cf. section IV.4.1.c). In the first step of the experiment, a misalignment of the pole transitions of magnet and the membrane has been created by a **displacement of the magnet in the $\boldsymbol{e}_1$–direction (Δx_1)**. Figure IV.29 shows a scheme of the misalignment. In the graphics a and b, a magnet and a membrane as well as their mechanical supports are represented in top view and in a sectional view. The direction of movement of the magnet is represented by a green arrow. The graphic c shows a negative misalignment ($\Delta x_1 < 0$) and a positive misalignment ($\Delta x_1 < 0$). The results of reduced surface measurements for various misalignments Δx_1 are shown in figure IV.30.

A big difference between the absolute values of displacement of the two specimens is observed, the displacement measured for mΦ1M2 is higher than the displacement of mΦ2M2. Possible reasons for this have been discussed in the previous paragraph (flexural rigidity, volume fraction, mounting). The influence of the misalignment on the membrane on the other hand is quite similar for the two specimens. The maximum displacement is achieved, when the pole transitions are aligned and the same magnetic poles face each other. A misalignment has two effects: firstly, it decreases the maximum displacement and secondly, the position of the maximum displacement is shifted in the direction opposite to the displacement of the mag-

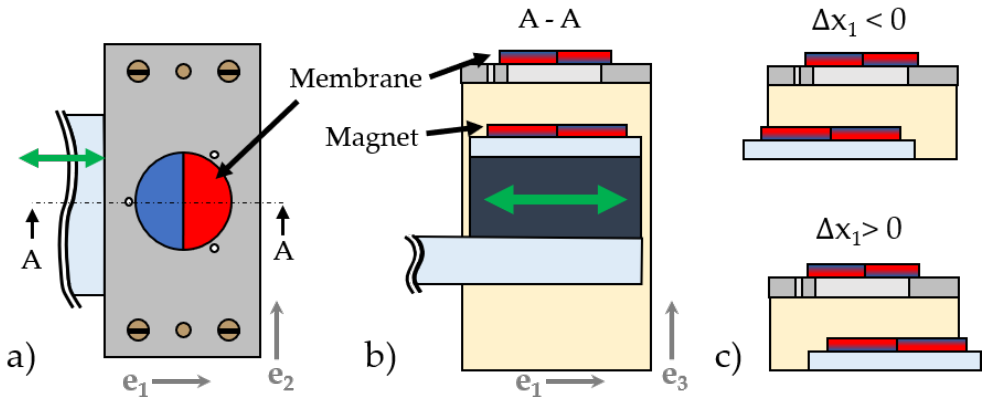

Figure IV.29: Schematic view of the misalignment of membrane and magnet in the $\boldsymbol{e}_1$–direction (Δx_1) : top view (a) and sectional view (b) of a magnet, a membrane and their mechanical supports and representation of negative and positive misalignment.

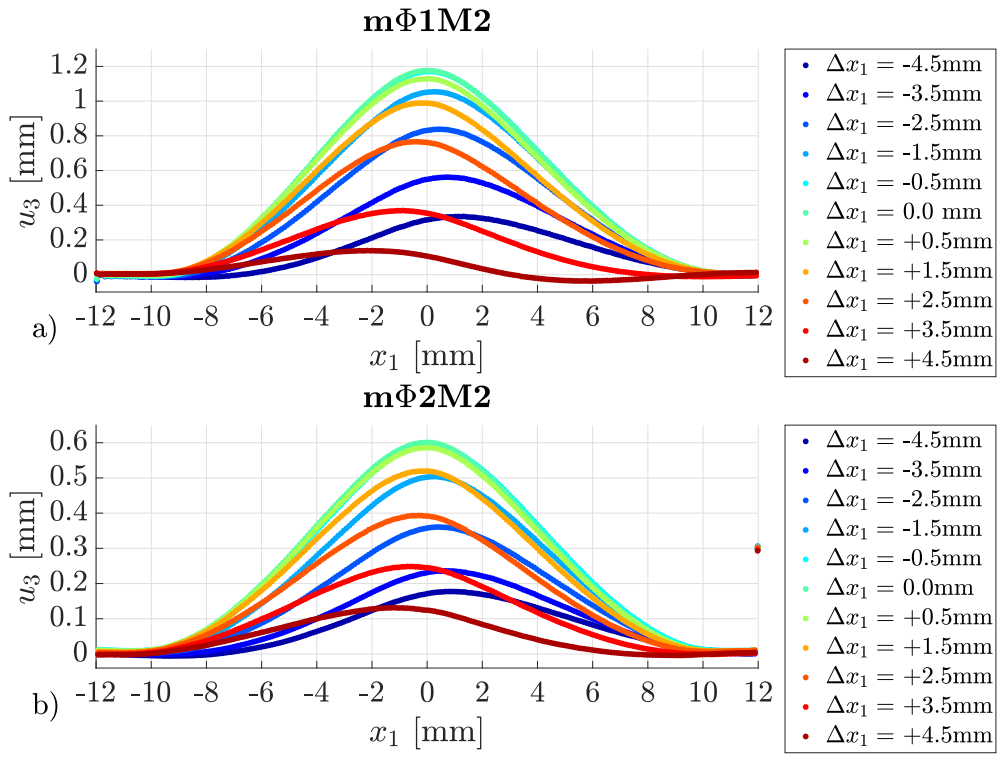

Figure IV.30: Out-of-plane displacement u_3 of the specimens mΦ1M2 (a) and mΦ2M2 (b) for various misalignments Δx_1.

net. Both effects increase with the misalignment. The behavior can be explained by the magnetization pattern. A displacement of the magnet in the direction $\boldsymbol{e}_1$ brings opposite magnetic poles closer together, which creates attraction forces. For $\Delta x_1 = -4.5\,\text{mm}$ for example, the magnet would be displaced in the left direction

in figure IV.30. In this configuration, opposite magnetic poles face each other in a range of $x_1 = [-4\,\text{mm}, -0.5\,\text{mm}]$ (pole transition width of $\pm 0.5\,\text{mm}$ around the zero position) and attraction forces develop. In addition, the regions in vicinity of the transition show a high magnetic flux density, which favors the development of local attraction forces. They decrease the displacement, but also generate a displacement in the $\boldsymbol{e}_1$-direction, opposed to the misalignment. This, in turn shifts the location of the maximum displacement in the same direction.

In the next step, the influence of **the displacement of the magnet in the $\boldsymbol{e}_2$–direction (Δx_2)**, which corresponds to the direction of the pole transition, has been studied. Figure IV.31 schematically represents the misalignment Δx_2. The results of the measurements, represented in in figure IV.32, show, that the influence of the misalignment on the displacement is relatively small for both specimens, mΦ1M2 (a) and mΦ2M2 (b) in the scanning area. Comparing the misalignments Δx_1 and Δx_2 with the same magnitude, it is observed that Δx_1 has a much bigger impact on the displacement than Δx_2. As the pole transitions are not misaligned for Δx_2, the regions of high magneto-mechanical interaction apparently stay face to face to each other in the scanned region. The range of Δx_2 stays relatively small, a variation of the magnetic interactions due to the displacement of the magnet presumably happens only in the outer regions which are not part of the scanning volume. For a Δx_2 bigger than the radius of the magnet, a decrease of the displacement would also be observed in the central region of the membrane. As a conclusion, it is stated that the maximum displacement is less sensitive to a misalignment in the direction of the pole transition than perpendicular to it in the present study.

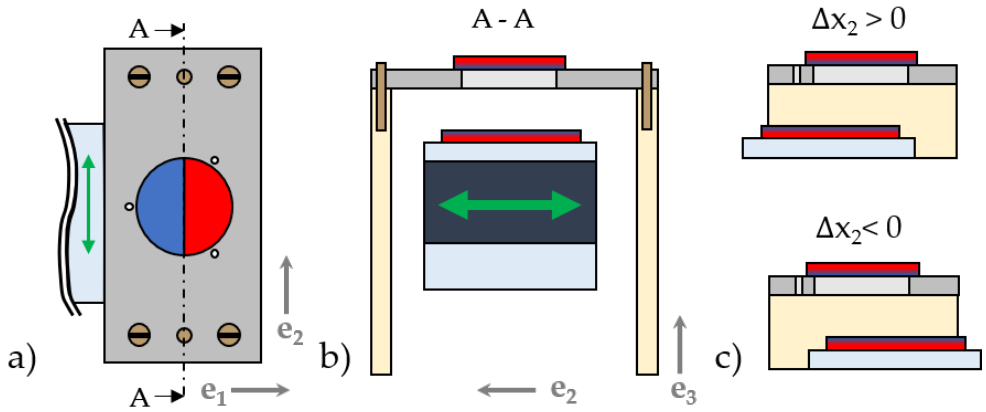

Figure IV.31: Schematic view of the misalignment of membrane and magnet in the $\boldsymbol{e}_2$–direction (Δx_2) : top view (a) and sectional view (b) of a magnet, a membrane and their mechanical supports and representation of positive and negative misalignment (c).

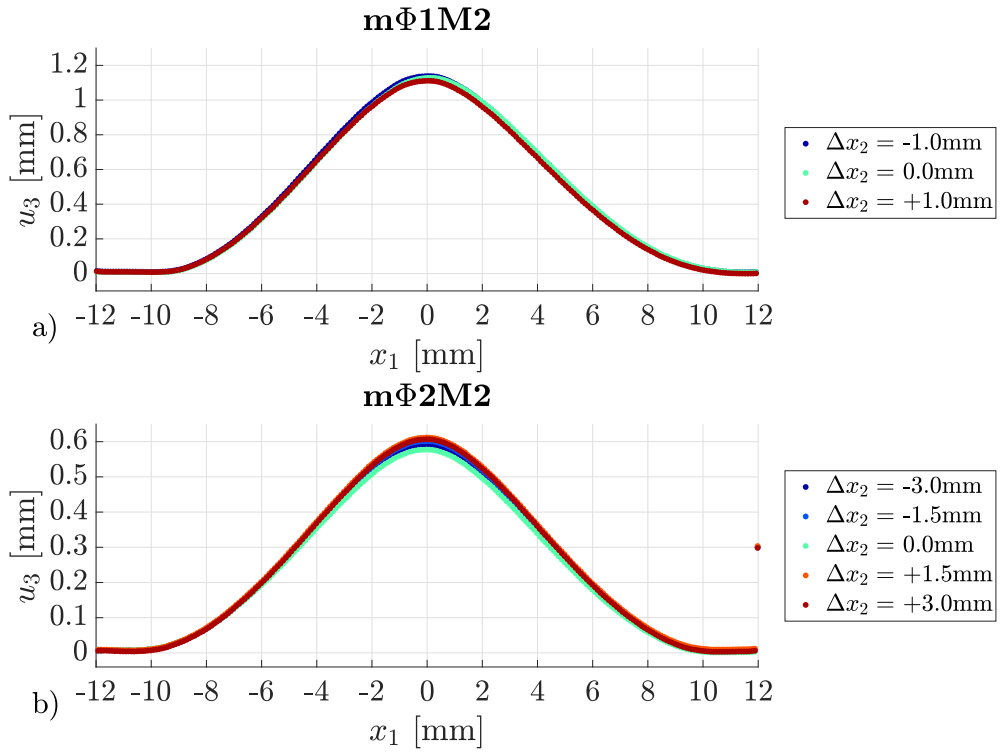

Figure IV.32: Out-of-plane displacement u_3 of the specimens mΦ1M2 (a) and mΦ2M2 (b) for various misalignments Δx_2.

The **displacement of the magnet in the e_3–direction** corresponds to a variation of the air gap between the magnet and the membrane (figure IV.33). The influence of the air gap on the displacement of the membranes has been analyzed and the results are shown in figure IV.34 for mΦ1M2 (a) and mΦ2M2 (b).

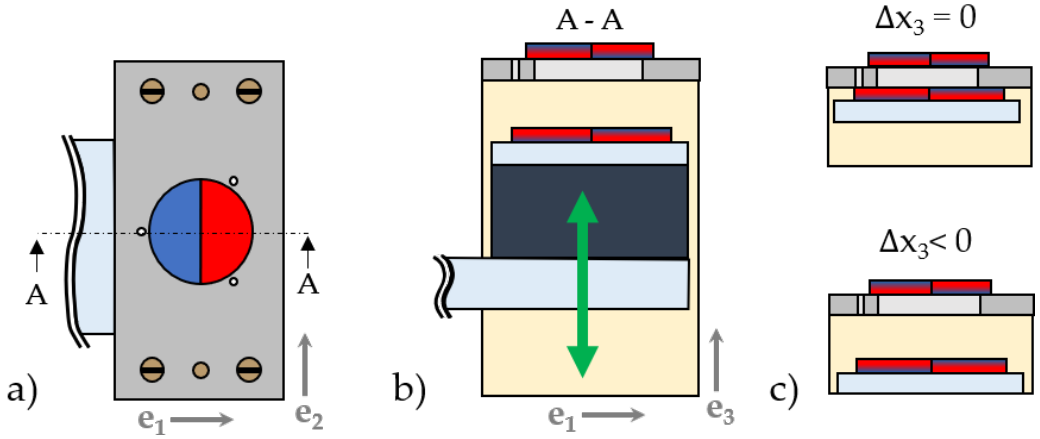

Figure IV.33: Schematic view of the position of the magnet with respect to the membrane in the e_3–direction (Δx_3) : top view (a) and sectional view (b) of a magnet, a membrane and their mechanical supports and representation of positive and negative misalignment (c).

During the study, The magnet was displaced in the position with the lowest possible air gap ($\Delta x_3 = 0$) for the first measurement and the measurement was repeated for positions with an increasingly high air gap. As figure IV.34 shows, an increase of the air gap diminishes the displacement for both specimens. The reason for this is the intensity of the magnetic field, that decreases with the distance between the specimen and the magnet. As a consequence, the magnetically induced forces become weaker and the elastic forces retract the membrane.

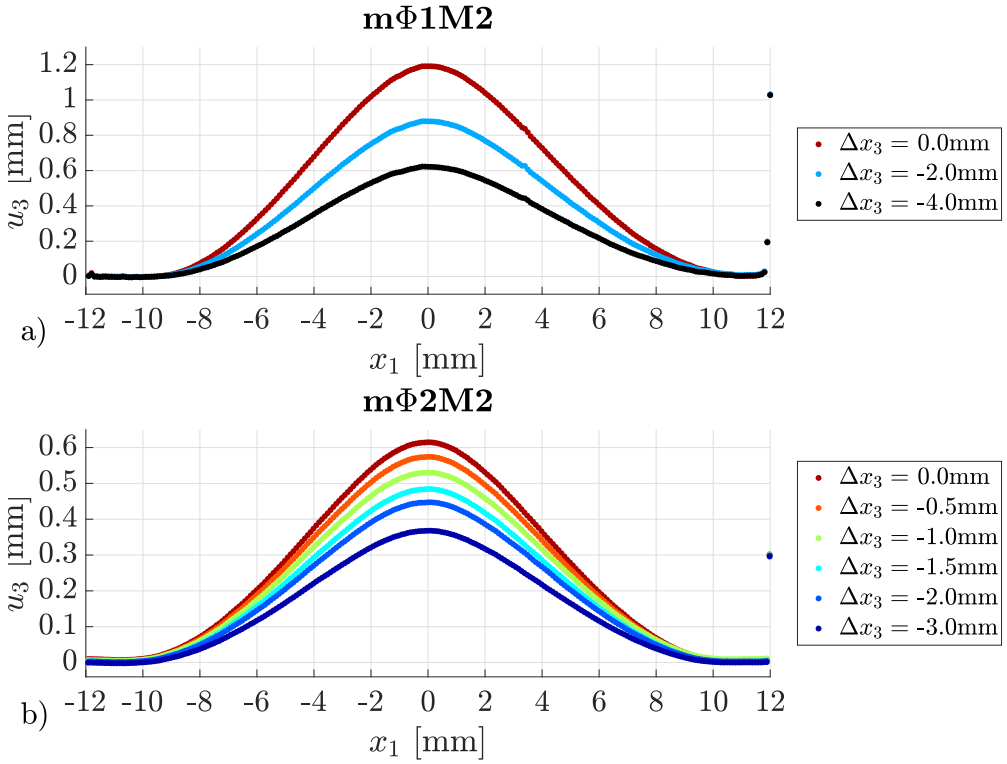

Figure IV.34: Out-of-plane displacement u_3 of the specimens mΦ1M2 (a) and mΦ2M2 (b) for various positions of the magnet Δx_3.

After the misalignment studies, the magnet was positioned as far away from the membrane. A **residual displacement** was observed and a reduced surface scan has been performed for the specimen mΦ2M2 directly after the measurements and once again 12 hours later. Figure IV.35 shows the two measurement results. The shape of the displacement curves corresponds to the shape of the membrane deformed by the magneto-mechanical interactions. The maximum residual displacement, revealed directly after the measurements, measures 0.11 mm which corresponds to about 17 % of the maximum displacement, measured for this specimen. During 12 hours without a loading, the residual displacement decreased and the maximum then measured 0.077 mm, which corresponds to about 13 % of the maximum displacement under magnetic loading.
The decrease of the residual displacement during the 12 hours without loading is an indicator for the viscous part of the material behavior. A visco-elastic behavior of MAE structures has also been observed in other actuation applications

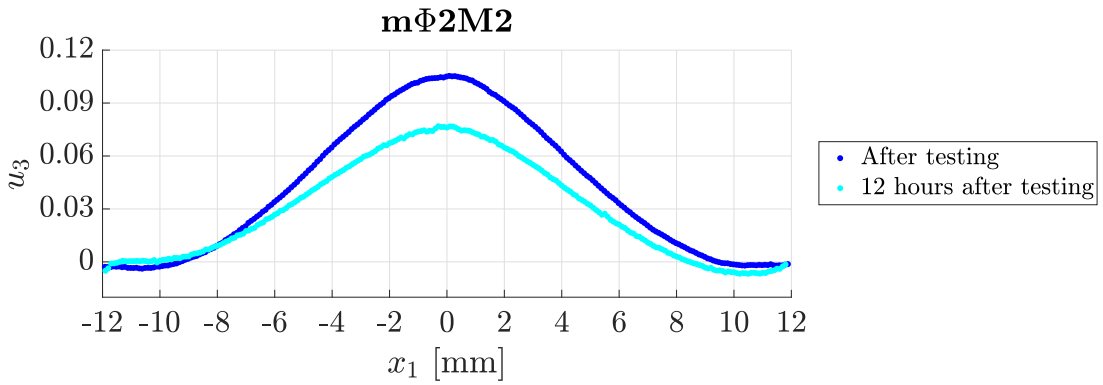

Figure IV.35: Residual displacement of the specimen mΦ2M2 directly after the measurements and 12 hours after the measurement.

([Singh+ 2014; Said+ 2016; Lee+ 2020]), causing a delay between the release of a strain and the decrease of the stress (relaxation behavior). This effect explains the decrease of the displacement of about 30 % between the two measurements. For the remaining residual displacements, two possible causes could be responsible. The first one is friction in the mechanical fixation, based on the assumption that the glue does not maintain a perfect contact between the aluminum plate and the membrane. When the membrane is deformed, the contact partly loosens and is re-established in a different deformation configuration of the membrane. Due to friction between the aluminum plate and the membrane, the new contact state remains when the membrane is unloaded. A second assumption is a magnetization induced residual deformation. During the measurements, the membrane has been kept in a deformed state during half a day at least. It could be possible, that the plasticity is induced by the magnetization of the particles in combination with the rheological properties of the material. Observations of other magnetized composite samples support the theory of magnetically induced plasticity: placed on a curved, ferromagnetic surface, thin specimens not only adapted to the surfaces instantaneously but also retained a part of the deformation when removed from the object a few days later. This is an interesting aspect for future studies on the rheological properties of H-MAE. Despite the residual displacement, the maximum displacement, measured on two consecutive days, remained unchanged.

IV.5 Modeling of bidirectionally magnetized membranes

In this section, the numerical modeling of the experimental study of the membranes with bidirectional magnetization is presented. At first, the implementation of the model is explained and the study cases are outlined. The cases include the

misalignment of the pole transitions (Δx_1) and the increase of the air gap (Δx_3). The analysis of the results includes the study of the deformed membrane surface and the comparison of the misalignment studies to the experimental results.

IV.5.1 Implementation of the model

The numerical simulations are carried out by the means of the finite element method. A 3D model, prepared for this study, contains a magnet and a membrane which are surrounded by an air volume. Stationary magnetic fields and the absence of electric currents are assumed. The simulations are performed as stationary mechanical cases as well. Figure IV.36 a shows the components of the model. Diameter and thickness of the membrane and the magnet correspond to the dimensions of the specimens used in the experimental investigation (table IV.3). The air gap between membrane and magnet is set to 1.4 mm. There are three parts that contribute to this value: firstly, the thickness of the aluminum plate (1.23 mm), secondly, the thickness of the glue layer, that is obtained from the difference of the specimen thickness and the height difference between the aluminum plate and the membrane surface measured with the microscope (0.1 mm), and thirdly, an additional gap of 0.07 mm that is added since the magnet is not in contact with the aluminum plate when it is moved during the misalignment studies. The symmetry of the mechanical boundary conditions and the magnetization pattern allow to reduce the model to half of the geometry for the study, hence the model is cut in the $\boldsymbol{e}_1$–$\boldsymbol{e}_3$–plane. To model the mechanical symmetry, only displacements in the $\boldsymbol{e}_3$-direction are allowed in the $\boldsymbol{e}_1$–$\boldsymbol{e}_3$–plane. The normal magnetic flux density equals zero in the $\boldsymbol{e}_1$–$\boldsymbol{e}_3$–plane, which generates a magnetic symmetry condition.

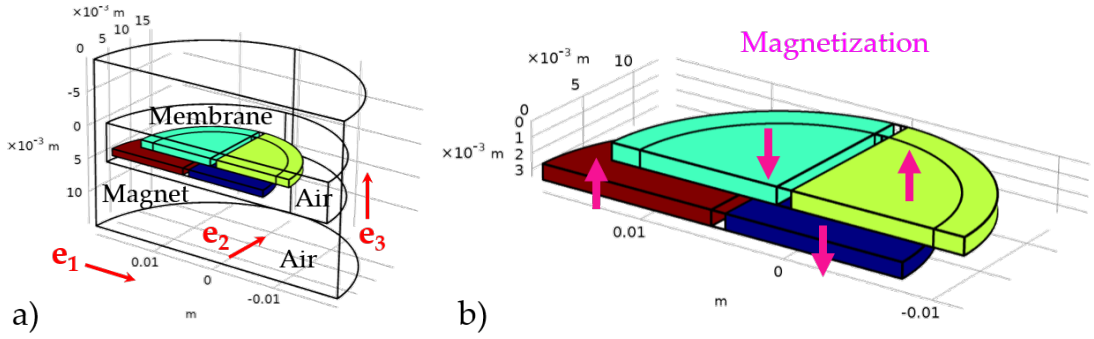

Figure IV.36: Numerical model of the experiment : functional components of the setup (a) and directions of magnetization of the membrane and the magnet (b).

The air volume is split into two parts: a smaller volume, surrounding the membrane and the magnet, and a bigger volume, that encloses the all parts of the model. The reason for the split is the element size of the mesh. The mesh in the small volume is refined to improve the calculation of the local magnetic quantities. The bigger air volume is discretized with a coarser mesh since the exact local quantities are less important in this region. The magnet and the membrane

volume are divided in domains with different magnetic properties as figure IV.36 b shows in detail. The colored domains are modeled as magnetized material with a linear magnetic behavior. The magnetic material parameters used for this study are summarized in table IV.4 of the former section. The membrane and the magnet have two regions, which are magnetized in opposite directions. To generate repulsive forces, the components of the model are arranged in the same manner as in the experiment: in the air gap, two identical pole pairs face each other. The transition zone is modeled as non-magnetized region. The membrane material is modeled as linear elastic material with a Poisson's ratio of 0.49 and a modulus of 2.64 MPa for specimen with Φ_1 and 6.84 MPa for specimen with Φ_2. The values used for the elastic moduli were obtained experimentally as the storage modulus from dynamic mechanical analysis at a low frequency (cf. chapter II). The exact elastic modulus of the material is lower, but the values of the storage modulus have the same order of magnitude and should give a good approximation. Linear strains are forced in the mechanical part of the simulation. To model the mechanical boundary conditions from the experiment, a ring-shaped surface in the outer region of the membrane is fixed in the numerical simulation. This surface is marked in red in figure IV.37. The position of the magnet is varied for the misalignment studies, the example of two different misalignment positions in the $\boldsymbol{e}_1$–direction is shown in figure IV.37.
The magneto-mechanical coupling is established on the surface of the membrane by the help of the Maxwell stress tensor, as shown for stationary cases in chapter I. The local constraints are calculated in the magnetic part of the model and are applied as boundary load in the mechanical model. To account for the change of the local magnetic quantities due to the deformation, several iterations between the mechanical and magnetic calculation are performed until the stationary configuration is reached in the magnetic and the mechanical domain. In the first study, the magnet and the membrane are perfectly aligned and the deformation of the whole surface is analyzed. Afterwards, the magnet is displaced, at first in the $\boldsymbol{e}_1$–direction and afterwards in the $\boldsymbol{e}_3$–direction, and the results are compared to the experiment.

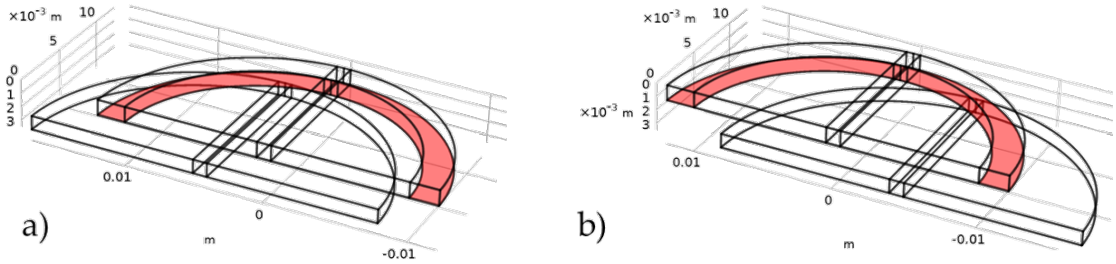

Figure IV.37: Fixation of the membrane in the simulation (red) and extreme cases of the misalignment $\Delta x_1 = -4.5\,\mathrm{mm}$ (a) and $\Delta x_1 = 4.5\,\mathrm{mm}$ (b)

IV.5.2 Results: Out-of-plane displacement

IV.5.2.a Deformed shape of the membranes

Figure IV.38 shows the normalized out-of-plane displacement, obtained from the numerical simulation for the specimens mΦ1M2 and mΦ2M2. Since the mechanical quantities are supposed to be symmetric, the result was duplicated and flipped with respect to the $\boldsymbol{e}_1$–$\boldsymbol{e}_3$–plane. In the top-view of the mirrored results, the color indicates the magnitude of the displacement. The same pattern as in the experimental result is observed, a comparatively large displacement in the middle of the membrane, that decreases more rapidly in the $\boldsymbol{e}_1$–direction than in the $\boldsymbol{e}_2$–direction (cf. figure IV.27). The qualitative results are in good accordance which means that the simulation gives a good approximation of the distribution of the local pressure, induced by magnetic interactions.

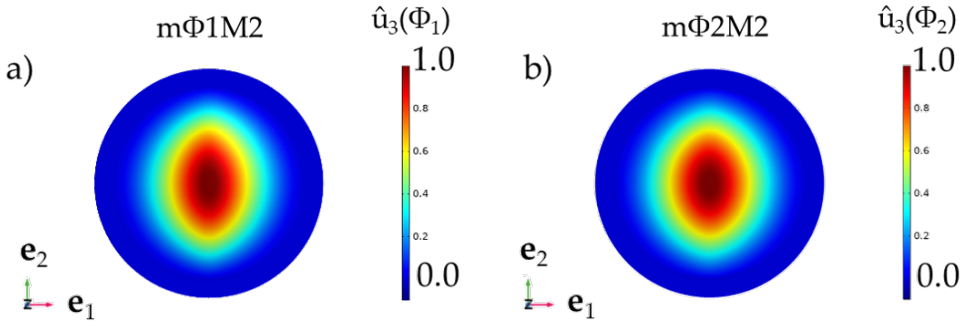

Figure IV.38: Normalized out–of–plane displacement $\hat{u}_3$ obtained from numerical simulations for the specimens mΦ1M2 (a) and mΦ2M2 (b).

In the following, the results of the misalignment studies are shown. To compare the numerical simulation to the experimental results, the displacement of the top surface of the membrane in the $\boldsymbol{e}_1$–$\boldsymbol{e}_3$–plane is exported from the simulation program and post-processed with Matlab. Figure IV.39 shows the position on the membrane used for the comparison of the results as a pink line.

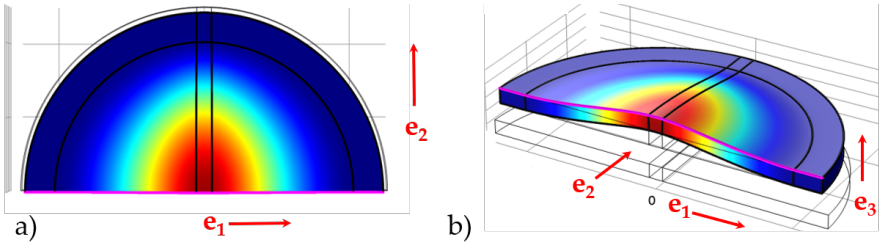

Figure IV.39: Deformed configuration of the membrane in top view (a) and perspective view (b), pink line = position of displacement evaluation for 2D representation.

IV.5.2.b Misalignment of the magnet and the membrane

The results for a misalignment of the pole transitions of the numerical study are shown in figure IV.40 (m$\Phi 1M2$) and in figure IV.41 (m$\Phi 2M2$). For each volume fraction, the results have been split into two graphics (for better visibility), showing either a positive or a negative displacement of the magnet in the $\boldsymbol{e}_1$-direction. The experimental results are also shown in the graphics to compare the experiment and the modeling. The results, obtained for the specimen m$\Phi 1M2$, are discussed in the following with reference to figure IV.40.

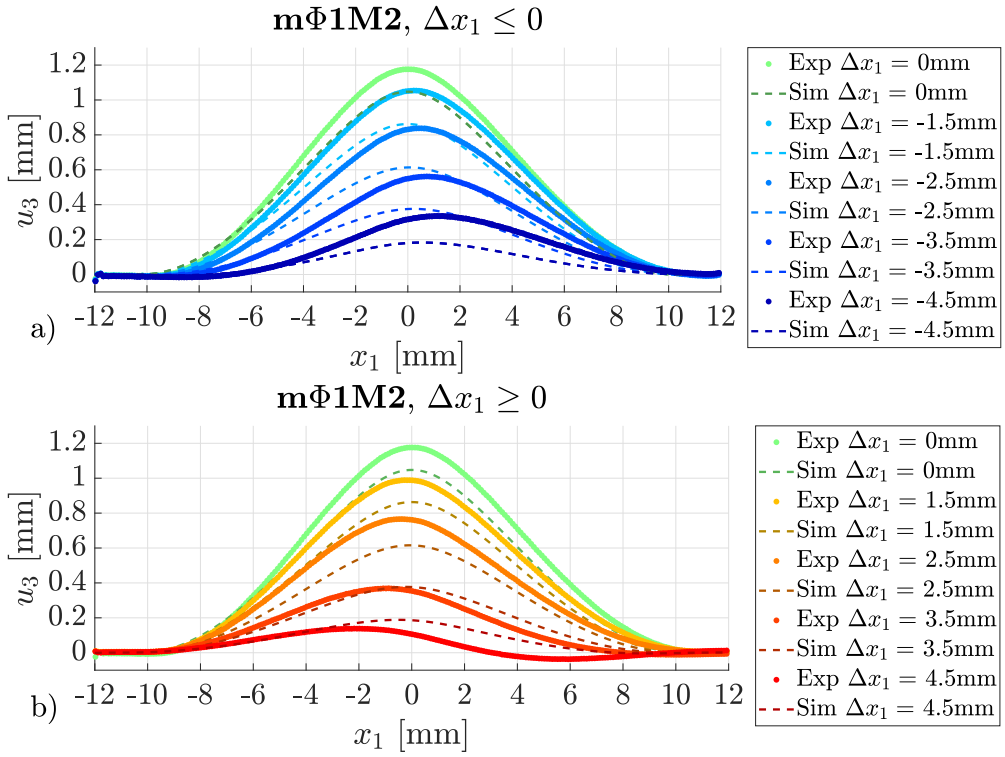

Figure IV.40: Out of plane displacement u_3 of specimen m$\Phi 1M2$ for negative (a) and positive (b) misalignment of the magnet with respect to the membrane, numerical results (dashed lines) and experimental results (data points).

While the shape of the deformed membrane, obtained from the simulation, corresponds the shape obtained experimentally, the absolute displacement values show a difference of about 20 % for the maximum displacement. For aligned pole transitions ($\Delta x_1 = 0$), the maximum displacement is underestimated by the model. This may be due to the forced linear constraints in the model but can also have its origins in the material parameters or the boundary conditions. A second difference is visible for the shift of the maximum displacement, which is present, but smaller in the numerical results than in the experimental results. In addition, misalignments of the same magnitude in the positive and negative direction create symmetric deformed configurations with respect to the $\boldsymbol{e}_3$–axis in the model.
The differences between experiment and simulation are probably also due to the

alignment of the magnet and the membranes. While the simulations allow a precise alignment of objects, this task is much more difficult in the experiment. Linear and angular misalignments in the experimental setup can be due to the assembly of the parts in the mechanical part of the test bench but also between the test bench and the measurement device. An angular displacement between magnet and the membrane for example generates a varying air-gap and hence a variation of the local magneto-mechanical forces. Figure IV.41 shows the experimental and simulation results for specimen m$\Phi 2M2$. The accordance between the two types of results is better this specimen than for m$\Phi 1M2$, especially for the maximum displacement. This could be due to the lower magnitude of the displacement; the hypothesis of linear strain may be more appropriate in this case.

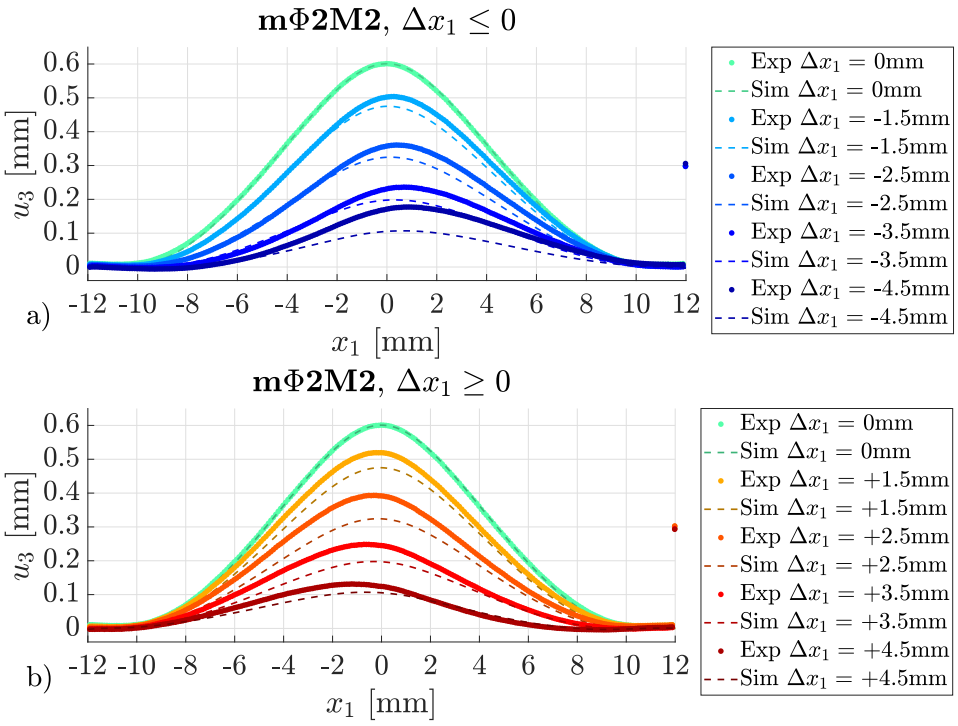

Figure IV.41: Out of plane displacement u_3 of specimen m$\Phi 2M2$ for negative (a) and positive (b) misalignment of the magnet with respect to the membrane, numerical results (dashed lines) and experimental results (data points).

A qualitative comparison of the influence of the misalignment of the pole transitions on the maximum displacement is shown in figure IV.42. The maximum normalized out-of-plane displacement $\hat{u}_{3\,max}$, normalized with respect to the maximum displacement for aligned pole transitions $u_{3\,max}$, is shown as a function of the misalignment Δx_1. The graphic contains two important information. Firstly, the decrease of the maximum displacement seems to take place almost independently from the volume fraction, since the results for the two specimens are similar, which can be observed for the experimental results as well as for the simulation results.

Secondly, the qualitative decrease of the maximum displacement obtained by the model fits the decrease in the experiments. The overall modeling approach seems to be applicable to model the experimental study.

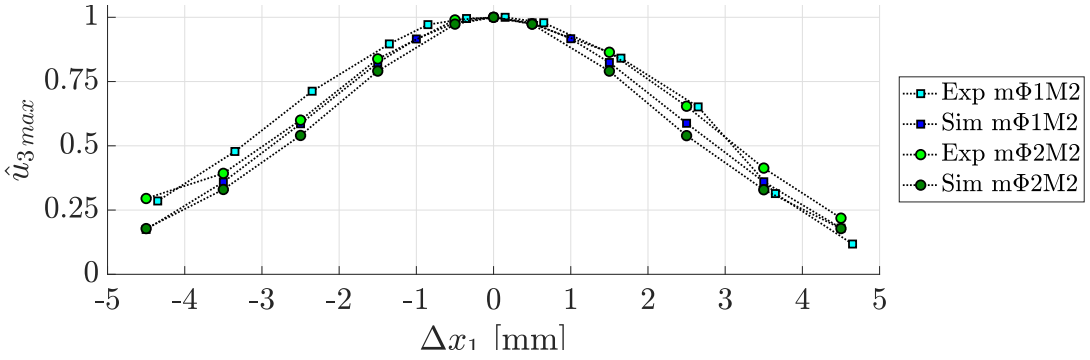

Figure IV.42: Normalized maximum displacement $\hat{u}_{3\,max}$ as a function of the misalignment Δx_1, experimental (light color) and numerical (dark color) results for the specimen m$\Phi 1M2$ (blue squares) and m$\Phi 2M2$ (green dots).

IV.5.2.c Varying air gap

The numerical results of the analysis with different air gaps between magnet and membrane are shown in figure IV.43 for m$\Phi 1M2$ (a) and m$\Phi 2M2$(b). The experimental results are also shown for the comparison to numerical results. The displacement of the membrane decreases with increasing air gap in both cases, but in a different manner. The maximum displacement for example decreases in an almost linear way in the experiment for both specimens while the simulation results show a big decrease at the beginning which becomes smaller with increasing air gap. These evolutions of the maximum displacement are represented as variation of the normalized maximum displacement $\hat{u}_{3\,max}$ with respect to the variation of the air gap in figure IV.44. While the experiment shows a similar evolution for both composites, the numerical results evolve in a different manner. The differences are bigger for the thinner membrane which supports the assumption that nonlinear stains should be included in the simulation due to the high aspect ratios. It is supposed, that the qualitative differences between numerical simulation and the experiments result from the residual displacement which prevents the membrane to release the deformation. Compared to the tests with Δx_1, the effect is more visible in this configuration as the magnetic interactions decrease more in this study than they do for the misalignment. However, a bigger decrease of the displacement with the misalignment for the model compared to the experimental results is also observed for Δx_1 (cf. figure IV.42).

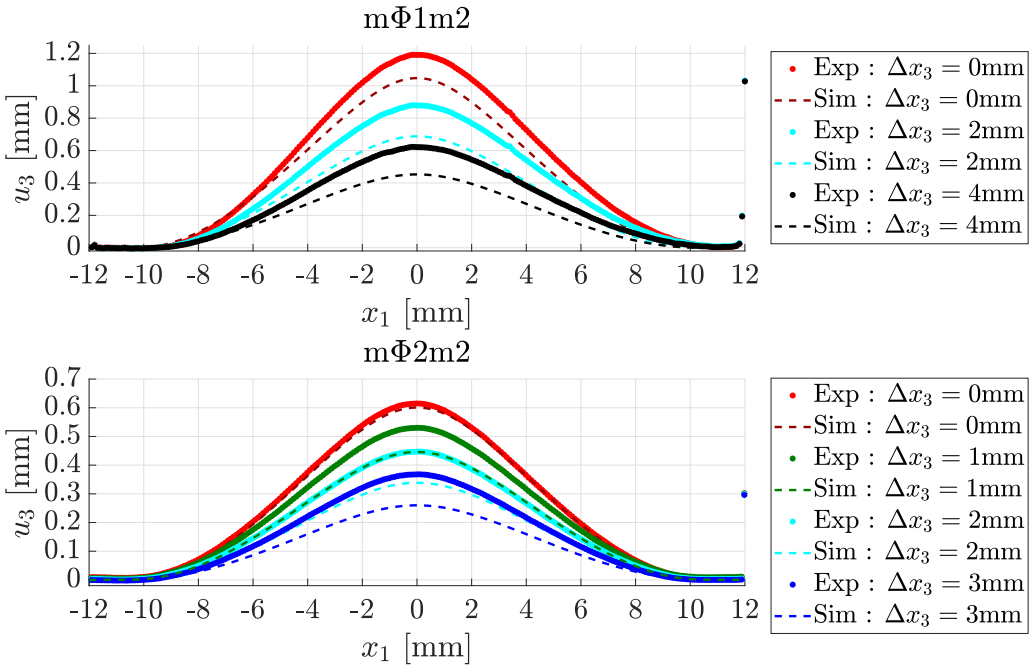

Figure IV.43: Out of plane displacement u_3 of specimens m$\Phi 1M2$ (a) and m$\Phi 2M2$ (b) for different positions Δx_3 of the magnet with respect to the initial air gap, numerical results (dashed lines) and experimental results (data points).

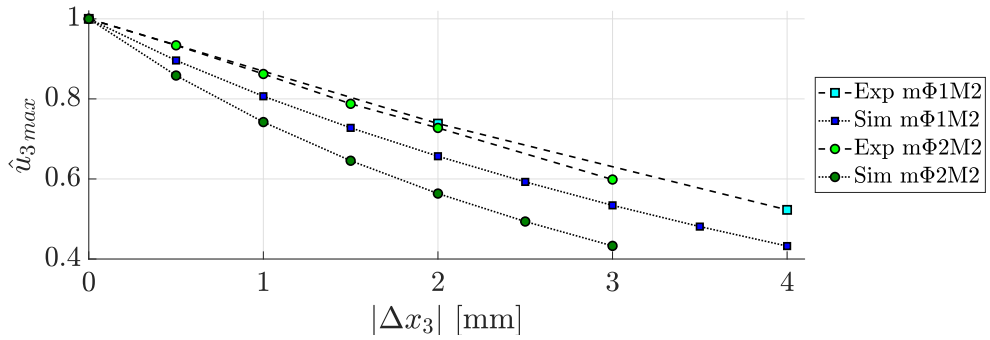

Figure IV.44: Normalized maximum displacement $\hat{u}_{3\,max}$ as a function of the air gap Δx_3, experimental (light color) and numerical (dark color) results for the specimen m$\Phi 1M2$ (blue squares) and m$\Phi 2M2$ (green dots).

IV.6 Conclusions and perspectives

The present work deals with the magneto-mechanical interactions, generated by magnetized H-MAE structures and their use for the actuation of membranes. After an introduction of the behavior of permanent magnets in electromechanical systems, the recent progress of the research on MAE actuators has been presented. In the first part of the study, the global forces which arise due to the magnetization of H-MAE in an electromagnetic circuit have been analyzed experimentally. It

is stated that, the volume fraction influences the force such as an increase of the magnetic particle content increases the force. Additionally, it is shown, that the geometry of the specimens plays a role for the magneto-mechanical interactions. When the thickness corresponds to the length of the specimen in the direction of magnetization, thin specimens generate weaker forces that thicker specimens due to the demagnetizing effect. This effect presents a difficulty for the development of H-MAE membrane actuators for which and a solution is presented in the present work: it consists of a bidirectional magnetization of membrane specimens. An analysis of the magnetic leakage flux density of specimen with unidirectional and bidirectional magnetization is presented at the beginning of the study. It is shown, that a pole transition allows not only to increase the intensity of the magnetic flux density, but also generates a gradient of the flux density field. A numerical simulation of the magnetized specimens shows, that the H-MAE specimens can be modeled as permanent magnets concerning their magnetic behavior. The subsequent two parts of this chapter present the actuation of H-MAE membranes, with different actuation patterns, by the help of permanent magnets. The membranes are fixed on their outer boundaries and a rigid magnet is approached to deform the structure. The displacement of membranes with bidirectional magnetization exceeds the displacement of unidirectional magnetized membranes by a large extend. Studies on the misalignment of the rigid magnet and the H-MAE membrane are performed and the air gap is varied in experiments. The experiments concerning the misalignment of the pole transitions and the variation of the air gap have been modeled by the help of the finite element method. The experimental and numerical results of the misalignment studies are in good accordance concerning the qualitative evolution of the maximum displacement. However, additional experimental studies and a simultaneous adaption of the model are necessary are necessary to enhance the quantitative accordance. Future studies should include the viscous component of the material behavior and analysis of the membrane fixation.
The actuation mechanism, presented in this work, shows a possibility to improve the magnetic actuation of membrane structures as it provides a mean to localize the magnetic loading . The experiments were carried out to prove the concept of an enhanced actuation by bidirectional magnetization, future studies should concentrate on the application of the concept and corresponding quantitative studies. In the present study, a permanent magnet was used for the actuation, but in subsequent studies it could be replaced by an electromagnetic actuator or an electro-permanent magnet (EPM) (cf. [Gholizadeh+ 2019] for example). A difficulty concerning the integration of H-MAE in electromagnetic circuits could arise from the forces generated by the remanent magnetization of the composite, as attraction forces towards other ferromagnetic materials could deform the membrane without any external actuation. On the other hand, these forces could be used as advantage for the generation of multi-stable actuators. Besides the analysis of the free deformation of the structure, an interesting perspective is the analysis of the force that can be generated when the maximum displacement is limited.

Chapter V
Magnetically induced friction damping

A dynamic loading can cause the vibration of mechanical structures, which generates undesired noises in the short term and can lead to material failure in the long term use. Since silent operating and durability are important goals for the majority of scientific and industrial applications, several damping techniques have been developed to counteract vibrations. In this chapter, the use of magnetoactive elastomers (MAE) in the field of structural dynamics for vibration mitigation due to dry friction dissipation is demonstrated. The first section provides general information about modal testing, nonlinear vibrations and friction damping. It furthermore contains a summary of damping approaches, based on magnetic interactions and applied to beam-like structures. An explanation of the concept of magnetically induced friction damping and the experimental proof follow in the next two sections respectively. In the last section, the conclusions of the study are outlined and perspectives for further studies are summarized.

V.1 Introduction to structural dynamics

This section summarizes different aspects of structural dynamics. The different steps of an experimental modal analysis are stated briefly at the beginning to define important technical terms. An overview over the interpretation of dynamic characteristics with a focus on nonlinear phenomena is given afterwards. In the second section, the mechanism of dry friction damping is detailed and a few examples of experimental studies on friction damping are outlined.

V.1.1 Experimental modal analysis

To determine the vibration characteristics (modal parameters) of a structure, dynamic tests are performed. **An experimental modal analysis** comprises, inter alia, the detection of the eigenmodes in a specified frequency range and the determination of the eigenfrequency for each eigenmode [Piranda 2001]. During an experimental modal analysis, a structure is forced to vibrate and its response to the excitation is studied. Figure V.1 gives a schematic overview of the steps and components involved in modal testing. The vibration can be generated, for example, by an electromagnetic shaker or manually with an impact hammer. Accelerometers and load cells are frequently used to quantify the dynamic excitation in experimental setups. The mechanical fixture of the structure greatly influences the way the latter oscillates, e.g. the response of a cantilevered beam is very different from the response of a simply supported beam. If functional parts of bigger structures are tested, the boundary conditions of the part in the real assembly have to be reconstructed as accurately as possible, to assess the modal characteristics that the part shows in the application. Commonly used sensors for the response of the structure are accelerometers and laser Doppler vibrometers. The response characteristics are hence obtained in form of the acceleration or the velocity of a measurement point (see figure V.1). The excitation as well as the measurement of

the response can take place at a single point or at multiple points of the structure, depending on the purpose of the analysis. Frequently used measurement configurations are the Single Input – Single Output (SI–SO), the Multiple Input – Single Output (MISO) and the Single Input – Multiple Output (SI–MO) approach. The first mentioned approach allows time efficient measurements, the second the reconstruction of the modal shape of the vibrating structure and the latter is used in combination with the impact hammer for time efficient measurements. The output is generally measured on points where the structure is strongly deformed by the vibrations ([Piranda 2001]), to obtain the best measurement signal and to characterize the points which are the target of vibration damping. The placement of the corresponding sensors is hence of great importance. Finite element methods can be used to optimize their employment ([Lallement+ 1998]).

Different **excitation signals** can be used to force the vibration of a structure. A random excitation is commonly used as it contains a wide frequency range and different amplitudes. However, non-linearities (like friction) are difficult to distinguish from noise disturbances ([Yuan+ 2019; Schoukens+ 2019]). Periodic excitations are used to restrict the analysis to a determined frequency range, which is helpful to detect non-linearities ([Caughey 1959; Schoukens+ 2019]). The sweep sine is a time-efficient measurement method because the frequency is rapidly increased ([Gloth+ 2004]), but there is a risk of modulation of the eigenfrequencies with excitation frequencies ([Dion+ 2013; Peyret+ 2016b]). A more time intensive method of measurement is the excitation with a stop-sine or a step-sine signal which excites the structure with a single frequency. To characterize the evolution of the response around the resonance, several tests have to be performed. Nevertheless, this experimental method has advantages for the characterization of the non-linear dynamic behavior of a structure like the possibility of mode isolation and, consequently, the jump-up and jump-down testing ([Teloli+ 2020]), which is explained in one of the following sections.
For the identification of the modal parameters, either time-based methods or **frequency-based methods** can be used. In the latter case signals are converted into the frequency domain (e.g. by a Fast Fourier Transformation (FFT)) where the response $Y(\Omega)$ of the system to the excitation $X(\Omega)$ is studied (Ω corresponds to the angular frequency). The behavior of the system is described by the **Frequency Response Function (FRF)** H:

$$Y(\Omega) = \mathsf{H}(\Omega)\, X(\Omega). \tag{V.1}$$

In experimental investigations, noise affects the measurement signals in the time domain and thus also in the frequency domain. The response function H is not exactly obtained by experimental means, but it can be estimated. Estimators of the FRF are based on the repetition of the same experiment and give an averaged estimation of the system response. A high number of repetitions increases the accuracy of the response under the condition, that the system remains unchanged and the transfer function is hence the same for all measurements. There are differ-

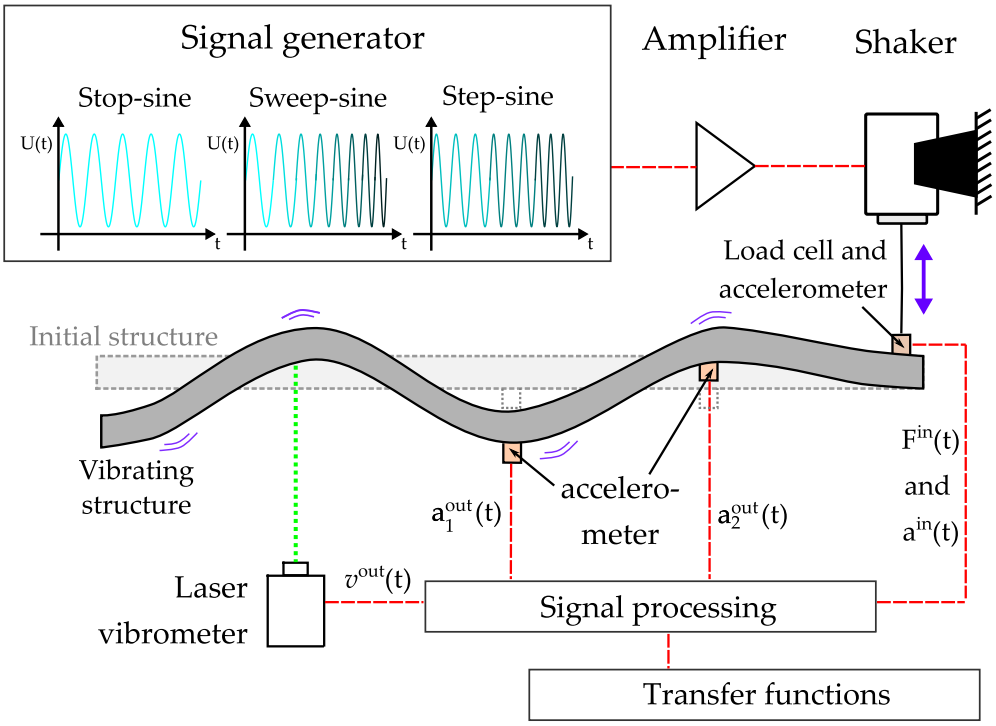

Figure V.1: Schematic drawing of an experimental modal analysis with periodic excitation, $U(t)$ – Input voltage, $F^{in}(t)$ – input force, $a^{in}(t)$ – input acceleration, $v^{out}(t)$ – output velocity and $a_k^{out}(t)$ – output acceleration.

ent types of estimators to approximate the FRF. The estimator H_1 is used, when the noise is mainly affecting the output signal. It is calculated from the average autopower $\overline{S}_{XX}$ of the input signals and the average crosspower $\overline{S}_{XY}$ of the same input signals and the output signals from n repetitions of a measurement. The response is estimated for each tested angular frequency Ω by H_1 by equation (V.2) where the symbol * denotes the complex conjugate transpose.

$$\mathsf{H}_1(\Omega) = \frac{\overline{S}_{XY}(\Omega)}{\overline{S}_{XX}(\Omega)} = \frac{\frac{1}{n}\sum_{k=1}^{n} X_k(\Omega) Y_k^*(\Omega)}{\frac{1}{n}\sum_{k=1}^{n} X_k(\Omega) X_k^*(\Omega)}\,. \tag{V.2}$$

A schematic example of the estimate H_1 is shown in figure V.2. The amplitude expresses the power ratio between the output and the input signal. The phase gives an information about the shift between the input and output signal. As it can be seen in figure V.2, the amplitude shows several peaks, representing a large amplitude ratio between input and output signal. The frequency of a peak corresponds to a resonance frequency of the structure if a negative 180° phase rotation occurs in addition to the amplitude maximum. A positive 180° phase rotation marks antiresonances. H_1 can be used to identify the location of vibration modes in the tested frequency range.
Using the FRFs, natural frequencies, damping ratios and eigenmodes can be identified. Many "Do-it-yourself" methods are available to achieve this goal, the most popular ones rely on "pick-picking" to obtain the frequency and the eigenmodes

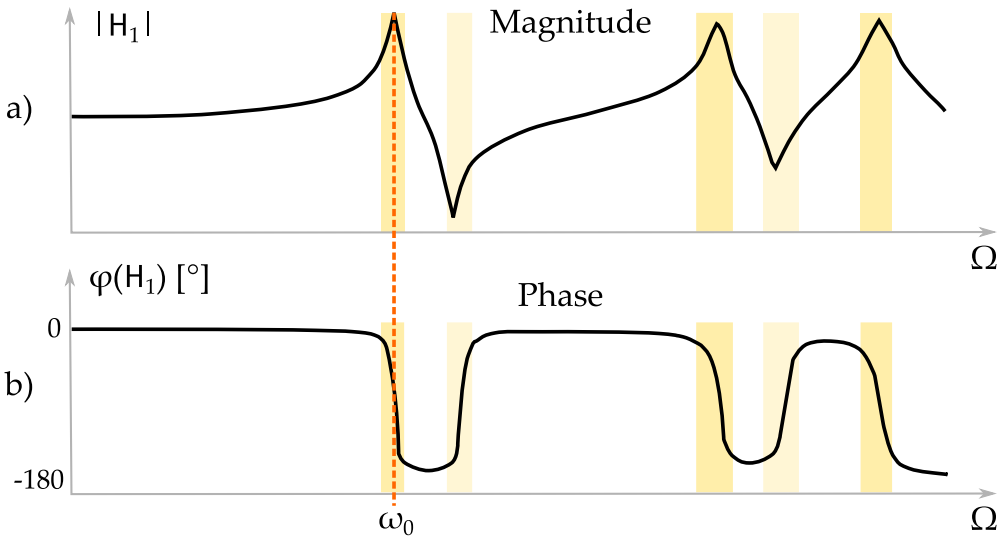

Figure V.2: Schematic drawing of magnitude (a) and phase (b) of the estimator H_1, highlighting the first resonance at ω_0 and the phase shifts (marked in yellow)

and on the "3dB – Bandwidth" method for the damping. In order to obtain accurate results regardless of the tested structure and the modal parameters, the "PolyMAX" or Least-Square Complex Frequency domain (LSCF) method became the new standard in the early 2000s [Peeters+ 2004]. It is based on the identification of the roots of the polynomial common denominators of all the FRFs. By increasing the polynomial order, one can identify higher order complex eigenfrequencies (i.e. natural frequencies and damping ratios) and the so-called stabilization diagrams.

V.1.2 Nonlinear dynamics

In addition to the modal characteristics, the linearity of the dynamic response can be analyzed. The **nonlinear behavior of a dynamic system** can have various origins like large vibration amplitudes during the dynamic analysis (geometric nonlinearities). Material nonlinearities (e.g. hyperelastic behavior) or multi-physical couplings are additional sources of non-linear behavior. Coupling phenomena include, for example, the interactions of vibration structure with the surrounding medium (air friction, liquid damping). Contacts at interfaces in an assembled structure are the fourth type of possible sources of non-linearities resulting from intermittent contacts, localized contacts (Hertz) or dry friction [Peyret+ 2016a; Thomas 2019].
The following description concerns the steady state response of a non-linear system under periodic excitation. A commonly used model to analyze non-linear vibrations is the Duffing equation, which corresponds to a single degree of freedom oscillator containing a cubic spring [Krack+ 2019]. A Duffing oscillator in forced periodic regime with a normalized mass is described by equation (V.3) and

schematically represented in figure V.3 a.

$$\ddot{q} + 2\xi\omega_0\dot{q} + \omega_0^2 q + \gamma q^3 = P\cos(\Omega t), \tag{V.3}$$

where q, $\dot{q}$ and $\ddot{q}$ denote the displacement, the velocity and the acceleration of the system, P and Ω correspond to the amplitude and the angular frequency of the forcing. The parameter γ determines the nonlinearity. For $\gamma = 0$, the system behaves linearly which means that the FRF remains unchanged if the input amplitude is varied. With $\gamma > 0$, the rigidity of the spring increases with the displacement (**stiffening effect**), and with $\gamma < 0$, it decreases with the displacement (**softening effect**). An example for a stiffening behavior of the system as a function of the input amplitude is shown in figure V.3 b. With increasing amplitude P, the resonance frequency increases visibly. Furthermore, the curves are more and more bent to the right the further the amplitude of the excitation increases. The evolution of the peak amplitudes of the response functions for different amplitudes with the frequency is described by the so-called backbone function for friction-based non-linearity [Kerschen+ 2009; Peyret+ 2016a]. The bending of a resonance peak indicates a nonlinear response of the system, in this case the system is nonlinear with respect to the amplitude of the forcing.

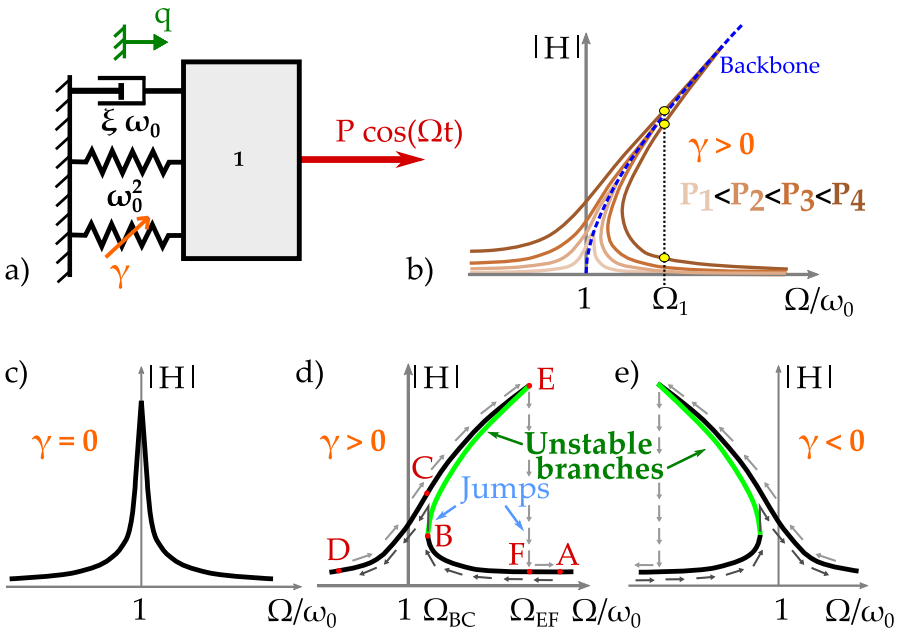

Figure V.3: Schematic representation of a Duffing oscillator according to equation V.3 (a), qualitative response curves for different levels of excitation P of a nonlinear stiffening system (b) and response functions for different oscillators with a linear spring ($\gamma = 0$), (c), a hardening spring ($\gamma > 0$),(b),(d) and a softening spring respectively (adapted from [Krack+ 2019] (a–b) and [Nayfeh+ 1995] (c–e)).

The form of the peak shown in figure V.3 b is a theoretical result, where P_4, for example, has three possible results at Ω_1 (yellow dots). The results of the middle branch cannot be measured experimentally, as the response is unstable. Instead, **amplitude jumps** occur in experiments with nonlinear systems, as shown in the bottom graphics of figure V.3: the first frequency response curve corresponds to the response of a linear system (c), the two subsequent graphics represent stiffening (d) and softening (e) systems respectively. To explain the jump phenomena in stiffening systems, [Nayfeh+ 1995] assume that a first experiment is conducted for $\gamma > 0$ starting a frequency above the resonance at point A (cf. figure V.3 d). The excitation amplitude is kept constant and the frequency is decreased very slowly in a quasi-stationary process following the path AFB. When the frequency is decreased below point B, the response jumps up from point B to point C and follows the upper part of the resonance peak towards D. In a second time, the experiment is started from a frequency below the resonance at point D and the frequency of the excitation signal is increased. The response follows the path DCE, as the amplitude evolves smoothly, towards the maximum. The response then jumps down to point F and follows the path towards point A. The amplitude jumps in a response, showing the softening effect (figure V.3 e), take place the opposite way: jump-up under increasing frequency and jump-down under decreasing frequency. Of the three possible values, the response could take between Ω_{BC} and Ω_{EF}, the solution between the upper and the lower path, marked in green in the graphics d and e of figure V.3, is unstable (see [Nayfeh+ 1995] for more details).

V.1.3 Friction damping

V.1.3.a Modeling

In the context of vibration mitigation, friction damping is a passive method since no energy source is needed for its activation. Two responsible damping mechanisms have been identified : total sliding and partial sliding of the contact surfaces. The mechanisms and effects of partial sliding are well reported in [Peyret+ 2010] for a flat contact between two substructures. More recent contributions are summarized in [Brake 2017]. Dampers based on total sliding are also called Coulomb dampers [Thomas 2019] or (nonlinear) Lanchester dampers [Vakilinejad+ 2020], the second designation refers to the 1914 patent on the passive vibration attenuation in crank shafts [Lanchester 1914]. This concept is widely used to mitigate vibrations turbomachinery blades [Salhi+ 2008]

A simple model of hysteretic damping due to total sliding can be found for example in [Nayfeh+ 1995] and is shown in figure V.4 a. A mass m is connected to an isolated support via two parallel branches. The first branch consists of a spring element with the stiffness k_1 and the second is composed of a spring with the stiffness k_2 and a friction element with the contact force F_c. For a displacement q of the mass, the two branches develop the restoring forces F_1 and F_2 respectively.

In the first branch, the force F_1 is determined by q and k_1. The behavior of the second branch depends on the magnitude of the displacement as the loading diagram in figure V.4 b shows.

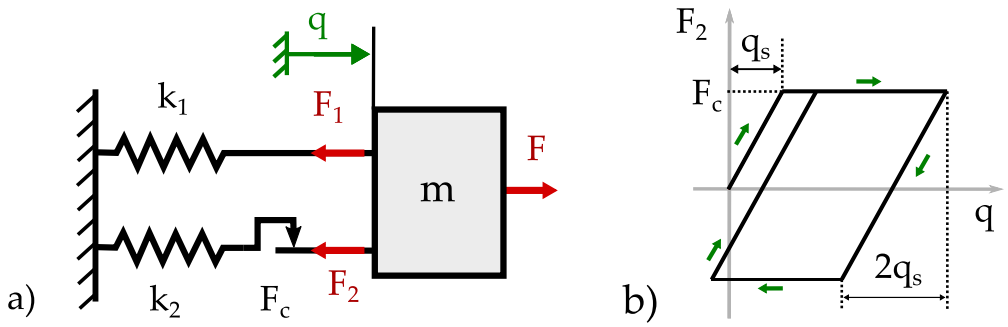

Figure V.4: Schematic representation of a system with hysteretic damping (a) and loading diagram for the second branch of the restoring mechanism adapted from [Nayfeh+ 1995].

If the displacement of the mass stays inferior to the amplitude q_s, the force in the second branch is determined by the stiffness of the spring element, k_2. A displacement beyond q_s causes the friction element to slide, the elongation of the spring stops increasing and the restoring force in the branch remains $F_2 = k_2 q_s = F_c$. When the motion is reversed, the spring is loaded in the opposite direction and as soon as the force in the branch exceeds the contact force, sliding occurs one again. The friction element shows two contact states: total stick and total sliding. Under cyclic loading, the change of the contact state causes a dissipative behavior as well as a **variation of the stiffness** in the system.
A dynamic reduced order model for assembled structures with variable stiffness has been proposed by [Bouaziz+ 2016]. It is represented as "System B" in figure V.5 and described by equation (V.4) and equation (V.5). The model is composed of two normalized masses each having a single translational degree of freedom. They are interconnected via a spring element and a friction element. The system is coupled by sticking forces and its natural frequency is ω_0. When the magnitude of the vibration increases, sliding occurs in the joint which leads to an out of phase mode between the two masses. The frequency of this mode is lower than ω_0 due to the stiffness change (cf. Δk effect in figure V.5). At the same time, the response is more damped and the resonance is interspersed between the natural frequencies.

$$\begin{aligned} \ddot{q}_1 + \omega_0^2 q_1 + F_c + k_c(q_1 - q_2) &= F\sin(\Omega t) \\ \ddot{q}_1 + \omega_0^2 q_2 - F_c + k_c(q_2 - q_1) &= 0 \end{aligned} \tag{V.4}$$

$$F_c \begin{cases} = -F_c^0 & \text{if } \dot{q}_2 - \dot{q}_1 > 0 \\ = +F_c^0 & \text{if } \dot{q}_2 - \dot{q}_1 < 0 \\ \in [-F_c^0, +F_c^0\,] & \text{if } \dot{q}_2 - \dot{q}_1 = 0 \end{cases} \tag{V.5}$$

A model for a nonlinear Lanchaster absorber based on the **change of the modal mass** has been presented by [Vakilinejad+ 2020]. The model of a primary system with a translational degree of freedom and the modal characteristics ω_0^2 and $2\xi\omega_0$ (stiffness and damping respectively) is shown as "System A" in figure V.5. The primary mass is normalized in this example. The mechanism applied for vibration attenuation is modeled by a second mass, represented by λ_m due to the normalization with the primary mass, and a dry friction contact force F_c, which connects the two masses. A relative displacement $q_d = q_2 - q_1$ between the two systems causes the second mass to slide on the primary mass and the friction in the contact dissipates some of the vibration energy. The system is described by equation (V.6) where the contact force depends on the relative velocity of the two masses (equation (V.5)). According to a semi-analytical study of the steady sate response of a nonlinear Lanchester damper, there are three types of responses of the system depending on the contact force F_c. A frequency shift of the resonance frequency as well as a change in the displacement amplitude of the primary mass due to the variation of the contact force can be observed in the response function.

$$\begin{aligned} \ddot{q}_1 + 2\xi\omega_0\dot{q}_1 + \omega_0^2 q_1 + F_c &= F\sin(\Omega t) \\ \lambda_m \ddot{q}_2 - F_c &= 0 \end{aligned} \tag{V.6}$$

In the case, that high contact forces are applied, the damper is connected to the primary system in rigid manner and there is no relative displacement between the two masses. If the contact force vanishes, the masses are no longer connected, the modal characteristics of the primary system determine the modal response (slip-only response). Since no other characteristic but the total mass of the system changes between these two contact states, the frequency shift is due to the evolution of the modal mass. Between these two extremes, the variation of the contact force generates an intermediate state between total stick and total slip, the response is therefore called stick-slip response.

Figure V.5 shows that the amplitude of the primary mass evolves in a non-linear way with the increase of the contact force (direction of the red arrow). Starting from no contact ($F_c = 0$), a raise of F_c causes a decrease of the vibration amplitude of the primary mass, which corresponds to an increase of the damping. By further increasing the contact force, the amplitude peak passes by a minimum and then starts to increase, the damping decreases thus. The sliding friction dissipates a part of the vibration energy in the stick-slip state where the ratio of stick and slip depends on the contact force. when the contact is established by small forces, an increase of F_c also increases the contact and thus the energy dissipated by sliding friction. However, if the contact force becomes too intense, it prohibits the sliding and the damping reduces as a consequence. The central graphic un figure V.5 shows that the systems A and B, proposed by [Vakilinejad+ 2020] and [Bouaziz+ 2016] respectively, behave in an opposite way with increasing contact force F_c due to the different effects Δm and Δk respectively.

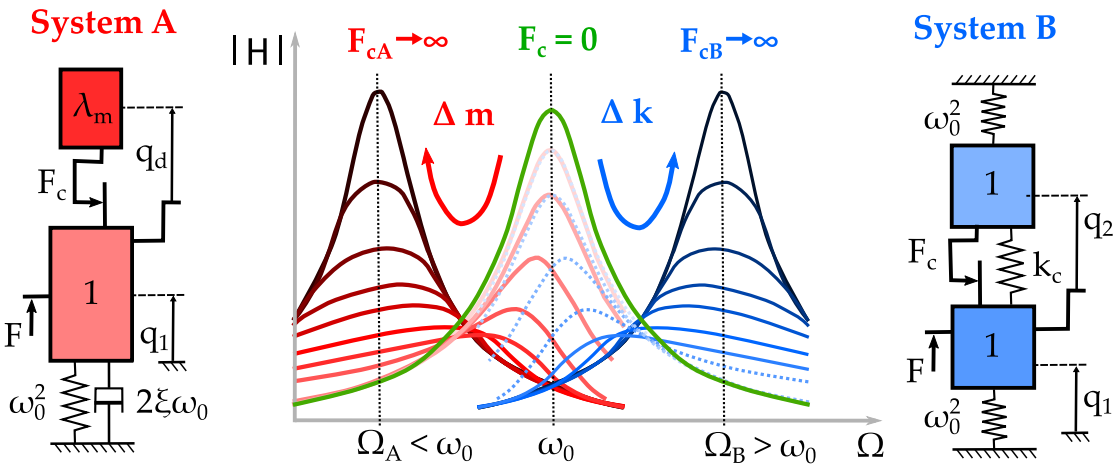

Figure V.5: Schematic view of dynamic systems in which the variation of the contact force F_c induces a change of the model mass (System A) [Vakilinejad+ 2020] or the stiffness (System B) [Bouaziz+ 2016], central graphic adapted from [Thomas 2019].

V.1.3.b Experimental characterization

Even though the model is a good basis to explain the influence of friction damping on the dynamic characteristics of a system, the friction state in real structures is rarely a single contact point with a constant force. The details of contact mechanics are too vast to be discussed in detail here but discussion of important factors is given in [Popp+ 2003]. The authors state that, in a **real contact area**, the **normal force shows a non-uniform distribution** on many contact points. A high contact pressure may cause some parts of the contact area to stick while other parts slide. The origins of the non-uniform distribution can be found on the macroscopic scale (uneven or wavy contact surfaces) and on the microscopic scale (surface roughness) of the contact surfaces [Peyret+ 2016a]. Furthermore, depending on the relative motion of the surfaces, the local point contacts are subjected to different relative displacement amplitudes. In the case that two plane surfaces are in torsional relative motion around their normal axes, the displacement depends on the observation point on the surface, regardless of the distribution of the contact pressure. The contact state, in which only parts of the contact zone are sliding, is also called micro-slip [Scheel+ 2020; Popp+ 2003] in contrast to macro-slip, for which the whole contact zone is sliding.
A commonly used **experimental setup to analyze dry friction** are cantilevered beam structures with one or various contact zones. The control of the contact state in the friction area turns out to be a difficult task in experimental investigations. According to [Brake+ 2019], the prediction of the dynamic behavior of jointed structures suffers from high uncertainty. Variations in dynamic behavior are measured between structures with nominally identical parts (variability) and even between several measurements on the same structure (repeatability). The origins of these uncertainties can be found on all length scales from the alignments

of the parts over variations of their curvature in the contact zone to the surface roughness. The influence of contact parameters in the contact areas of a so-called Brake-Reuß beam (see for example [Brake 2017]) have been investigated in a four-year experimental study. The structure consists of a 2.54 cm square cross-section beam presenting a three bolt lap joint in the middle. Both contact surfaces in the beam are from 304 stainless steel. It has been found, that the contact pressure is localized around the joint when the surface roughness is rather high. The pressure is distributed more evenly in the contact surface for lower surface roughness and in addition, the repeatability increases and the assembly is less sensitive to the preload generated by the bolts.
The sensitivity of normal preloads in jointed structures is a recurring subject of investigation in friction damping which is also addressed by [Teloli+ 2020]. The experimental setup contains a three lap-joint configuration with contact patches in the contact interfaces between beams. The patches are inserted for the control of the contact area size. The experiments are carried out on the beam under clamped – free conditions with step-sine tests. A high sensitivity of the vibration attenuation on the tightening torque of the external bolts is stated: a lower tightening torque results in higher damping. In addition, softening effects in the response have been observed with increasing excitation amplitude. The contact stiffness is modified by the amplitude which is an indicator for the change of the contact state. According to the authors, the design of the contact area provides a high repeatability of the experimental measurement.
Another approach for better control of the contact surface in experimental nonlinear modal analysis has been suggested by [Scheel+ 2020]. A modular design of a beam structure, in which contact elements can be connected on different positions of a cantilevered beam, is presented. The clamping is designed to avoid stress concentration and the normal preload in the contact area can be varied. The contact is established between the 16MnCr5 beam and 90MnCrV8 contact elements. Under varying excitation amplitude, contact states ranging from full stick to mainly sliding have been identified. Due to dry friction, a frequency decrease of 36 % and a maximum modal damping of 15 % have been measured. The concept for vibration mitigation proposed in this work is based on dry friction and puts forward the use of magnetically Hard MagnetoActive Elastomers (H-MAE) for the generation of evenly distributed contact forces.

V.2 Modal damping in magnetoactive sandwich structures

The use of MAE for vibration mitigation has been intensively studied on **functional sandwich structures**. A classic sandwich structure consists of two skins, that enclose a core in the middle. The skins are thin sheets which primarily resist the in plane lateral bending loads, while the core can consist of passive structures like a foam, honeycomb structures or web structures as well as corrugated or truss

geometries. In comparison to a monocoque structure, sandwich structures have a higher stiffness to weight ratio, leading to a lower structural weight [Vinson 1999]. When functional materials are included in the core, this type of structure offers many possibilities to achieve vibration attenuation.
Changing the modal characteristics of a system means varying the mass, the stiffness and the damping separately or at the same time. The control of the structural parameters can either be performed in a passive manner, without external energy supply, or in a semi-active or adaptive manner. The term **adaptive control** is used in this context since the external energy is used to tune parameters of the system and not to actively counteract the excitation [Butaud+ 2020]. Magnetically soft magnetoactive elastomers (S-MAE) have been used in semi-active control elements in sandwich structures as the following paragraphs show.

V.2.1 Damping based on magnetoactive structures

The adaptive tuning of the damping and the stiffness has been experimentally demonstrated with sandwich structures including a **magnetorheological fluid (MRF)** ([Sun+ 2003; Yalcintas+ 2003]). An analysis of stiffness and loss modulus of the MRF prior to the dynamic analysis shows an increase of both characteristics with increasing magnetic field ([Sun+ 2003]). To conduct the modal analysis, the specimens were assembled from the two aluminum skins, two spacers, assuring a constant thickness of the MRF film, a silicone surrounding the outer boundaries of the sandwich to prevent leakage and the MRF, which was injected in the sandwich with a syringe. The simply supported beam structure was subjected to a transverse excitation in presence or absence of a magnetic field, which was generated by permanent magnets. In one study, the vibration amplitudes could be reduced up to 20 dB, while the resonance frequencies shifted up to 20 % ([Sun+ 2003]). In the second study ([Yalcintas+ 2003]), the same trends were observed. Although the results seem interesting, the authors report difficulties concerning sandwich assembly and the generation of a homogeneous magnetic field, which has been assumed in their models.
As the magnetorheological effect also occurs in magneto active elastomers (MAE), a variety of studies on MAE beam structures can be found, which generally build upon magnetically soft composites (S-MAE). Analytical investigations on **S-MAE sandwich structures** with conductive skins have been presented by [Zhou+ 2006b]. The model considered a core of 2 mm thickness and two skins of 0.1 mm thickness. A magnetic field perpendicular to the direction of vibration was considered and a change of the core's shear modulus from 0.388 MPa of up to 60 % depending on the field intensity was specified. A distribution function was implemented for the material parameters which allowed the analysis of sandwiches with a full S-MAE core or sandwiches with S-MAE and non MAE core. The change of the shear modulus only applied to the S-MAE parts. The magnetic loads were calculated on the discontinuous surfaces by the help of the Maxwell stress tensor (cf. chapter I). Furthermore, the model includes the effect of the magnetic pertur-

bation field, that occur as the skins move in a stationary external magnetic field and hence currents are induced [Zhou+ 2006a]. These loads are only applied to the electrically conductive skins.
An out of plane excitation force has been applied in the middle of the simply supported sandwich beam. The results show, that the flexural rigidity of the beam increases in the external magnetic field. The effect of the magnetic field is especially visible in vicinity of the resonances. It is shown, that the change of the shear modulus of the S-MAE has a significantly higher impact on the modal characteristics than the inductive loads during the study. Furthermore, the study indicates, that the increase in stiffness can be maximized by maximizing the amount of S-MAE in the core.
Based on the same modeling approach for magnetic loads, [Nayak+ 2013] analyzed the influence of axial mechanical excitation on S-MAE sandwiches in a numerical study. The stiffness of the S-MAE was supposed to vary with the external magnetic field. Position and length of S-MAE patches in a multi-material core, composed of S-MAE and a passive viscoelastic material, has been altered to analyze the influence on the modal characteristics. The study was carried out with free and forced excitations on simply supported in a clamped-free condition. The magnetic field causes a shift of the resonance frequency as well as a variation of the loss factor of the structure. For the first six vibration modes it is shown, inter alia, that the optimum configuration for vibration attenuation of the beam depends on the length as well as the positioning of the S-MAE patch, the magnetic field and the boundary conditions. During another study, the authors observe that that an increasing magnetic field strength under periodic axial loading allows to shift the instable behavior to a different frequency region [Nayak+ 2011]. The shift is explained with the stiffness change, provoked by the external magnetic field.
The study conducted by [Hu+ 2011] demonstrates, how local magnetic fields, applied on different points of the beam, influence the frequency response. Figure V.6 schematically shows the experimental setup. To assemble the sandwich structure, an uncured mix of silicone rubber, silicone oil and carbonyl iron powder has been spread on one of the two aluminum skins. The second skin was pressed on the composite layer from above and the polymerization took place directly in the sandwich structure.
A dynamic excitation of the sandwich under clamped-free boundary conditions has been performed. The magnetic field was generated by the help of two magnets, facing the top and the bottom skin respectively. The length of the magnets was significantly smaller than the length of the beam, the magnetic field was thus mainly applied locally to the structure. The axial position of the magnets towards the beam has been altered in a first time: the two magnets were displaced gradually from the clamped end to the free end of the beam, to change the magnetic conditions. In a second time, the distance between one of the magnets and the skins has been varied. A variation of the amplitude and of the resonance frequency of the first mode due to different magnetic conditions is stated. The variation is attributed to the local change of the shear modulus of the composite, which ranged from 1 to 20 kPa depending on the magnetic field intensity according to the au-

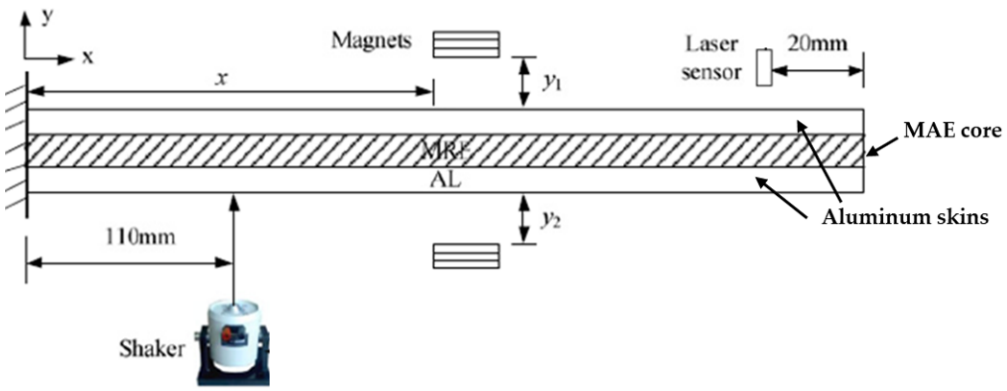

Figure V.6: Schematic view of the experimental setup used by [Hu+ 2011], where permanent magnets modify the stiffness of the S-MAE locally.

thors. A free oscillation experiment on a cantilevered sandwich beam, on which two electromagnets were fixed on the free end, has been conducted by [Dyniewicz+ 2015]. The sandwich structure was composed of 2 aluminum sheets and a S-MAE with a shear modulus of 310 kPa. A field of 700 mT provoked a modulus change of about 10 %. A control strategy is presented, which allows to change the shear modulus and hence adapt the stiffness of the structure in real time. The reduction of the free vibration amplitude of the beam tip with respect to the initial amplitude after 60 s is compared between the three states “no magnetic field” , “continuous magnetic field” and “adapted magnetic field”. The decrease measures 80 %, 93 % and 96 % respectively.

An experimental parametric study on the influence of the particle volume fraction and the matrix stiffness of the S-MAE core on the effect of the magnetic field on a sandwich beam structure has been conducted by [Szmidt+ 2019]. Anisotropic S-MAE, containing either 11.5 % or 33 % of carbonyl iron particles, were elaborated. The shore hardness (A) of the matrix materials measured 10A and 40A respectively. Composite patches, which measured $16 \times 15 \times 5$ mm^3, were glued between the tips of two steel beams with a length of 800 mm, a width of 15 mm and a thickness of 2 mm (figure V.7). An investigation on the shear storage modulus and loss modulus of the four composite materials shows, that both characteristics increase under magnetic field and that a soft matrix and a high volume fraction favor the change of the modulus. During a first study, two permanent magnets were placed at both sides of the beam at the tip, to generate a magnetic field.

To vary the magnetic field, three different pairs of magnets were used. An additional brass plate was inserted near the patch to prevent it from compression due to the attraction forces between the magnets. In a second study, one of the magnets was replaced with an electromagnet and a semi-active control strategy for the magnetic field was applied (figure V.8). The deflection of the free oscillation of the cantilevered beam in the first mode was measured for different combinations of patches and magnets. The vibration period as well as the damping factor were obtained from the response in the time domain. The highest increase of the dam-

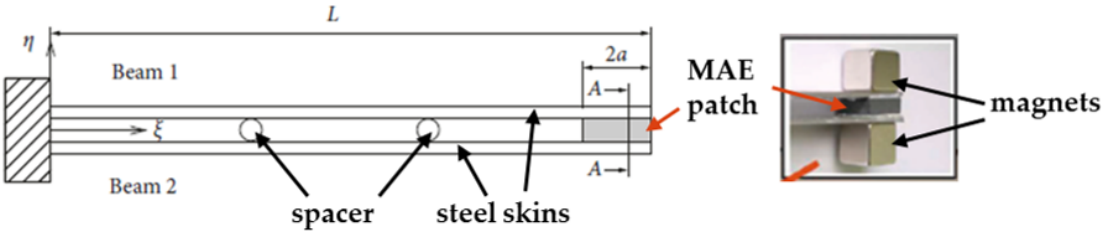

Figure V.7: Specimen, assembled from steel skins, spacers and a S-MAE patch, glued between the tips of the skins; the magnets are added to the specimen to modify the stiffness of the S-MAE [Szmidt+ 2019].

ping is observed for the patch, made from the matrix with the lower shore hardness and the lower volume fraction. Another result of the study is the increase of the vibration period due to the attachment of the magnets, which increases the inertia. The increase in damping due to the magnetic field is lower than predicted by the model, additional other sources of damping in the measurement setup are suspected.

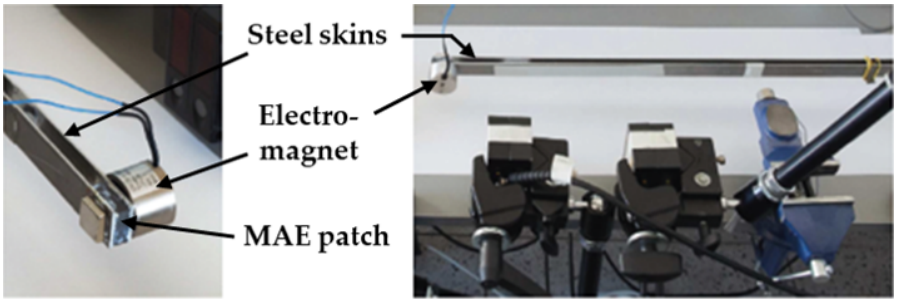

Figure V.8: Specimen used by [Szmidt+ 2019] for the adaptive control of the stiffness of an S-MAE, element glued between the tips of two steel sheets, via an electromagnets.

The following two examples show the **use of permanent magnets** for vibration mitigation. To reduce vibrations of a beam structure, permanent magnets can not only be employed to generate quasi-static magnetic fields in S-MAE but also as structural elements, as shown by [Xia+ 2019]. The experimental part of the study contains a cantilever beam excited on its base. Locally resonant elements, composed of smaller beams with attached magnets, are located on the beam (figure V.9). Supplementary magnets are put in place near each resonant cell and the interaction of the magnets causes the small beams to behave in a bistable manner. Under small excitation amplitudes, the attachments resonate locally, but with increasing amplitude a nonlinear attenuation of vibration in the global structure is observed due to the chaotic vibrations of the local attachments. This study does not contain MAE, but it is an example of passive, amplitude dependent vibration attenuation due to magnetic interaction forces.
Recently, [Amjadian+ 2018] have proposed the prototype of a damper based, inter alia, on a combination of friction and magnetism. A schematic view of the

experimental setup is shown in figure V.10. The repulsive interactions between permanent magnets PM_1 and PM_2 generate the normal force N_f between the friction pad and the stainless steel sheet. During the test, the assembly "Rotor" is moved with respect to the assembly "Stator" (cf. figure V.10). For small excitation amplitudes, the tangential forces do not overcome the friction forces and the friction pad does not slide. The damping in this configuration is due to eddy currents since the permanent magnets are in motion with respect to the copper plate. For high excitation amplitudes, friction damping occurs in addition to eddy current damping. The normal force, and consequently the friction force, can be adjusted by the air-gap between PM_1 and PM_2.

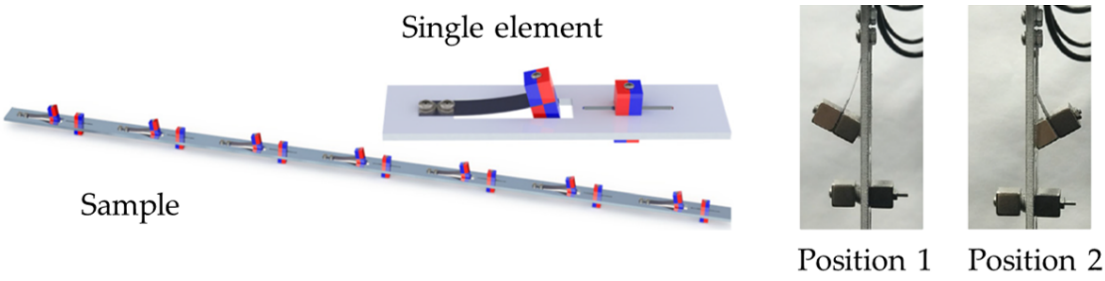

Figure V.9: Specimen, used by [Xia+ 2019], containing several bistable locally resonant elements consisting of magnet pairs.

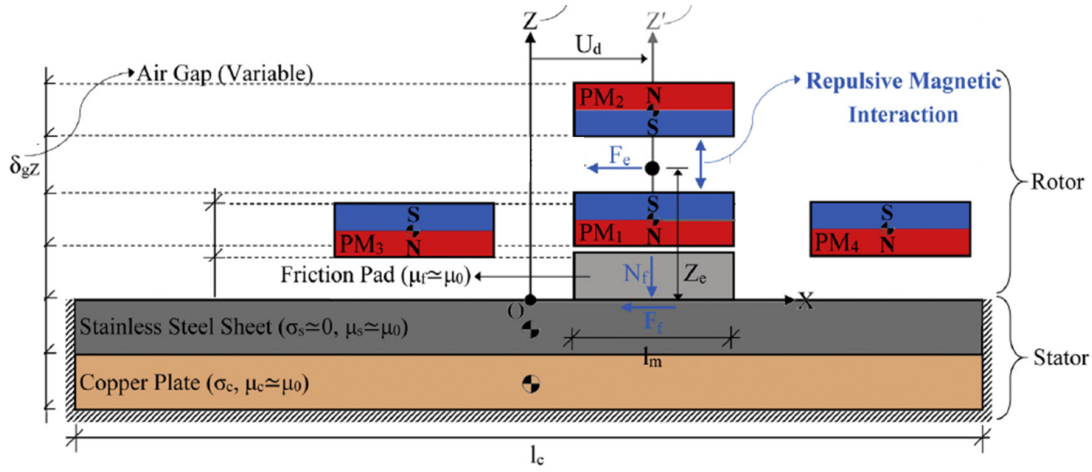

Figure V.10: Scheme of the experimental setup used by [Amjadian+ 2018]: The relative motion between the assemblies "Rotor" and "Stator" generates a friction force F_f and induces eddy currents in the copper plate, which counteracts the movement.

V.2.2 Context of this work

In the context of modal analysis, S-MAE composites have been employed in sandwich structures and external magnetic fields have been applied to change the material parameters. A shift of resonance frequencies as well as an increase in damping have been reported due to the application of the magnetic field. The functional principle of these structures is the magnetic field dependent stiffness of the composite materials (MR effect). The effect is favored by a soft matrix and is dependent on the particle content of the composite. Interesting results concerning the length and number of composite patches were obtained during the modeling: both parameters influence the modal characteristics of the tested structures. Difficulties arise for the application of the magnetic field, especially when the experimental setup is compared to the modeling. The models assume a unidirectional and homogeneous external magnetic field which is difficult to realize in a dynamic experimental setup. Furthermore, the use of an additional magnetic field source either complicates the experimental setup or modifies the modal characteristics in form of supplementary masses added to the beams. Permanent magnets generate quasi-static magnetic fields in the S-MAE which have to be varied manually between two measurements. To the knowledge of the author, magnetically hard elastomers have not been employed in sandwich beam structures for vibration attenuation yet.
The S-MAE patches in previous studies have been connected to the two skins such as to establish a rigid contact. A completely different contact state is targeted during friction damping. As the literature shows, partial or micro-slip is needed in the contact interface to dissipate a part of the vibration energy. The contact pressure plays an important role in this dissipation process, but it is difficult to establish and to control this quantity in experiments. A big effort has been made in the design of the setup and the structure to study friction damping generated by rigid material pairs. For a constant contact pressure, a nonlinear behavior with respect to the excitation amplitude has been observed. The damping is reported to be most effective for moderate contact pressures. The purpose of this work is the use H-MAE for vibration mitigation. In the contrast to previous studies on S-MAE beam structures, which build upon the MR effect, the concept presented in the following is based on friction damping and magnetically induced contact forces. The concept will be presented in detail in the following section.

V.3 Concept of magnetically induced friction damping

The concept, presented in this section, employs a magnetized H-MAE on the purpose of friction damping in a sandwich beam. Figure V.11 a shows the sketch of an oscillating sandwich beam. It is composed of a magnetized H-MAE (soft core), enclosed by two ferromagnetic skins. The magnetic field, generated by the core, magnetizes the skins; the propagation of the magnetic flux is schematically

shown in (figure V.11 b). The skins are attracted by the magnetized H-MAE and the forces, generated by this interaction, maintain the skins close to the core without additional means of fixation (figure V.11 c). The sandwich structure can hence easily be disassembled and reassembled. When the structure is subjected to transverse vibrations, the beam structure is deformed (figure V.11 a) and shear stresses arise throughout the structure. Normal forces and tangential forces are present in the contact area (figure V.11 d). For small vibration amplitudes, it is supposed that the normal forces prevail and a rigid contact is maintained. With an increasing vibration amplitude, the tangential forces increase. Throughout the contact area, more and more parts begin to slide and a state of partial sliding is generated. The damping maximizes for a specific ratio of sticking and sliding, which is determined by the vibration amplitude. By further increasing the amplitude, the tangential forces become predominant, until the contact surfaces mainly slide. The H-MAE sandwich structure presents a passive, amplitude dependent mechanism for vibration attenuation due to dry friction. The concept is detailed in the following.

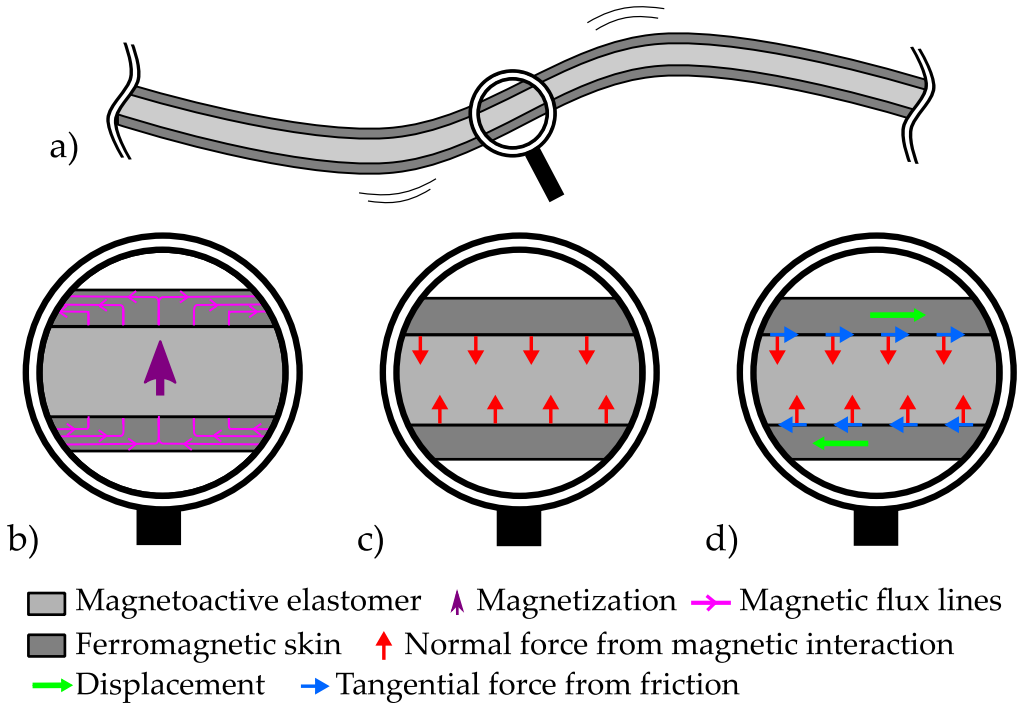

Figure V.11: Schematic view of a part of an oscillating sandwich beam structure (a) and a zoom on one part of the structure sketching the magnetic state (b), the preload (c) and the contact situation (d) in the beam.

V.3.1 Normal force - a magnetically induced preload

The MAE used in the sandwich structure is a mechanically soft permanent magnet. Its magnetization generates a magnetic flux, that propagates in the magnet, but also outside the magnet (figure V.12 a). The local quantity, associated with the magnetic flux, is the magnetic flux density $\boldsymbol{B}$. Important parameters, that determine the distribution of the flux and its local density are the characteristics of the surrounding environment, also called magnetic circuit. In the context of this study, the circuit is supposed to consist of non-magnetic or ferromagnetic materials. Depending on the magnetic permeability μ, materials in the circuit can be a good conductors of the magnetic flux (e.g. iron or some steel grades) or a bad conductors (e.g. air or aluminum). In isotropic materials, the permeability can be described by a scalar value μ, in anisotropic materials by a second order tensor $\mathbb{\mu}$. When a ferromagnetic material with high permeability is approached to the magnet, the magnetic flux tends to propagate more easily in this material than in the air and is redirected, as the comparison of figure V.12 a and b shows. The part of the flux ,that, for energetic reasons, cannot be guided by the iron in figure V.12 b, is called leakage flux. The amount of the leakage flux can be adjusted with the air gap (compare figure V.12 b and c). The intensity of the magnetization can also be expressed by the residual magnetic flux density $\boldsymbol{Br}$. In absence of an external field, this is the maximum amount of magnetic flux density that can be generated theoretically by the magnet. The effective amount of $\boldsymbol{B}$, also called operating point, depends on the geometry of the magnet and the magnetic circuit. For further information about the determination of the operating point, the reader is referred to chapter IV or [Jufer 1998] for example. In the sandwich structure, the ferromagnetic skins are close to the soft core and supposed to guide a maximum amount of the magnetic flux (figure V.12 c).

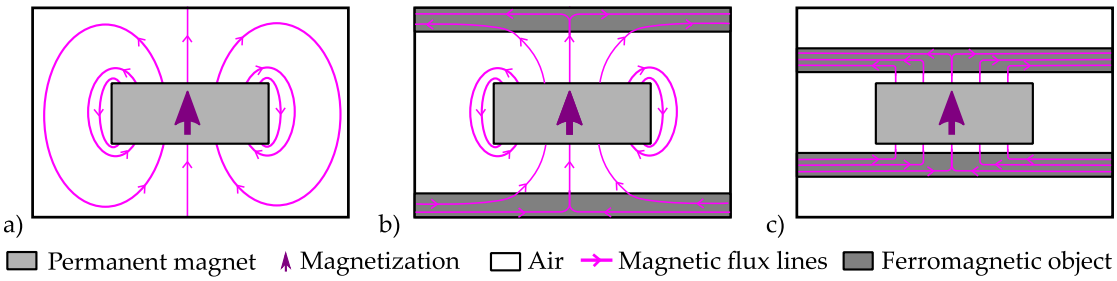

Figure V.12: Scheme of a permanent magnet, surrounded by air (a) and highly permeable ferromagnetic objects located at a large distance (big air gap) (b) and a small distance (small air gap) (c).

A part of the electromagnetic energy, stored in the magnet can be provided for magnetomechanical interaction. As shown in chapter I of this thesis (section I.3.1), tensor quantities are used to describe magnetically induced forces. A consistent method for the estimation of the local force on the surface of an object, i.e. the pressure, is the use of the jump of the stress tensor $\mathbb{t}$ over the surface (cf. section I.3.2). The expression of the tensor jump on discontinuity surfaces like material interfaces

is shown in equation (V.7) where σ^{mag} is the magnetically induced stress on the interface, $\mathbb{t}^+$ and $\mathbb{t}^-$ correspond to the expression of the magnetic stress tensor one sides $+$ and $-$ of the interface respectively and $\boldsymbol{n}$ is the surface normal pointing in the direction of the side $+$ (cf. figure I.5). In the present work, the effect of the velocity on the magnetic quantities is neglected. This is an initial assumption; the validation could be part of future theoretical and experimental work concerning magnetically induced friction damping.

$$\sigma^{mag} = [[\,\mathbb{t}\,]]\,\boldsymbol{n} = (\mathbb{t}^+ - \mathbb{t}^-)\,\boldsymbol{n}\ , \tag{V.7}$$

V.3.2 Tangential force : friction generated by vibrations

Bending vibrations of thin sandwich structures generate tensile stresses mainly in the skins and shear stresses mainly inside the core. The compliance discontinuity between the skins and the core makes the strain field discontinuous. When the shear stresses are greater than the Coulomb threshold, the skins can locally slide over the core and the shear stresses are constant, regardless of the vibration magnitude.

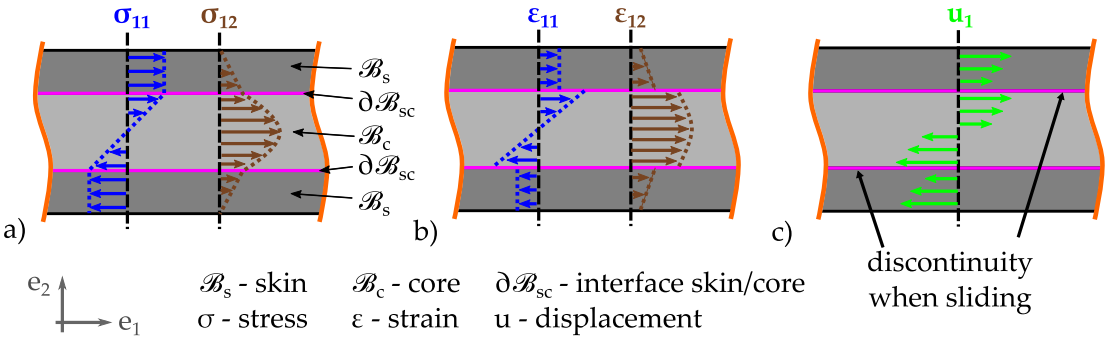

Figure V.13: Section of the vibration sandwich beam sandwich: representation of the in plane stresses (a), strains (b) and the displacement field u_1 (c).

The motions and stresses are governed by the following set of equations :

$$\begin{aligned} \text{in } \mathscr{B}_s \cup \mathscr{B}_c &: \boldsymbol{div}(\sigma) = \rho^m \frac{\partial^2 \boldsymbol{u}}{\partial t^2}\ , \\ \text{in } \mathscr{B}_s &: \sigma = \mathcal{C}^s : \varepsilon\ , \\ \text{in } \mathscr{B}_c &: \sigma = \mathcal{C}^c : \varepsilon\ , \\ \text{on } \partial\mathscr{B}_{sc} &: \sigma_{22} = \sigma_{mag}\ , \end{aligned} \tag{V.8}$$

and the Coulomb friction model with the friction coefficient c_μ

$$\begin{cases} |\sigma_{12}| = c_\mu |\sigma_{22}| & \text{and} \quad [[\dot{u}_1]] \neq 0 \\ |\sigma_{12}| < c_\mu |\sigma_{22}| & \text{and} \quad [[\dot{u}_1]] = 0 \\ (\,|\sigma_{12}| - c_\mu |\sigma_{22}|\,)\ \dot{u}_1 = 0 \end{cases} \tag{V.9}$$

where $\mathscr{B}_s$ denotes the domain occupied by the skin, $\mathscr{B}_c$ the domain occupied by the core and $\partial\mathscr{B}_{sc}$ the material interface. During a relative movement of $\mathscr{B}_c$ with respect to $\mathscr{B}_s$, the contact state on $\partial\mathscr{B}_{sc}$ may become dependent on the position in $\boldsymbol{e}_1$: some sections are sliding whereas others are sticking. This leads to the dissipation of energy through friction and hence to vibration damping.

V.4 Experimental proof

This section describes the experimental investigation on magnetically induced friction damping. The test sample and the test bench are described in the first part. In the following, the measurement procedures and results are presented. The section closes with the interpretation and a discussion of the results.

V.4.1 Sandwich assembly and experimental setup

A sandwich structure is assembled for the experimental investigation from five magnetic polymer patches, two ferromagnetic metal sheets and an aluminum spacer (figure V.14). The magnetic polymer is elaborated by the procedure described in chapter II. The patches used in the present study have a volume fraction of 36 % of NdFeB particles and show a remanent magnetization of 0.3 T. They measure 29 mm × 10 mm × 1.6 mm and are magnetized perpendicular to their surface. The sheets consist of the steel alloy M400-50A with a thickness is 0.5 mm. The spacer is made from 1.6 mm thick aluminum, a magnetically neutral material. A sample holder is used to assemble the sandwich structure as shown in figure V.14. The alignment of the metal sheets and the spacer is assured by two pins and the cavity of the holder in which the parts are placed for the assembly process.

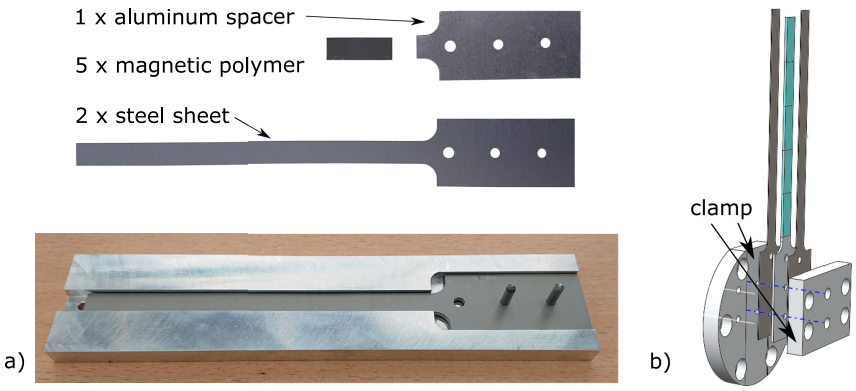

Figure V.14: Different components of the magnetic sandwich beam separately (top view) and assembled in the sample holder (a) and schematic view of the clamping (exploded view) (b).

At first, one of the metal sheets is placed in the holder. Afterwards, the aluminum spacer is placed on top of the sheet. The five magnetic patches are placed on the sheet one by one afterwards, starting from the bottom, where the first patch is placed directly above the aluminum spacer. The patches are oriented such as the magnetization of two adjacent ones is opposed. Finally, the upper magnetic sheet is put on top of the assembly and the magnetic sandwich is removed from the holder. The dimension of the sandwich structure measures 220 mm × 30 mm × 2.6 mm and the length of part, consisting of the narrow beam is 150 mm. The upper part of the sandwich is held together by the magnetic forces between the polymer the metal sheets. The aluminum spacer is maintained in place by the clamping force, that fixes the sandwich in the measurement setup.
The clamping consists of two aluminum parts (figure V.14 b). The sandwich is placed in the cavity of the first parts, which has the same width as the bottom part of the sandwich, and maintained in place with two brass screws. A second aluminum part is fixed on the first one by four brass screws and thus clamps the bottom part of the sandwich. The rigidity of the aluminum spacer in the clamping prevents a dependence of the clamping on the tightening torque of the screws. In addition, the geometry of the lower part of the sandwich has been designed to minimize the damping in the clamping. The assembly is connected to an electromagnetic shaker (Tyra 150N, figure V.15 a). A triaxial DeltaTron® accelerometer (Type 4520) is fixed to the upper part of the clamping with an instant adhesive (Super Glue-3, Loctite). Its z-axis is aligned with the direction of movement of the shaker. The acceleration of the base of the shaker is used as reference signal. The velocity of the sandwich beam due to the acceleration of the shaker is measured with the contactless Polytec vibrometer PSV-500. The control of the shaker as well as the data acquisition is managed via a NI9234 hardware in combination with a control algorithm implemented in Matlab. An amplifier is interconnected between shaker and the NI system to deliver the necessary power for the amplifier. A schematic view of the measurement setup is shown in figure V.15 b.

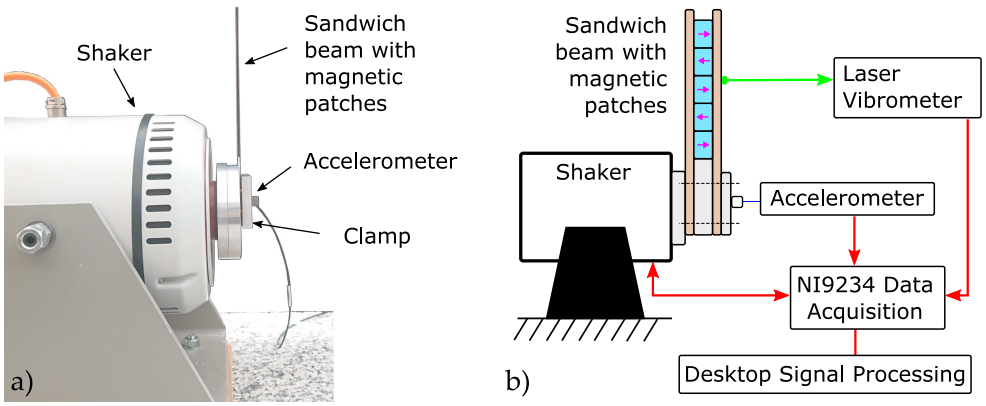

Figure V.15: Experimental setup with specimen mounted on the electromagnetic shaker in side view : photograph (a) and schematic view (b).

V.4.2 Measurement procedure and results

V.4.2.a Single-point measurement (SI–SO)

A single point measurement of the velocity has been performed on the beam. The aim of this study was to analyze the influence of the acceleration magnitude on the damping behavior of the beam. For this purpose, the measurements were performed with seven different amplitudes, ranging from $1\,\mathrm{m/s^2}$ to $75\,\mathrm{m/s^2}$. A step-sine is chosen as excitation signal type, since it allows tests in an adjustable frequency band, jump-up and jump-down testing and a steady-state response. The control algorithm is briefly described in the appendix (cf. appendix A.3.1); a more detailed description can be found in [Teloli+ 2020]. The frequencies of the tests lie between 200 Hz and 340 Hz. The sensitivity of the laser was set to 250 mm/s during all the tests. Since the first and second bending modes could not accurately be measured with the experimental setup, due to noise disturbances in the low frequency range, the third bending mode is chosen for the analysis. Bending modes are chosen, as the axial displacements, supposed to cause the relative movement between skins and core, are bigger during bending than during torsion. The frequency response functions (FRFs) are estimated based on the velocity and the acceleration signals in the tested frequency range. For accelerations above $5\,\mathrm{m/s^2}$, the measurement has been performed with increasing and decreasing frequency to assure, that the evolution of the response in vicinity of the resonance frequency is well captured. At the same time, multiple measurements with the same amplitude can be compared to obtain an indication about the repeatability of the experimental setup. In total, eleven FRF have been obtained from the measurements. The evolution of their amplitudes with the frequency is shown in figure V.16. The different acceleration magnitudes are separated by the line color in the graphic.

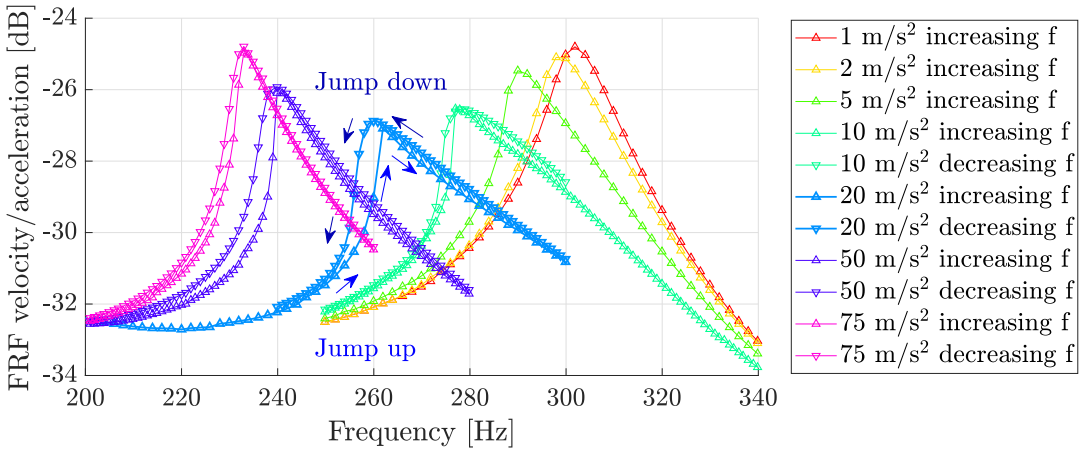

Figure V.16: Results of the single-point measurement : Amplitudes of the FRFs obtained for seven different acceleration amplitudes with either increasing or decreasing frequency during the measurement.

A measurement, during which the frequency was increased, is represented by a triangular marker pointing upwards, whereas a triangle pointing downwards represents a measurement series with decreasing frequency. The comparison of two measurements with the same excitation amplitude shows, that measurements are performed in a repeatable manner with the experimental setup. The acceleration amplitude influences the response in two ways. On the one hand, the resonance frequency decreases with increasing amplitude. On the other hand, the shape of the amplitude peaks is strongly influenced by the acceleration magnitude. For relatively low magnitudes, the FRF is symmetric around the resonance frequency. The increase of the acceleration amplitude up to $20\,\mathrm{m/s^2}$ decreases the maximum value of the FRF and the peak tends to incline to the left. In addition, amplitude jump-up and jump-down phenomena are observed for measurements with increasing and decreasing frequency respectively. They indicate a non-linear behavior of the system and are indicated in figure V.16 for the acceleration magnitude of $20\,\mathrm{m/s^2}$. When the acceleration magnitude increased above $20\,\mathrm{m/s^2}$, the peak of the transfer function straightens and its shape becomes more symmetric. The effect of the jumps becomes less visible. They are more pronounced for the intermediate excitation magnitudes than for the lowest and highest acceleration magnitudes.
Figure V.17 shows the evolution of the phase with the frequency for the different acceleration magnitudes. The frequencies of the abrupt phase shifts coincide with frequencies of the amplitude peaks, which confirms that the peaks correspond to a resonance. The jump phenomena are also visible in the evolution of the phase. A continuous variation of the phase, even far from jumps, is observed. This variation is caused by a time delay between the laser sensor and the accelerometer due to the signal transfer.

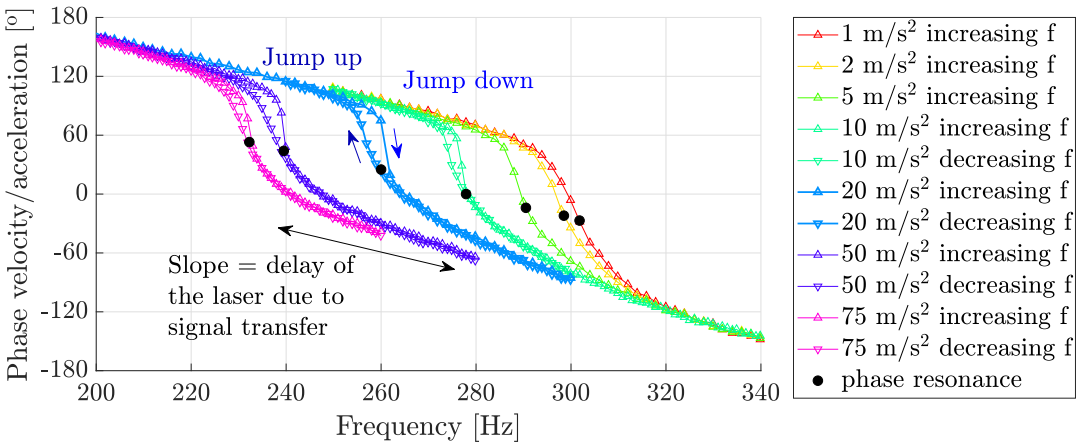

Figure V.17: Results of the single-point measurement : Phase of the FRFs obtained for seven different acceleration amplitudes with either increasing or decreasing frequency during the measurement.

The structure shows a nonlinear behavior with respect to the excitation amplitude: when the amplitude increases, the resonance frequency decreases. This is a softening-effect, that appears in assembled structures when partial slippage re-

duces the contact stiffness. In addition, the resonance peak bends to the left for intermediate excitation magnitudes, which is a typical nonlinear effect, observed in experiments which include friction dissipation. The variation of the peak amplitude of the FRF can also be linked to the damping. At small amplitudes, the magnetically induced normal forces are big enough to prevent most of the slippage in the contact. The contact is quasi rigid, the response of the structure linear and the damping low. As the amplitude of the excitation signal increases, the displacement of the sandwich sheets becomes greater. The tangential forces increase but the contact is still maintained by the magnetic normal forces and partial slippage occurs. The friction dissipates a part of the energy and the damping increases. When the excitation amplitude is further increased, the contact of the sandwich structure passes more and more from partial slippage to total slippage. The friction and hence the damping are more and more reduced and the FRF recovers an upright form with higher peak amplitude. An additional study with a high-speed camera has revealed a relative motion between the soft core and the skins during the vibration.

V.4.2.b Multi-point measurement (SI–MO)

In a second measurement series of the present study, a surface scan has been performed. During the scan, the velocity of the oscillating beam was measured consecutively on various points on the beam and the base and the measurements are used to reconstruct the velocity field on the beam. The comparison of the velocity fields for different excitation amplitudes is supposed to show, whether the mode shape is amplitude dependent. The experimental setup was almost the same as for the single point measurement, but the acceleration and the velocity were recorded by the software of the laser Doppler vibrometer instead of the NI Data Acquisition tool.
Three surface scans have been performed in total. The excitation was carried out with a sine signal for three different amplitudes: $1\,\mathrm{m/s^2}$, $20\,\mathrm{m/s^2}$ and $75\,\mathrm{m/s^2}$. To highlight the mode shape for each excitation amplitude, the excitation frequency has been chosen according to the phase resonance (cf. figure V.17). The excitation frequencies, chosen by the help of the results for the single point measurement, measured 302 Hz for $1\,\mathrm{m/s^2}$, 260 Hz for $20\,\mathrm{m/s^2}$ and 232 Hz for $75\,\mathrm{m/s^2}$. The results for various points on the beam and reference points on the base were recorded and post-processed with Matlab. In a first graphic analysis of the results, the local velocity field are compared. Figure V.18 a shows the velocity fields of the deformed structure for the three tested configurations. The fields are normalized for each configuration with reference to the base (light green), hence the absolute values corresponding to the colors are not important for the comparison. The deformed configurations confirm, that the frequency range excites the third vibration mode as two regions with a strong displacements and three vibration nodes with the same velocity as the base are observed. The comparison of the three configuration shows no significant difference of the velocity fields.

In a second analysis, the velocity fields, measured for the different configurations, are compared point by point. For each configuration, the field contains N velocities measured on the different points j which, at the resonance, form the eigenvector $\boldsymbol{\Phi}$ of the resonance mode k as shown in equation (V.10), where the exponent $^{\mathrm{T}}$ indicates the transpose of the vector.

$$\boldsymbol{\Phi}_k = [v_1,\ v_2,\ \cdots,\ v_j,\ \cdots,\ v_N]^{\mathrm{T}}\ , \tag{V.10}$$

To compare the vectors between the three different configurations, the coefficients of a Modal Assurance Criterion (MAC) matrix are calculated by

$$MAC_{kl} = \frac{\boldsymbol{\Phi}_k^{\mathrm{T}} \cdot \boldsymbol{\Phi}_l}{||\boldsymbol{\Phi}_k||\,||\boldsymbol{\Phi}_l||^2} \qquad k,l = 1,2,3\ , \tag{V.11}$$

where k and l correspond to one of the three configurations. A coefficient MAC_{kl} of the matrix represents the correlation between velocity fields of the configuration k and l. If the coefficient is equal to 1, the eigenvectors are co-linear and that the velocity fields are identical. A coefficient equal to 0 means that the eigenvectors are oriented in an orthogonal manner and that the velocity fields are very different. The 3x3 MAC matrix for the three tested configurations is shown in figure V.18 b in form of squares with size and color depending on the coefficient. The three values on the diagonal are equal to 1 since the velocity field of the three configurations are compared to themselves. The matrix shows, that there is a monotonic evolution of the mode shape with the excitation magnitude since the coefficients are different from 1, but the variation is very small. In conclusion, it is stated that the non-linearity does not affect the mode shape in a significant manner.

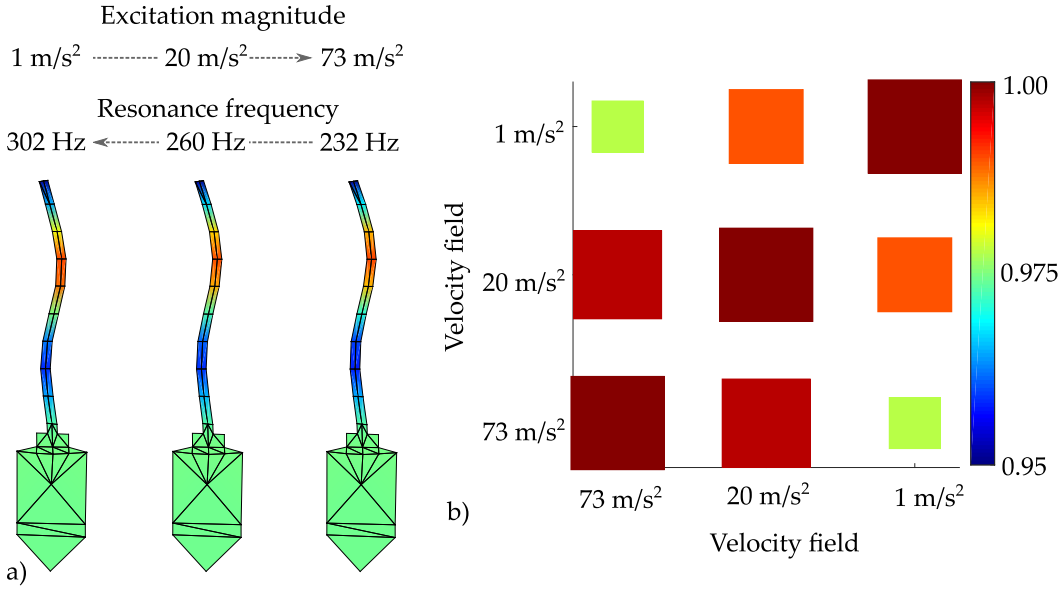

Figure V.18: Normalized mode shapes of the structure for the three excitation amplitudes (a) and modal assurance criterion (MAC) for the three configurations (b).

V.5 Discussion and conclusions

In the present work, the concept of magnetically induced friction damping based on H-MAE is introduced along with a proof of concept. An introduction to the basics of structural dynamics is given in the first section of this chapter, containing experimental modal analysis, nonlinear dynamics and friction damping. An overview over damping strategies, which have been developed based on magnetoactive fluids, elastomers and magnetically induced forces generated by permanent magnets, has been presented subsequently. In previous studies, S-MAE have been employed in beam-like sandwich structures with the aim to vary the damping by a semi-active control of the viscoelastic material parameters, which leads to a variation of the modal characteristics and vibration damping. The concept of magnetically induced friction damping, differentiates from this approach mainly in two points : the contact between the third section of the present study, the skins and the core of the sandwich is not rigid and the damping mechanism is not triggered in a semi-active but in a passive way.
The experimental investigations, presented in the fourth section of the present work, show, that it is possible to prove the concept in a relatively simple setup in which no external magnetic source is needed for the generation of a magnetic field. In addition, the core maintains the sandwich assembled with no need for glue or bolts. An advantage of the concept, presented in this work, for friction damping, is the generation of the contact pressure. The control of the contact pressure over the surface is conducted by the material itself and the intensity of the contact pressure is moderate which favors friction damping. The compliant material can adapt to the rigid skins and the influence of surface asperities or fabrication tolerances is supposed to have a lower influence than in a contact area formed by two stiff materials. During the deformation of the beam, the soft core deforms as well and maintains the surface pressure presumably constant. The two former statements are suppositions which have to be confirmed experimentally. One of the difficulties when working with magnetic fields is the guidance of the magnetic flux. A lot of the materials employed in supporting structures and measurement equipment are made from materials with a high magnetic permeability. It has to be assured that magnetic flux stays in the circuit established by the sandwich core and the skins which is the reason for the choice of aluminum and brass in the clamping. The latter also provided a spacing towards the electromagnetic shaker.
The damping strategy is passive, which means that it is restricted to a specific magnitude range. One solution could be the inclusion of external magnetic fields in the measurement setup, which has already been realized for S-MAE. But the magnetic field could also be altered by a change in the magnetic circuit around the core. Varying the air gap or guiding the flux in a secondary magnetic circuit could be interesting design concepts to create a semi-active control mechanism for magnetically induced friction damping. With regard to the sandwich, instead of using a full MAE core, the latter could be positioned intentionally at the places where the structure deforms the most. This would not only lead to a gain in weight

but could also influence the relative movement between skins and the core since the patches are less blocked by surrounding material and the contact force would be different compared to situation with a full core MAE sandwich. Modeling the physical processes will be helpful for the design of friction damping MAE sandwich structures. Multi-physical models containing the magnetic and mechanical behavior of the structure as well as the coupled contact mechanics have to be established on this purpose.

Conclusions and perspectives

The present PhD thesis deals with a mechanically **st**iff and magnetically **H**ard **M**agneto**A**ctive **E**lastomer (stH-MAE), composed of NdFeB particles and a silicone matrix. Chapter I provides an overview over the basics of continuum mechanics, magnetism and the description of the magneto-mechanical coupling. This state of the art and the number of assumptions, which are used to derive the required expressions, show the complexity of the magneto-mechanical coupling and are helpful to put the present work in the context of continuum physics. In the following, general conclusions on the work with stH-MAE are drawn and perspectives for future investigations are outlined. This chapter is separated thematically in two sections, which cover the material behavior of the stH-MAE (chapters II and III) and the application cases (chapters IV and V) respectively.

Material behavior of stH-MAEs

The isotropic composite materials, used throughout the present thesis, have been elaborated manually and the manufacturing process is described in detail at the beginning of chapter II. Several **experimental characterization** methods have been used to reveal the material properties of the composite. The magnetic behavior is demonstrably determined by the magnetic particles and the volume fraction: firstly, the coercive field strength of composite and particles is similar. Secondly, the evolution of coercive field and residual flux density with increasing temperature can be predicted by the temperature coefficients of the magnetic powder. These properties are independent from the volume fraction. The residual flux density shows a linear dependence on the volume fraction with a proportionality coefficient corresponding to the residual flux density of the powder. Important magnetic characteristics of an isotropic stH-MAE can hence be predicted by the help of the magnetic characteristics of the powder and the particle content. A quasi-static mechanical characterization has revealed an isotropic behavior and typical characteristics of filled elastomers. The visco-elastic properties of the matrix material and composites with different filling ratios were determined by dynamic-mechanical analysis (DMA). The stiffness and the dissipation increase with the particles content during dynamic loading. The influence of the dynamic loading frequency and the temperature on the material behavior has furthermore been demonstrated and underlines the importance of the loading conditions and the environment on the mechanical behavior of stH-MAE. The comparison of storage modulus and loss factor of magnetized and non-magnetized composites reveals, that the magnetization does not have a significant influence on the dynamic mechanical properties of the stH-MAE studied in this work. In addition, quasi-static mechanical tests in

present of a magnetic field show no significant variation of the elastic properties. The magneto-mechanical coupling in the tested stH-MAEs due to the magnetization of the composite and due to moderate external magnetic fields (40 kA/m) is characterized as weak. Nevertheless, first results with the magneto-mechanical test bench[1] indicate the presence of an additional constraint provoked by magnetic fields when the deformation of a specimen is blocked.
In addition to the experimental investigations on the macroscopic properties, stH-MAEs are studied on the microscopic scale by the help of **numerical modeling** in chapter III. An analysis of the interactions between two spherical magnetized particles has been performed to enhance the understanding of the magneto-mechanical interactions. The resulting forces and torques are dependent on the orientation of the magnetization with respect to the direction of alignment of the particles. An analytic model, based on magnetic dipoles, leads to similar results as the numerical simulation and furthermore provides the results instantaneously. Considering the limits of the dipole approximation (discussed in the corresponding section), the approach proofs to be a time saving modeling tool for particle interactions. Just like the resulting forces and torques, generated by the remanent magnetization of the particles, the mechanical stress in the matrix of a composite is also dependent on the spatial configuration of the particles with respect to the direction of magnetization. This result is highlighted in a two dimensional numerical study with two particles in different spatial configurations. To analyze the influence of the particle interactions on the macroscopic material behavior, a magneto-mechanical homogenization framework has been developed and is presented in this thesis. It is based on two dimensional numerical simulations assuming in plane stress and magnetic fields. The framework comprises the automatized generation of structures with randomly dispersed circular inclusions in a square matrix element, the implementation of periodic magnetic and mechanical boundary conditions, the implementation of the coupling and the determination of the properties of an equivalent homogeneous material. Convergence studies of the properties with respect to the number of inclusions have been performed for two composite types with different volume fractions. As stated before, the particles' magnetization generates initial mechanical and magnetic constraints, which are revealed by the simulations and called operating point. The initial constraints are separated from the constraints caused by an external loading, to determine the behavior of an initially magnetized composite. The simulations reveal an insignificant influence of the particle magnetization on the elastic properties, which is in accordance with the experimental results. Concerning the magnetized composite, the numerical simulations show the same tendencies as the experimental results: The material is mechanically isotropic, the stiffness and the residual flux density increase with the volume fraction of magnetic particles. In addition, the residual flux density, obtained by the homogenization procedure at the operating point, is in good accordance with the experimental results. The qualitative results for the mechanical properties are in accordance with the experimental results only for the smaller volume fraction.

[1] developed in cooperation with the company MMT during the PhD thesis

Additional mechanical simulations show, that the accordance can be improved by considering the third spatial dimension. The coupling coefficients, obtained by 2D numerical simulations, are evaluated qualitatively for this reason. The strongest coupling is obtained when the magnetization and the loading are aligned with the direction of the observed quantity. The constraints, generated by the magneto-mechanical coupling, are relatively weak. A linear PiezoMagnetic(PM) model is established on the macroscopic scale by the help of the effective properties. It comprises the effective stiffness and permeability as well as the coupling coefficients, determined by the numerical simulations. The comparison of the PM model to numerical simulations shows, that the first-mentioned is capable to represent the coupled material behavior in vicinity of the operating point. The coupling is well approximated for small mechanical or magnetic loadings, where the behavior is linear.

A definite perspective of the experimental work on the material behavior is the further development and use of the magneto-mechanical test rig, presented in chapter II. Further experimental investigations have to be performed to confirm the results and the conclusions of the first tests. The simultaneous improvement of the numerical model is another short-term perspective. In the current state, the magnetic part of the setup is represented in a sufficiently detailed manner in contrast to the mechanical part. A "digital twin" of the experimental setup will be helpful to validate experimental results and forward the modeling of the composite material. Additional experimental tests could comprise materials different from the one presented in this work. Softer elastomer matrices could be used for example to generate a stronger magneto-mechanical coupling. If the composite is supposed to act as a permanent magnet, the increase of the residual flux density is a possible topic for future studies and could comprise the analysis of transversely isotropic structures or composites based on particles with different material properties and shape compared to the present study. The numerical homogenization framework, presented in this thesis, can be used in this context for the design of the material and guide the choice of primary materials for example. The comparison of experimental and numerical results shows, that the model is not yet operational for the prediction of quantitative mechanical and coupled properties. The three-dimensional representation of the microstructure improves the approximation of the mechanical properties and the addition of further details like irregularly shaped particles should further improve the model. However, knowing that the actual microstructure cannot be represented and future improvements of the model should target the estimations of reasonable boundaries for the effective behavior and not its exact prediction.
Less immediate perspectives concern the loading conditions and additional material properties. The magnetic material behavior could be studied in dynamic magnetic fields which would provide useful information for the design of actively controlled applications. An important topic for future studies is the viscous component of the mechanical material behavior, which plays a significant role in dynamic applications and has only partly been addressed by the present work. Cor-

responding studies could comprise the influence of the magnetization and external magnetic fields on the viscous component. Experimental results for the viscous behavior or the magnetic hysteresis for example could be used to expand the validity of the material model. In the present work, a unidirectional coupling was analyzed for a configuration where the loading and the polarization of the specimen were oriented in the same direction. In future studies, the coupling could be studied for other loading configurations (compression, shear) and with a different orientation of the polarization with respect to the loading direction. The magnitude of the loading was kept small during the experiments presented in this work. Future studies could comprise the analysis of the large strain behavior of the composite. From an experimental point of view, this is especially challenging for the magnetic part of the tests. Structural effects will come into play, the change of the specimen's shape for example is likely to influence the internal magnetic field and the generation of homogeneous magnetic fields in large volumes is difficult. In addition, structural damage effects like the debonding of particles and the matrix may occur.

Application possibilities for stH-MAE

In the second part of this PhD thesis, two application possibilities of stH-MAE are presented. The functional principles rely on the combination of a permanent magnetization and the low stiffness (chapter IV) and the combination of the permanent magnetization and the friction coefficient (chapter V).

Chapter IV deals with the forces, generated by magnetized stH-MAE composites and presents a study dedicated to the **magnetic actuation of membrane structures**. A preliminary study on magnetically induced forces shows, that the force increases with the particle content. The influence of the shape of an stH-MAE specimen on its capacity to induce mechanical interactions is experimentally demonstrated with specimens of different thickness. It is shown, that the force, generated by the specimens, increases with the aspect ratio in the direction of magnetization. The numerical modeling of the experimental tests validates the conclusions and visualizes the demagnetizing effect. In addition, the model underlines how important the knowledge of material parameters and the geometry of the magnetic circuit are for the numerical modeling of magneto-mechanical interactions at the macroscopic scale. Afterwards, the chapter addresses the difficulties of the magnetic actuation of H-MAE membranes. The results of the preliminary study indicate, that the aspect ratio of membranes is disadvantageous for the generation of high actuation forces which inhibits high deflections. In addition, the forces are developed primarily in the outer regions of a membrane where, a high field gradient and a higher flux density are present, but which is fixed in general. The present work suggests a bidirectional magnetization of stH-MAE membranes to overcome these problems. Magnetic measurements show, that a pole transition,

crossing the membrane in the middle, increases the intensity of the magnetic flux density and generates a gradient in the flux density field. In experimental tests, membranes with unidirectional and bidirectional magnetization were deformed due to interactions with corresponding permanent magnets and the out of plane displacement has been analyzed. The displacement of membranes with bidirectional magnetization exceeds the displacement of unidirectionally magnetized membranes by a large extend. The misalignment of magnet and membrane are studied experimentally and by the help of numerical simulations. The study shows, that pole transitions offer the possibility to localize the magnetically induced forces.
The results, presented in chapter IV, are a proof of concept. Additional tests are necessary to quantify the actuation properties of bidirectionally magnetized stH-MAE membranes. The maximum deflection of the membranes could be studied as a function the aspect ratio and the content of magnetic particles. Besides the deflection, the force, which is developed by the membrane, is an interesting characteristic for the development of actuators based on the composite membranes. The dynamic actuation properties are another important factor which should be characterized, especially in view of the viscous behavior of the composite material. A bidirectional actuation may be preferable to the use of the elastic restoring forces. The permanent magnet could be replaced by an electromagnetic actuator or an Electro-Permanent Magnet (EPM). The integration of magnetized stH-MAE membranes in magnetic circuits is probably a challenging task due to the interaction forces generated by the membrane itself. On the other hand, the forces may be useful to generate stable states of the membrane actuator without additional energy supply.

Chapter V demonstrates the application of stH-MAE for passive vibration attenuation in the context of **magnetically induced friction damping**. Patches of the magnetized composite are inserted between ferromagnetic skins. The magnetic forces between the stH-MAE and the skins maintain the assembly together in a sandwich configuration. The sandwich is subjected to continuous oscillations and the response of the structure is recorded for different frequencies and amplitudes in vicinity of the phase resonance. The resonance frequency and the modal damping frequency response function varies with the excitation magnitude. The resonance frequency decreases with increasing excitation magnitude. The damping, on the contrary, increases at first with the excitation magnitude and then decreases for further increase of the excitation magnitude. Jump phenomena indicate a nonlinear behavior for moderate excitation amplitudes. The decrease of the resonance frequency in combination with the variation of the damping is characteristic for friction damping with varying contact stiffness. In the experiment, the amplitude dependence is caused by the varying contact state between the elastomer core and the skins. Three different contact states are supposed to be responsible for the variation of the frequency response: Total stick for low amplitudes, partial sliding for moderate amplitudes and total sliding for high amplitudes. The application of stH-MAE for friction damping is advantageous since the material generates a moderate contact pressures that is furthermore distributed on the surface due to

the physical mechanism and the compliance of the composite. The core is supposed to be capable to follow the deformations of the skins which probably favors the maintain of the contact force but the assumption has to be confirmed experimentally. The damping mechanism is passive, which means that it is restricted to a specific magnitude range. To overcome this limit and develop a semi-active control, external magnetic fields could be included in the measurement setup of future studies. Another possibility is the modification of the magnetic circuit around the core by varying the air gap for example or by guiding the flux in a secondary magnetic circuit. Instead of using a full MAE core, the patches could be positioned intentionally at the places where the structure deforms the most to gain weight and maybe increase the relative movement between skins and the core. Modeling the physical processes will be helpful for the design of friction damping MAE sandwich structures. Multi-physical models containing the magnetic and mechanical behavior of the structure as well as the coupled contact mechanics have to be established for this purpose. In addition, the modeling has to include, inter alia, non-stationary magnetic fields and phenomena like Eddy currents.

Appendix A
Appendix

A.1 Appendix chapter II

A.1.1 Properties of the samples, used for the experimental analysis

Specimen	Φ [%]	w [mass%]	diameter [mm]	height [mm]
S_{mag1}	29.8	75	5.80	0.85
S_{mag2}	21.6	66	5.78	0.90
S_{mag3}	29.8	75	4.25	0.82
S_{mag4}	12.4	50	5.50	0.97
S_{mag5}	12.4	50	5.50	0.97
S_{mag6}	12.4	50	5.50	0.97
S_{mag7}	21.6	66	5.50	0.97
S_{mag8}	21.6	66	5.50	0.97
S_{mag9}	21.6	66	5.50	0.97
S_{mag10}	29.8	75	5.50	0.97
S_{mag11}	29.8	75	5.50	0.97
S_{mag12}	29.8	75	5.50	0.97
S_{mag13}	32.2	77	5.50	0.97
S_{mag14}	32.2	77	5.50	0.97
S_{mag15}	32.2	77	5.50	0.97

Table A.1: Characteristics of samples for magnetic analysis

Specimen	Φ [%]	w [mass%]	L_0 [mm]	h_1 [mm]	h_2 [mm]
S_{mec1}	36.2	80	59.00	12.00	4.31
S_{mec1}	36.2	80	59.00	12.00	4.31
S_{mec2}	36.2	80	59.00	12.00	4.31
S_{mec3}	36.2	80	59.00	12.00	4.31
S_{mec4}	0	0	15.00	18.50	2.50
S_{mec5}	19.4	63	15.00	18.30	3.00
S_{mec6}	36.2	80	15.00	18.30	3.41

Table A.2: Characteristics of samples for mechanical analysis.

sample	Φ [vol%]	w [mass%]	L_0 [mm]	h_1	h_2	$\boldsymbol{M}$
before magnetization						
S_{mm1}	19.4	63	12.30 12.33 12.32	18	3.16	-
S_{mm2}	19.4	63	12.41 12.33 12.23	18	3.14	-
S_{mm3}	19.4	63	12.32 12.12 12.24	18	3.12	-
S_{mm4}	19.4	63	12.42 12.24 12.37	18	3.11	-
S_{mm5}	19.4	63	12.49 12.33 12.41	18	3.13	-
S_{mm6}	19.4	63	12.25 12.31 12.39	18	3.12	-
S_{mm7}	19.4	63	12.33 12.33 12.29	18	3.12	-
S_{mm8}	19.4	63	12.31 12.31 12.31	18	3.12	-
after magnetization						
S_{mm1}	19.4	63	12.24 12.31 12.31	18	3.16	$\boldsymbol{M} \parallel L_0$
S_{mm2}	19.4	63	12.30 12.30 12.16	18	3.14	$\boldsymbol{M} \parallel L_0$
S_{mm3}	19.4	63	12.46 12.22 12.23	18	3.13	$\boldsymbol{M} \parallel L_0$
S_{mm4}	19.4	63	12.37 12.30 12.24	18	3.12	$\boldsymbol{M} \parallel L_0$
S_{mm5}	19.4	63	12.25 12.24 12.32	18	3.12	$\boldsymbol{M} \perp L_0$
S_{mm6}	19.4	63	12.25 12.30 12.24	18	3.11	$\boldsymbol{M} \perp L_0$
S_{mm7}	19.4	63	12.32 12.24 12.31	18	3.12	$\boldsymbol{M} \perp L_0$
S_{mm8}	19.4	63	12.32 12.25 12.24	18	3.12	$\boldsymbol{M} \perp L_0$
S_{mm9}	36.2	80	8.90	17	2.00	$\boldsymbol{M} \parallel L_0$
S_{mm10}	36.2	80	7.90	18	2.00	$\boldsymbol{M} \parallel L_0$

Table A.3: Characteristics of sample for magneto-mechanical analysis.

A.2 Appendix chapter III

Generation of random microstructures

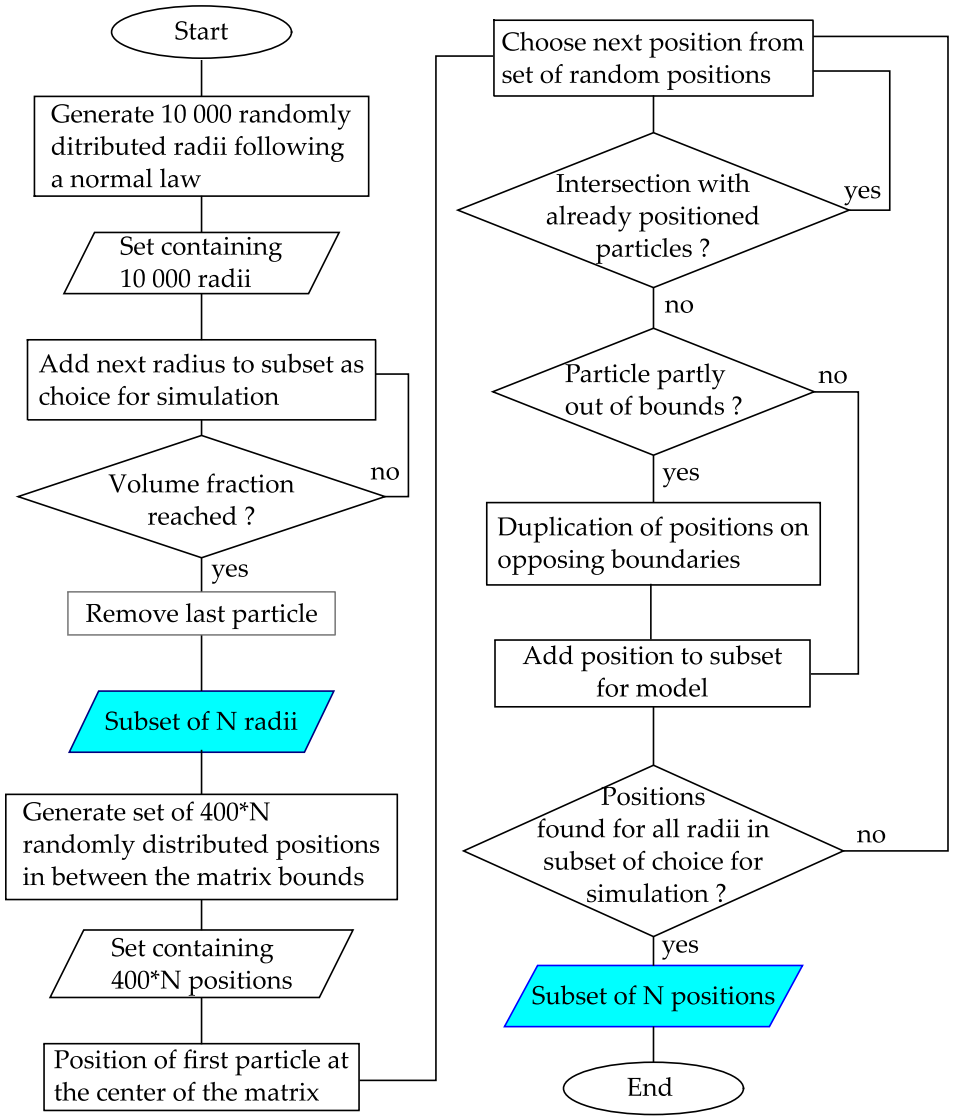

Figure A.1: Program flow chart of the algorithm used generate particle radii and positions.

A.2.1 Framework applied to 3D cases

A.2.1.a Load cases

load case	ε_1 [%]	ε_2 [%]	ε_3 [%]	ε_4 [%]	ε_5 [%]	ε_6 [%]	H_1 [kA/m]	H_2 [kA/m]	H_3 [kA/m]
OP	–	–	–	–	–	–	–	–	–
A	$1+\varepsilon_1^{OP}$	ε_2^{OP}	ε_3^{OP}	ε_4^{OP}	ε_5^{OP}	ε_6^{OP}	0	0	0
B	ε_1^{OP}	$1+\varepsilon_2^{OP}$	ε_3^{OP}	ε_4^{OP}	ε_5^{OP}	ε_6^{OP}	0	0	0
C	ε_1^{OP}	ε_2^{OP}	$1+\varepsilon_3^{OP}$	ε_4^{OP}	ε_5^{OP}	ε_6^{OP}	0	0	0
D	ε_1^{OP}	ε_2^{OP}	ε_3^{OP}	$1+\varepsilon_4^{OP}$	ε_5^{OP}	ε_6^{OP}	0	0	0
E	ε_1^{OP}	ε_2^{OP}	ε_3^{OP}	ε_4^{OP}	$1+\varepsilon_5^{OP}$	ε_6^{OP}	0	0	0
F	ε_1^{OP}	ε_2^{OP}	ε_3^{OP}	ε_4^{OP}	ε_5^{OP}	$1+\varepsilon_6^{OP}$	0	0	0
G	0	0	0	0	0	0	15	0	0
H	0	0	0	0	0	0	0	15	0
I	0	0	0	0	0	0	0	0	15

Table A.4: Required load cases for the determination of the coupled properties in a 3D study

A.2.1.b Determination of the mechanical properties

$$\begin{pmatrix} \varepsilon_1 \\ \varepsilon_2 \\ \varepsilon_3 \\ 2\varepsilon_4 \\ 2\varepsilon_5 \\ 2\varepsilon_6 \end{pmatrix} = \begin{pmatrix} 1/E_1 & -\nu_{21}/E_2 & -\nu_{31}/E_3 & 0 & 0 & 0 \\ -\nu_{12}/E_1 & 1/E_2 & -\nu_{32}/E_3 & 0 & 0 & 0 \\ -\nu_{13}/E_1 & -\nu_{23}/E_2 & 1/E_3 & 0 & 0 & 0 \\ 0 & 0 & 0 & 1/G_4 & 0 & 0 \\ 0 & 0 & 0 & 0 & 1/G_5 & 0 \\ 0 & 0 & 0 & 0 & 0 & 1/G_6 \end{pmatrix} \begin{pmatrix} \sigma_1 \\ \sigma_2 \\ \sigma_3 \\ \sigma_4 \\ \sigma_5 \\ \sigma_6 \end{pmatrix} \tag{A.1}$$

$$\begin{pmatrix} \varepsilon_1^A \\ \varepsilon_2^A \\ \varepsilon_3^A \\ \varepsilon_1^B \\ \varepsilon_2^B \\ \varepsilon_3^B \\ \varepsilon_1^C \\ \varepsilon_2^C \\ \varepsilon_3^C \\ 2\varepsilon_4^D \\ 2\varepsilon_5^E \\ 2\varepsilon_6^F \end{pmatrix} = \begin{pmatrix} \sigma_1^A & \sigma_2^A & \sigma_3^A & 0 & 0 & 0 & 0 & 0 & 0 & 0 & 0 & 0 \\ 0 & 0 & 0 & \sigma_1^A & \sigma_2^A & \sigma_3^A & 0 & 0 & 0 & 0 & 0 & 0 \\ 0 & 0 & 0 & 0 & 0 & 0 & \sigma_1^A & \sigma_2^A & \sigma_3^A & 0 & 0 & 0 \\ \sigma_1^B & \sigma_2^B & \sigma_3^B & 0 & 0 & 0 & 0 & 0 & 0 & 0 & 0 & 0 \\ 0 & 0 & 0 & \sigma_1^B & \sigma_2^B & \sigma_3^B & 0 & 0 & 0 & 0 & 0 & 0 \\ 0 & 0 & 0 & 0 & 0 & 0 & \sigma_1^B & \sigma_2^B & \sigma_3^B & 0 & 0 & 0 \\ \sigma_1^C & \sigma_2^C & \sigma_3^C & 0 & 0 & 0 & 0 & 0 & 0 & 0 & 0 & 0 \\ 0 & 0 & 0 & \sigma_1^C & \sigma_2^C & \sigma_3^C & 0 & 0 & 0 & 0 & 0 & 0 \\ 0 & 0 & 0 & 0 & 0 & 0 & \sigma_1^C & \sigma_2^C & \sigma_3^C & 0 & 0 & 0 \\ 0 & 0 & 0 & 0 & 0 & 0 & 0 & 0 & 0 & 2\sigma_4^D & 0 & 0 \\ 0 & 0 & 0 & 0 & 0 & 0 & 0 & 0 & 0 & 0 & 2\sigma_5^E & 0 \\ 0 & 0 & 0 & 0 & 0 & 0 & 0 & 0 & 0 & 0 & 0 & 2\sigma_6^F \end{pmatrix} \begin{pmatrix} 1/E_1 \\ -\nu_{21}/E_2 \\ -\nu_{31}/E_3 \\ -\nu_{12}/E_1 \\ 1/E_2 \\ -\nu_{32}/E_3 \\ -\nu_{13}/E_1 \\ -\nu_{23}/E_2 \\ 1/E_3 \\ 1/G_{23} \\ 1/G_{31} \\ 1/G_{12} \end{pmatrix} \tag{A.2}$$

$$\begin{pmatrix} \sigma_1^A & \sigma_2^A & \sigma_3^A & 0 & 0 & 0 & 0 & 0 & 0 & 0 & 0 & 0 \\ 0 & 0 & 0 & \sigma_1^A & \sigma_2^A & \sigma_3^A & 0 & 0 & 0 & 0 & 0 & 0 \\ 0 & 0 & 0 & 0 & 0 & 0 & \sigma_1^A & \sigma_2^A & \sigma_3^A & 0 & 0 & 0 \\ \sigma_1^B & \sigma_2^B & \sigma_3^B & 0 & 0 & 0 & 0 & 0 & 0 & 0 & 0 & 0 \\ 0 & 0 & 0 & \sigma_1^B & \sigma_2^B & \sigma_3^B & 0 & 0 & 0 & 0 & 0 & 0 \\ 0 & 0 & 0 & 0 & 0 & 0 & \sigma_1^B & \sigma_2^B & \sigma_3^B & 0 & 0 & 0 \\ \sigma_1^C & \sigma_2^C & \sigma_3^C & 0 & 0 & 0 & 0 & 0 & 0 & 0 & 0 & 0 \\ 0 & 0 & 0 & \sigma_1^C & \sigma_2^C & \sigma_3^C & 0 & 0 & 0 & 0 & 0 & 0 \\ 0 & 0 & 0 & 0 & 0 & 0 & \sigma_1^C & \sigma_2^C & \sigma_3^C & 0 & 0 & 0 \\ 0 & 0 & 0 & 0 & 0 & 0 & 0 & 0 & 0 & 2\sigma_4^D & 0 & 0 \\ 0 & 0 & 0 & 0 & 0 & 0 & 0 & 0 & 0 & 0 & 2\sigma_5^E & 0 \\ 0 & 0 & 0 & 0 & 0 & 0 & 0 & 0 & 0 & 0 & 0 & 2\sigma_6^F \end{pmatrix}^{-1} \begin{pmatrix} \varepsilon_1^A \\ \varepsilon_2^A \\ \varepsilon_3^A \\ \varepsilon_1^B \\ \varepsilon_2^B \\ \varepsilon_3^B \\ \varepsilon_1^C \\ \varepsilon_2^C \\ \varepsilon_3^C \\ 2\varepsilon_4^D \\ 2\varepsilon_5^E \\ 2\varepsilon_6^F \end{pmatrix} = \begin{pmatrix} 1/E_1 \\ -\nu_{21}/E_2 \\ -\nu_{31}/E_3 \\ -\nu_{12}/E_1 \\ 1/E_2 \\ -\nu_{32}/E_3 \\ -\nu_{13}/E_1 \\ -\nu_{23}/E_2 \\ 1/E_3 \\ 1/G_{23} \\ 1/G_{31} \\ 1/G_{12} \end{pmatrix} \tag{A.3}$$

A.2.2 Results for 2D simulations with uniform particle size

A.2.2.a Operating point

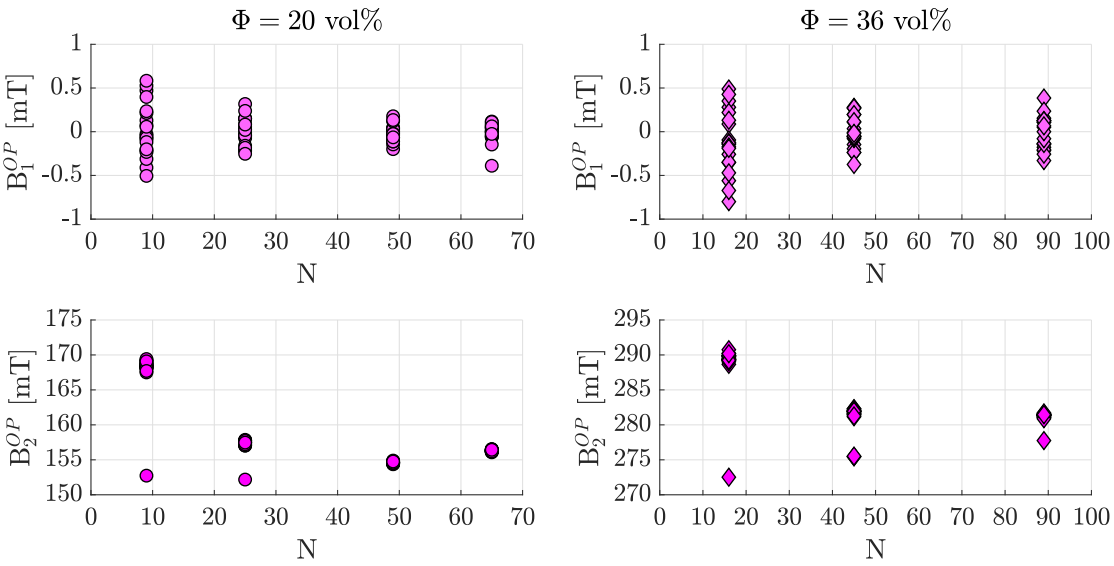

Figure A.2: Results for B^{OP} for the two tested volume fractions Φ as a function of the number of particles N.

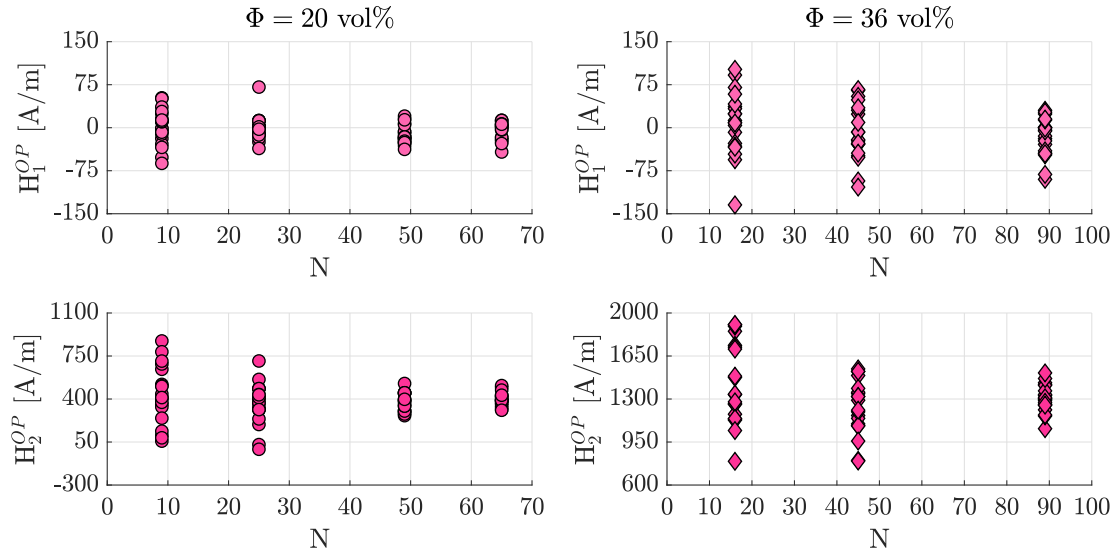

Figure A.3: Results for H^{OP} for the two tested volume fractions Φ as a function of the number of particles N.

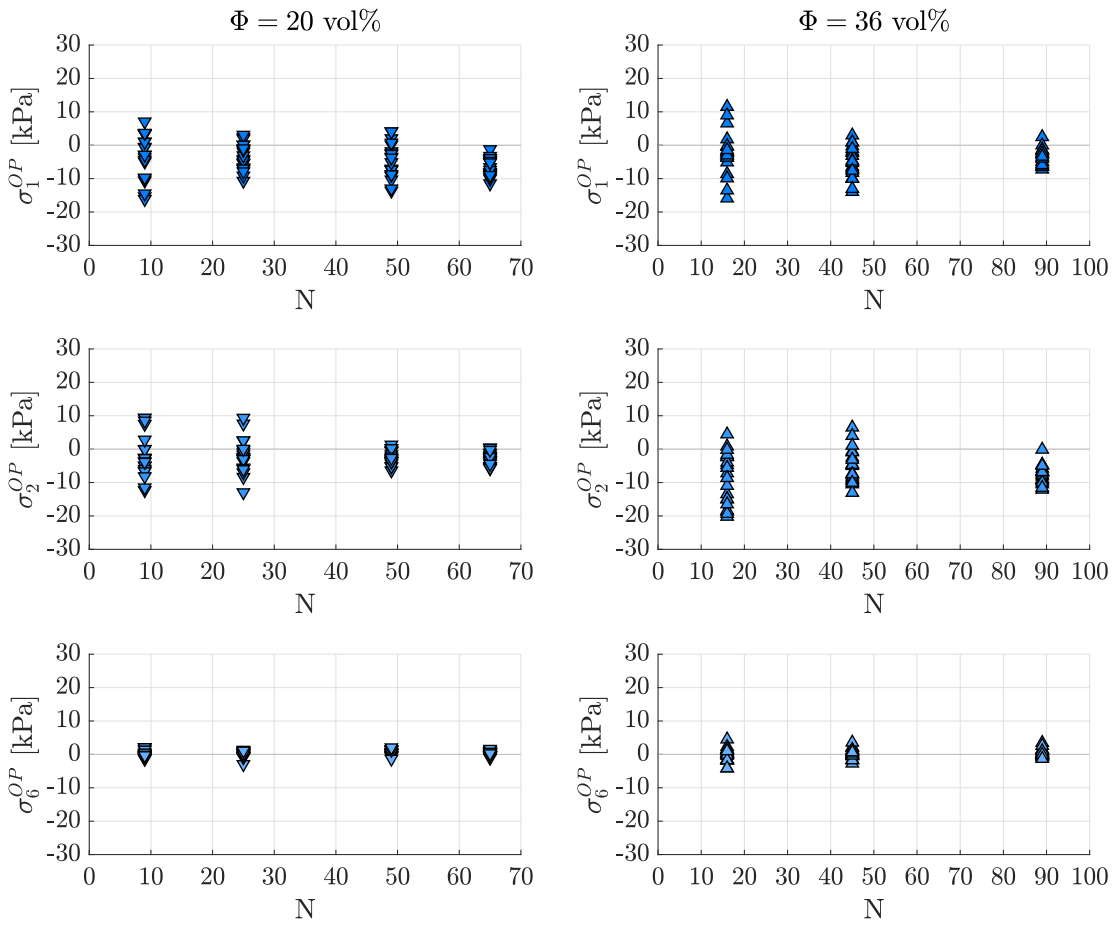

Figure A.4: Results for σ^{OP} for the two tested volume fractions Φ as a function of the number of particles N.

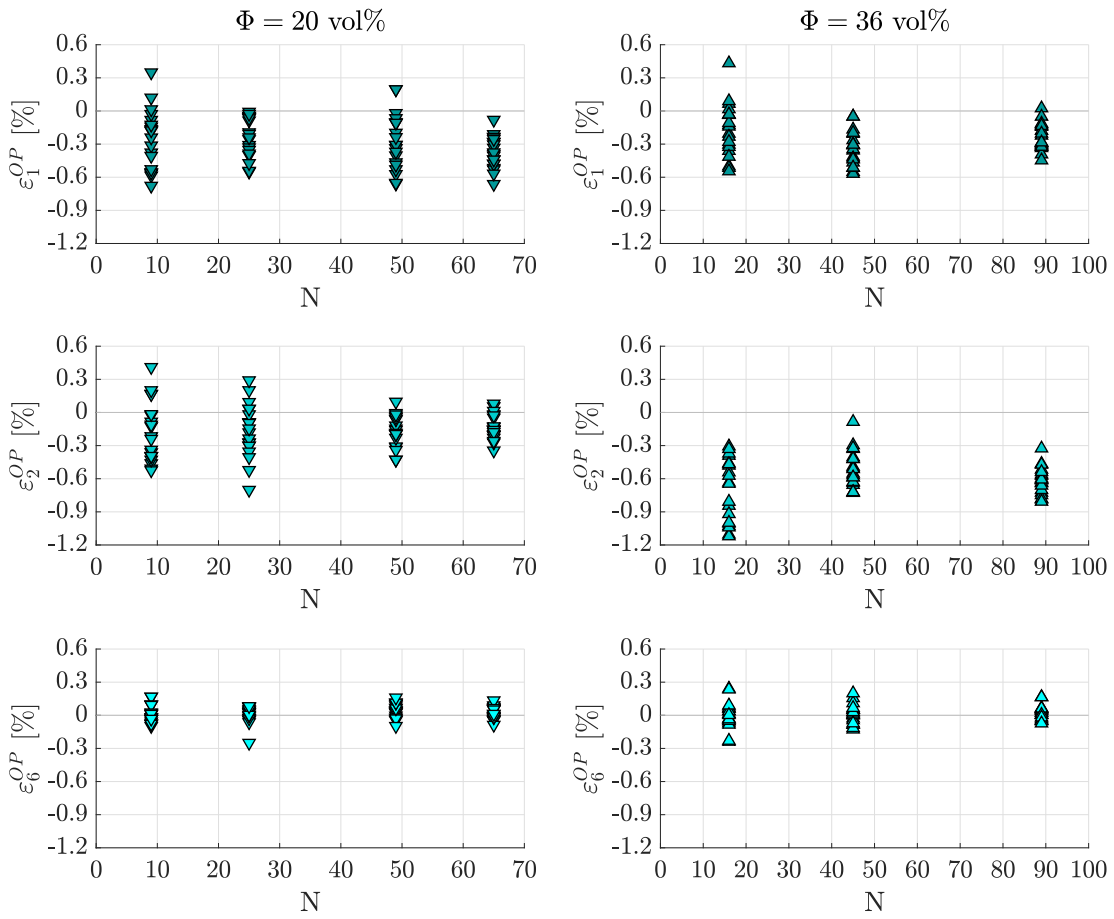

Figure A.5: Results for ε^{OP} for the two tested volume fractions Φ as a function of the number of particles N.

A.2.2.b Mechanical properties

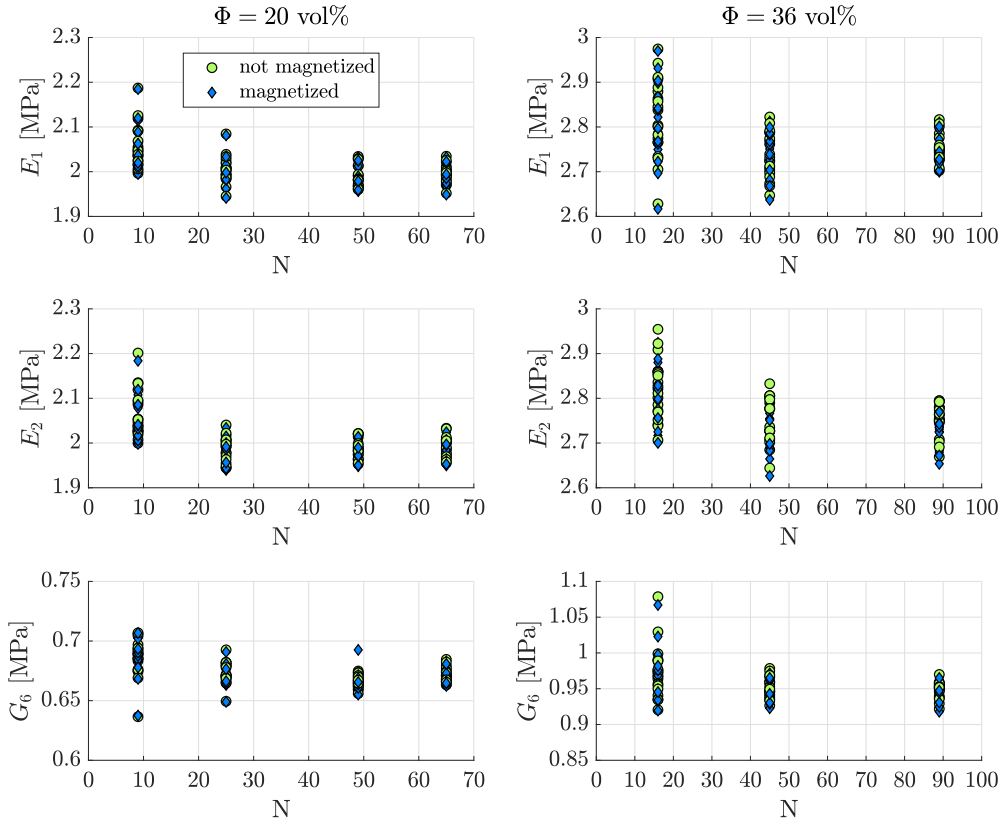

Figure A.6: Elastic moduli as a function of the number of particles N.

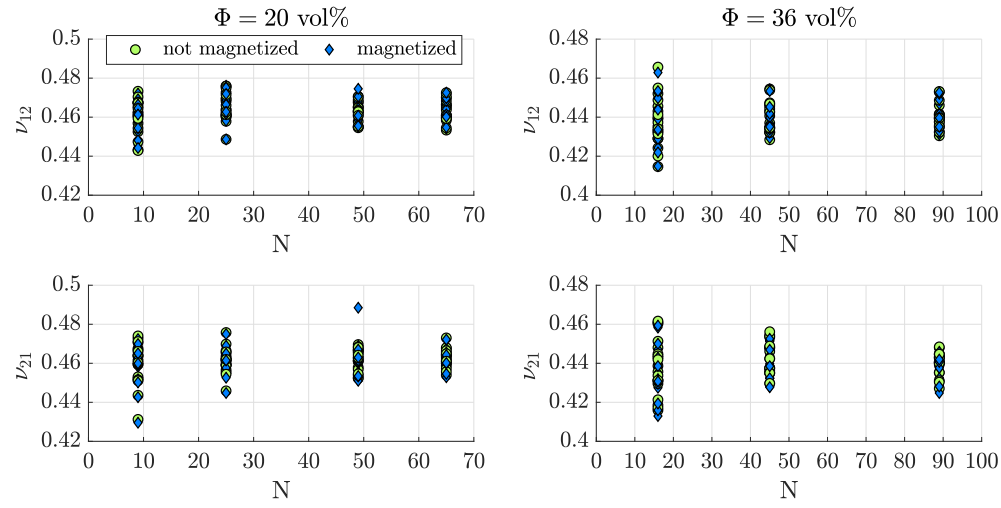

Figure A.7: Poisson's ratios as a function of the number of particles N.

A.2.2.c Relative permeability

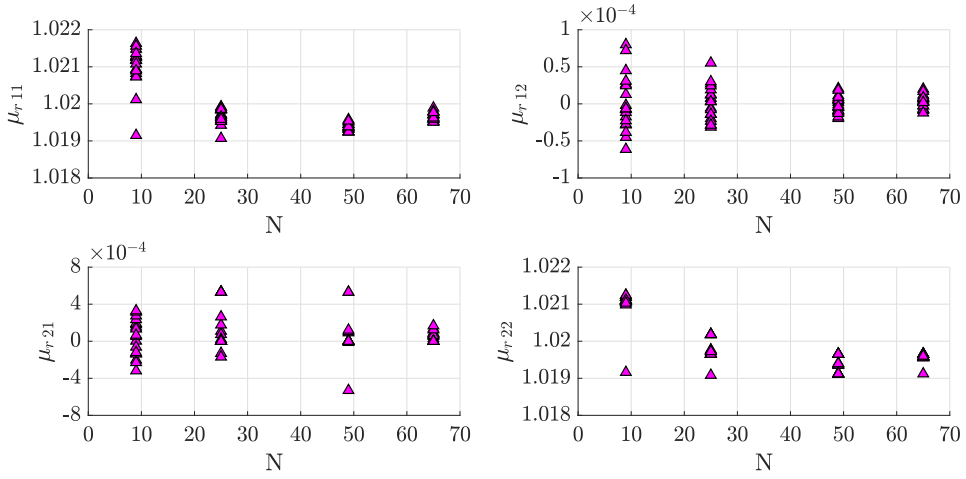

Figure A.8: Components of the relative permeability tensor as a function of the number of particles N for $\Phi = 20\%$

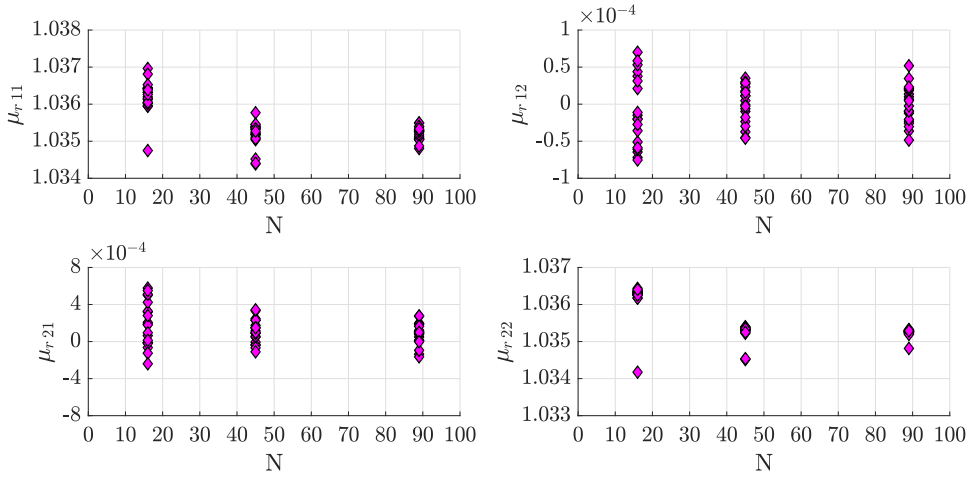

Figure A.9: Components of the relative permeability tensor as a function of the number of particles N for $\Phi = 36\%$

A.2.3 Numerical results from 2D - distributed particle size

	uniform particle size		variable particle size	
	average	standard dev.	average	standard dev.
B_1^{OP} [T]	<0.001	± <0.001	<0.001	± <0.001
B_2^{OP} [T]	0.156	± <0.001	0.156	± 0.001
H_1^{OP} [A/m]	5.6	± 15.7	-7.9	± 20.5
H_2^{OP} [A/m]	398	± 64.4	358.3	± 121.1
ε_1^{OP} [%]	-0.38	± 0.14	-0.17	± 0.18
ε_2^{OP} [%]	-0.14	± 0.11	-0.19	± 0.21
ε_6^{OP} [%]	-0.02	± 0.06	-0.03	± 0.07
σ_1^{OP} [kPa]	-6.67	± 2.71	-1.97	± 3.15
σ_2^{OP} [kPa]	-2.85	± 1.88	-2.04	± 3.91
σ_6^{OP} [kPa]	-0.16	± 0.68	-0.38	± 0.96

Table A.5: Results obtained for the operating point

	Uniform particle size		Variable particle size	
	average	standard dev.	average	standard dev.
	non-magnetized particles			
E_1 [MPa]	1.995	± 0.020	1.994	± 0.023
E_2 [MPa]	1.992	± 0.022	1.987	± 0.021
G_6 [MPa]	0.670	± 0.006	0.671	± 0.006
ν_{12}	0.463	± 0.006	0.464	± 0.004
ν_{21}	0.463	± 0.005	0.463	± 0.005
	magnetized particles			
E_1 [MPa]	1.992	± 0.020	1.991	± 0.023
E_2 [MPa]	1.986	± 0.022	1.982	± 0.020
G_6 [MPa]	0.670	± 0.006	0.670	± 0.006
ν_{12}	0.464	± 0.005	0.464	± 0.004
ν_{21}	0.462	± 0.005	0.462	± 0.005

Table A.6: Results obtained for the mechanical properties

	Uniform particle size		Variable particle size	
	average	standard dev.	average	standard dev.
$\mu_{r\,11}$	1.020	± <0.001	1.020	± <0.001
$\mu_{r\,12}$	<0.001	± <0.001	<0.001	± <0.001
$\mu_{r\,21}$	<0.001	± <0.001	<0.001	± <0.001
$\mu_{r\,22}$	1.020	± <0.001	1.020	± <0.001

Table A.7: Results obtained for the magnetic properties

		Uniform particle size		Variable particle size	
factor	coupling	average	standard dev.	average	standard dev.
$d_{11}^{H=0}$ [mT]	$\varepsilon_1 \rightarrow B_1$	||<0.01	± 1.02	-0.01	± 1.20
$d_{12}^{H=0}$ [mT]	$\varepsilon_2 \rightarrow B_1$	-0.32	± 0.96	-0.57	± 0.99
$d_{16}^{H=0}$ [mT]	$\varepsilon_6 \rightarrow B_1$	34.28	± 2.59	34.03	± 2.55
$d_{21}^{H=0}$ [mT]	$\varepsilon_1 \rightarrow B_2$	60.37	± 1.72	60.77	± 1.65
$d_{22}^{H=0}$ [mT]	$\varepsilon_2 \rightarrow B_2$	98.06	± 1.78	97.86	± 1.64
$d_{26}^{H=0}$ [mT]	$\varepsilon_6 \rightarrow B_2$	-1.19	± 1.83	-1.52	± 1.47
$d_{11}^{\varepsilon=0}$ [mT]	$H_1 \rightarrow \sigma_1$	0.90	± 0.77	0.83	± 1.23
$d_{12}^{\varepsilon=0}$ [mT]	$H_1 \rightarrow \sigma_2$	-1.94	± 0.64	-1.77	± 0.96
$d_{16}^{\varepsilon=0}$ [mT]	$H_1 \rightarrow \sigma_6$	15.12	± 0.98	15.55	± 1.18
$d_{21}^{\varepsilon=0}$ [mT]	$H_2 \rightarrow \sigma_1$	61.21	± 1.10	61.36	± 1.33
$d_{22}^{\varepsilon=0}$ [mT]	$H_2 \rightarrow \sigma_2$	96.90	± 1.38	96.09	± 1.87
$d_{26}^{\varepsilon=0}$ [mT]	$H_2 \rightarrow \sigma_6$	-0.13	± 0.76	-0.08	± 1.05

Table A.8: Results obtained for the coupling

A.2.4 Variation of coupling coefficients

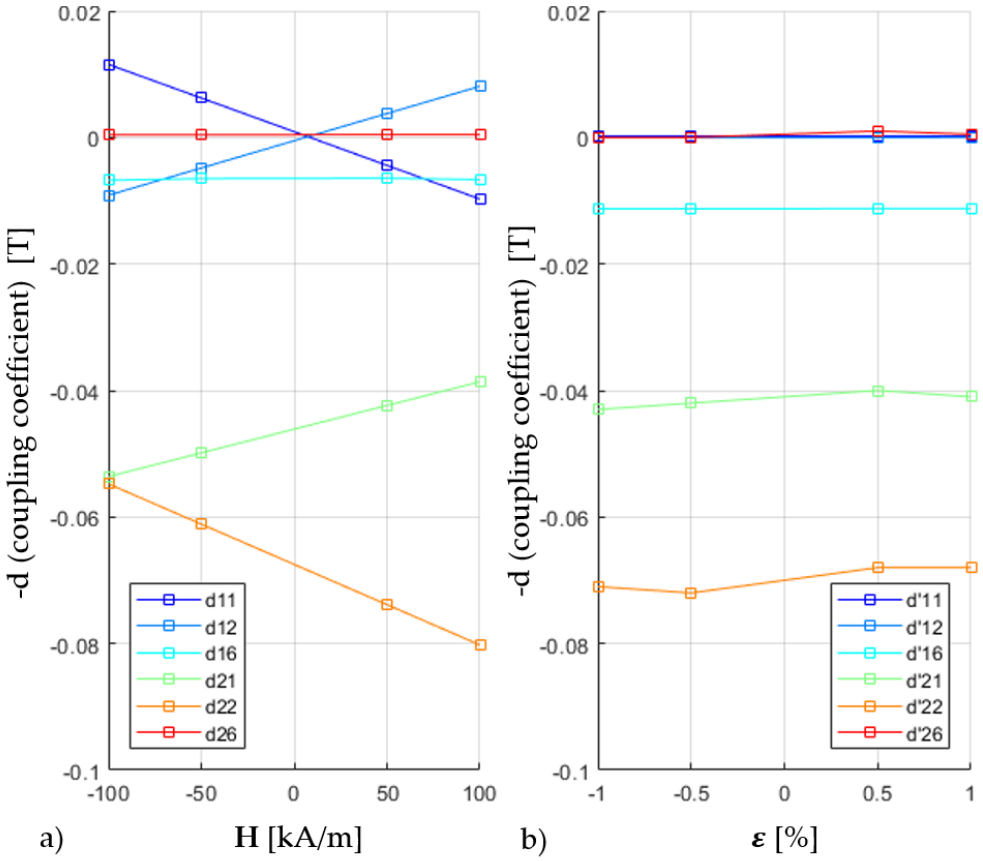

Figure A.10: Variation of the negative coupling coefficients $-d$ with the magnetic field (a) and the mechanical strain (b).

A.3 Appendix chapter V

A.3.1 Single mode control at different excitation amplitudes

The frequency range around the third bending mode is scanned in the following to study the influence of the excitation amplitude on the mode shape. A step-sine signal is used as excitation signal since it allows to excite the system at its steady state at multiple frequencies, which is important to avoid harmonic distortions. An important point of the excitation is the amplitude control of the input signal (acceleration in this case). The force drop out of the structure which increases when the resonance frequency is approached as the vibration of the structure increases. The energy which is necessary to move the structure increases and thus the input voltage for the shaker has to be increased. To assure a constant excitation signal over the whole frequency range around the resonance the input voltage for the shaker has to be adapted. This adaptation is realized by an iterative control algorithm.

The control algorithm needs one step to reach convergence in general with two two exceptions. The first exception is the starting voltage. To secure the shaker, the starting voltage is kept very small and increased step by step. Therefore, the first measurement with an acceleration of $50\,\mathrm{mm/s^2}$ needs 20 iterations until convergence. The second case of exception is the variation of the output voltage due to the force drop out in vicinity of the resonance. The single point measurement has been realized in a frequency range from 180 Hz to 350 Hz. In between this range, seven different acceleration amplitudes at the base ranging from $1\,\mathrm{m/s^2}$ to $75\,\mathrm{m/s^2}$ have been tested. The construction of the FRF is explained at the example of measurements at $50\,\mathrm{m/s^2}$ in the following.

Figure A.11 shows the measurement results for the acceleration at the base (a) and the velocity on the beam (b) where the left part of the figure shows the two signals for the complete measurement period of 5.63 s and the right part represents a zoom on the first 0.5 s of the excitation. In general, the measurement signals remain relatively stable during the whole measurement period. At the beginning of the excitation, acceleration and velocity are in a transient state. The acceleration reaches the steady state after 0.1 s and the velocity at about 0.3 s.

After the first measurement at 280 Hz, the frequency is decreased in steps of 1 Hz until 200 Hz. As former described, a control of the output voltage is necessary due to the force drop out to assure a constant acceleration amplitude. The voltage, the acceleration and the velocity over the frequency range are shown in figure A.12 a to c respectively. Using the adaptive control of the acceleration, 0.79 V are used assure an acceleration of $(50 \pm 1)\,\mathrm{m/s^2}$ at 280 Hz. A first correction of the output voltage is necessary in the third step since the value approaches the lower limit.

In the following, the acceleration stays in the tolerance interval until but decreases in vicinity of the resonance, therefore a second correction of the output voltage is necessary at 239 Hz. The acceleration increases in the following but stays in the tolerance interval until the end of the measurement at 200 Hz so that a further adaptation of the voltage amplitude is not necessary.

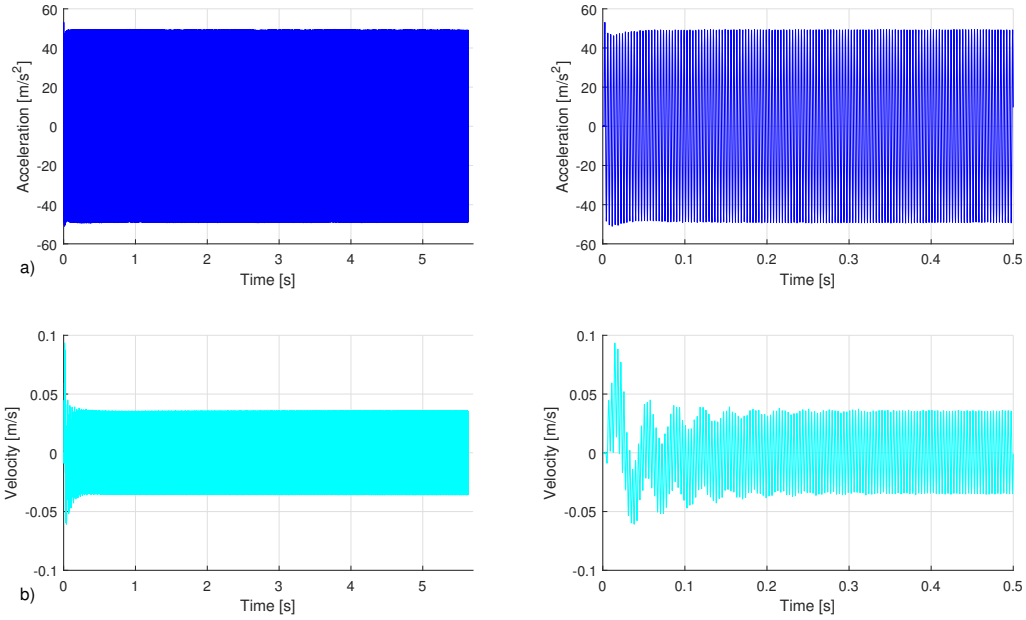

Figure A.11: Measurement signals at 280 Hz : a) acceleration of the base controlled at 50 mm/s^2, b) velocity measured with the interferometer.

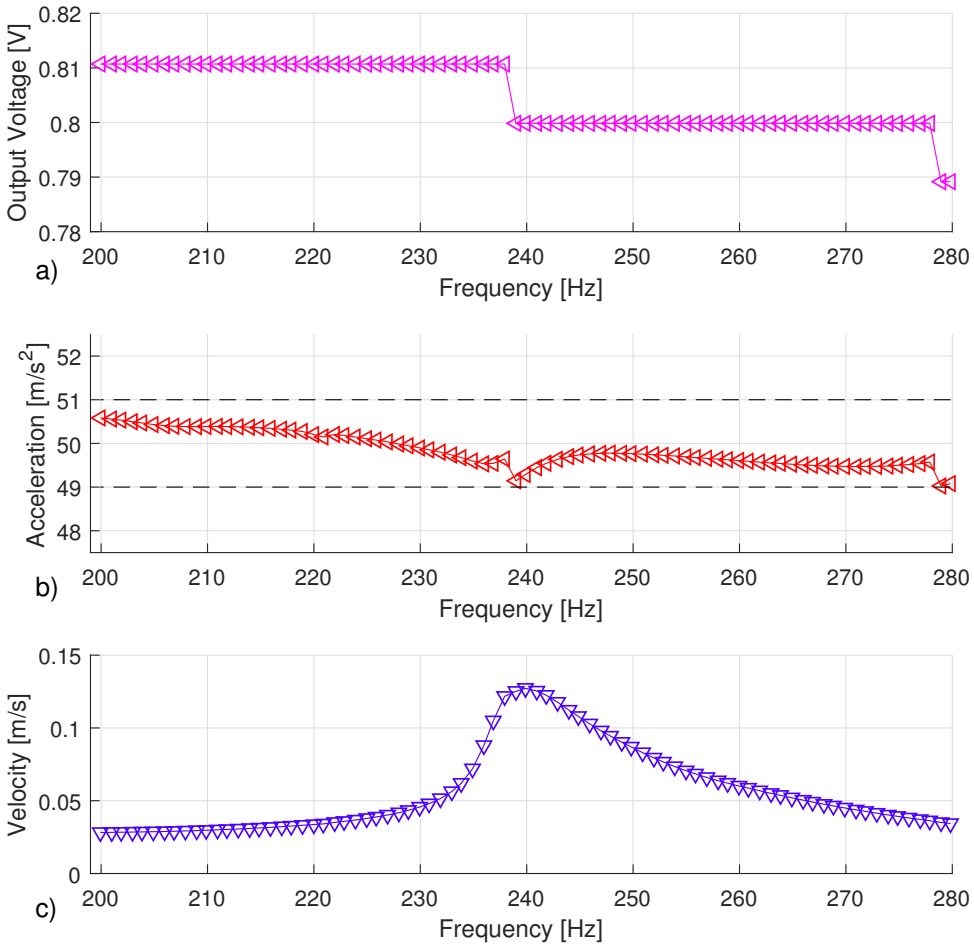

Figure A.12: Frequency domain : output voltage for the shaker a), acceleration amplitude measured at the base b) and velocity c).

Bibliographie

[Amiot+ 2013] F. Amiot, M. Bornert, P. Doumalin, J.-C. Dupré, M. Fazzini, J.-J. Orteu, C. Poilâne, L. Robert, R. Rotinat, E. Toussaint, et al. "Assessment of digital image correlation measurement accuracy in the ultimate error regime: main results of a collaborative benchmark." In: *Strain* 49.6 (2013), pp. 483–496.

[Amjadian+ 2018] M. Amjadian and A.K. Agrawal. "Modeling, design, and testing of a proof-of-concept prototype damper with friction and eddy current damping effects." In: *Journal of Sound and Vibration* 413 (2018), pp. 225–249.

[Bekemans 2006] M. Bekemans. "Modélisation des machines électriques en vue du contrôle des efforts radiaux [Modeling of electrical machines with regard to the control of radial loading]." PhD thesis. Université catholique de Louvain, 2006.

[Bira+ 2020] N. Bira, P. Dhagat, and J.R. Davidson. "A Review of Magnetic Elastomers and Their Role in Soft Robotics." In: *Frontiers in Robotics and AI* 7 (2020), p. 146.

[Bodelot+ 2018] L. Bodelot, J.P. Voropaieff, and T. Pössinger. "Experimental investigation of the coupled magneto-mechanical response in magnetorheological elastomers." In: *Experimental Mechanics* 58.2 (2018), pp. 207–221.

[Borcea+ 2001] L. Borcea and O. Bruno. "On the magneto-elastic properties of elastomer-ferromagnet composites." In: *J. Mech Phys. Solids* 49 (2001), pp. 2877–2919.

[Borin+ 2013] D.Y. Borin, G.V. Stepanov, and S. Odenbach. "Tuning the tensile modulus of magnetorheological elastomers with magnetically hard powder." In: *Journal of Physics: Conference Series* 412.1 (2013), 012040 (5pp).

[Bornert+ 2001] M. Bornert, T. Bretheau, and P. Gilormini. *Homogénéisation en mécanique des matériaux, Tome 1: Matériaux aléatoires élastiques et milieux périodiques*. Hèrmes Science Publications, 2001.

[Böse+ 2009] H. Böse and R. Röder. "Magnetorheological elastomers with high variability of their mechanical properties." In: *Journal of physics: Conference series* 149.1 (2009), 012090 6pp.

[Böse+ 2021] H. Böse, T. Gerlach, and J. Ehrlich. "Magnetorheological elastomers — An underestimated class of soft actuator materials." In: *Journal of Intelligent Material Systems and Structures* (2021), p. 1045389X21990888.

[Bouaziz+ 2016] H. Bouaziz, N. Peyret, M.S. Abbes, G. Chevallier, and M. Haddar. "Vibration reduction of an assembly by control of the tightening load." In: *International Journal of Applied Mechanics* 8.06 (2016), p. 1650081.

[Bozorth 1993] R.M. Bozorth. *Ferromagnetism*. 1993.

[Brake 2017] M.R.W. Brake. *The mechanics of jointed structures: recent research and open challenges for developing predictive models for structural dynamics*. Springer, 2017.

[Brake+ 2019] M.R.W. Brake, C.W. Schwingshackl, and P. Reuß. "Observations of variability and repeatability in jointed structures." In: *Mechanical Systems and Signal Processing* 129 (2019), pp. 282–307.

[Brown 1966] W.F. Brown. *Magnetoelastic interactions*. Vol. 9. Springer, 1966.

[Butaud+ 2018] P. Butaud, M. Ouisse, V. Placet, F. Renaud, T. Travaillot, A. Maynadier, and C. Rogueda-Berriet. "Identification of the viscoelastic properties of the tBA/PEGDMA polymer from multi-loading modes conducted over a wide frequency–temperature scale range." In: *Polymer Testing* 69 (2018), pp. 250–258.

[Butaud+ 2020] P. Butaud, D. Renault, B. Verdin, M. Ouisse, and G. Chevallier. "In-core heat distribution control for adaptive damping and stiffness tuning of composite structures." In: *Smart Materials and Structures* 29.6 (2020), p. 065002.

[Caborgan 2011] R. Caborgan. “Contribution à l’analyse expérimentale du comportement thermomécanique du caoutchouc naturel.” PhD thesis. Université Montpellier II-Sciences et Techniques du Languedoc, 2011.

[Cantera+ 2017] M. A. Cantera, M. Behrdooz, R. F. Gibson, and F. Gordaninejad. “Modeling of magneto-mechanical response of magnetorheological elastomers (MRE) and MRE-based systems: a review.” In: *Smart Mater. Struct.* 26 (2017), p. 023001.

[Caughey 1959] T.K. Caughey. “Response of a nonlinear string to random loading.” In: *Journal of Applied Mechanics* 26.3 (1959), pp. 341–344.

[Chen+ 2007] L. Chen, X.L. Gong, and W.H. Li. “Microstructures and viscoelastic properties of anisotropic magnetorheological elastomers.” In: *Smart materials and structures* 16.6 (2007), p. 2645.

[Coirier 2001] J. Coirier. *Mécanique des milieux continus*. Dunod, 2001.

[Corcolle 2009] R. Corcolle. “Détermination de lois de comportement couplé par des techniques d’homogénéisation: application aux matériaux du génie électrique.” PhD thesis. Paris 11, 2009.

[Danas+ 2012] K. Danas, S.V. Kankanala, and N. Triantafyllidis. “Experiments and modeling of iron-particle-filled magnetorheological elastomers.” In: *Journal of the Mechanics and Physics of Solids* 60.1 (2012), pp. 120–138.

[Daniel+ 2007] L. Daniel and R. Corcolle. “A note on the effective magnetic permeability of polycrystals.” In: *IEEE transactions on magnetics* 43.7 (2007), pp. 3153–3158.

[Diermeier+ 2016] A. Diermeier, D. Sindersberger, and G.J. Monkman. “Magneto-active polymer actuator.” In: *Conference ACTUATOR, Bremen (Germany), 2016*. 2016, pp. 1–4.

[Dion+ 2013] J.-L. Dion, G. Chevallier, and N. Peyret. “Improvement of measurement techniques for damping induced by micro-sliding.” In: *Mechanical Systems and Signal Processing* 34.1-2 (2013), pp. 106–115.

[Dyniewicz+ 2015] B. Dyniewicz, J.M. Bajkowski, and C.I. Bajer. “Semi-active control of a sandwich beam partially filled with magnetorheological elastomer.” In: *Mechanical Systems and Signal Processing* 60 (2015), pp. 695–705.

[Electrical+ 1990] The Institute of Electrical and Inc Electronics Engineers. *IEEE Standard of Magnetostrictive Materials : Piezomagnetic Nomenclature*. Tech. rep. IEEE Std 319-1990. Subcommittee on Magnetostrictive Materials of the Standards Activities Comittee of the IEEE Ultrasonics, Ferroelectrics, and Frequency Control Society, 1990.

[Eringen+ 1990] A.C. Eringen and G.A. Maugin. “Electrodynamics of Continua 1.” In: *Springer-Verlag New York Inc* (1990).

[Fiorillo 2010] F. Fiorillo. “Measurements of magnetic materials.” In: *Metrologia* 47.2 (2010), S114.

[Fröhlich+ 2015] J. Fröhlich, W. Niedermeier, and H. D. Luginsland. “The effect of filler-–filler and filler—elastomer interaction on rubber reinforcement.” In: *Composites Part A: Applied Science and Manufacturing* 36.4 (2015), pp. 449–460.

[Galipeau+ 2012] E. Galipeau and P. Ponte Castañeda. “The effect of particle shape and distribution on the macroscopic behavior of magnetoelastic composites.” In: *International Journal of Solids and Structures* 49.1 (2012), pp. 1–17.

[Galipeau+ 2013a] E. Galipeau and P. Ponte Castañeda. “A finite-strain constitutive model for magnetorheological elastomers: magnetic torques and fiber rotations.” In: *Journal of the Mechanics and Physics of Solids* 61.4 (2013), pp. 1065–1090.

[Galipeau+ 2013b] E. Galipeau and P. Ponte Castañeda. “Giant field-induced strains in magnetoactive elastomer composites.” In: *Proceedings of the Royal Society A: Mathematical, Physical and Engineering Sciences* 469.2158 (2013), p. 20130385.

[Galipeau+ 2014] E. Galipeau, S. Rudykh, G. deBotton, and P. Ponte Castañeda. “Magnetoactive elastomers with periodic and random microstructures.” In: *International journal of solids and structures* 51.18 (2014), pp. 3012–3024.

[Gholizadeh+ 2019] A. Gholizadeh, S. Abbaslou, P. Xie, A. Knaian, and M. Javanmard. “Electronically actuated microfluidic valves with zero static-power consumption using electropermanent magnets.” In: *Sensors and Actuators A: Physical* 296 (2019), pp. 316–323.

[Gloth+ 2004] G. Gloth and M. Sinapius. “Analysis of swept-sine runs during modal identification.” In: *Mechanical systems and signal processing* 18.6 (2004), pp. 1421–1441.

[Guan+ 2008] X. Guan, X. Dong, and J. Ou. “Magnetostrictive effect of magnetorheological elastomer.” In: *Journal of Magnetism and magnetic materials* 320 (2008), pp. 158–163.

[Han+ 2013] Y. Han, W. Hong, and L. E. Faidley. “Field-stiffening effect of magneto-rheological elastomers.” In: *Int. J. Solids Struct* 50 (2013), pp. 2281–2919.

[Hilber 2016] W. Hilber. “Stimulus-active polymer actuators for next-generation microfluidic devices.” In: *Applied Physics A* 122.8 (2016), pp. 1–39.

[Hirsinger 1994] L. Hirsinger. “Étude des déformations magnetoélastiques dans les matériaux ferromagnétiques doux: application à l’étude des déformations d’une structure de machine électrique.” PhD thesis. Paris 6, 1994.

[Hirsinger+ 2013] L. Hirsinger and N. Daher. “Les Tenseurs de contraintes électromagnétiques [Electromagnetic stress tensors].” In: *Congrès français de mécanique, Bordeaux, 26–30 august 2013* (2013).

[Hu+ 2011] G. Hu, M. Guo, W. Li, H. Du, and G. Alici. “Experimental investigation of the vibration characteristics of a magnetorheological elastomer sandwich beam under non-homogeneous small magnetic fields.” In: *Smart materials and structures* 20.12 (2011), p. 127001.

[Immersion Corp 2018] Immersion Corp. “Magneto-sensitive elastomers for haptic feedback.” US20180151281A1. 2018.

[Jolly+ 1996a] M.J. Jolly, J.D. Carlson, and B.C. Muňoz. “A model of the behavior of manetorheological materials.” In: *Smart Mater. Struct* 5 (1996), pp. 607–614.

[Jolly+ 1996b] M.R. Jolly, J.D. Carlson, B.C. Muñoz, and T.A. Bullions. "The magnetoviscoelastic response of elastomer composites consisting of ferrous particles embedded in a polymer matrix." In: *Journal of Intelligent Material Systems and Structures* 7.6 (1996), pp. 613–622.

[Jolly+ 1999] M.R. Jolly, J.W. Bender, and J.D Carlson. "Properties and applications of commercial magnetorheological fluids." In: *Journal of intelligent material systems and structures* 10.1 (1999), pp. 5–13.

[Jufer 1998] M. Jufer. *Electromécanique [Electromechanics]*. Vol. TE IX. Presses Polytechniques et Universitaires Romandes, 1998.

[Kalina+ 2016] K.A. Kalina, P. Metsch, and M. Kästner. "Microscale modeling and simulation of magnetorheological elastomers at finite strains: a study on the influence of mechanical preloads." In: *International Journal of Solids and Structures* 102 (2016), pp. 286–296.

[Kalina+ 2017] K.A. Kalina, J. Brummund, P. Metsch, M. Kästner, D.Y. Borin, J.M. Linke, and S. Odenbach. "Modeling of magnetic hystereses in soft MREs filled with NdFeB particles." In: *Smart Materials and Structures* 26.10 (2017), p. 105019.

[Kalina+ 2020] K.A. Kalina, P. Metsch, J. Brummund, and M. Kästner. "A macroscopic model for magnetorheological elastomers based on microscopic simulations." In: *International Journal of Solids and Structures* 193 (2020), pp. 200–212.

[Kankanala+ 2004] S.V. Kankanala and N. Triantafyllidis. "On finitely strained magnetorheological elastomers." In: *Journal of the Mechanics and Physics of Solids* 52.12 (2004), pp. 2869–2908.

[Keip+ 2016] M.-A. Keip and M. Rambausek. "A multiscale approach to the computational characterization of magnetorheological elastomers." In: *International Journal for Numerical Methods in Engineering* 107.4 (2016), pp. 338–360.

[Kerschen+ 2009] G. Kerschen, M. Peeters, J.-C. Golinval, and A.F. Vakakis. “Nonlinear normal modes, Part I: A useful framework for the structural dynamicist.” In: *Mechanical systems and signal processing* 23.1 (2009), pp. 170–194.

[Kim+ 2018] Y. Kim, H. Yuk, R. Zhao, S.A. Chester, and X. Zhao. “Printing ferromagnetic domains for untethered fast-transforming soft materials.” In: *Nature* 558.7709 (2018), pp. 274–279.

[Koo+ 2012] J.H. Koo, A Dawson, and H.J. Jung. “Characterization of actuation properties of magnetorheological elastomers with embedded hard magnetic particles.” In: *Journal of Intelligent Material Systems and Structures* 23.9 (2012), pp. 1049–1054.

[Kovetz 2000] A. Kovetz. *Electromagnetic theory*. Oxford University Press Oxford, 2000.

[Krack+ 2019] M. Krack and J. Gross. *Harmonic balance for nonlinear vibration problems*. Springer, 2019.

[Kramarenko+ 2015] E.Y. Kramarenko, A.V. Chertovich, G.V. Stepanov, A.S. Semisalova, L.A. Makarova, N.S. Perov, and A.R. Khokhlov. “Magnetic and viscoelastic response of elastomers with hard magnetic filler.” In: *Smart materials and structures* 24.3 (2015), 035022 (11p).

[Lacheisserie+ 1999] E. d. Trémolet de Lacheisserie, L. Néel, M. Cyrot, M. Décorps, and B. Dieny, eds. *Magnétisme - I - Fondéments*. Presses universitaires de Grenoble, 1999.

[Lallement+ 1998] G. Lallement, A. Ramanitranja, and S. Cogan. “Optimal sensor deployment: application to model updating.” In: *Journal of Vibration and Control* 4.1 (1998), pp. 29–46.

[Lanchester 1914] F.W. Lanchester. *Damping torsional vibrations in crank-shafts*. US Patent 1,085,443. Jan. 1914.

[Landecker+ 1999] P.B. Landecker, D.D. Villani, and K.W. Yung. “An analytic solution for the torque between two magnetic dipoles.” In: *Magnetic and Electrical Separation* 10 (1999), pp. 29–33.

[Lanotte+ 2004] L. Lanotte, G. Ausanio, C. Hison, V. Iannotti, C. Luponio, and C. Luponio Jr. “State of the art and development trends of novel nanostructured elastomagnetic composites.” In: *Journal of Optoelectronics and Advanced Materials* 6 (2004), pp. 523–532.

[Lee+ 2020] M. Lee, T. Park, C. Kim, and S.-M. Park. “Characterization of a magneto-active membrane actuator comprising hard magnetic particles with varying crosslinking degrees.” In: *Materials & Design* 195 (2020), p. 108921.

[Lefèvre+ 2017] V. Lefèvre, K. Danas, and O. Lopez-Pamies. “A general result for the magnetoelastic response of isotropic suspensions of iron and ferrofluid particles in rubber, with applications to spherical and cylindrical specimens.” In: *Journal of the Mechanics and Physics of Solids* 107 (2017), pp. 343–364.

[Lemaitre+ 2009] J. Lemaitre, J. Chaboche, A. Benallal, and R. Desmorat. *Mécanique des matériaux solides-3ème édition*. Dunod, 2009.

[Li+ 2011] J. Li, M. Zhang, L. Wang, W. Li, P. Sheng, and W. Wen. “Design and fabrication of microfluidic mixer from carbonyl iron–PDMS composite membrane.” In: *Microfluidics and nanofluidics* 10.4 (2011), pp. 919–925.

[Linke+ 2016] J.M. Linke, D.Y. Borin, and S. Odenbach. “First-order reversal curve analysis of magnetoactive elastomers.” In: *RSC Advances* 6.102 (2016), pp. 100407–100416.

[Lokander+ 2003] M. Lokander and B. Stenberg. “Performance of isotropic magnetorheological rubber materials.” In: *Polymer Testing* 22.3 (2003), pp. 245–251.

[Małecki+ 2015] P. Małecki, M. Królewicz, J. Krzak, J. Kaleta, and J. Pigłowski. “Dynamic mechanical analysis of magnetorheological composites containing silica-coated carbonyl iron powder.” In: *Journal of Intelligent Material Systems and Structures* 26.14 (2015), pp. 1899–1905.

[Menard 1999] K.P. Menard. *Dynamic Mechanical Analysis - A practical introduction*. CRC Press, 1999.

[Metsch+ 2016] P. Metsch, K.A. Kalina, C. Spieler, and M. Kästner. "A numerical study on magnetostrictive phenomena in magnetorheological elastomers." In: *Computational Materials Science* 124 (2016), pp. 364–374.

[Mukherjee+ 2020] D. Mukherjee, L. Bodelot, and K. Danas. "Microstructurally-guided explicit continuum models for isotropic magnetorheological elastomers with iron particles." In: *International Journal of Non-Linear Mechanics* 120 (2020), p. 103380.

[Mullins 1969] L. Mullins. "Softening of rubber by deformation. Rubber chemistry and technology." In: *Journal of Physics: Condensed Matter* 42.1 (1969), pp. 339–362.

[Nagel+ 2006] J.J. Nagel, G. Mikhail, H. Noh, and J. Koo. "Magnetically actuated micropumps using an Fe-PDMS composite membrane." In: *Smart Structures and Materials 2006: Smart Electronics, MEMS, BioMEMS, and Nanotechnology*. Vol. 6172. International Society for Optics and Photonics. 2006, p. 617213.

[Nanni+ 2012] G. Nanni, S. Petroni, D. Fragouli, M. Amato, M. De Vittorio, and A. Athanassiou. "Microfabrication of magnetically actuated PDMS–Iron composite membranes." In: *Microelectronic engineering* 98 (2012), pp. 607–609.

[Nayak+ 2011] B. Nayak, S.K. Dwivedy, and K.S.R.K. Murthy. "Dynamic analysis of magnetorheological elastomer-based sandwich beam with conductive skins under various boundary conditions." In: *Journal of Sound and Vibration* 330.9 (2011), pp. 1837–1859.

[Nayak+ 2013] B. Nayak, S.K. Dwivedy, and K.S.R.K. Murthy. "Vibration analysis of a three-layer magnetorheological elastomer embedded sandwich beam with conductive skins using finite element method." In: *Proceedings of the Institution of Mechanical Engineers, Part C: Journal of Mechanical Engineering Science* 227.4 (2013), pp. 714–729.

[Nayfeh+ 1995] A.H. Nayfeh and D.T. Mook. *Nonlinear oscillations*. John Wiley & Sons, 1995.

[Norouzi+ 2017] M. Norouzi, M. Gilani, S.S. Alehashem, and H. Vatandoost. “Dynamic characterization and modeling of isotropic magnetorheological elastomers under tensile-compressive loadings.” In: *IEEE Transactions on Magnetics* 53.9 (2017), pp. 1–12.

[NuSil 2020] NuSil. *MED-4014*. Acessed february 20, 2020. 2020. URL: https://nusil.com/product/med-4014%5C_high-consistency-silicone-elastomer.

[Ogden 2011] R.W. Ogden. “Magnetostatics: from basic principles to nonlinear interactions in deformable media.” In: *Mechanics and Electrodynamics of Magneto- and Electro-elastic Materials*. Springer, 2011, pp. 107–152.

[Oh+ 2006] K.W. Oh and C.H. Ahn. “A review of microvalves.” In: *Journal of micromechanics and microengineering* 16.5 (2006), R13.

[Paknahad+ 2019] A.A. Paknahad and M. Tahmasebipour. “An electromagnetic micro-actuator with PDMS-Fe3O4 nanocomposite magnetic membrane.” In: *Microelectronic Engineering* 216 (2019), p. 111031.

[Payne 1962] A.R. Payne. “The dynamic properties of carbon black-loaded natural rubber vulcanizates. Part 1.” In: *Journal of applied polymer science* 6.19 (1962), pp. 57–63.

[Peeters+ 2004] B. Peeters, H. Van der Auweraer, P. Guillaume, and J. Leuridan. “The PolyMAX frequency-domain method: a new standard for modal parameter estimation?” In: *Shock and Vibration* 11.3, 4 (2004), pp. 395–409.

[Peyret+ 2010] N. Peyret, J.-L. Dion, G. Chevallier, and P. Argoul. “Micro-slip induced damping in planar contact under constant and uniform normal stress.” In: *International Journal of Applied Mechanics* 2.02 (2010), pp. 281–304.

[Peyret+ 2016a] N. Peyret, G. Chevallier, and J.-L. Dion. “Dynamic damping in joints: multiscale model taking into account defects in a nominally plane surface.” In: *International Journal of Applied Mechanics* 8.08 (2016), p. 1650097.

[Peyret+ 2016b] N. Peyret, J.-L. Dion, and G. Chevallier. “A framework for backbone experimental tracking: Piezoelectric actuators, stop-sine signal and Kalman filtering.” In: *Mechanical Systems and Signal Processing* 78 (2016), pp. 28–42.

[Pindera+ 2009] M.-J. Pindera, H. Khatam, A.S. Drago, and Y. Bansal. “Micromechanics of spatially uniform heterogeneous media: a critical review and emerging approaches.” In: *Composites Part B: Engineering* 40.5 (2009), pp. 349–378.

[Piranda 2001] J. Piranda. “Analyse modale expérimentale [Experimental modal analysis].” In: *Techniques de l’ingénieur, traité Mesures et Contrôle* R6 180 (2001), 29pp.

[Ponte Castañeda+ 2011] P. Ponte Castañeda and E. Galipeau. “Homogenization-based constitutive models for magnetorheological elastomers at finite strain.” In: *Journal of the Mechanics and Physics of Solids* 59.2 (2011), pp. 194–215.

[Popp+ 2003] K. Popp, L. Panning, and W. Sextro. “Vibration damping by friction forces: theory and applications.” In: *Journal of Vibration and Control* 9.3–4 (2003), pp. 419–448.

[Qian+ 2020] J.-Y. Qian, C.-W. Hou, X.-J. Li, and Z.-J. Jin. “Actuation mechanism of microvalves: A review.” In: *Micromachines* 11.2 (2020), p. 172.

[Renaud+ 2011] F. Renaud, J.-L. Dion, G. Chevallier, I. Tawfiq, and R. Lemaire. “A new identification method of viscoelastic behavior: Application to the generalized Maxwell model.” In: *Mechanical Systems and Signal Processing* 25.3 (2011), pp. 991–1010.

[Rigbi+ 1983] Z. Rigbi and L. Jilkén. “The response of an elastomer filled with soft ferrite to mechanical and magnetic influences.” In: *Journal of magnetism and magnetic materials* 37.3 (1983), pp. 267–276.

[RS Components 2020] RS Components. *10m Magnetic Tape, 0.5mm Thickness*. Acessed february 20, 2020. 2020. URL: https://uk.rs-online.com/web/p/magnetic-tapes/7602704/.

[Said+ 2016] M.M. Said, J. Yunas, R.E. Pawinanto, B.Y. Majlis, and B. Bais. "PDMS based electromagnetic actuator membrane with embedded magnetic particles in polymer composite." In: *Sensors and Actuators A: Physical* 245 (2016), pp. 85–96.

[Salhi+ 2008] B. Salhi, J. Lardiès, and M. Berthillier. "Parameter Identification of Bladed Assemblies Using a Subspace Method." In: *International Journal for Simulation and Multidisciplinary Design Optimization* 2.4 (2008), pp. 267–272.

[Scheel+ 2020] M. Scheel, T. Weigele, and M. Krack. "Challenging an experimental nonlinear modal analysis method with a new strongly friction-damped structure." In: *Journal of Sound and Vibration* 485 (2020), p. 115580.

[Schoukens+ 2019] J. Schoukens and L. Ljung. "Nonlinear system identification: A user-oriented road map." In: *IEEE Control Systems Magazine* 39.6 (2019), pp. 28–99.

[Schümann+ 2017] M. Schümann, D.Y. Borin, S. Huang, G.K. Auernhammer, R. Müller, and S. Odenbach. "A characterisation of the magnetically induced movement of NdFeB-particles in magnetorheological elastomers." In: *Smart Materials and Structures* 26.9 (2017), p. 095018.

[Siboni+ 2012] M.H. Siboni and P. Ponte Castañeda. "A magnetically anisotropic, ellipsoidal inclusion subjected to a non-aligned magnetic field in an elastic medium." In: *Comptes Rendus Mécanique* 340.4-5 (2012), pp. 205–218.

[Singh+ 2014] A. Singh, L. Hirsinger, P. Delobelle, and C. Khan-Malek. "Rapid prototyping of magnetic valve based on nanocomposite Co/PDMS membrane." In: *Microsystem technologies* 20.3 (2014), pp. 427–436.

[Spieler+ 2013] C. Spieler, M. Kästner, J. Goldmann, J. Brummund, and V. Ulbricht. "XFEM modeling and homogenization of magnetoactive composites." In: *Acta Mechanica* 224.11 (2013), pp. 2453–2469.

[Stepanov+ 2008] G.V. Stepanov, D.Y. Borin, Y.L. Raikher, P.V. Melenev, and N.S. Perov. "Motion of ferroparticles inside the polymeric matrix in magnetoactive elastomers." In: *Journal of Physics: Condensed Matter* 20.20 (2008), 204121 6pp.

[Stepanov+ 2012] G.V. Stepanov, A.V. Chertovich, and E.Y. Kramarenko. “Magnetorheological and deformation properties of magnetically controlled elastomers with hard magnetic filler.” In: *M. Journal of Magnetism and Magnetic Materials* 324.21 (2012), pp. 3448–3451.

[Stepanov+ 2014] G.V. Stepanov, D.Y. Borin, E.Y. Kramarenko, V.V. Bogdanov, D.A. Semerenko, and P.A. Storozhenko. “Magnetoactive elastomer based on magnetically hard filler: synthesis and study of viscoelastic and damping properties.” In: *Polymer science series A* 56.5 (2014), pp. 603–613.

[Stepanov+ 2017] G.V. Stepanov, D.Y. Borin, and P.A. Storozhenko. “Rotation of magnetic particles inside the polymer matrix of magnetoactive elastomers with a hard magnetic filler.” In: *Journal of Magnetism and Magnetic Materials* 431 (2017), pp. 138–140.

[Sun+ 2003] Q. Sun, J.-X. Zhou, and L. Zhang. “An adaptive beam model and dynamic characteristics of magnetorheological materials.” In: *Journal of Sound and Vibration* 261.3 (2003), pp. 465–481.

[Sutrisno+ 2015] J. Sutrisno, A. Purwanto, and S.A. Mazlan. “Recent progress on magnetorheological solids: materials, fabrication, testing, and applications.” In: *Advanced engineering materials* 17.5 (2015), pp. 563–597.

[Szmidt+ 2019] T. Szmidt, D. Pisarski, R. Konowrocki, S. Awietjan, and A. Boczkowska. “Adaptive Damping of a Double-Beam Structure Based on Magnetorheological Elastomer.” In: *Shock and Vibration* 2019 (2019), p. 16.

[Tao+ 2017] K. Tao, J. Wu, A.G.P. Kottapalli, D. Chen, Z. Yang, G. Ding, S.W. Lye, and J. Miao. “Micropatterning of resin-bonded NdFeB magnet for a fully integrated electromagnetic actuator.” In: *Solid-State Electronics* 138 (2017), pp. 66–72.

[Teloli+ 2020] R. Teloli, P. Butaud, G. Chevallier, and S. da Silva. “Good practices for designing and experimental testing of dynamically excited jointed structures: the Orion beam.” Submitted to MSSP. 2020.

[TheMagnetShop 2020] TheMagnetShop. *10 A4 Magnetic Sheets 0.4mm for Spellbinder Dies/Craft*. Acessed february 20, 2020. 2020. URL: https://themagnetshop.co.uk/product/10-plain-a4-0-4mm-thick-magnetic-sheets/.

[Thomas 2019] O. Thomas. "Vibrations non linéaires : I – Phénoménologie et modèles." Presentation during doctoral training École Doctorale VISHNO (VIbrations SHocks & NOise), Valmorel (France), 17 – 22 march. 2019.

[University of Nevada 2004] Nevada System of Higher Education University of Nevada. "Controllable magneto-rheological elastomer vibration isolator." US7086507B2. 2004.

[Vakilinejad+ 2020] M. Vakilinejad, A. Grolet, and O. Thomas. "A comparison of robustness and performance of linear and nonlinear Lanchester dampers." In: *Nonlinear Dynamics* (2020), pp. 1–19.

[Vernay Laboratories 2015] Vernay Laboratories. "Magneto-Rheological Elastomeric Fluid Control Armature Assembly." US2015184770A1. 2015.

[Vinson 1999] J.R. Vinson. *The behavior of sandwich structures of isotropic and composite materials*. CRC Press, 1999.

[Voropaieff 2019] J.P. Voropaieff. "Modeling and identification of the constitutive behaviour of magneto-rheological elastomers." PhD thesis. Université Paris-Saclay, 2019.

[Wen+ 2017] Q. Wen, Y. Wang, and X. Gong. "The magnetic field dependent dynamic properties of magnetorheological elastomers based on hard magnetic particles." In: *Smart Materials and Structures* 26.7 (2017), 075012 (9p).

[Xia+ 2019] Y. Xia, M. Ruzzene, and A. Erturk. "Dramatic bandwidth enhancement in nonlinear metastructures via bistable attachments." In: *Applied Physics Letters* 114.9 (2019), p. 093501.

[Yalcintas+ 2003] M. Yalcintas and H. Dai. "Vibration suppression capabilities of magnetorheological materials based adaptive structures." In: *Smart Materials and Structures* 13.1 (2003), p. 1.

[Yamahata+ 2005] C. Yamahata, C. Lotto, E. Al-Assaf, and M.A.M. Gijs. “A PMMA valveless micropump using electromagnetic actuation.” In: *Microfluidics and Nanofluidics* 1.3 (2005), pp. 197–207.

[Yuan+ 2019] P.-P. Yuan, W.-X. Ren, and J. Zhang. “Dynamic tests and model updating of nonlinear beam structures with bolted joints.” In: *Mechanical Systems and Signal Processing* 126 (2019), pp. 193–210.

[Yung+ 1998] K.W. Yung, P.B. Landecker, and D.D. Villani. “An analytic solution for the force between two magnetic dipoles.” In: *Magnetic and Electrical Separation* 9 (1998), pp. 39–52.

[Zabihyan+ 2018] R. Zabihyan, J. Mergheim, A. Javili, and P. Steinmann. “Aspects of computational homogenization in magneto-mechanics: Boundary conditions, RVE size and microstructure composition.” In: *International Journal of Solids and Structures* 130 (2018), pp. 105–121.

[ZF Friedrichshafen AG 2016] ZF Friedrichshafen AG. “Magnetically actuated valve.” DE102016211658A1. 2016.

[Zhou+ 2006a] G.Y. Zhou and Q. Wang. “Use of magnetorheological elastomer in an adaptive sandwich beam with conductive skins. Part I: Magnetoelastic loads in conductive skins.” In: *International Journal of Solids and Structures* 43.17 (2006), pp. 5386–5402.

[Zhou+ 2006b] G.Y. Zhou and Q. Wang. “Use of magnetorheological elastomer in an adaptive sandwich beam with conductive skins. Part II: Dynamic properties.” In: *International Journal of Solids and Structures* 43.17 (2006), pp. 5403–5420.

[Zhou+ 2011] Y. Zhou and F. Amirouche. “An electromagnetically-actuated all-PDMS valveless micropump for drug delivery.” In: *Micromachines* 2.3 (2011), pp. 345–355.

List of Figures

List of Tables

sp|m

Titre : Investigations sur les élastomères magnétoactifs magnétiquement durs et mécaniquement rigides – Des phénomènes d'interactions locales vers le développement de structures fonctionnelles.

Mots clefs: Élastomères MagnétoActifs (stH-MAE), Modélisation multi-échelle, Actionneurs à membranes, Amortissement par frottement

Résumé : Au centre de cette thèse est un élastomère magnétoactif qui est mécaniquement rigide et magnétiquement dur (StH-MAE). Les études expérimentales présentées comprennent l'élaboration du composite ainsi que la caractérisation des propriétés mécaniques, magnétiques et couplées. Un modèle pour la détermination des propriétés effectives du composite est présenté ; il est basé sur des simulations numériques des microstructures statistiquement homogènes. Pour la modélisation du comportement autour du point de fonctionnement du matériau, l'utilisation d'un modèle piézomagnétique est proposé. Les travaux comprennent deux preuves de concept pour l'utilisation des StH-MAE pour les actionneurs à membrane ainsi que pour l'amortissement passif des vibrations. Ces deux exemples mettent en avant l'avantage de l'aimantation rémanente pour les applications mécatroniques futures.

Title : Investigations on magnetically hard and mechanically stiff magnetoactive elastomers – From local interactions towards the development of functional structures.

Keywords : MagnetoActive Elastomers (StH-MAE), multiscale modeling, membrane actuators, vibration damping

Abstract : This doctoral work focuses on a magnetically hard and mechanically stiff magnetoactive elastomer (stH-MAE) composite material. Experimental studies are presented concerning the manufacturing of the composite as well as the characterization of its mechanical, magnetic and coupling properties. A multiscale model is developed using a continuum approach at the microstructural scale with classic homogenization techniques on statistically homogeneous composites. The effective properties are determined with numerical simulations and the behavior law around the operating point of the material is modeled with a piezomagnetic approach. Two proofs of concept are presented using stH-MAE composites for membrane actuators and passive vibration damping. Both concepts are based on the magnetically induced forces resulting from the remnant magnetization and provide promising results for future applications of stH-MAE in mechatronic devices.

UBFC UNIVERSITÉ BOURGOGNE FRANCHE-COMTÉ

Université Bourgogne Franche-Comté
32, avenue de l'Observatoire
25000 Besançon